Metal–Halide Covalency, Exchange Coupling, and Slow Magnetic Relaxation in Triangular $(Cp^{iPr5})_3U_3X_6$ (X = Cl, Br, I) Clusters

Daniel J. Lussier,[†,§] Emi Ito,[†,⊥] K. Randall McClain,[*,δ,⊥] Patrick W. Smith,[§] Hyunchul Kwon,[†] Ryte Rutkauskaite,[†] Benjamin G. Harvey,[δ] David K. Shuh,[*,§] and Jeffrey R. Long[*,†,‡,§,#]

[†]Department of Chemistry and [‡]Department of Chemical and Biomolecular Engineering, University of California, Berkeley, Berkeley, California 94720, United States
[δ]U.S. Navy, Naval Air Warfare Center, Weapons Division, Research Department, Chemistry Division, China Lake, California, 93555, United States
[§]Chemical Sciences Division and [#]Materials Sciences Division, Lawrence Berkeley National Laboratory, Berkeley, California, 94720, United States

Correspondence to: K. Randall McClain, kenneth.r.mcclain7.civ@us.navy.mil; David K. Shuh, dkshuh@lbl.gov; Jeffrey R. Long, jrlong@berkeley.edu

Supporting Information

1. Experimental Procedures

1.1 General Procedures and Considerations.

Depleted uranium (primary isotope ^{238}U) is a weak α-emitter (4.197 MeV) with a half-life of 4.47×10^9 years; all manipulations involving uranium were carried out in a radiation laboratory equipped with α– and β-counting equipment. Unless otherwise specified, all chemical manipulations were performed using Schlenk or glovebox techniques under an atmosphere of purified argon with rigorous exclusion of water and oxygen. Glassware and Celite® were stored in an oven at ca. 150 °C for at least 3 h prior to use. Molecular sieves (4 Å) were activated by heating to 200 °C overnight under vacuum prior to storage in a glove box. Proton NMR spectra were recorded at room temperature, unless otherwise stated, on Bruker AVB-400, AVQ-400, or AV-600 spectrometers. Proton chemical shifts are given relative to residual solvent peaks[1] and are recorded in units of parts per million (ppm). Default (0.3 Hz) line broadening functions were applied to ^1H NMR spectra in MestReNova (version 14.1.2), unless stated otherwise. Fourier-transform infrared (FTIR) spectra were collected inside of a N_2 glovebox on polycrystalline samples using a Shimadzu IRSpirit FTIR spectrometer operating in ATR mode. Elemental analyses were determined at the Microanalytical Facility at the College of Chemistry, University of California, Berkeley. UV-Vis-NIR spectra were collected on a Varian Cary® 5000 UV-Vis-NIR Spectrophotometer. A 1-cm path length quartz cell was used, and a blank was subtracted from each run.

1.2 Materials

The solvents diethyl ether, toluene, tetrahydrofuran (THF), n-hexane, and n-pentane, were sparged with argon and then dried by passing through alumina columns in a Glass Contour solvent purification system from JC Meyer. NMR solvents were purchased from Sigma-Aldrich, and were degassed via several freeze-pump-thaw cycles prior to transferring to a glove box, where they were stored over molecular sieves to dry for at least 48 h prior to use. The compounds sodium pentaisopropylcyclopentadienyl ($NaCp^{iPr5}$)[2,3] and $UI_3(dioxane)_{1.5}$[4] were prepared via previously published methods. Uranium triiodide (UI_3) and UBr_3 were was prepared by a modification of the method of Cloke and Hitchock.[5] Fine uranium powder was synthesized by preparation of UH_3[6] followed by removal of hydrogen under dynamic vacuum at 400 °C. Subsequent heating of the resulting metal powder with a stochiometric amount of either HgI_2 or $HgBr_2$ (in a sealed tube under vacuum at 320 °C) for 2 days afforded the black UI_3 and brown UBr_3 starting materials. The compound 4-*tert*-butylphenol was purchased from Sigma-Aldrich and purified via vacuum sublimation at 50 °C prior to bringing into the glovebox. All other chemicals were purchased from commercial sources and used as received.

1.3 Syntheses.

Attempted Synthesis of Halide-Bridged Uranium Complexes via Salt Metathesis. Using a slightly modified procedure based on the methods used to isolate the halide-bridged dinuclear complexes, $(Cp^{iPr5})_2Ln_2I_4$ (Ln = Y, Gd, Tb, Dy),[7] under argon, UBr_3 (0.2812 g, 0.5886 mmol) and $NaCp^{iPr5}$ (0.1757 g, 0.5886 mmol) were combined in a 100 mL pressure flask containing a glass-coated magnetic stirring bar, then toluene (40 mL) was added. The reaction flask was covered in aluminum foil and then heated gradually to 80 °C with vigorous stirring. The reaction temperature was increased gradually over a period of 8 d, in approximate increments of 5 °C every 24 h, until a final temperature of 120 °C was achieved. The resulting brown slurry was filtered hot (~60 °C) through a Celite-padded coarse-porosity fritted filter and rinsed with additional hot toluene (3 × 5 mL), leaving behind a dark brown solid (presumably unreacted UBr_3). The resulting pale green filtrate was dried under reduced pressure to yield a crude, dark-green solid (0.012 g). X-ray quality crystals were grown from concentrated pentane at −25 °C over the course of 12 h, and single crystal X-ray diffraction analysis revealed the green solid was the metallocene, $(Cp^{iPr5})_2UBr$ (see Figure S34). Similar results were obtained when using UI_3 or $UI_3(dioxane)_{1.5}$, resulting in the isolation of $(Cp^{iPr5})_2UI$.[8]

$KOPh^{tBu}$. Under argon, 4-*tert*-butylphenol (1.0771 g, 7.1702 mmol) was added to a 20-mL borosilicate glass scintillation vial containing a Teflon-coated magnetic stirring bar and 10 mL THF. A solution of potassium bis(trimethylsilyl)amide ($KN(SiMe_3)_2$, 1.4249 g, 7.1430 mmol) in THF (8 mL) was subsequently added slowly, in a dropwise fashion, to the stirring 4-*tert*-butylphenol solution. The reaction mixture was vigorously stirred at 25 °C for 12 h, after which the mixture was filtered through a Celite-padded plug, and the resulting filtrate was placed under reduced pressure to remove THF, yielding a white solid. This solid was subsequently washed with toluene (3 × 8 mL) and hexane (3 × 5 mL) in order to remove any remaining 4-*tert*-butylphenol reactant, as well as residual ethereal solvent; the washed solid was then placed under reduced-pressure to dry for 2 h at 100 °C, leaving behind potassium 4-*tert*-butylphenoxide, $KOPh^{tBu}$, as an analytically pure, white solid (1.2514 g, 93.0% yield). ^{1}H NMR (THF-d_8, 400 MHz, 300 K): δ = 6.89 (d, J = 8.2 Hz, 2 H), 6.24 (d, J = 8.2 Hz, 2 H), 1.19 (s, 9 H). Anal. Calcd for $C_{10}H_{13}KO$: C, 63.78; H, 6.96. Found: C, 63.40; H, 6.71.

Modified synthesis of $U(BH_4)_3(THF)_2$. As a modification of previously reported methods,[9,10] a 200-mL borosilicate glass jar with a Teflon-lined cap was charged with $UI_3(dioxane)_{1.5}$ (5.5000 g, 7.3315 mmol), KBH_4 (1.1338 g, 22.717 mmol), and a Teflon-coated magnetic stirring bar. The mixture was dissolved in 150 mL of THF and allowed to stir vigorously at 25 °C for 5 d, over which time there was a gradual color change from dark blue to dark red. The mixture was filtered through a Celite-padded coarse-porosity fritted filter to remove insoluble KI solids and excess KBH_4. The resulting filtrate was then placed under reduced-pressure to remove THF, leaving behind $U(BH_4)_3(THF)_2$ as an analytically pure, dark red solid (3.0781 g, 98.1 % yield). Anal. Calcd for $C_8H_{28}B_3O_2U$: C, 22.52; H, 6.61. Found: 22.55; H, 6.57.

$(Cp^{iPr5})U(BH_4)_2(THF)$. Under argon, $U(BH_4)_3(THF)_2$ (1.0877 g, 2.5487 mmol) was added to a 200 mL Schlenk flask containing a Teflon-coated magnetic stirring bar, then dissolved in 50 mL of toluene. A suspension of $NaCp^{iPr5}$ (0.7596 g, 2.545 mmol) in toluene (20 mL) was subsequently added dropwise to the $U(BH_4)_3(THF)_2$ solution, resulting in a gradual color change from dark red

to black. The reaction mixture was vigorously stirred at 25 °C for 16 h, after which the mixture was placed under reduced pressure to remove toluene, yielding a crude, black solid, which was further dried under reduced pressure for 2 h. The Schlenk flask was subsequently transferred to a glove box, and the crude solid was dissolved in hexane (50 mL), then filtered through a Celite-padded coarse-porosity fritted filter to remove insoluble $NaBH_4$ solids. The resulting filtrate was then placed under reduced pressure to remove hexane, leaving behind a black solid. This black solid was further purified through recrystallization by dissolving the solid in minimal hot hexane (18 mL, 60 °C) and then allowing the solution to slowly cool, first at room temperature, then at −25 °C for 12 h, yielding $(Cp^{iPr5})U(BH_4)_2(THF)$ as dark black-green crystals (0.4859 g). The remaining mother liquor was subsequently concentrated to a volume of 2 mL, then stored at −25 °C to yield a second crop of $(Cp^{iPr5})U(BH_4)_2(THF)$ crystals (0.3327 g, total yield 0.8186 g, 52.3% yield). X-ray quality crystals were obtained by storing a concentrated hexane solution of $(Cp^{iPr5})U(BH_4)_2(THF)$ into a 4 mL borosilicate glass scintillation vial −25 °C for 12 h. ^{1}H NMR (THF-d_8, 400 MHz, 300 K): δ = 9.51 (br s, CH_3 from Cp^{iPr5}, 15 H), 5.33 (s, CH from Cp^{iPr5}, 5 H) −13.76 (vbr s, BH_4), −22.93 (br s, CH_3 from Cp^{iPr5}, 15 H). Anal. Calcd for $C_{24}H_{51}B_2OU$: C, 46.85; H, 8.35. Found: C, 47.09; H, 8.23.

$(Cp^{iPr5})U_2(OPh^{tBu})_4$. Under argon, $(Cp^{iPr5})U(BH_4)_2(THF)$ (0.7094 g, 1.153 mmol) was added to a 200 mL Schlenk flask containing a Teflon-coated magnetic stirring bar, then dissolved in 40 mL of toluene. A suspension of $KOPh^{tBu}$ (0.4346 g, 2.308 mmol) in toluene (15 mL) was added dropwise to the $(Cp^{iPr5})U(BH_4)_2(THF)$ solution, resulting in a color change from black to a dark red-brown. The reaction mixture was vigorously stirred at 25 °C for 12 h, after which time the mixture was placed under reduced pressure to remove toluene, yielding a black, crude solid, which was allowed to further dry for 2 h. The Schenk flask was subsequently transferred to a glove box, and the crude solid was dissolved in pentane (70 mL), then filtered through a Celite-padded porous fritted filter to remove insoluble, gray KBH_4 solids. The resulting dark red-brown filtrate was then placed under reduced pressure to remove pentane, and the resulting black solid was allowed to further dry for 1 h under reduced pressure at ambient temperature, yielding $(Cp^{iPr5})_2U_2(OPh^{tBu})_4$ as an analytically pure red-brown solid (0.7341 g, 78.4 % yield). X-ray quality crystals were grown from a concentrated pentane solution of $(Cp^{iPr5})_2U_2(OPh^{tBu})_4$ stored at −25 °C for 2 d. ^{1}H NMR (benzene-d_6, 400 MHz, 300 K): δ = 24.09, 19.16, 16.44, 14.58, 13.71, 11.34, 10.52, 6.26, 5.72, 5.04, 2.54, 1.06, 0.29, −2.76, −5.80, −8.68, −25.30, −37.48, −38.83, −50.30. Peak assignments were made difficult by the restricted rotation of the U–Cp^{iPr5} bond, resulting in each –*i*Pr substituent being inequivalent with respect to the other substituents. In total, 20 out of the 21 total possible peaks could be found. Restricted rotation of U–Cp bonds have previously led to complicated NMR spectra in uranium metallocenes of the form $(Cp^{iPr4H})_2UX_2$ (X = F, Cl, Br, and I).[11] Proton NMR measurements performed at higher temperatures (Figure S5) did not improve our attempts to assign resonances for this complex. Anal. Calcd for $C_{80}H_{122}O_4U_2$: C, 59.17; H, 7.57. Found: C, 59.49; H, 7.47.

$(Cp^{iPr5})_3U_3Cl_6$ (1-Cl). Under argon, $(Cp^{iPr5})_2U_2(OPh^{tBu})_4$ (0.7096 g, 0.4370 mmol) was placed inside a 20 mL borosilicate glass scintillation vial with a Teflon-coated magnetic stirring bar, then dissolved in 10 mL of toluene. Subsequently, an excess of chlorotrimethylsilane (0.230 g, 2.117 mmol, 0.269 mL) was added dropwise and the reaction mixture was stirred vigorously at 25 °C for 1 week, during which time a gradual color change occurred, from dark red-brown to navy blue. The navy blue solution was placed under reduced pressure to remove toluene and unreacted

Me_3SiCl, yielding a crude, dark blue solid that was allowed to further dry for 1 h under reduced pressure at ambient temperature. This crude solid was further purified by dissolving in minimal hot pentane (5 mL, 35 °C), then storing at −25 °C for 12 h, yielding $(Cp^{iPr5})_3U_3Cl_6$ as dark navy blue crystals (0.1674 g, 32.8 % yield). X-ray quality crystals of $(Cp^{iPr5})_3U_3Cl_6$ were obtained from a concentrated pentane solution stored at −25 °C for 2 d. ^{1}H NMR (benzene-d_6, 400 MHz, 300 K): δ = 13.51 (broad, CH_3 from Cp^{iPr5}, 45 H), 8.75 (broad, CH from Cp^{iPr5}, 15 H), −27.81 (broad, CH_3 from Cp^{iPr5}, 45 H). Anal. Calcd for $C_{60}H_{105}Cl_6U_3$: C, 41.10; H, 6.04. Found: C, 41.49; H, 6.10.

$(Cp^{iPr5})_3U_3Br_6$ (1-Br). Under argon, $(Cp^{iPr5})_2U_2(OPh^{tBu})_4$ (0.6731 g, 0.4145 mmol) was placed inside a 20 mL borosilicate glass scintillation vial with a Teflon-coated magnetic stirring bar, then dissolved in 12 mL of toluene. Subsequently, an excess of bromotrimethylsilane (0.3211 g, 2.097 mmol, 0.277 mL) was added dropwise and the reaction mixture was stirred vigorously at 25 °C for 4 d, during which time a gradual color change occurred, from dark red-brown to navy blue. The navy blue solution was placed under reduced pressure to remove toluene and unreacted Me_3SiBr, yielding a crude, dark blue solid that was allowed to dry for an additional 1 h under reduced pressure at ambient temperature. This crude solid was further purified by dissolving in minimal hot pentane (10 mL, 35 °C), then storing at −25 °C for 12 h, yielding $(Cp^{iPr5})_3U_3Br_6$ as dark navy blue crystals (0.2254 g). The remaining supernatant was further concentrated to 2 mL, then stored at −25 °C for 1 d, yielding a second crop of dark blue crystals (0.1821 g, total mass of 0.4075 g, 73.0 % yield). X-ray quality crystals of $(Cp^{iPr5})_3U_3Br_6$ were obtained from a concentrated hexane solution stored at −25 °C for 2 d. ^{1}H-NMR (benzene-d_6, 400 MHz, 300 K): δ = 13.98 (broad, CH_3 from Cp^{iPr5}, 45 H), 9.10 (broad, CH from Cp^{iPr5}, 15 H), −25.73 (broad, CH_3 from Cp^{iPr5}, 45 H). Anal. Calcd for $C_{60}H_{105}Br_6U_3$: C, 35.68; H, 5.24. Found: C, 35.89; H, 5.17.

$(Cp^{iPr5})_3U_3I_6$ (1-I). Under argon, $(Cp^{iPr5})_2U_2(OPh^{tBu})_4$ (0.5226 g, 0.3218 mmol) was placed inside a 20 mL borosilicate glass scintillation vial with a Teflon-coated magnetic stirring bar, then dissolved in 10 mL of toluene. Subsequently, an excess of iodotrimethylsilane (0.330 g, 1.649 mmol, 0.235 mL) was added dropwise and the reaction mixture was stirred vigorously at 25 °C for 2 d, during which time a color change occurred, from dark red-brown to blue-green. The blue-green solution was placed under reduced pressure to remove toluene and unreacted Me_3SiI, yielding a crude solid that was allowed to further dry for 1 h under reduced pressure at ambient temperature. This crude solid was then dissolved in pentane (10 mL) and filtered through a Celite-padded plug to remove insoluble, dark blue solids. The resulting dark green filtrate was concentrated to a volume of 1 mL, then stored at −25 °C for 12 h, yielding a teal-blue solid at the bottom of the vial. The green mother liquor was decanted from the teal-blue solid, and this solid was washed with cold pentane (−25 °C, 3 × 1 mL) until the initially olive-green colored washes turned teal-blue. The remaining teal-blue solid, $(Cp^{iPr5})_3U_3I_6$ was analytically pure by elemental analysis (0.044 g, 9.0 % yield). X-ray quality crystals of $(Cp^{iPr5})_3U_3I_6$ were obtained from a concentrated toluene solution stored at −25 °C for 2 d. ^{1}H NMR (benzene-d_6, 400 MHz, 300 K): δ = 14.39 (v broad, CH_3 and CH from Cp^{iPr5}, 60 H), −23.43 (v broad, CH_3 from Cp^{iPr5}, 45 H). Anal. Calcd for $C_{60}H_{105}I_6U_3$: C, 31.31; H, 4.60. Found: C, 31.69; H, 4.36.

2. NMR Spectroscopy

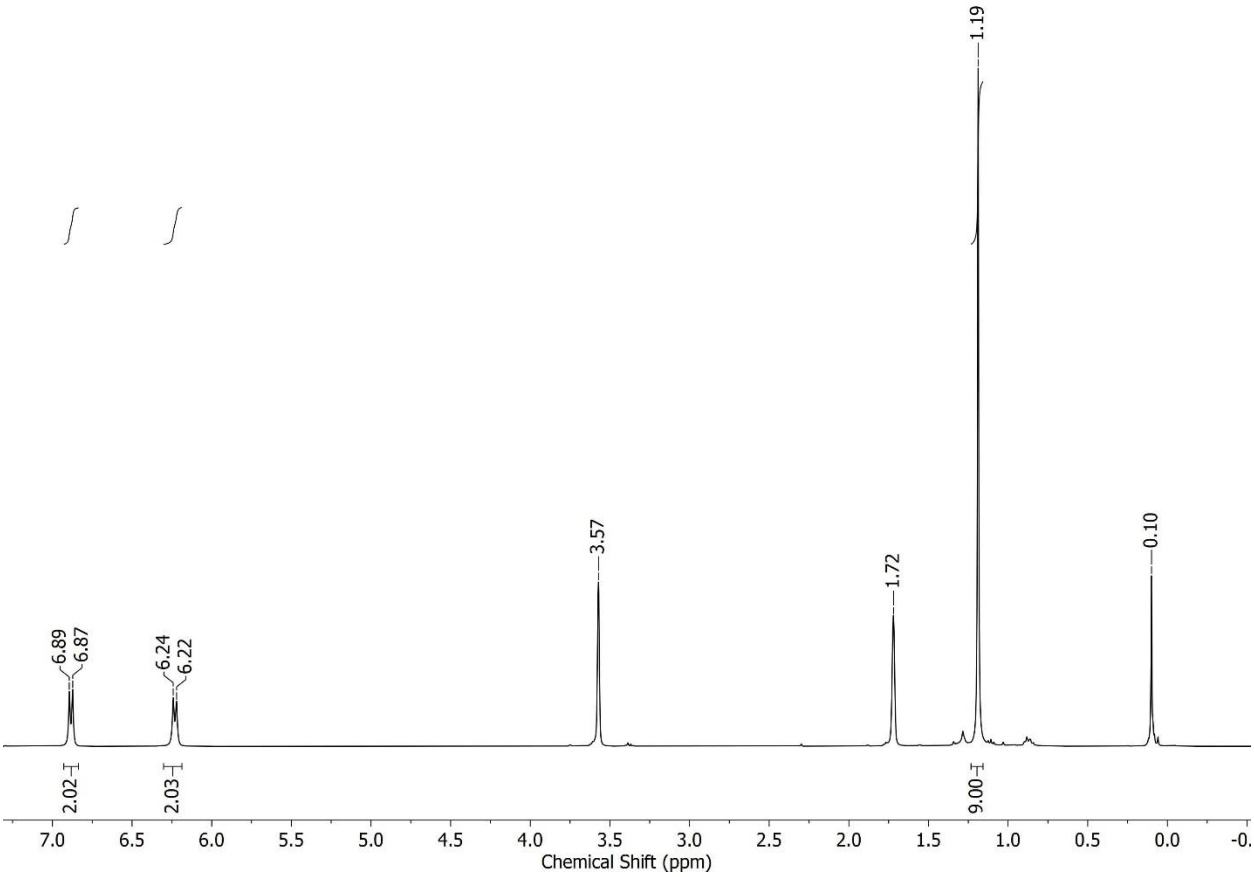

Figure S1. Proton NMR spectrum of KOPh$^{t\mathrm{Bu}}$ in THF-d_8. The peak at 0.10 ppm is due to a minor amount of hexamethyldisilazane ($HN(SiMe_3)_2$) side-product.

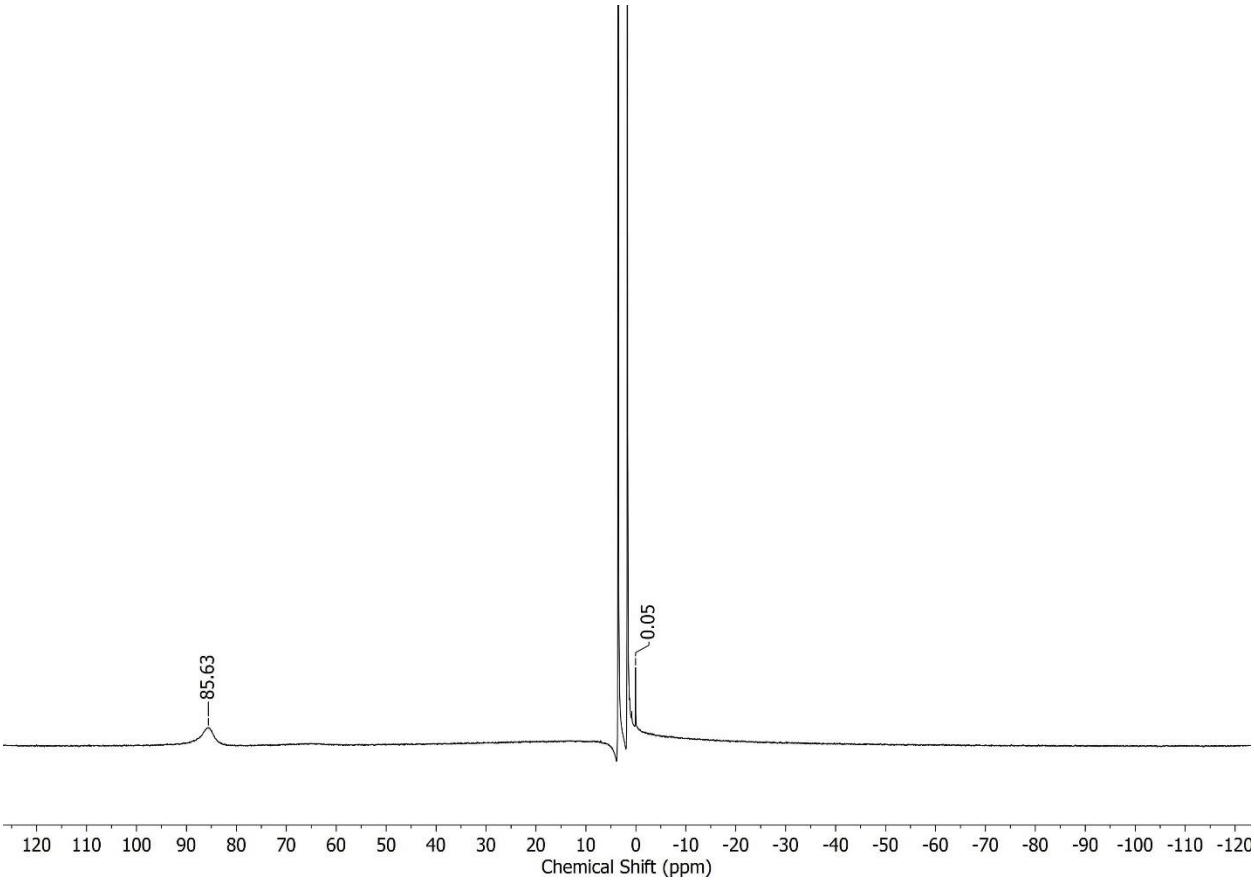

Figure S2. Proton NMR spectrum of $U(BH_4)_3(THF)_2$ in THF-d_8. The resonance at δ = 86.63 ppm is consistent with borohydride protons, as previously reported.[9]

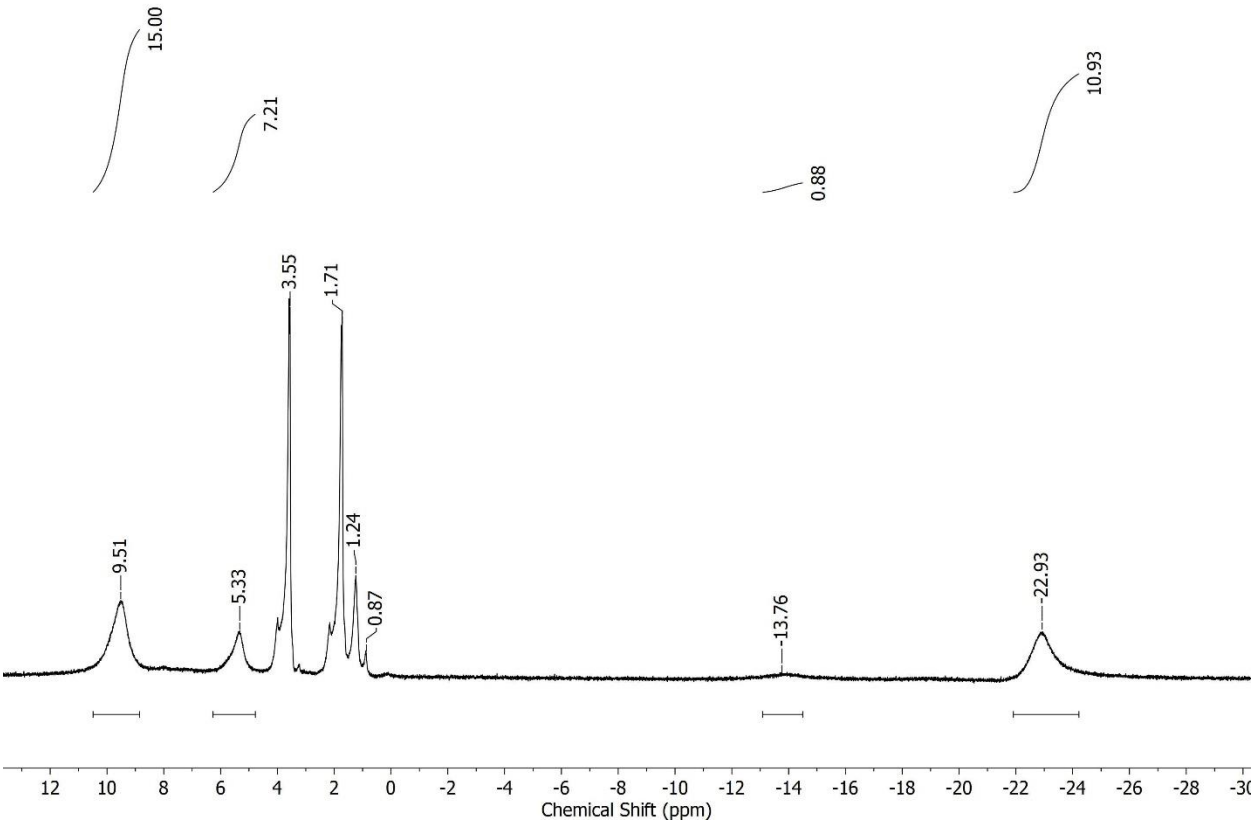

Figure S3. Proton NMR spectrum of $(Cp^{iPr5})U(BH_4)_2(THF)$ in THF-d_8. Minor quantities of organic impurities, namely n-pentane (0.87 ppm and 1.24 ppm) appear as much sharper peaks and are thus visible despite low concentrations relative to $(Cp^{iPr5})U(BH_4)_2(THF)$.

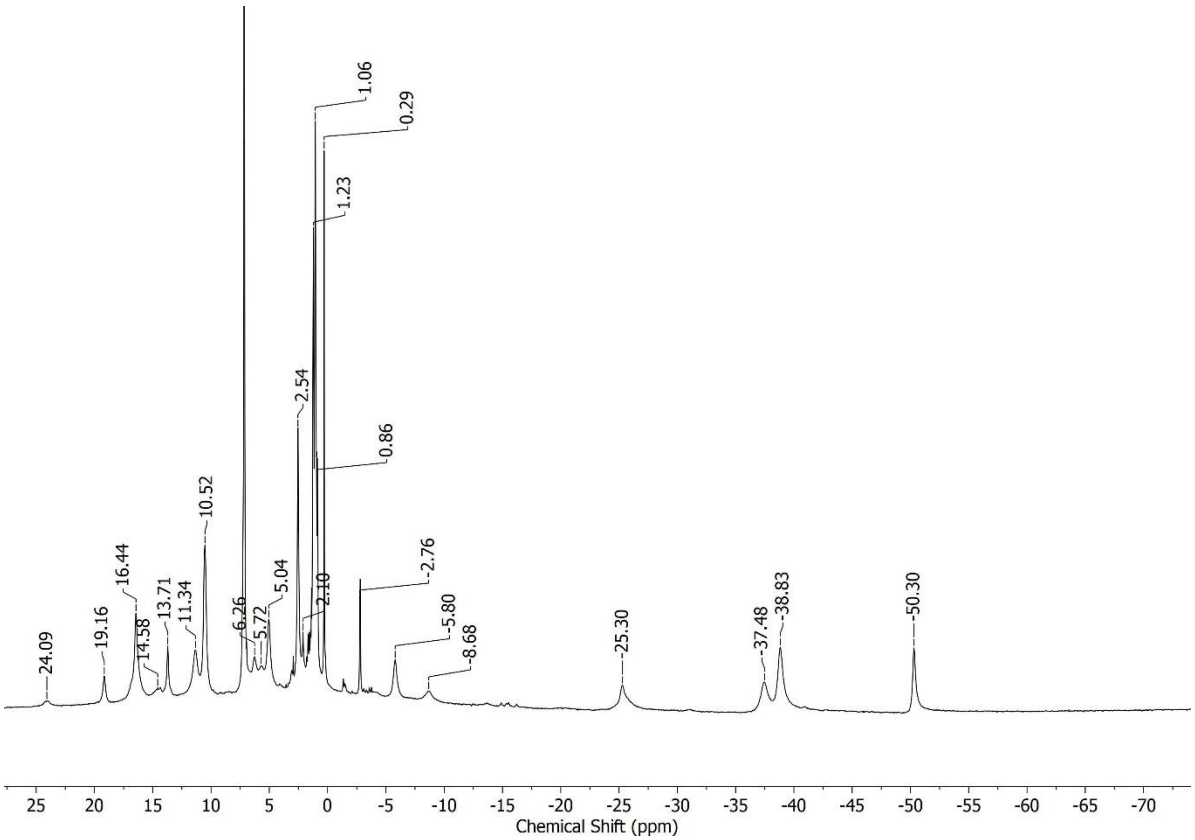

Figure S4. Proton NMR spectrum of $(Cp^{iPr5})_2U_2(OPh^{tBu})_4$ in C_6D_6 at room temperature. Minor quantities of organic impurities, namely n-pentane (0.86 ppm and 1.23 ppm) and toluene (2.10 ppm) appear as much sharper peaks and are thus visible despite low concentrations relative to $(Cp^{iPr5})_2U_2(OPh^{tBu})_4$. Peak assignments were made difficult for this complex because of the restricted rotation of the U–Cp^{iPr5} bond, such that each –*i*Pr substituent is inequivalent with respect to each other, resulting in—when accounting for the two types of –OPh^{tBu} ligands—21 possible peaks, in total.

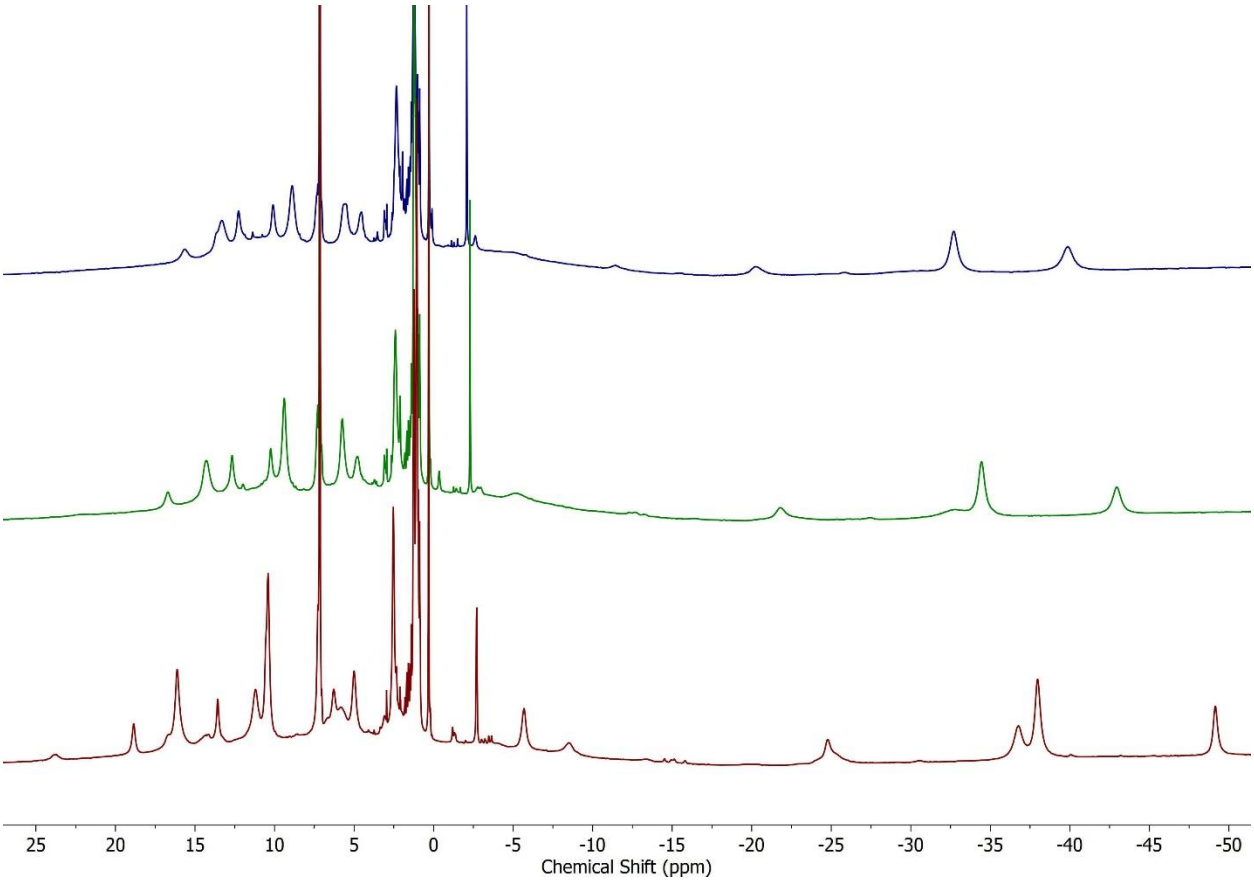

Figure S5. Variable-temperature ^{1}H NMR spectra of $(Cp^{iPr5})_2U_2(OPh^{tBu})_4$ in C_6D_6 taken at 65 °C (top, blue), 50 °C (middle, green), and 25 °C (bottom, red). Spectra were collected on a Bruker AV-600 spectrometer.

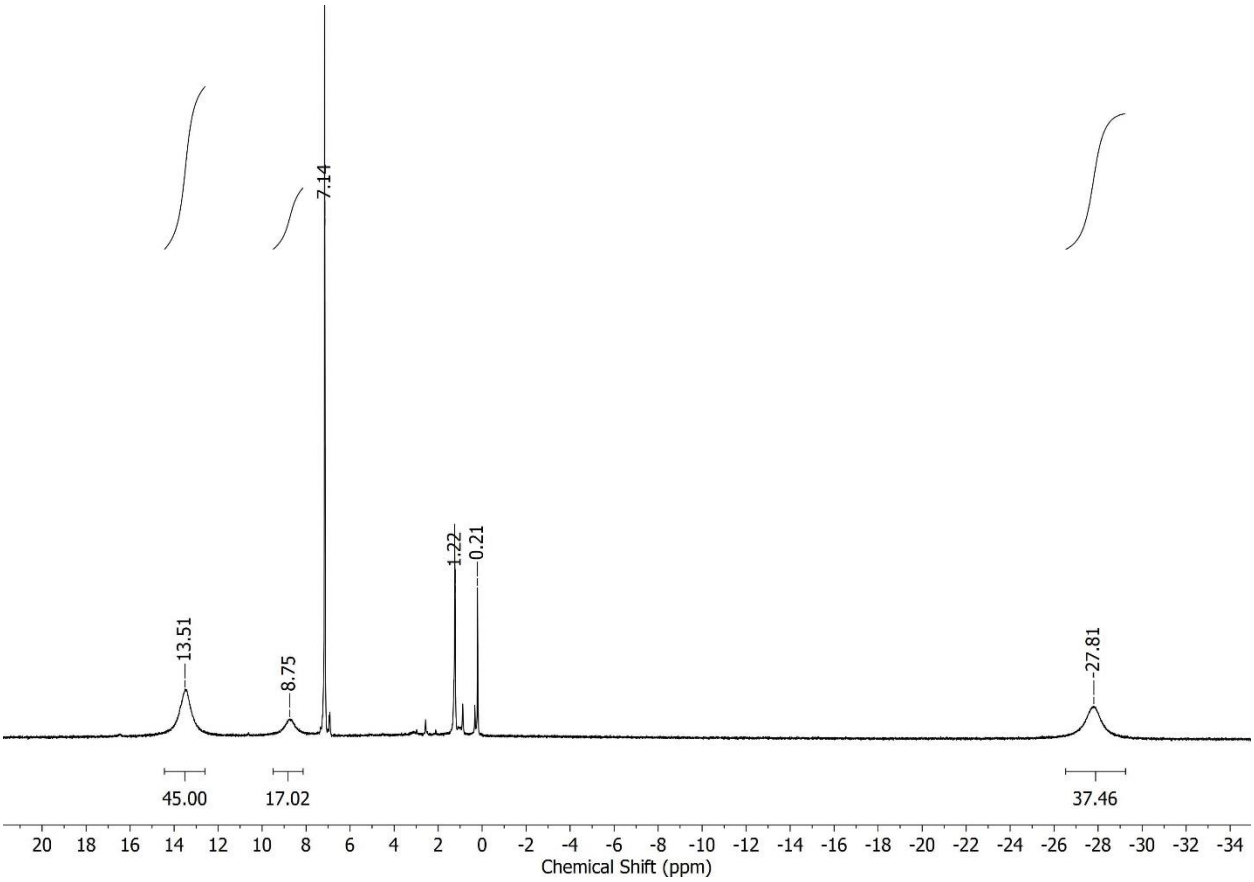

Figure S6. Proton NMR spectrum of $(Cp^{iPr5})_3U_3Cl_6$ (**1-Cl**) in C_6D_6. Minor quantities of organic impurities, namely the trimethyl(4-*tert*-butylphenoxy)silane (0.21, $–SiMe_3$) side-product, appear as much sharper peaks and are thus visible despite low concentrations relative to **1-Cl**.

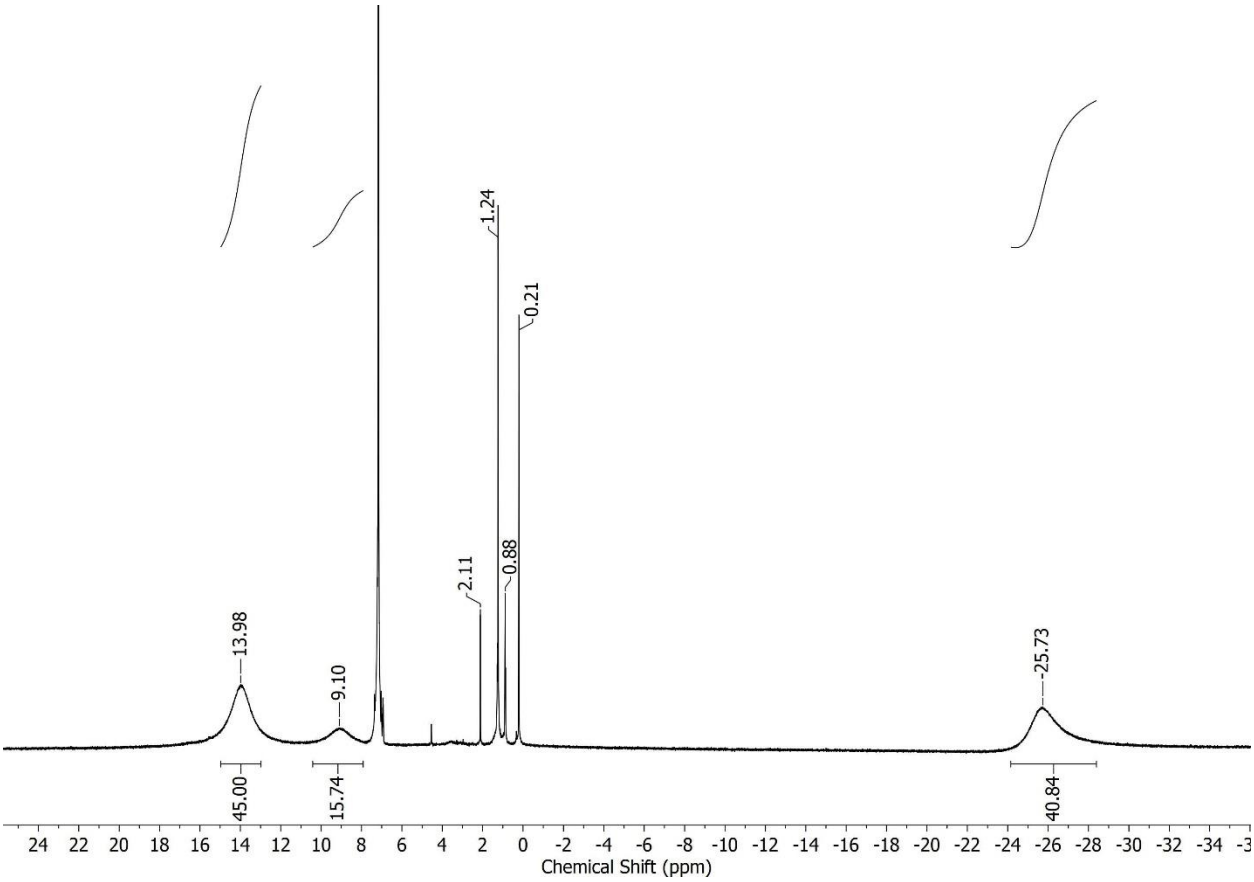

Figure S7. Proton NMR spectrum of $(Cp^{iPr5})_3U_3Br_6$ (**1-Br**) in C_6D_6. Minor quantities of organic impurities, namely n-pentane (0.88 ppm and 1.24 ppm), toluene (2.11 ppm), and the trimethyl(4-*tert*-butylphenoxy)silane (0.21, $–SiMe_3$) side-product, appear as much sharper peaks and are thus visible despite low concentrations relative to **1-Br**.

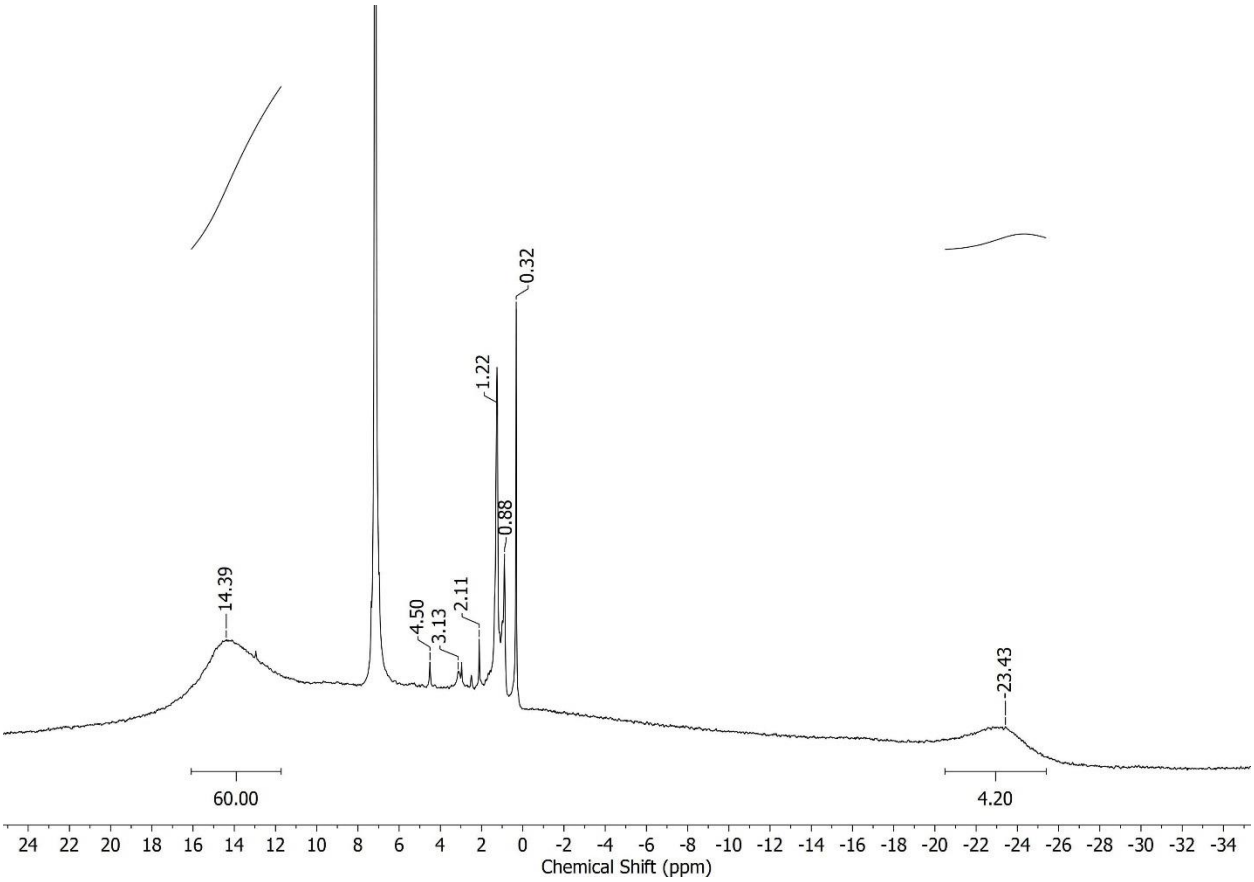

Figure S8. Proton NMR spectrum of $(Cp^{iPr5})_3U_3I_6$ (**1-I**) in C_6D_6. Minor quantities of organic impurities, namely n-pentane (0.88 ppm and 1.23 ppm) and toluene (2.11 ppm) appear as much sharper peaks and are thus visible despite low concentrations relative to **1-I**. The peaks assignable to **1-I** (14.39 ppm and −23.43 ppm) are extremely broad and a 10 Hz line broadening function was applied to the spectrum to better assist in identifying them, further revealing the presence of very small quantities of unknown impurities at 4.50 ppm and 3.13 ppm, as well as an extremely broad paramagnetic feature between 24 ppm and −12 ppm, making accurate comparison of the peak integrations for **1-I** difficult.

3. IR Spectroscopy

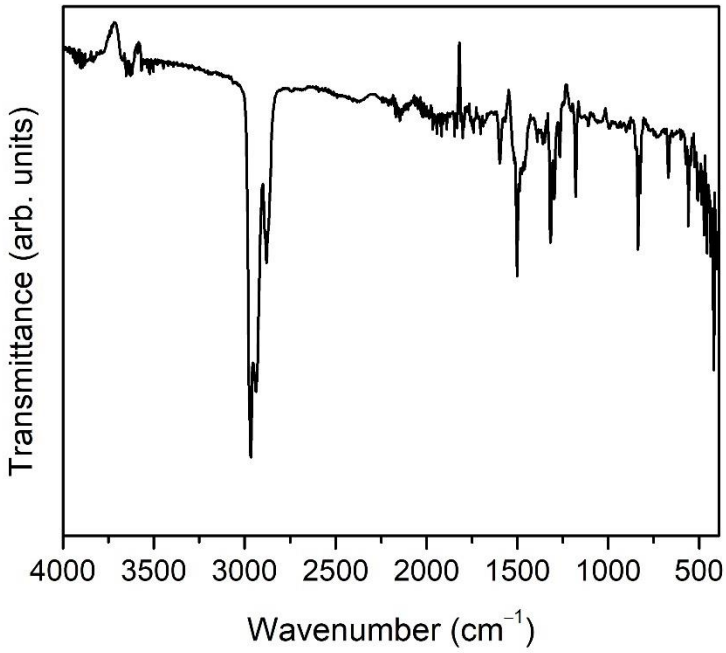

Figure S9. IR spectrum of KOPh^{tBu} at 25 °C.

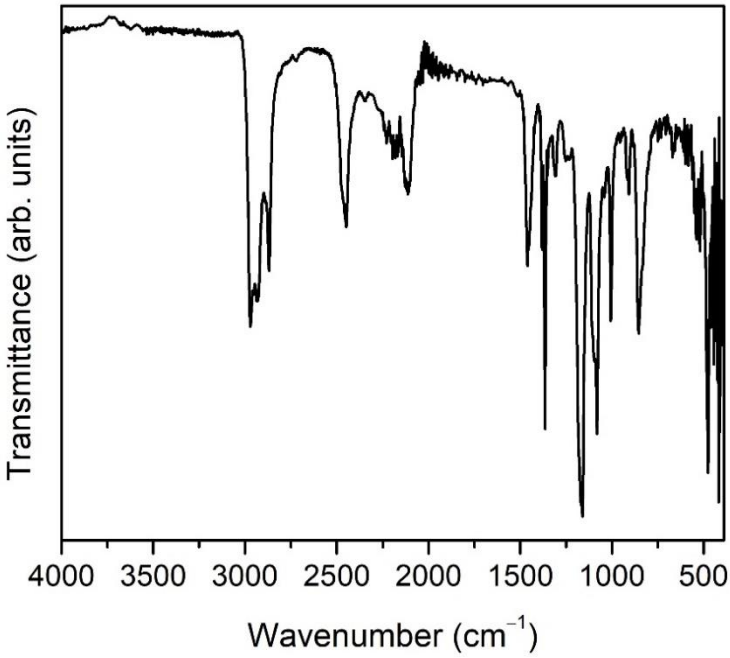

Figure S10. IR spectrum of (Cp^{iPr5})U(BH$_4$)$_2$(THF) at 25 °C.

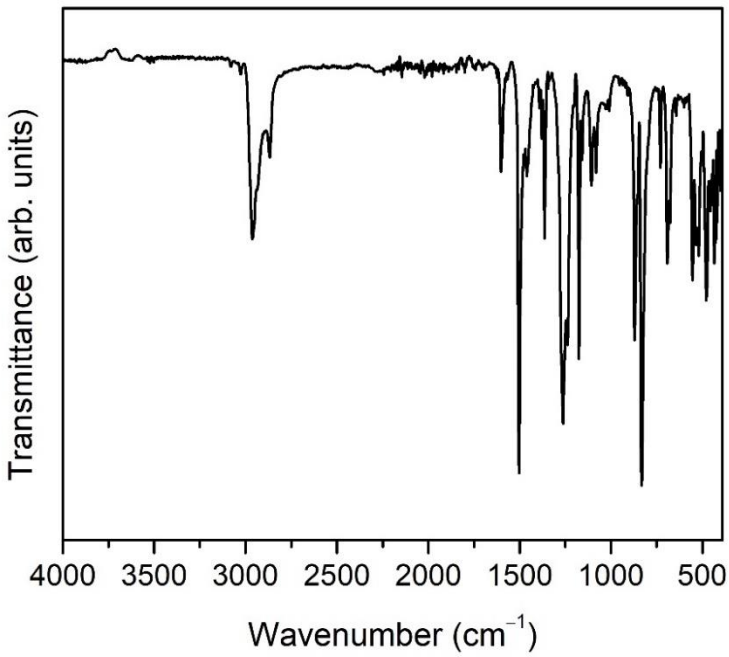

Figure S11. IR spectrum of $(Cp^{iPr5})_2U_2(OPh^{tBu})_4$ at 25 °C.

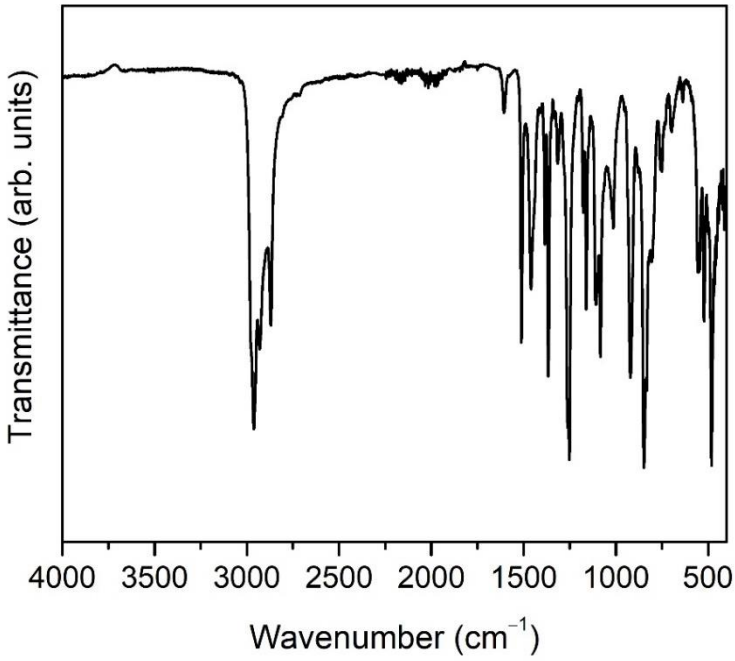

Figure S12. IR spectrum of $(Cp^{iPr5})_3U_3Cl_6$ (**1-Cl**) at 25 °C.

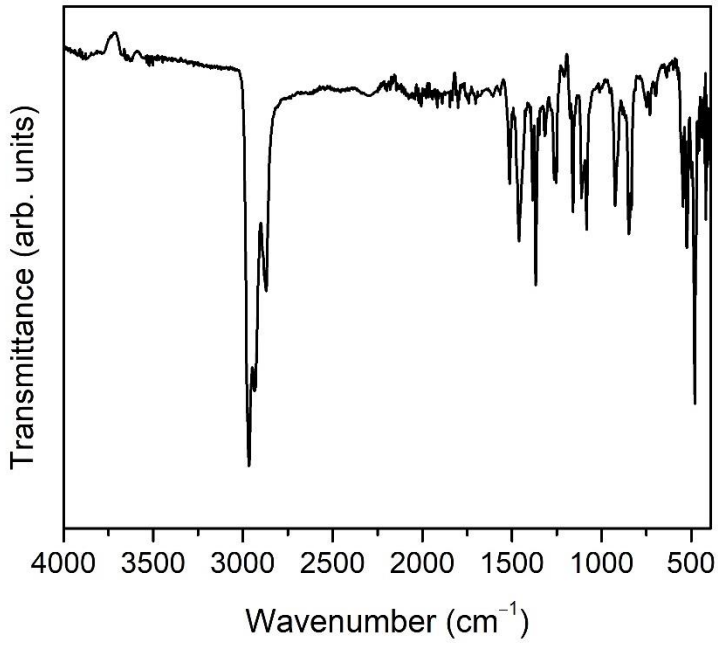

Figure S13. IR spectrum of $(Cp^{iPr5})_3U_3Br_6$ (**1-Br**) at 25 °C.

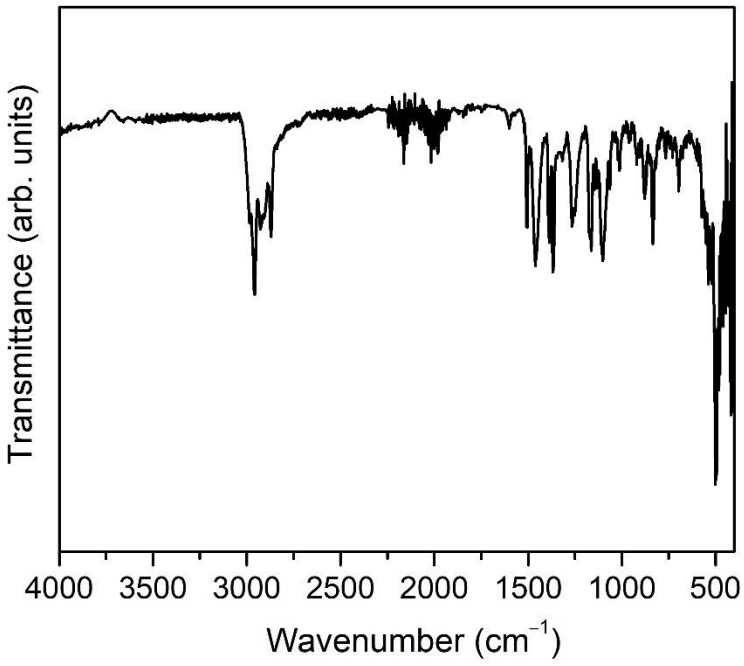

Figure S14. IR spectrum of $(Cp^{iPr5})_3U_3I_6$ (**1-I**) at 25 °C.

4. UV-Vis-NIR Spectroscopy

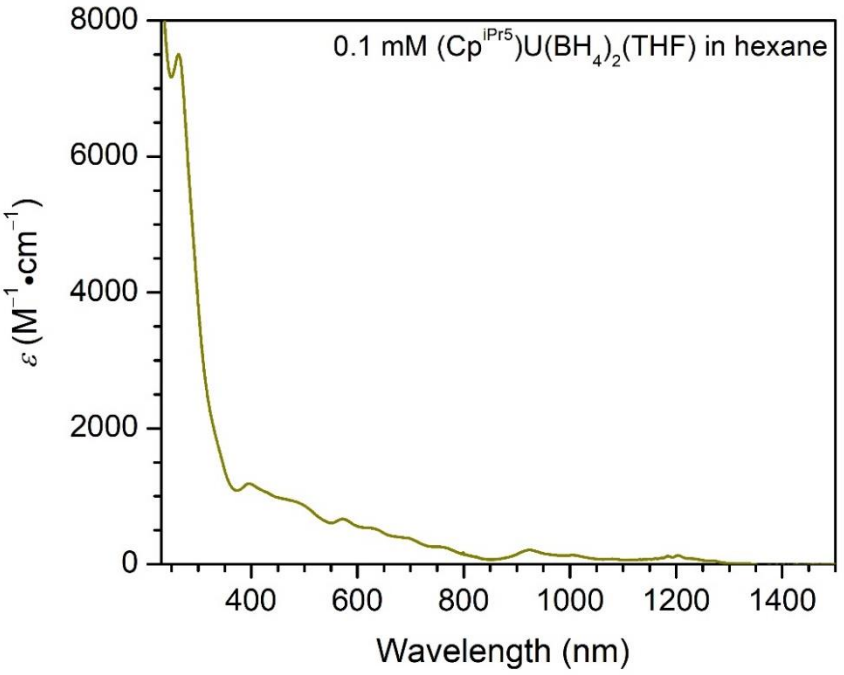

Figure S15. Full UV-Vis-NIR spectrum of $(Cp^{iPr5})U(BH_4)_2(THF)$ between 230 and 1500 nm, collected at 25 °C.

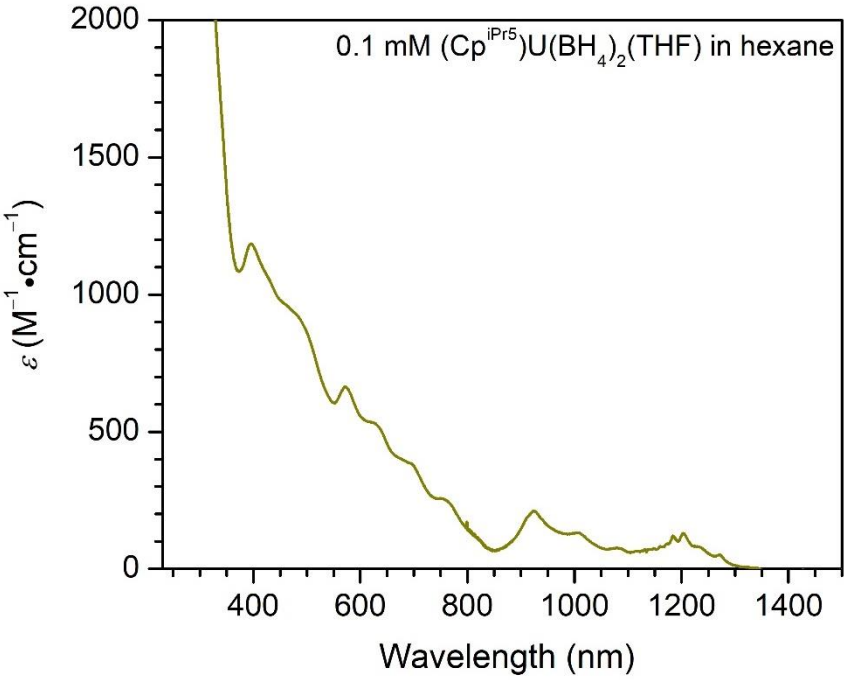

Figure S16. Portion of the UV-Vis-NIR spectrum of $(Cp^{iPr5})U(BH_4)_2(THF)$ between 230 and 1500 nm, collected at 25 °C, with focus on absorption features below 2000 $M^{-1}cm^{-1}$.

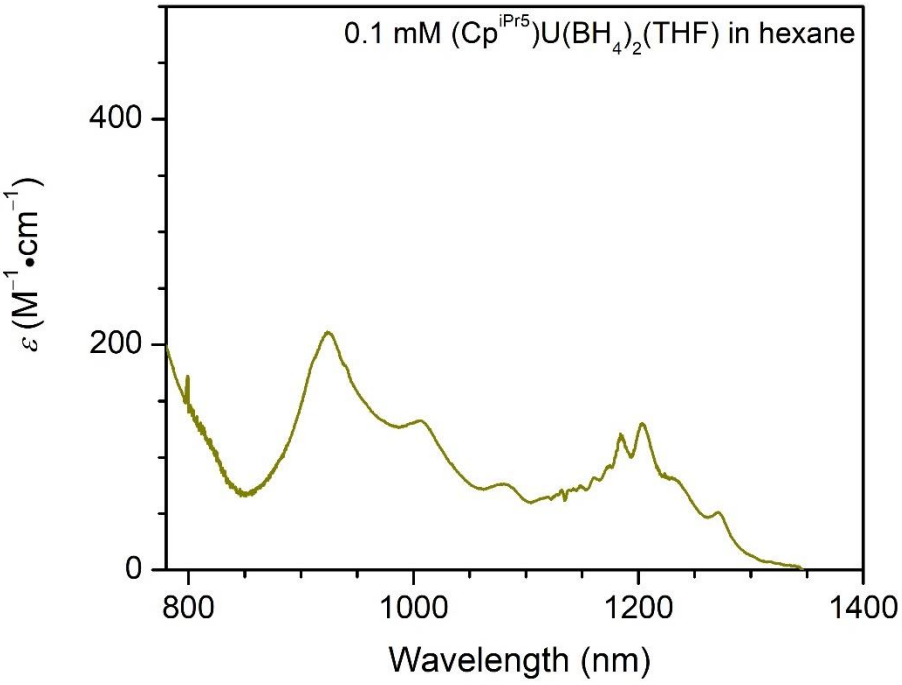

Figure S17. Near-IR spectrum of $(Cp^{iPr5})U(BH_4)_2(THF)$ between 780 and 1500 nm, at 25 °C. The narrow spike around 800 nm is an instrument artifact.

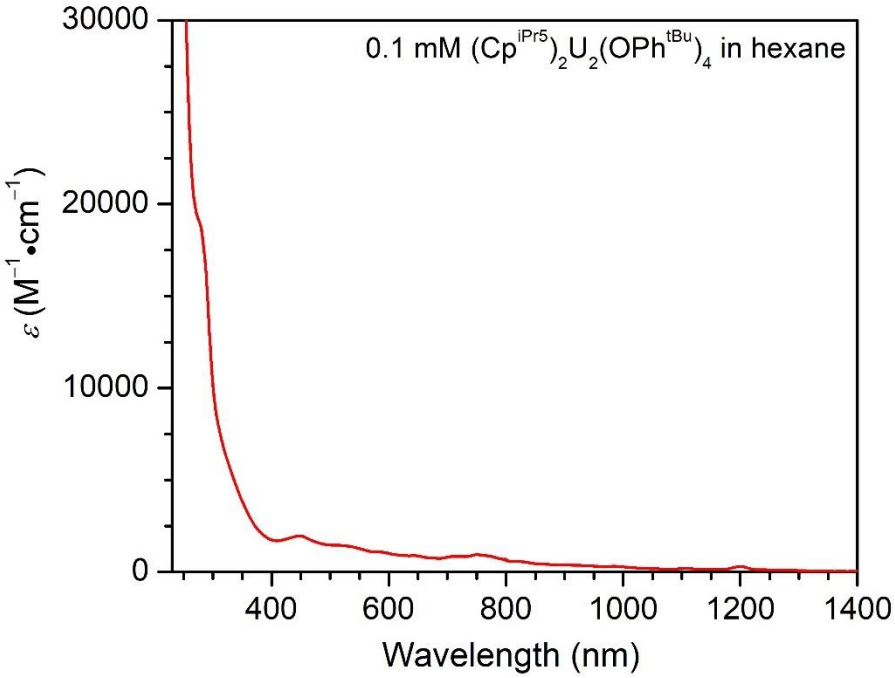

Figure S18. UV-Vis-NIR spectrum of a 0.1 mM solution of $(Cp^{iPr5})_2U_2(OPh^{tBu})_4$ in hexane at 25 °C.

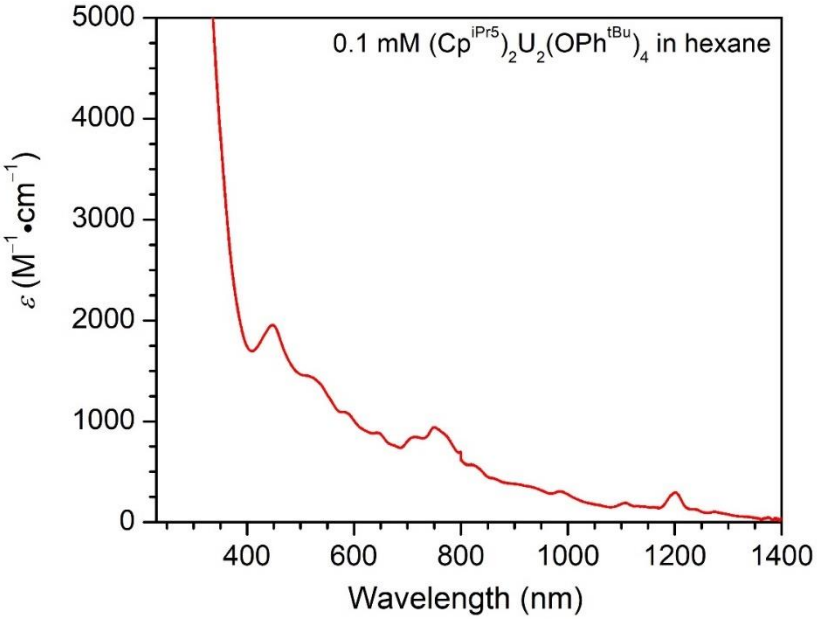

Figure S19. UV-Vis-NIR spectrum of a 0.1 mM solution of $(Cp^{iPr5})_2U_2(OPh^{tBu})_4$ in hexane at 25 °C.

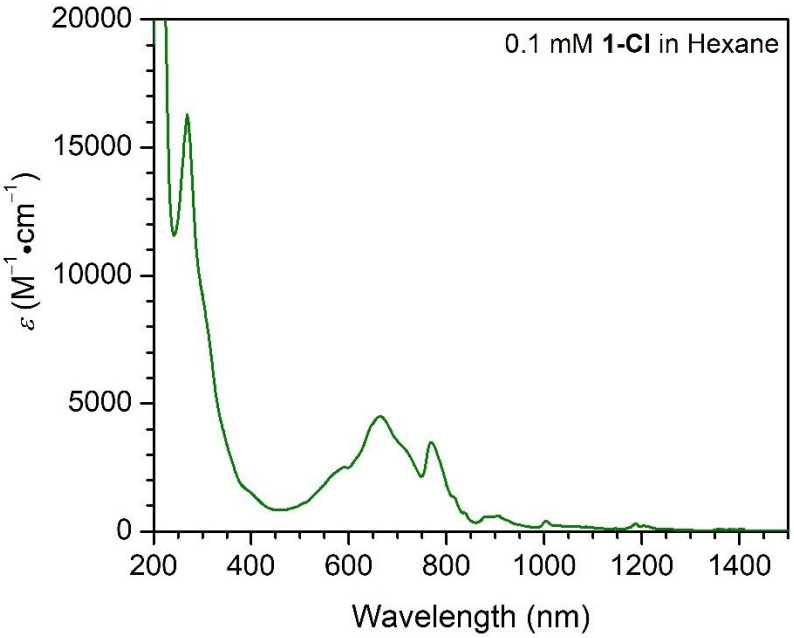

Figure S20. UV-Vis-NIR spectrum of a 0.1 mM solution of $(Cp^{iPr5})_3U_3Cl_6$ (**1-Cl**) in hexane at 25 °C, between 200 and 1500 nm.

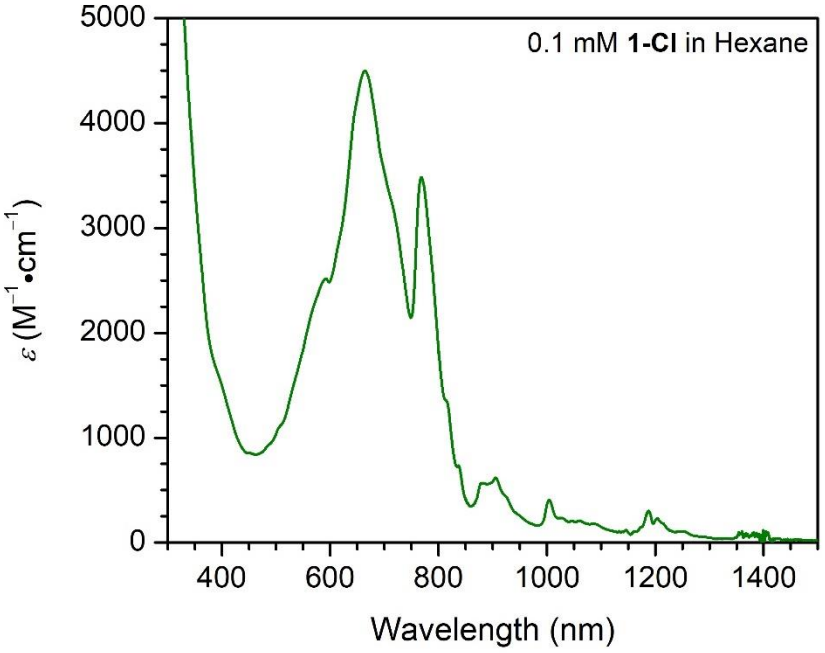

Figure S21. Expanded view of the UV-Vis-NIR spectrum of a 0.1 mM solution of $(Cp^{iPr5})_3U_3Cl_6$ (**1-Cl**) in hexane at 25 °C (300 to 1500 nm) highlighting visible and near-IR features.

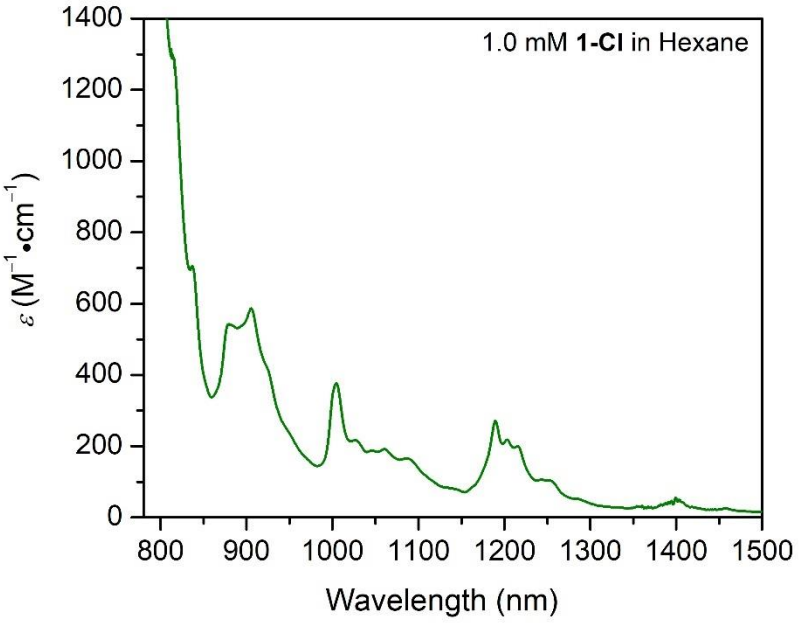

Figure S22. Near-IR spectrum of a 1.0 mM solution of $(Cp^{iPr5})_3U_3Cl_6$ (**1-Cl**) in hexane at 25 °C, between 780 and 1500 nm.

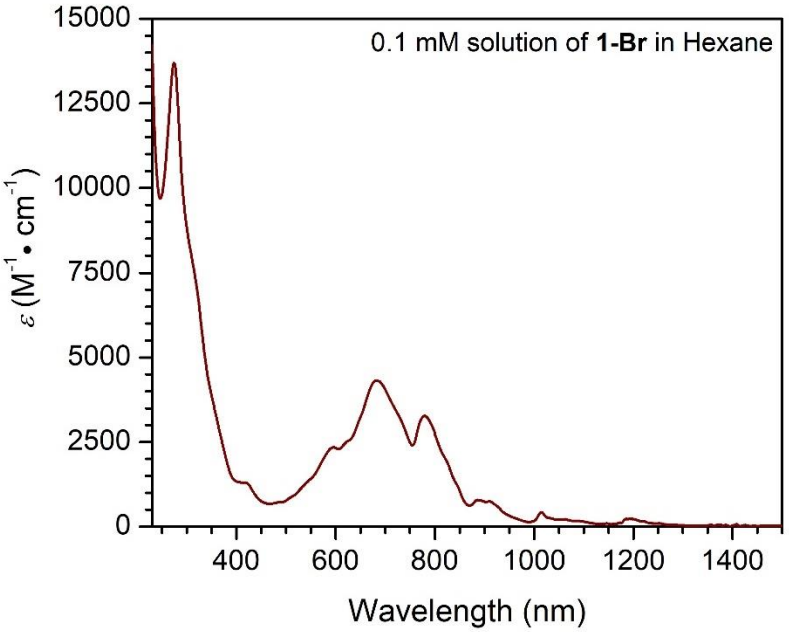

Figure S23. UV-Vis-NIR spectrum of a 0.1 mM solution of $(Cp^{iPr5})_3U_3Br_6$ (**1-Br**) in hexane at 25 °C, between 200 and 1500 nm.

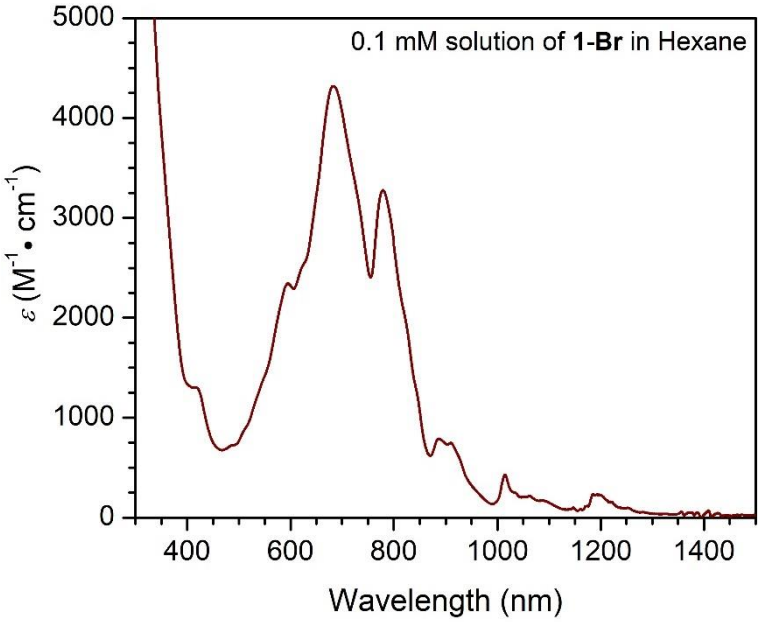

Figure S24. Expanded view of the UV-Vis-NIR spectrum of a 0.1 mM solution of $(Cp^{iPr5})_3U_3Br_6$ (**1-Br**) in hexane at 25 °C, between 300 and 1500 nm, highlighting visible and near-IR features.

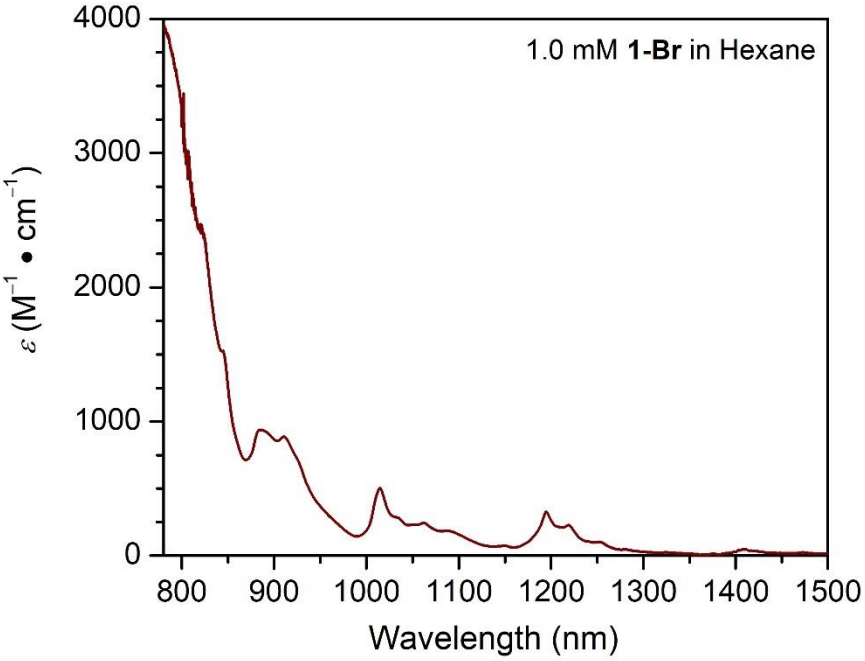

Figure S25. Near-IR spectrum of a 1.0 mM solution of $(Cp^{iPr5})_3U_3Br_6$ (**1-Br**) in hexane at 25 °C, between 780 and 1500 nm.

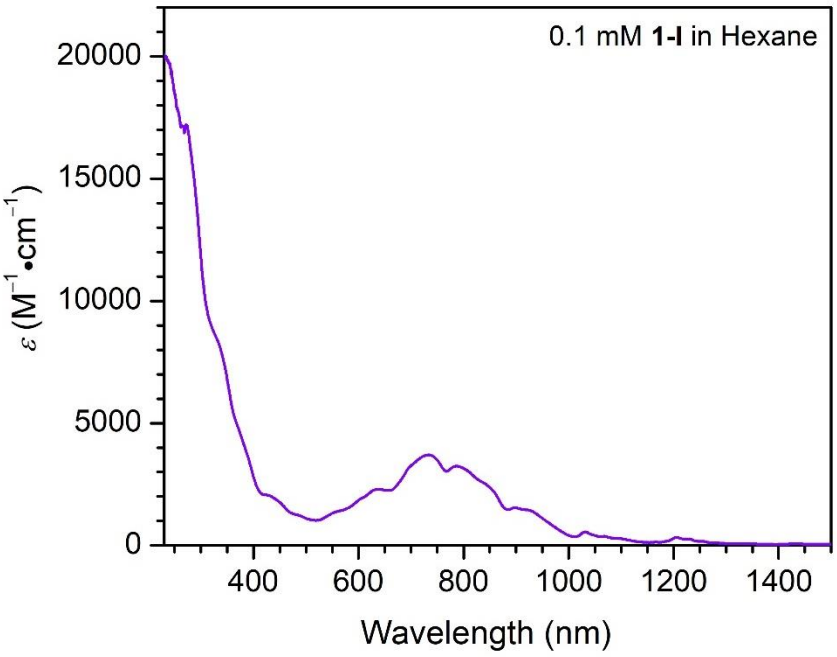

Figure S26. Full UV-Vis-NIR spectrum of a 0.1 mM solution of $(Cp^{iPr5})_3U_3I_6$ (**1-I**) in hexane at 25 °C.

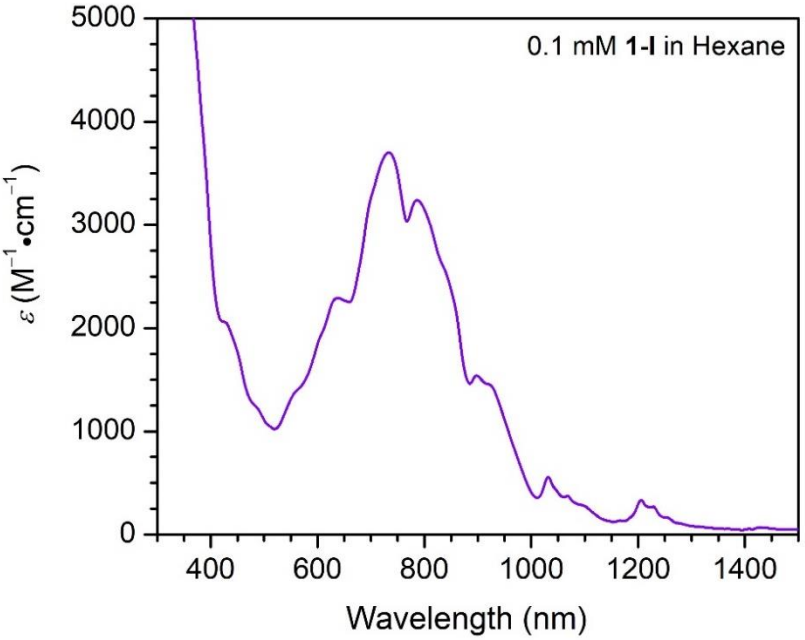

Figure S27. Expanded view of the UV-Vis-NIR spectrum of a 0.1 mM solution of $(Cp^{iPr5})_3U_3I_6$ (**1-I**) in hexane at 25 °C highlighting visible and near-IR features.

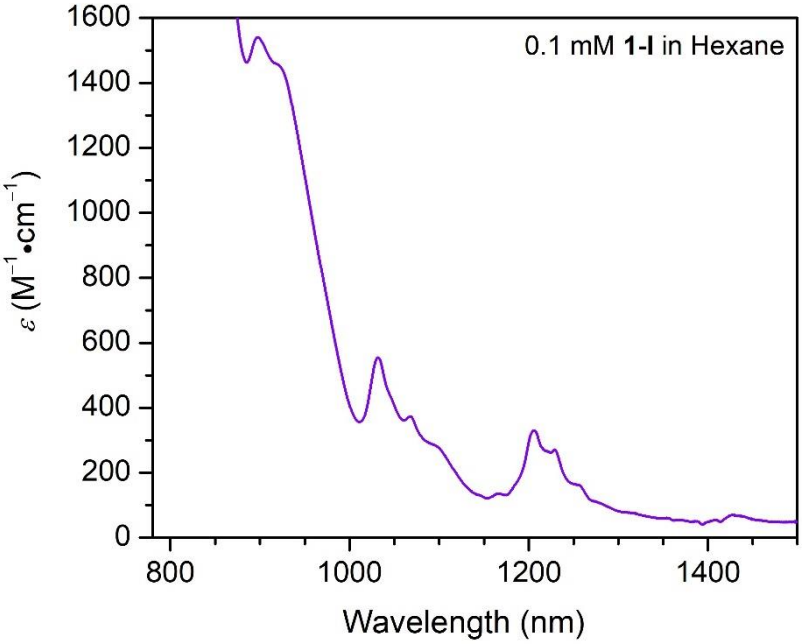

Figure S28. Near-IR spectrum of a 0.1 mM solution of $(Cp^{iPr5})_3U_3I_6$ (**1-I**) in hexane at 25 °C, between 780 and 1500 nm.

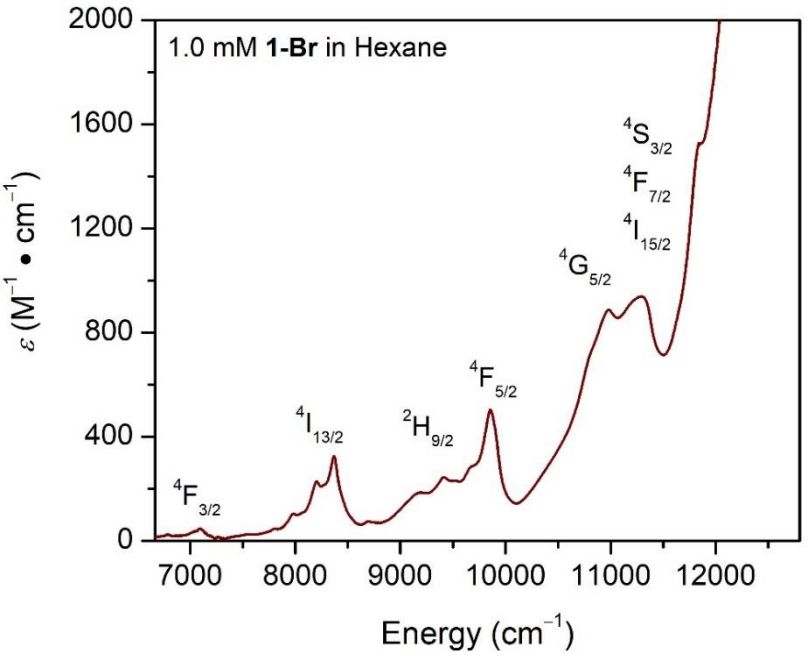

Figure S29. Near-IR spectrum of a 1.0 mM solution of $(Cp^{iPr5})_3U_3Br_6$ (**1-Br**) in hexane at 25 °C, between 6670 and 12800 cm^{-1}, with assignments of the f → f transitions, based on features previously reported for uranium formate and other uranium complexes.[12,13]

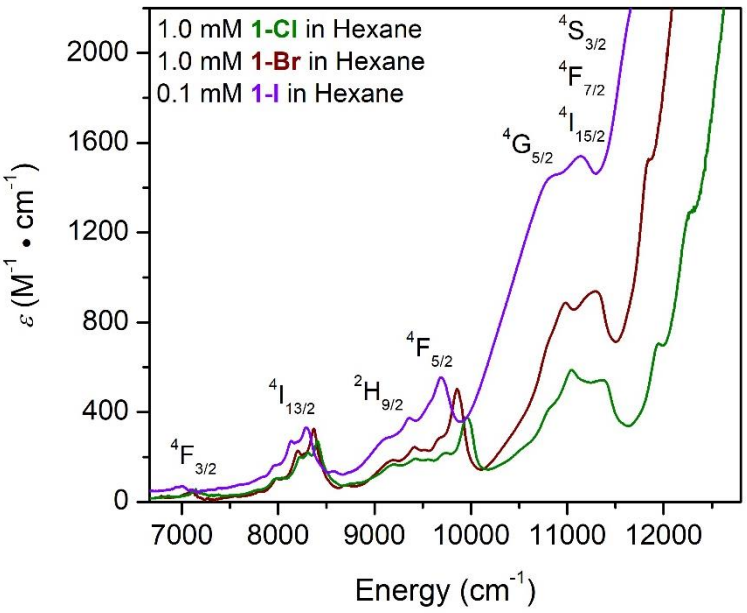

Figure S30. Near-infrared (NIR) spectra of hexane solutions of **1-X,** with assignments of the f→f transitions made based on previous work on uranium formate and other uranium complexes.[12,13]

Table S1. Energies (in cm^{-1}) of the main feature(s) from the observed f → f transitions in the NIR for **1-X** (Figure S30). Only the features for the two lowest energy transitions (involving the $^4F_{3/2}$ and $^4I_{13/2}$ multiplets) could be assigned confidently because they are well-resolved. The $^2H_{9/2}$, $^4F_{5/2}$, and other higher-energy transitions are less-resolved with respect to each other, allowing for only a general estimate of their locations with respect to each other.

$^4I_{9/2} \rightarrow {}^{2S+1}L_J$	**1-Cl**	**1-Br**	**1-I**
$^4F_{3/2}$	7,146	7,099	7,003
$^4I_{13/2}$	7,991	7,985	7,950
	8,230	8,206	8,139
	8,408	8,371	8,292

Since compounds **1-X** are isostructural, a comparison of their f → f transitions can provide insight into the relative crystal field splitting of the ground $^4I_{9/2}$ multiplet in each complex. The energies of the f → f transitions are largely dominated by the strength of the spin-orbit interaction (Figure S31; however, the transitions themselves involve excitations from crystal field states, M_J, in the ground $^4I_{9/2}$ multiplet into crystal field states of higher energy $^{2S+1}L_J$ multiplets (Figure S32).[14,15] Differences in the transition energies for **1-X** might thus be reflective of the relative energies of these crystal field states in the ground multiplet. The f → f transitions, namely from the $^4I_{9/2}$ ground state to $^4F_{3/2}$, $^4I_{13/2}$, and $^2H_{9/2}$ excited states, all shift to slightly lower energies upon moving from **1-Cl** to **1-I**, suggesting that the overall crystal field splitting of the uranium ions decreases moving down the halide series. We note that this is highly speculative and would require validation from *ab initio* calculations. In lanthanide complexes, the crystal field splitting can be determined *via* a combination of NIR and luminescence spectroscopies.[16] Such measurements are beyond the scope of this study, however.

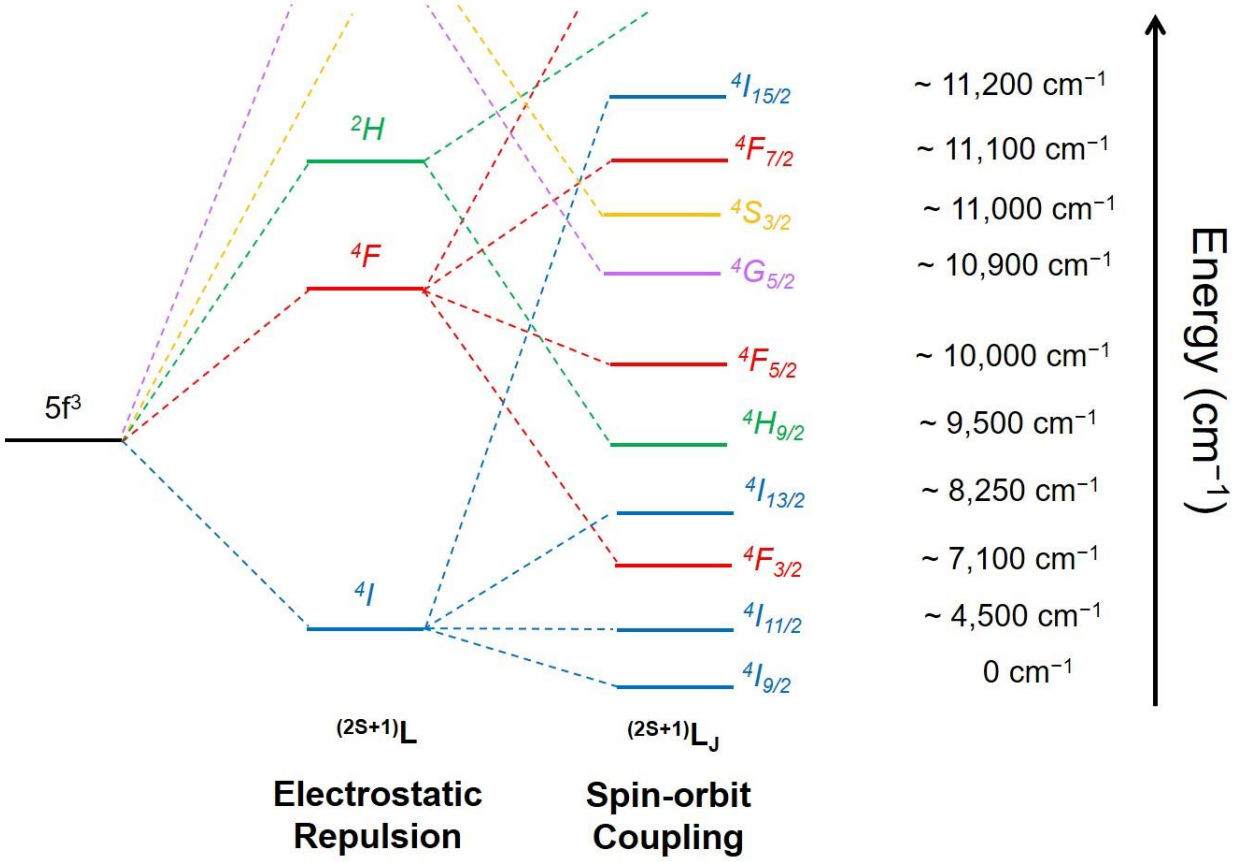

Figure S31. Ordering of the spin-orbit coupled states for uranium(III) based on previous work on uranium(III) formate.[12]

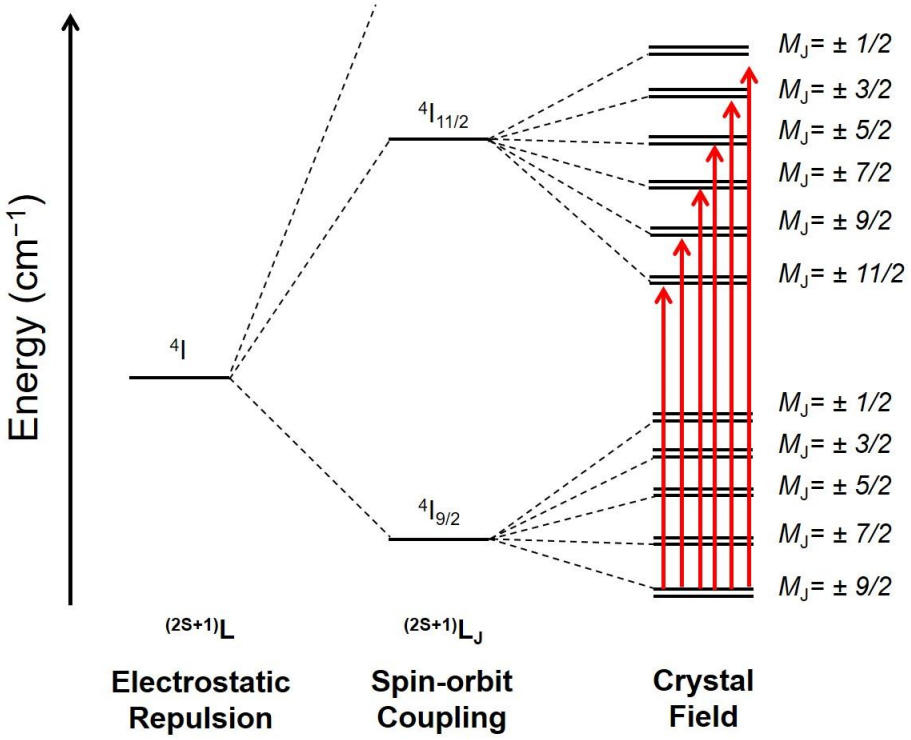

Figure S32. Qualitative depiction of f → f transitions involving the ground $^4I_{9/2}$ and excited $^4I_{11/2}$ spin orbit coupled states of uranium(III), such as those in **1-X**. The effects of magnetic exchange coupling are not shown. Our assignment of the M_J states is meant to be qualitative, and we highlight two important caveats: (1) the M_J states are not likely pure, but rather admixed as a result of the low symmetry of the uranium ions in **1-X**,[17,18] and (2) it is not always the case that the ordering of M_J states in f-element complexes is sequential, with each successive M_J state being smaller than the previous state as the energy is increased.[19] Many uranium(III) complexes in particular possess non-maximal M_J ground states (i.e., M_J = ± 7/2, ± 5/2, etc.).[17] Since UV-Vis-NIR spectra for **1-X** were collected in solution, all three uranium ions may be considered equivalent. Transitions involving the higher-energy spin orbit coupled states, such as those shown in Figure S31, are omitted for clarity. The f → f transitions themselves involve excitations from crystal field states (M_J).[15] Only transitions involving the ground M_J = ± 9/2 state of the $^4I_{9/2}$ multiplet are shown, for simplicity, but transitions involving the excited M_J states also occur. Because of the greater number of valence electrons, f → f transitions in uranium(III) are far more complicated than for uranium(V) ($5f^1$, $^3F_{5/2}$), and there are good discussions on this topic in the literature.[20,21] In principle, for uranium(III), 181 different crystal field states can be involved in f → f transitions across all possible spin-orbit coupled states.[14] Because of the large crystal field splitting in uranium complexes, however, not all excited M_J states in the $^4I_{9/2}$ multiplet will be thermally occupied, even at room temperature. In the case of **1-X**, this is corroborated by the dc magnetic susceptibilities at 300 K (Figure 4, upper, in the main text). Because such transitions do not satisfy the electric dipole selection rules, they are forbidden and result in very weak absorption intensities in the near-infrared region.[14]

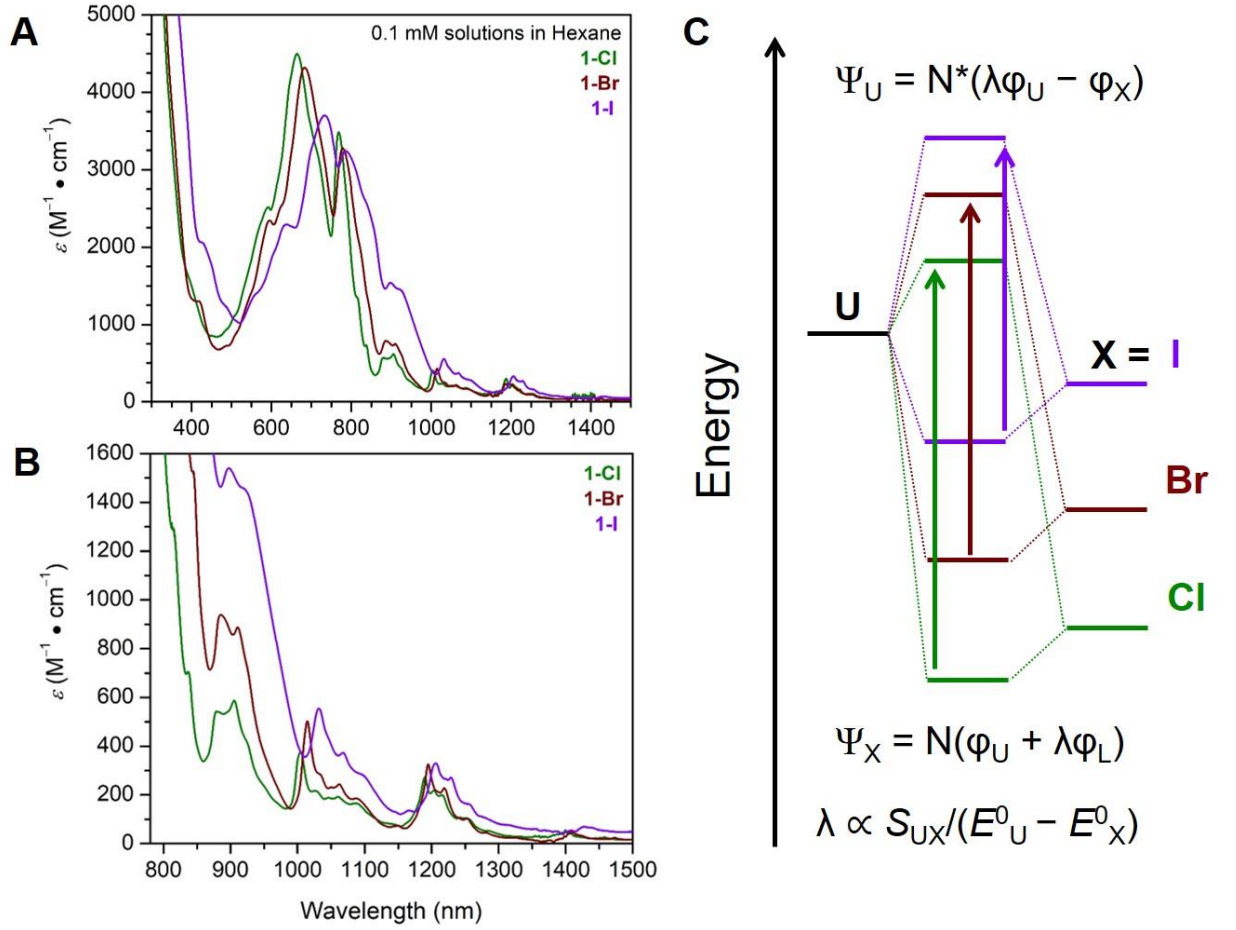

Figure S33. UV-Vis-NIR (**A**, 300 nm to 1500 nm) and NIR (**B**, 780 to 1500 nm) spectra of the complexes $(Cp^{iPr5})_3U_3X_6$ (**1-X**, X = Cl, Br, I); **C** Qualitative diagram for the interaction of uranium and halide atomic orbitals, giving rise to bonding orbitals of primarily ligand character, Ψ_X, and uranium character, Ψ_U.[22] The arrows illustrate the proposed transitions giving rise to the LMCT feature observed in the visible spectrum. Metal–ligand covalency can be evaluated on the basis of the mixing coefficient, λ, which is proportional to both orbital overlap, given by the overlap integral, S_{UX}, and the energy difference between the metal and ligand atomic orbitals (E^0_U–E^0_X). Uranium–halide covalency will increase down the halide series because orbital overlap increases and the frontier, atomic orbitals of U and X become closer in energy.

5. X-ray Crystallography

Structure solutions were determined by SHELXT using direct methods and these solutions were refined via least-square refinement against F^2 by SHELXL, as implemented in OLEX2 crystallographic software.[23,24] For all structures, all non-hydrogen atoms were refined anisotropically. All hydrogen atoms were placed at geometrically calculated positions using the riding model and refined isotropically.

(Cp^{iPr5})U(BH_4)$_2$(THF). The compound crystallized in the space group $P2_1/c$ with two molecules in the asymmetric unit. The structural refinement gives free R factors of R_1 = 3.11% and wR_2 = 7.93%. No A or B alerts were found using CheckCIF.

(Cp^{iPr5})$_2$U$_2$(OPh^{tBu})$_4$. The compound crystallized in the space group $P\bar{1}$ with half of a molecule in the asymmetric unit and an inversion center located in the middle of two U atoms within the molecule. The Cp^{iPr5} ligand showed positional disorder over two sites, and the occupancies of these two components were refined while constraining the sum to unity, yielding ratios of 0.701(7):0.299(7). The application of SIMU restraints to the displacement parameters of the cyclopentadienyl carbons, and EADP constraints to the displacement parameters of the disordered carbon atoms gave free R factors of R_1 = 3.84% and wR_2 = 10.23%. In CheckCIF, two level A (PLAT971_ALERT_2_A) and one level B alerts (PLAT972_ALERT_2_B) were generated from residual density near U atoms. This residual density could not be modelled as any chemically reasonable species and likely arises due to strongly absorbing U or due to problems with the absorption correction.

(Cp^{iPr5})$_3$U$_3$Cl$_6$ (**1-Cl**). The compound crystallized in the space group *Pbca* with one molecule in the asymmetric unit. Three Cp^{iPr5} ligands showed positional disorder over two sites, and the occupancies of these two components were refined while constraining the sum to unity, yielding ratios of 0.741(8):0.259(8), 0.652(8):0.348(8) and 0.561(7):0.439(7), respectively. The application of the standard combination of SIMU, DELU restraints and EADP constraints to the displacement parameters of the cyclopentadienyl carbons gave free R factors of R_1 = 3.42% and wR_2 = 8.78%. In CheckCIF, three level A alerts (PLAT971_ALERT_2_A) and one level B alert (PLAT971_ALERT_2_B) were generated from positive residual density near U atoms. This residual density could not be modelled as any chemically reasonable species and likely arises due to strongly absorbing U or due to problems with the absorption correction.

(Cp^{iPr5})$_3$U$_3$Br$_6$ (**1-Br**). The compound crystallized in the space group $P\bar{1}$ with one molecule in the asymmetric unit. One of Cp^{iPr5} ligands showed positional disorder over two sites, and the occupancies of these two components were refined while constraining the sum to unity, yielding a ratio of 0.727(6):0.272(6). The application of the standard combination of SIMU, DELU restraints and EADP constraints to the displacement parameters of the cyclopentadienyl carbons gave free R factors of R_1 = 3.27% and wR_2 = 8.66%. No A or B alerts were found in CheckCIF.

(Cp^{iPr5})$_3$U$_3$I$_6$ (**1-I**). The compound crystallized in the space group $P\bar{1}$ with one $(Cp^{iPr5})_3U_3I_6$ molecule and two toluene molecules in the asymmetric unit. Two Cp^{iPr5} ligands showed positional disorder over two sites, and the occupancies of these two components were refined while constraining the sum to unity, yielding a ratio of 0.75(4):0.25(4) and 0.55(3):0.45(3), respectively. A solvent mask was calculated and 62 electrons were found in a volume of 327 Å^3 in three voids per unit cell. This is consistent with the presence of 0.5[C_7H_8] per unit cell which account for 50 electrons per unit cell. One toluene molecule in the lattice showed an occupancy of 0.5. This

reduced occupancy might be a consequence of either solvent evaporation or solvent masking. The application of the standard combination of SIMU, DELU restraints to the displacement parameters of the cyclopentadienyl carbons gave free *R* factors of R_1 = 5.16% and wR_2 = 12.23%. In CheckCIF, four level A alerts (PLAT971_ALERT_2_A and PLAT972_ALERT_2_A) and three level B alerts (PLAT971_ALERT_2_B) were generated from residual density near U atoms. This residual density could not be modelled as any chemically reasonable species and likely arises due to strongly absorbing U or due to problems with the absorption correction. One B alert (PLAR250_ALERT_2_B) is generated due to the presence large voids with volatile solvent molecules that leads to poor diffraction data, however, these alerts do not affect the main results in this manuscript.

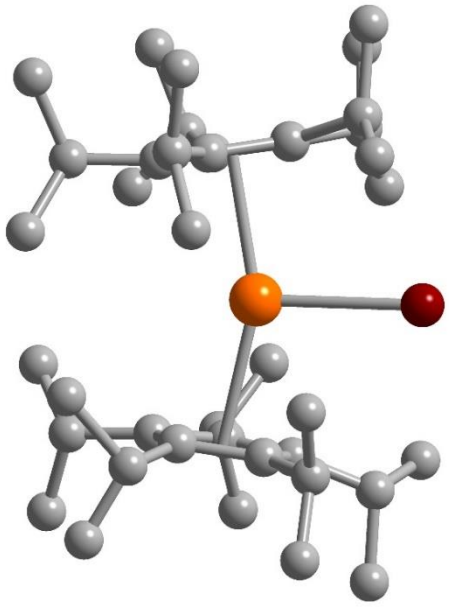

Figure S34. Molecular structure of $(Cp^{iPr5})_2UBr$ from X-ray diffraction analysis at 100 K, showing the connectivity. Hydrogen atoms have been omitted for clarity. Orange, brown, and gray spheres represent U, Br, and C atoms, respectively. The product forms as dark, emerald green rectangular plates; however, multiple attempts at collecting a structure acceptable for publication only resulted in badly twinned diffraction data, so we have not reported a structure for publication. Nevertheless, for the purpose of reproducibility by others, we found that this compound crystallizes in a $P2_1$ space group, with unit cell parameters: a = 17.2974(1) Å, b = 22.9848(2) Å, c = 19.6492(2) Å, $\alpha = \gamma = 90°$, β = 91.619(1)°, and V = 7808.96(11) Å^3.

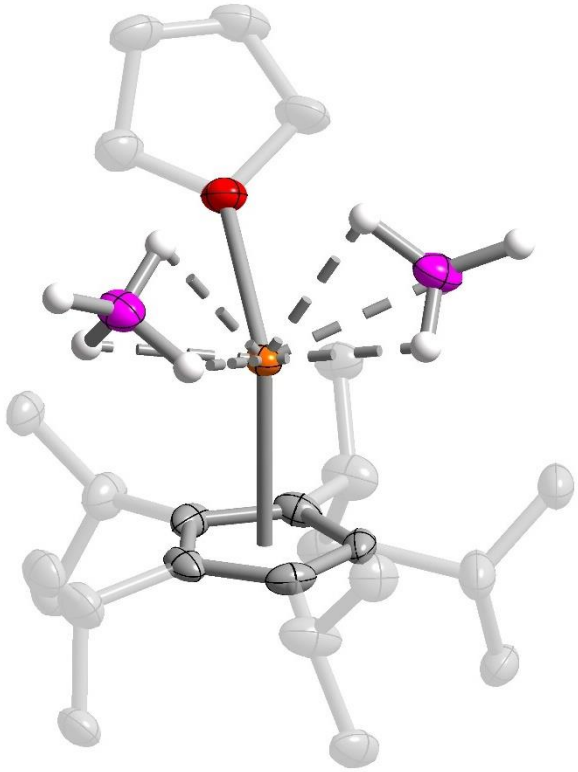

Figure S35. Solid-state structure of $(Cp^{iPr5})U(BH_4)_2(THF)$ with thermal ellipsoids—with the exception of hydrogen atoms—at the 50% probability level. Hydrogen atoms (except for those on BH_4^-) are omitted for clarity. Orange, red, gray, pink, and off-white represent U, O, C, B, and H atoms, respectively.

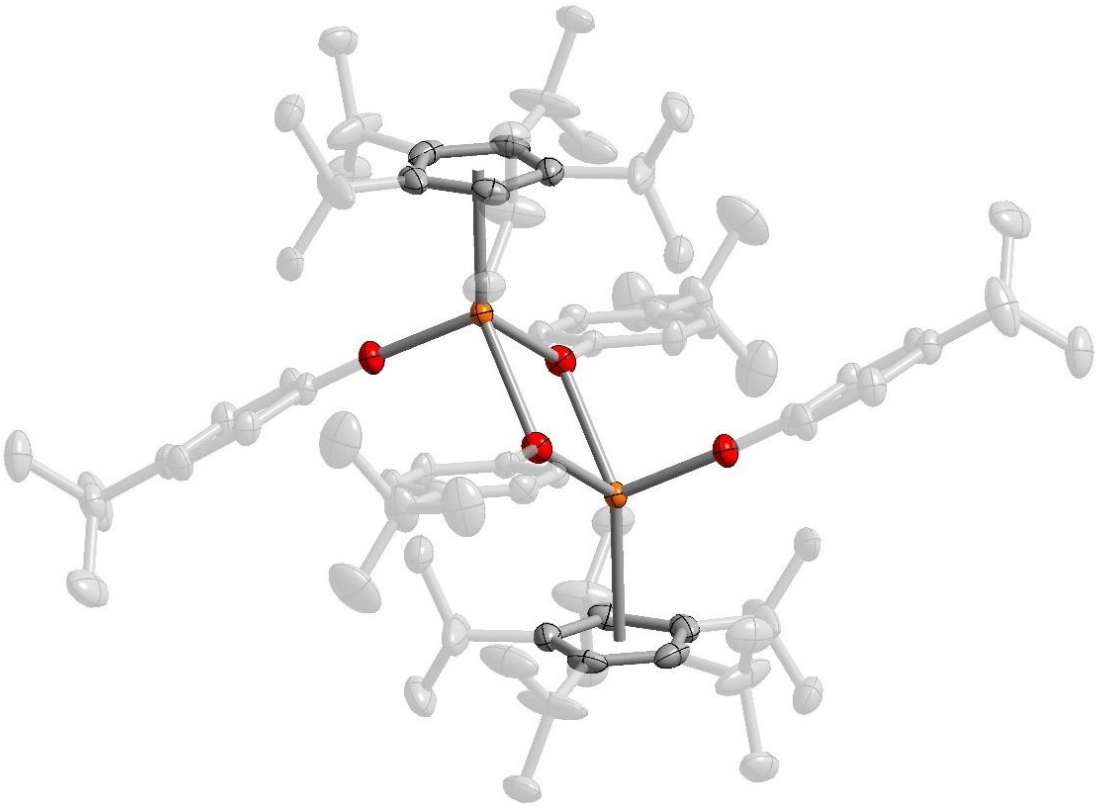

Figure S36. Solid-state structure of $(Cp^{iPr5})_2U_2(OPh^{tBu})_4$ with thermal ellipsoids at the 50% probability level. Hydrogen atoms are omitted for clarity. Orange, red, and gray ellipsoids represent U, O, and C atoms, respectively.

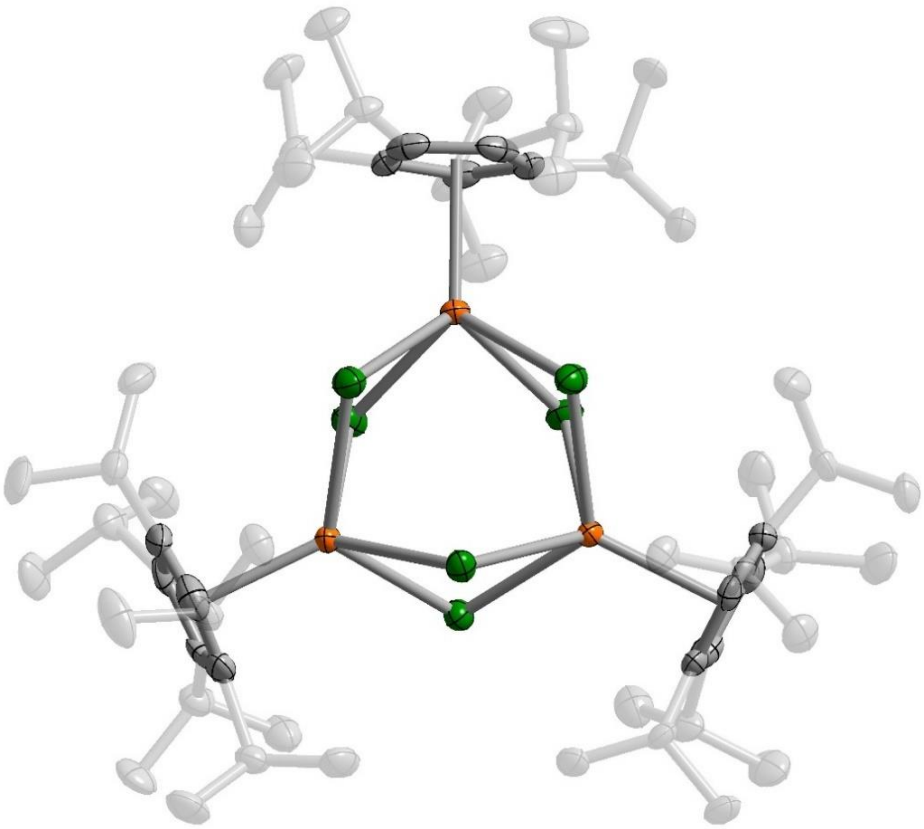

Figure S37. Solid-state structure of $(Cp^{iPr5})_3U_3Cl_6$ (**1-Cl**) with thermal ellipsoids at the 50% probability level. Hydrogen atoms are omitted for clarity. Orange, green, and gray ellipsoids represent U, Cl, and C atoms, respectively.

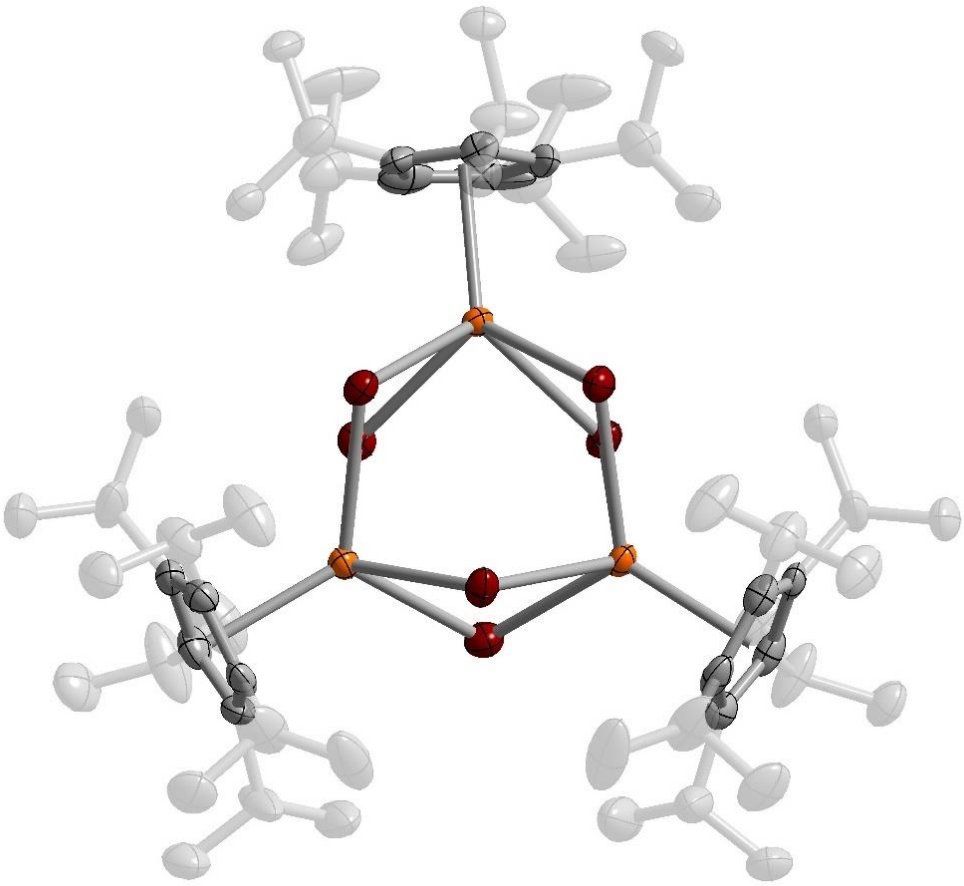

Figure S38. Solid-state structure of $(Cp^{iPr5})_3U_3Br_6$ (**1-Br**) with thermal ellipsoids at the 50% probability level. Hydrogen atoms are omitted for clarity. Orange, brown, and gray ellipsoids represent U, Br, and C atoms, respectively.

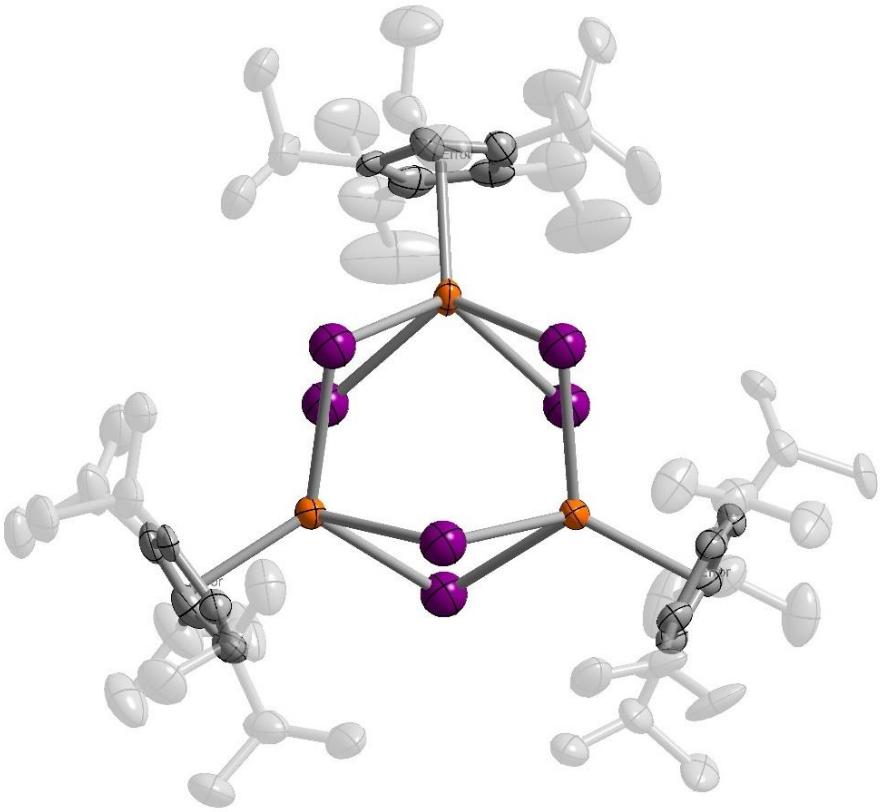

Figure S39. Solid-state structure of $(Cp^{iPr5})_3U_3I_6$ (**1-I**) with thermal ellipsoids at the 50% probability level. Hydrogen atoms, as well as co-crystallized toluene molecules, are omitted for clarity. Orange, purple, and gray ellipsoids represent U, I, and C atoms, respectively.

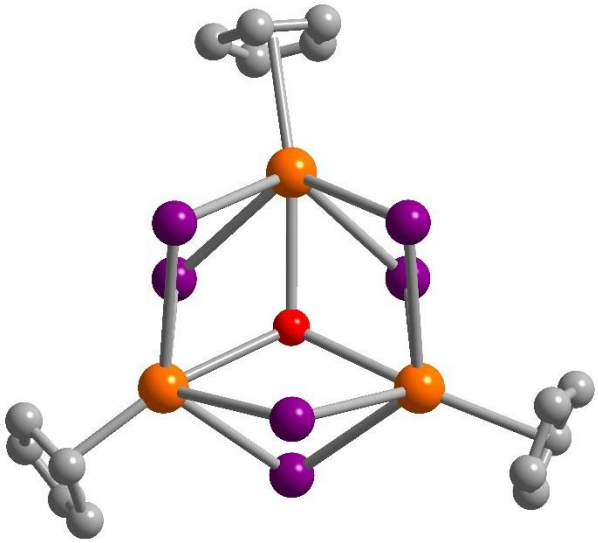

Figure S40. Molecular structure of the uranium(III/IV) mixed-valence complex $(Cp^{iPr5})_3U_3I_6(\mu_3\text{-}O)$ from X-ray diffraction experiments at 100 K, showing connectivity. The isopropyl substituents on the Cp rings were badly disordered, and not all q-peaks corresponding to their C atoms could easily be identified. Hydrogen atoms have been omitted for clarity. Orange, red, purple, and gray spheres represent U, O, I, and C atoms, respectively. The product forms as dark olive-green needles; however, multiple attempts at collecting a structure acceptable for publication revealed that the crystals are badly twinned, so we have not reported a structure for publication. Based on connectivity, the structure of this compound is analogous to structures previously reported for $[\{(Cp^{Me5})_3U_3I_6(\mu_3\text{-}O)\}\{Li(THF)_3\}_{0.5}]_2[Li(THF)_4]$ and $(Cp^{Me4R})_3U_3I_6(\mu_3\text{-}O)$ (R = Me, H) by Liddle[25] and Cloke,[26] respectively. Nevertheless, for the purpose of reproducibility by others, our attempts at obtaining a crystal structure suggest that this compound crystallizes in a *P−3* space group, with unit cell parameters: $a = b = 15.8519(2)$ Å, $c = 16.1514(3)$ Å, $\alpha = \beta = 90°$, $\gamma = 120°$, and $V = 3514.82(9)$ Å^3.

Table S2. Crystallographic data for $(Cp^{iPr5})U(BH_4)_2(THF)$

Empirical formula	$C_{48}H_{101}B_4O_2U_2$	
Formula weight	1229.58	
Temperature/K	100(2)	
Crystal system	Monoclinic	
Space group	$P2_1/c$	
Unit cell dimensions	a = 9.9306(1) Å	α = 90°
	b = 34.2386(3) Å	β = 94.275(1)°
	c = 16.2466(1) Å	γ = 90°
Volume	5508.63(8) Å^3	
Z	4	
ρ_{calc}/g/cm^3	1.483	
μ/mm^{-1}	16.640	
F(000)	2436.0	
Crystal size	0.24 × 0.16 × 0.06	
Radiation	CuKα (λ = 1.54184)	
2Θ range for data collection	6.036 to 157.872°	
Index ranges	$-12 \leq h \leq 12$, $-42 \leq k \leq 43$, $-19 \leq l \leq 20$	
Reflections collected	60959	
Independent reflections	11646 [R_{int} = 0.0442, R_{sigma} = 0.0302]	
Data / restraints / parameters	11646/0/590	
Goodness-of-fit on F^2	1.057	
Final R indices [I > 2σ(I)]	R_1 = 0.0311, wR_2 = 0.0778	
Final R indices (all data)	R_1 = 0.0339, wR_2 = 0.0793	
Largest diff. peak and hole	1.97 and −1.11e·Å^{-3}	

Table S3. Crystallographic data for $(Cp^{iPr5})_2U_2(OPh^{tBu})_4$

Empirical formula	$C_{40}H_{61}O_2U$	
Formula weight	811.91	
Temperature/K	100(2)	
Crystal system	Triclinic	
Space group	$P\bar{1}$	
Unit cell dimensions	a = 12.7253(3) Å	α = 75.640(2)°
	b = 12.7254(2) Å	β = 65.908(2)°
	c = 14.4410(3) Å	γ = 75.654(2)°
Volume	2039.51(8) $Å^3$	
Z	2	
ρ_{calc}/g/cm^3	1.322	
μ/mm^{-1}	11.399	
F(000)	818.0	
Crystal size	0.18 × 0.10 × 0.06	
Radiation	CuKα (λ = 1.54184)	
2Θ range for data collection	7.272 to 159.008°	
Index ranges	$-16 \leq h \leq 16$, $-12 \leq k \leq 16$, $-18 \leq l \leq 18$	
Reflections collected	41445	
Independent reflections	8596 [R_{int} = 0.0542, R_{sigma} = 0.0294]	
Data / restraints / parameters	8596/240/438	
Goodness-of-fit on F^2	1.039	
Final R indices [I > 2σ(I)]	R_1 = 0.0384, wR_2 = 0.1017	
Final R indices (all data)	R_1 = 0.0396, wR_2 = 0.1023	
Largest diff. peak and hole	4.53 and −2.68 e·$Å^{-3}$	

Table S4. Crystallographic data for $(Cp^{iPr5})_3U_3Cl_6$ (**1-Cl**)

Empirical formula	$C_{60}H_{105}Cl_6U_3$	
Formula weight	1753.22	
Temperature/K	100(2)	
Crystal system	Orthorhombic	
Space group	*Pbca*	
Unit cell dimensions	a = 25.7298(2) Å	α = 90°
	b = 18.9672(1) Å	β = 90°
	c = 27.5268(2) Å	γ = 90°
Volume	13433.7(2) $Å^3$	
Z	8	
ρ_{calc}/g/cm^3	1.734	
μ/mm^{-1}	22.564	
F(000)	6744.0	
Crystal size	0.12 × 0.08 × 0.02	
Radiation	CuKα (λ = 1.54184)	
2Θ range for data collection	6.422 to 157.688°	
Index ranges	$-30 \leq h \leq 32$, $-24 \leq k \leq 23$, $-28 \leq l \leq 34$	
Reflections collected	83089	
Independent reflections	14249 [R_{int} = 0.0357, R_{sigma} = 0.0240]	
Data / restraints / parameters	14249/945/754	
Goodness-of-fit on F^2	1.089	
Final R indices [I > 2σ(I)]	R_1 = 0.0342, wR_2 = 0.0867	
Final R indices (all data)	R_1 = 0.0363, wR_2 = 0.0878	
Largest diff. peak and hole	4.32 and −1.54 e·$Å^{-3}$	

Table S5. Crystallographic data for $(Cp^{iPr5})_3U_3Br_6$ (**1-Br**)

Empirical formula	$C_{60}H_{105}Br_6U_3$	
Formula weight	2019.98	
Temperature/K	100(2)	
Crystal system	Triclinic	
Space group	$P\bar{1}$	
Unit cell dimensions	a = 15.4938(3) Å	α = 115.460(1)°
	b = 15.9558(2) Å	β = 91.413(1)°
	c = 16.6391(1) Å	γ = 97.759(1)°
Volume	3664.22(9) Å^3	
Z	2	
ρ_{calc}/g/cm^3	1.831	
μ/mm^{-1}	22.502	
F(000)	1902.0	
Crystal size	0.23 × 0.12 × 0.06	
Radiation	CuKα (λ = 1.54184)	
2Θ range for data collection	5.908 to 157.566°	
Index ranges	$-19 \leq h \leq 19$, $-20 \leq k \leq 19$, $-21 \leq l \leq 20$	
Reflections collected	78954	
Independent reflections	15479 [R_{int} = 0.0531, R_{sigma} = 0.0328]	
Data / restraints / parameters	15479/631/781	
Goodness-of-fit on F^2	1.056	
Final R indices [I > 2σ(I)]	R_1 = 0.0327, wR_2 = 0.0849	
Final R indices (all data)	R_1 = 0.0349, wR_2 = 0.0866	
Largest diff. peak and hole	2.37 and −2.58 e·Å^{-3}	

Table S6. Crystallographic data for $(Cp^{iPr5})_3U_3I_6$ (**1-I**)

Empirical formula	$C_{72.25}H_{118.5}I_6U_3$	
Formula weight	2462.65	
Temperature/K	100(2)	
Crystal system	Triclinic	
Space group	$P\bar{1}$	
Unit cell dimensions	a = 16.1304(2) Å	α = 94.846(1)°
	b = 16.2920(2) Å	β = 107.637(1)°
	c = 17.9220(1) Å	γ = 107.385(1)°
Volume	4203.36(8) $Å^3$	
Z	2	
ρ_{calc}/g/cm^3	1.946	
μ/mm^{-1}	33.629	
F(000)	2292.0	
Crystal size	0.15 × 0.15 × 0.04	
Radiation	CuKα (λ = 1.54184)	
2Θ range for data collection	5.792 to 158.164°	
Index ranges	$-20 \le h \le 20$, $-20 \le k \le 20$, $-20 \le l \le 22$	
Reflections collected	89406	
Independent reflections	17796 [R_{int} = 0.0490, R_{sigma} = 0.0298]	
Data / restraints / parameters	17796/936/887	
Goodness-of-fit on F^2	1.017	
Final R indices [I > 2σ(I)]	R_1 = 0.0508, wR_2 = 0.1138	
Final R indices (all data)	R_1 = 0.0551, wR_2 = 0.1166	
Largest diff. peak and hole	6.75 and −3.76 e·$Å^{-3}$	

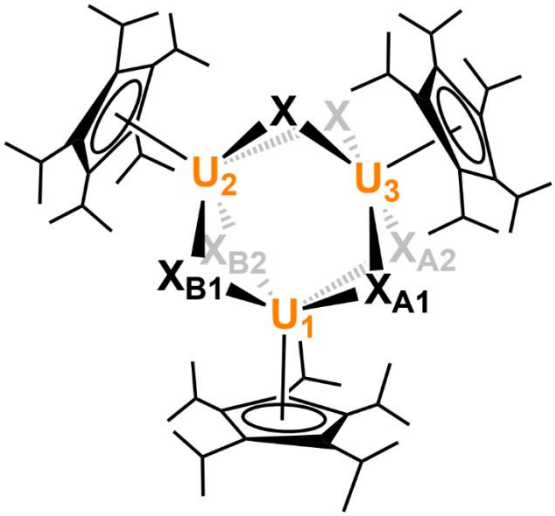

Figure S41. Generalized drawing of the structure of $(Cp^{iPr5})_3U_3X_6$ (**1-X**). All three uranium ions are inequivalent in the solid-state. The labeling scheme for the halide bridging ligands (for the purpose of Tables S7-S10) is as follows: when comparing halides that bridge the same pair of uranium ions (e.g., U_1 and U_3), the halides have the same letter subscript (e.g., X_A). When comparing halides that bridge different pairs of uranium ions, they are differentiated by the letters in their subscripts (e.g., X_A versus X_B). Bridging halides located below the plane of the uranium ions additionally are given the subscript 1, and halides below the plane of the uranium ions are given the subscript 2.

Table S7. Selected average bond distances (Å) and angles (°) for $(Cp^{iPr5})_3U_3Cl_6$ (**1-Cl**), $(Cp^{iPr5})_3U_3Br_6$ (**1-Br**), and $(Cp^{iPr5})_3U_3I_6$ (**1-I**). The values for the intermolecular U···U separations tabulated represent the range of separations between nearest-neighbor molecules.

	1-Cl	**1-Br**	**1-I**
U···U	4.1946(7)	4.3762(5)	4.5700(5)
U–Cp(cent)	2.4836(5)	2.5046(4)	2.4806(4)
U–X	2.812(1)	2.9677(7)	3.1914(8)
U–X–U	96.48(4)	95.01(2)	91.46(2)
X–U–X			
X_1–U–X_2	73.11(4)	74.57(2)	76.55(2)
X_{A1}–U–X_{B1}	78.22(4)	77.69(2)	79.07(2)
X_{A1}–U–X_{B2}	120.28(4)	121.33(2)	125.26(2)
X–U–Cp(cent)	119.83(3)	119.24(2)	117.33(2)
Intermolecular U···U	8.5360(6) to 11.9888(6)	8.9389(4) to 12.0261(4)	9.2002(5) to 13.5844(5)

[a]The standard deviation of the average value was estimated from $\sigma = \sqrt{\Sigma \sigma_i^2 / N}$, where σ_i is the standard deviation of each bond distance (or angle), i and N is the number of distances (or angles) averaged.

Table S8. Selected bond distances (Å) and angles (°) for each individual uranium ion in **1-Cl.**

1-Cl	**U_1**	**U_2**	**U_3**
$U_1 \cdots U_2$		4.1964(7)	
$U_2 \cdots U_3$		4.2034(7)	
$U_3 \cdots U_1$		4.1839(7)	
U–Cp(cent)	2.4798(5)	2.4858(5)	2.4850(5)
U–Cl	2.813(1) 2.774(1) 2.828(1) 2.824(2)	2.821(1) 2.819(1) 2.844(1) 2.793(2)	2.814(1) 2.806(1) 2.780(1) 2.824(2)
U_1–Cl–U_2		95.97(4) 96.09(4)	
U_2–Cl–U_3		96.72(4) 96.88(4)	
U_3–Cl–U_1		96.07(4) 97.16(4)	
Cl_1–U–Cl_2	73.06(4) 72.20(4)	72.39(4) 73.97(4)	74.49(4) 72.56(4)
Cl_{A1}–U–Cl_{B1}	77.14(4) 82.05(4)	75.61(4) 80.12(4)	78.90(4) 75.51(4)
Cl_{A1}–U–Cl_{B2}	119.17(4) 123.39(4)	118.23(4) 121.65(4)	119.81(4) 119.43(4)
Cl–U–Cp(cent)	119.27(3) 116.27(3) 124.55(3) 117.34(3)	125.59(4) 120.31(3) 118.02(3) 116.12(3)	122.37(3) 120.83(3) 119.46(3) 117.82(3)

Table S9. Selected bond distances (Å) and angles (°) for each individual uranium ion in **1-Br.**

1-Br	**U_1**	**U_2**	**U_3**
$U_1 \cdots U_2$		4.4351(5)	
$U_2 \cdots U_3$		4.3114(5)	
$U_3 \cdots U_1$		4.3822(5)	
U–Cp(cent)	2.5266(3)	2.4998(4)	2.4874(4)
U–Br	2.9873(7) 2.9917(8) 2.9478(8) 2.9708(7)	3.0127(7) 2.9686(6) 2.9736(8) 2.9169(7)	2.9617(7) 2.9221(8) 2.9914(7) 2.9682(6)
U_1–Br–U_2		96.16(2) 95.32(2)	
U_2–Br–U_3		95.19(2) 93.17(2)	
U_3–Br–U_1		95.10(2) 95.09(2)	
Br_1–U–Br_2	72.97(2) 74.06(2)	76.94(2) 72.93(2)	77.05(2) 73.47(2)
Br_{A1}–U–Br_{B1}	76.40(2) 80.38(2)	78.36(2) 75.83(2)	77.83(2) 77.34(2)
Br_{A1}–U–Br_{B2}	120.60(2) 121.30(2)	120.19(2) 121.91(2)	123.06(2) 120.94(2)
Br–U–Cp(cent)	115.97(2) 116.57(2) 123.43(2) 121.85(2)	117.47(2) 109.72(2) 128.26(2) 122.01(2)	113.30(2) 123.36(2) 115.63(2) 123.32(2)

Table S10. Selected bond distances (Å) and angles (°) for each individual uranium ion in **1-I.**

1-I	**U_1**	**U_2**	**U_3**
$U_1 \cdots U_2$		4.5874(5)	
$U_2 \cdots U_3$		4.5148(5)	
$U_3 \cdots U_1$		4.6077(4)	
U–Cp(cent)	2.4773(4)	2.4949(4)	2.4695(3)
U–I	3.2021(7) 3.1791(9) 3.2212(8) 3.1562(6)	3.1732(8) 3.2183(9) 3.192(1) 3.2211(6)	3.1738(8) 3.1747(9) 3.1876(8) 3.1974(8)
U_1–I–U_2		92.05(2) 91.62(2)	
U_2–I–U_3		92.74(2) 92.18(2)	
U_3–I–U_1		89.57(2) 90.56(2)	
I_1–U–I_2	76.39(2) 76.98(2)	75.96(2) 76.23(2)	76.87(2) 76.88(2)
I_{A1}–U–I_{B1}	77.18(2) 83.05(2)	78.86(2) 76.78(2)	80.52(2) 78.07(2)
I_{A1}–U–I_{B2}	126.26(2) 127.00(2)	125.15(2) 121.30(2)	127.249(2) 124.60(2)
I–U–Cp(cent)	116.44(2) 112.56(2) 120.28(2) 117.31(2)	121.56(2) 121.41(2) 113.33(2) 117.06(2)	116.37(2) 113.42(2) 119.33(2) 118.86(2)

6. Magnetic Measurements

6.1 General. Samples for magnetic measurements were prepared by adding polycrystalline powder (23.4 mg $(Cp^{iPr5})_2U_2(OPh^{tBu})_4$, 12.7 mg $(Cp^{iPr5})_3U_3Cl_6$ (**1-Cl**), 24.7 mg $(Cp^{iPr5})_3U_3Br_6$ (**1-Br**), and 13.1 mg $(Cp^{iPr5})_3U_3Br_6$ (**1-I**)) to 7 mm quartz tubes, which were subsequently packed with eicosane (25.7 mg for $(Cp^{iPr5})_2U_2(OPh^{tBu})_4$, 30.5 mg for **1-Cl**, 15.1 mg for **1-Br**, and 22.2 mg for **1-I**) to prevent crystallite torqueing and provide good thermal contact between the samples and the bath. Additionally, to show reproducibility, a second solid-state sample of **1-Cl** was prepared (from a separately synthesized batch of compound), consisting of 10.7 mg of **1-Cl** and 21.1 mg of eicosane. The tubes were fitted with Teflon sealable adapters, evacuated on a Schlenk line or using a glove box vacuum pump, and flame-sealed under static vacuum using a H_2/O_2 torch. Following flame sealing, the solid eicosane was melted in a water bath held at 45 °C. Solution samples of **1-Cl** and **1-Br** were prepared by dissolving the compounds (14.1 mg of **1-Cl** and 12.3 mg of **1-Br**) in toluene (205 mg for **1-Cl** and 210.1 mg for **1-Br**) into 5 mL glass scintillation vials, which were subsequently placed in a −25 °C freezer for 1 h, after which time the solutions were filtered through a celite-padded plug to remove any insoluble materials. The filtered solutions were then transferred into 7 mm quartz tubes, with total sample masses of 118.5 mg (**1-Cl**) and 102.0 mg (**1-Br**). The quartz tubes were fitted with Teflon sealable adapters, frozen with liquid nitrogen, evacuated on a Schlenk line, then flame-sealed. Unless specified otherwise, all magnetic measurements were performed using a Quantum Design MPMS2 superconducting quantum interference device (SQUID) magnetometer. All data were corrected for diamagnetic contributions from eicosane ($\chi_d = -2.4306 \times 10^{-4}$ cm^3·mol^{-1}) or toluene solvent ($\chi_d = -6.56 \times 10^{-5}$ cm^3·mol^{-1}), and from the core diamagnetism of the sample ($\chi_d = -9.68 \times 10^{-4}$ cm^3·mol^{-1} ($(Cp^{iPr5})_2U_2(OPh^{tBu})_4$), -9.78×10^{-4} cm^3·mol^{-1} (**1-Cl**), -1.038×10^{-3} cm^3·mol^{-1} (**1-Br**), and -1.134×10^{-3} cm^3·mol^{-1} (**1-I**)), which were estimated using Pascal's constants.[27]

6.2 Dc magnetic susceptibility and variable field magnetization measurements. Unless otherwise stated, dc magnetic susceptibility data were collected at temperatures ranging from 2 to 300 K at applied fields of 0.1, 1.0, and 7.0 T for $(Cp^{iPr5})_2U_2(OPh^{tBu})_4$ and **1-X** (X = Cl, Br, I). In the case of the dc magnetic susceptibility data for $(Cp^{iPr5})_2U_2(OPh^{tBu})_4$ and **1-I**, the 0.1 T data do not overlay with the 1 and 7 T data at high temperatures (Figures S42 and S77). This difference is due to the presence of a minor ferromagnetic impurity; such impurities are common, and can be introduced through, for example, the use of stainless-steel laboratory equipment, which can introduce small quantities of metal oxides (such as magnetite and other ferrites).[28–31] We corrected the dc susceptibility data of $(Cp^{iPr5})_2U_2(OPh^{tBu})_4$ and **1-I** for the presence of a ferromagnetic impurity by performing a least-squares fitting of the susceptibilities at 0.1 and 1 T (Figures S45 and S81) as described in references 28-31. The fits suggest ferromagnetic impurity contributions of 1.74×10^{-5} and 4.99×10^{-5} cm^3 for $(Cp^{iPr5})_2U_2(OPh^{tBu})_4$ and **1-I**, respectively—consistent with values determined in references 28-31. Variable-field magnetization measurements were performed on all samples in the magnetic field range of ±7 T using an average sweep rate of 140(4) Oe/s for $|H_{dc}| > 20$ kOe (2 T) and 33(1) Oe/s for $|H_{dc}| < 20$ kOe. The sample masses for toluene solutions of **1-Cl** and **1-Br** were estimated from their magnetization values at 7 T and 2 K, which were compared with those measured for the polycrystalline samples. For polycrystalline **1-Cl** at 7 T and 2 K, M is 2976.8 cm^3/mol; a M value of 0.0103 cm^3 was found for the dilute frozen toluene solution of **1-Cl** at 2 K and 7 T, corresponding to a mass of 6.1 mg of **1-Cl** and a concentration of 26.7 mM. Likewise, for polycrystalline **1-Br** at 7 T and 2 K, M is 3245.1 cm^3/mol and a M value of 0.0083 cm^3 was found for the dilute frozen toluene solution, corresponding to a mass of 5.2 mg

of **1-Br** and a concentration of 23.0 mM. We acknowledge that slight structural changes of **1-Cl** and **1-Br** upon dissolution in toluene will lead to changes in the exchange-coupled ground states of the complexes when compared with the properties in the solid-state, including the measured magnetization, leading to some errors in using this method to determine sample masses that is not typically present when used for mononuclear complexes.[11]

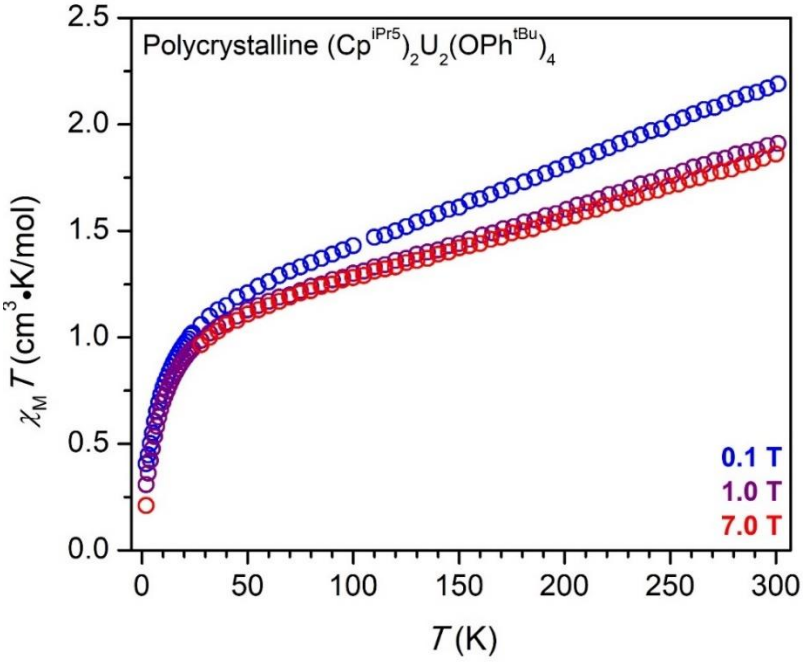

Figure S42. Plot of the molar magnetic susceptibility times temperature ($\chi_M T$) versus temperature (without a ferromagnetic correction) for polycrystalline $(Cp^{iPr5})_2U_2(OPh^{tBu})_4$ under dc fields of 0.1 T (blue circles), 1 T (purple circles), and 7 T (red circles) without a ferromagnetic correction.

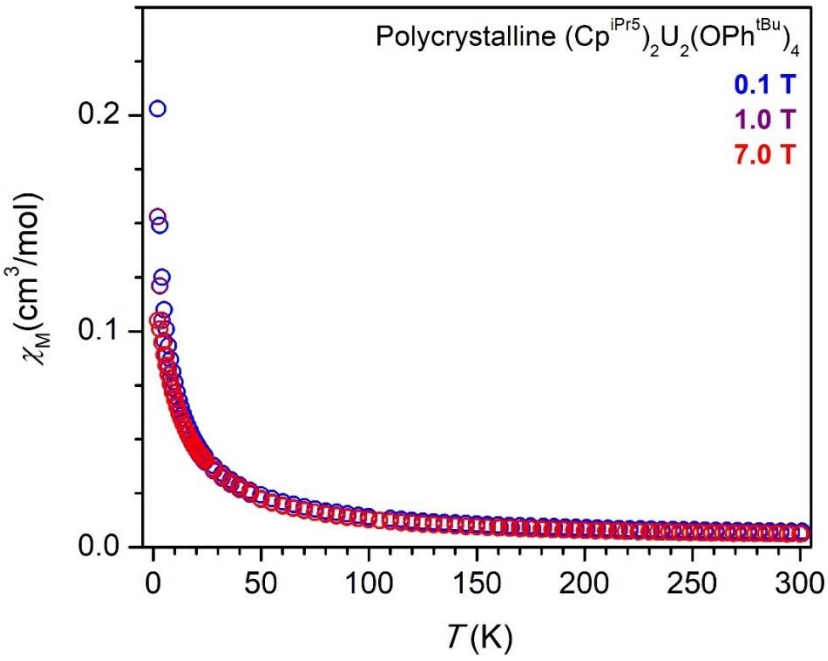

Figure S43. Plot of the molar magnetic susceptibility (χ_M) versus temperature (without a ferromagnetic correction) for polycrystalline $(Cp^{iPr5})_2U_2(OPh^{tBu})_4$ under dc fields of 0.1 T (blue circles), 1 T (purple circles), and 7 T (red circles).

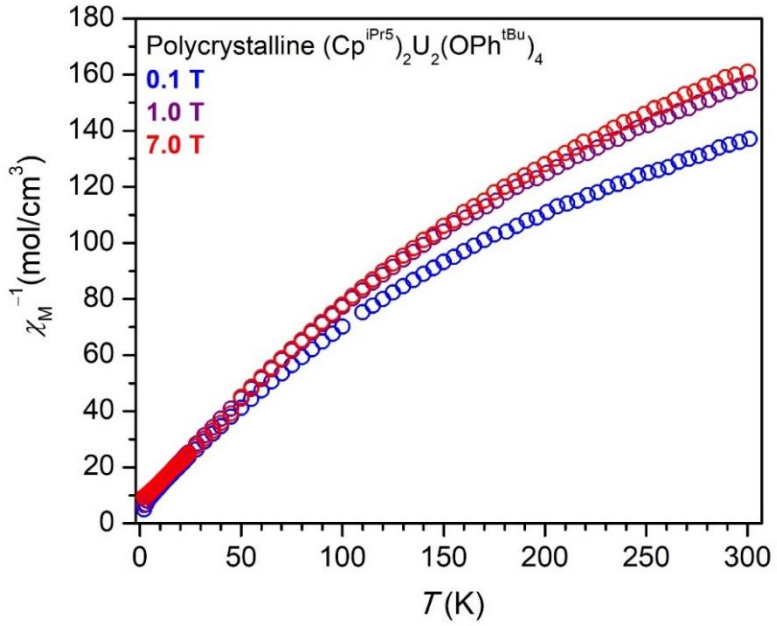

Figure S44. Plot of the inverse of the molar magnetic susceptibility (χ_M^{-1}) versus temperature (without a ferromagnetic correction) for polycrystalline $(Cp^{iPr5})_2U_2(OPh^{tBu})_4$ under dc fields of 0.1 T (blue circles), 1 T (purple circles), and 7 T (red circles).

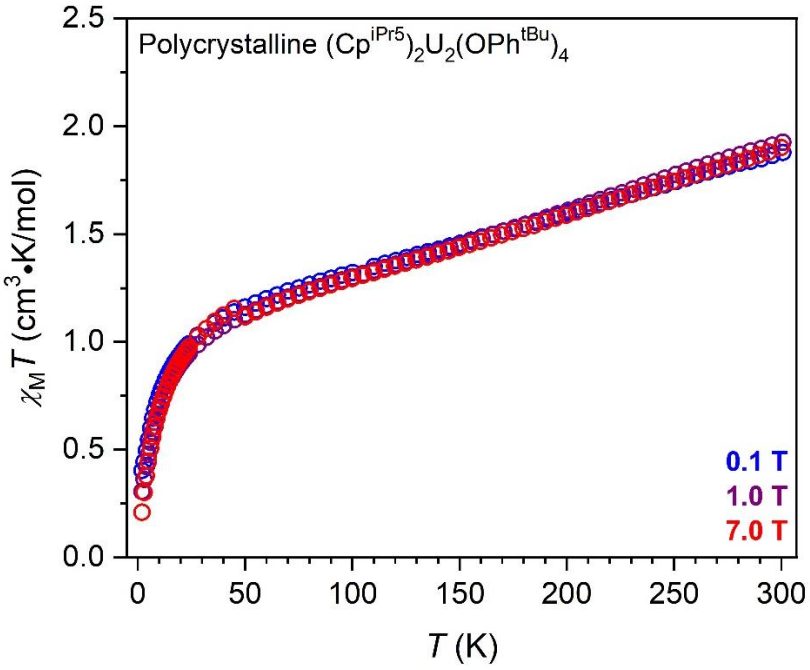

Figure S45. Plot of the molar magnetic susceptibility times temperature ($\chi_M T$) versus temperature for polycrystalline (Cp^{iPr5})$_2$U$_2$(OPh^{tBu})$_4$ under dc fields of 0.1 T (blue circles), 1 T (purple circles), and 7 T (red circles). The susceptibilities have been corrected for the presence of a ferromagnetic impurity. The decrease in $\chi_M T$, particularly at low temperatures, is ascribed to thermal depopulation of excited crystal field states (i.e., M_J states) as a result of magnetic anisotropy, as well as strong Zeeman splitting.

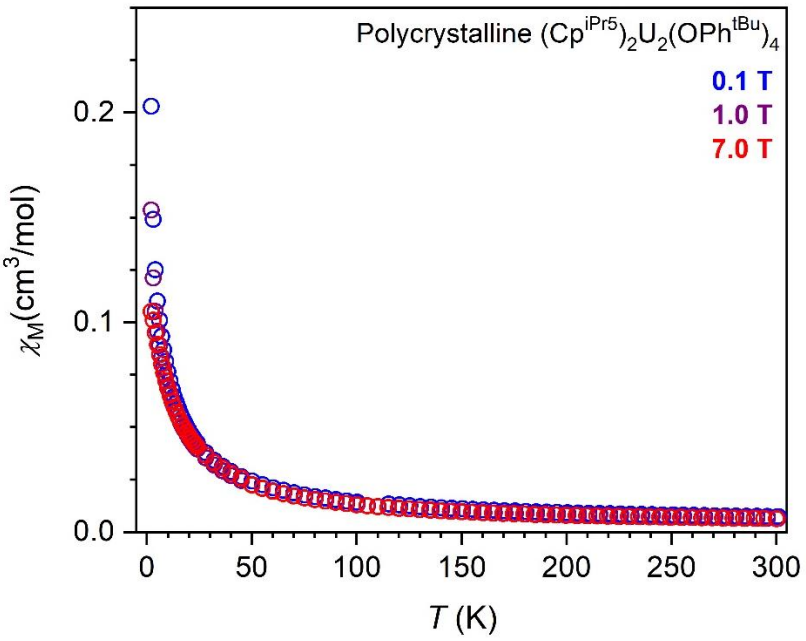

Figure S46. Plot of the molar magnetic susceptibility (χ_M) versus temperature for polycrystalline (Cp^{iPr5})$_2$U$_2$(OPh^{tBu})$_4$ under dc fields of 0.1 T (blue circles), 1 T (purple circles), and 7 T (red circles). The susceptibilities have been corrected for the presence of a ferromagnetic impurity.

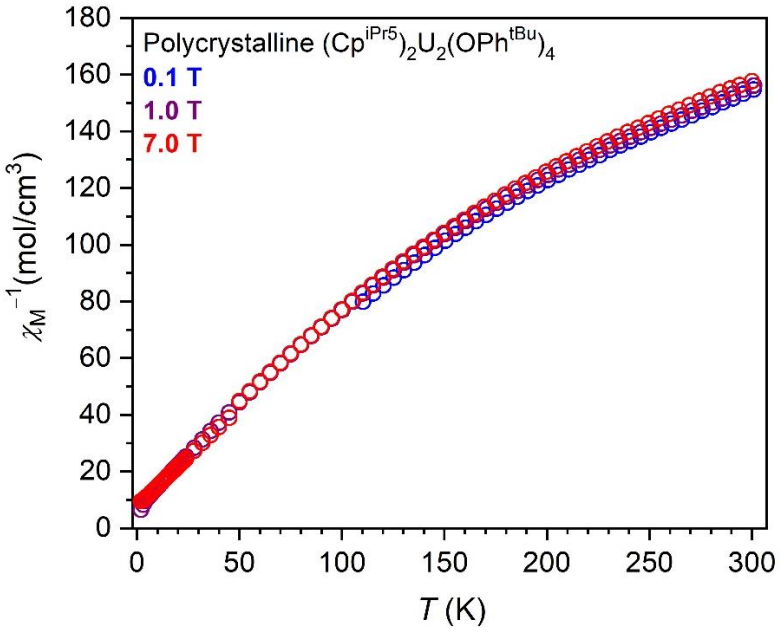

Figure S47. Plot of the inverse of the molar magnetic susceptibility (χ_M^{-1}) versus temperature for polycrystalline (Cp$^{i\text{Pr5}}$)$_2$U$_2$(OPh$^{t\text{Bu}}$)$_4$ under dc fields of 0.1 T (blue circles), 1 T (purple circles), and 7 T (red circles). The susceptibilities have been corrected for the presence of a ferromagnetic impurity.

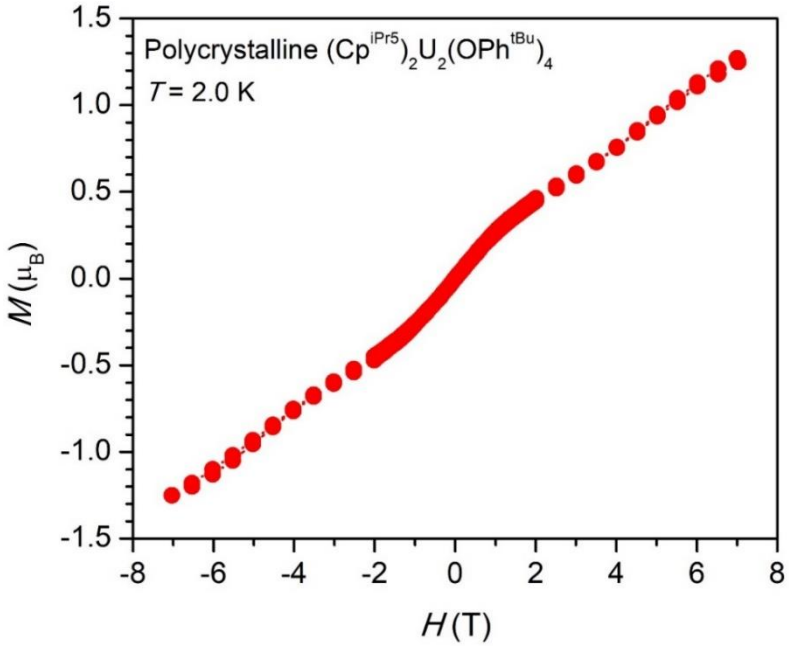

Figure S48. Variable-field magnetization, *M*, versus field, *H*, data collected on polycrystalline $(Cp^{iPr5})_2U_2(OPh^{tBu})_4$ at 2.0 K under applied fields from ± 7 T. Sweep rates of 140(4) Oe/s and 33(1) Oe/s were used for $|H_{dc}| > 20$ kOe and $|H_{dc}| < 20$ kOe, respectively. The steady increase in magnetization above 2 T, coupled with the presence of an inflection point near 4 T, is strongly suggestive of a thermally-broadened ground state-crossover due to strong Zeeman splitting. Specifically, in cases where there is weak antiferromagnetic exchange, strong Zeeman splitting results in stabilization of a thermally-accessible ferromagnetic excited state.[32]

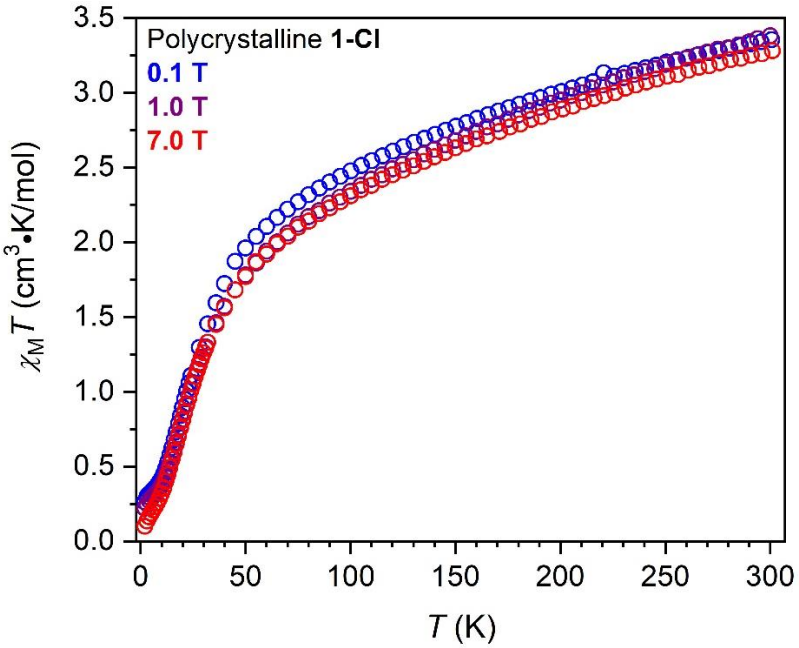

Figure S49. Plot of $\chi_M T$ versus T for polycrystalline $(Cp^{iPr5})_3U_3Cl_6$ (**1-Cl**) under dc fields of 0.1 T (blue circles), 1 T (purple circles), and 7 T (red circles). The decrease in $\chi_M T$, particularly at low temperatures, is the result of a combination of antiferromagnetic exchange coupling, as well as the thermal depopulation of excited crystal field states (i.e., M_J states) resulting from magnetic anisotropy and strong Zeeman splitting.

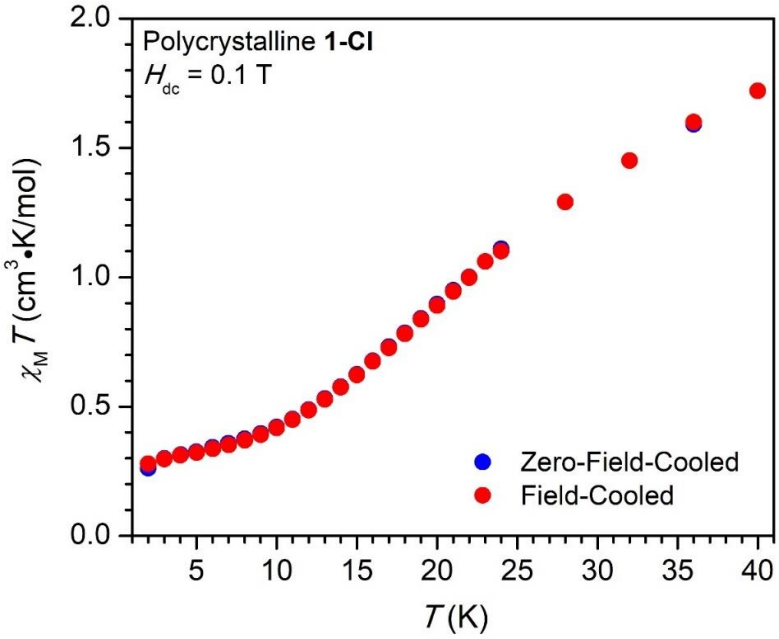

Figure S50. Field-cooled (red) and zero-field cooled (blue) $\chi_M T$ versus T data for polycrystalline $(Cp^{iPr5})_3U_3Cl_6$ (**1-Cl**) under a dc field of 0.1 T.

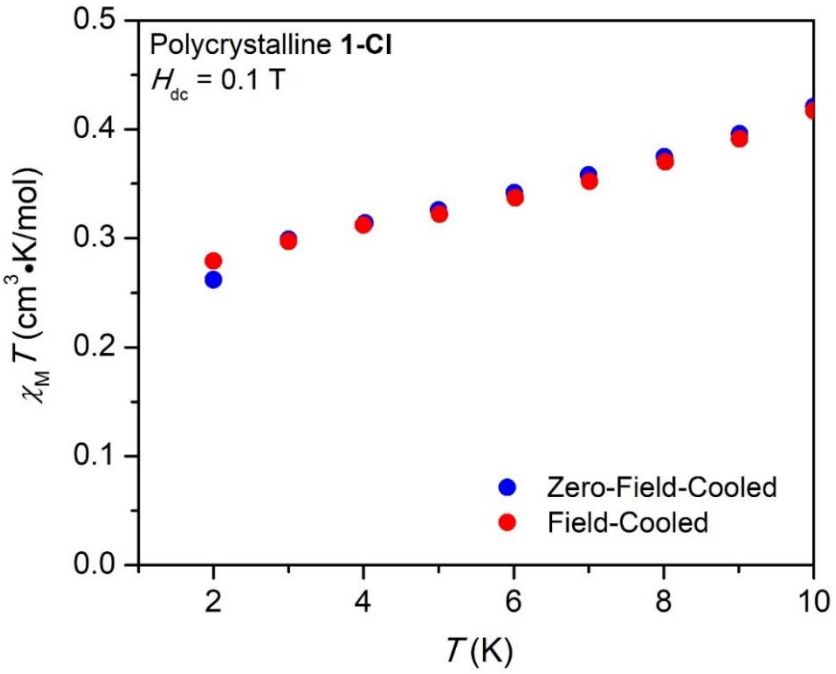

Figure S51. Expanded view of the field-cooled (red) and zero-field cooled (blue) $\chi_M T$ versus T data collected for polycrystalline **1-Cl** under a dc field of 0.1 T between 2 and 10 K. The divergence in the measurements at 2 K is the result of magnetic blocking.

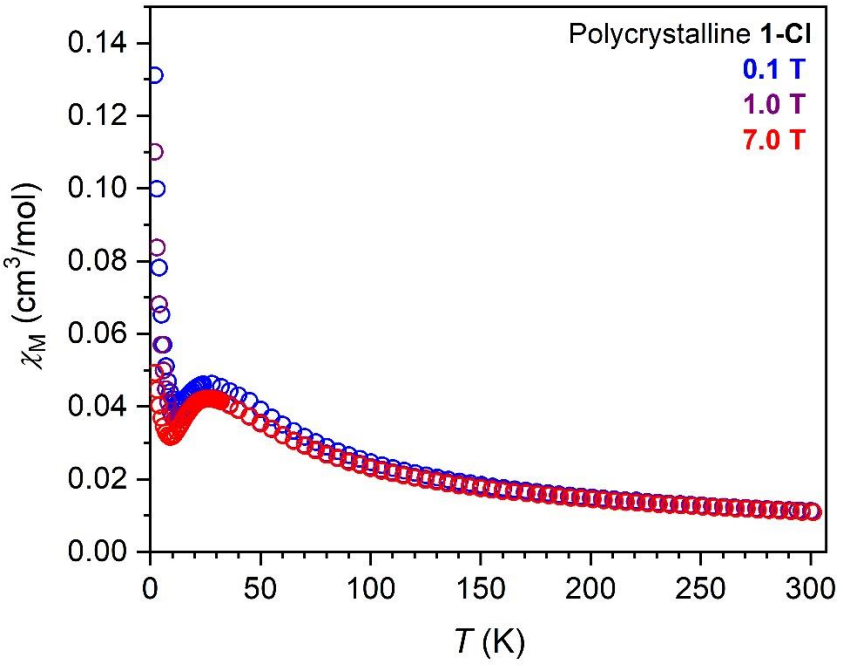

Figure S52. Plot of the molar magnetic susceptibility (χ_M) versus temperature for polycrystalline **1-Cl** under dc fields of 0.1 T (blue circles), 1 T (purple circles), and 7 T (red circles).

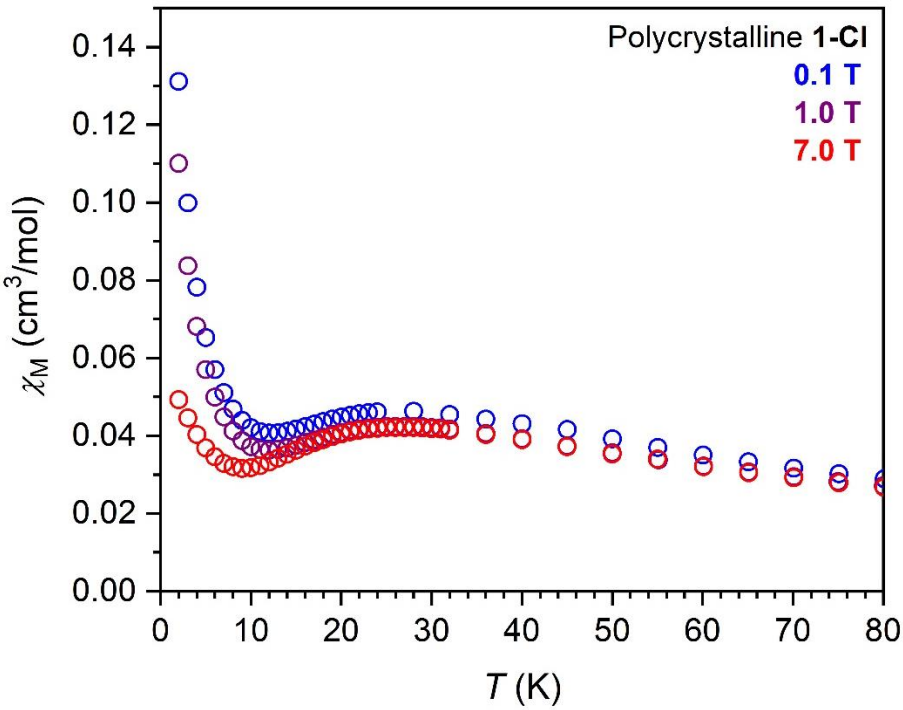

Figure S53. Plot χ_M versus T for polycrystalline **1-Cl** under dc fields of 0.1 T (blue circles), 1 T (purple circles), and 7 T (red circles) between 2 and 80 K. There are maxima in χ_M at approx. 28 K at all applied fields, ascribed to antiferromagnetic coupling between uranium ions.

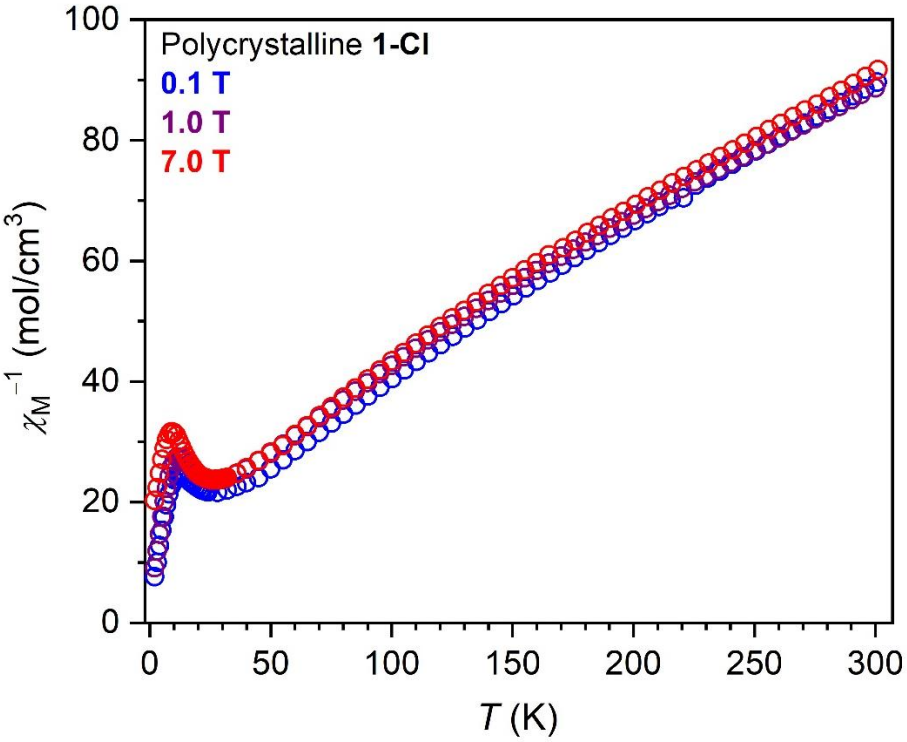

Figure S54. Plot of χ_M^{-1} versus T for polycrystalline **1-Cl** under dc fields of 0.1 T (blue circles), 1 T (purple circles), and 7 T (red circles).

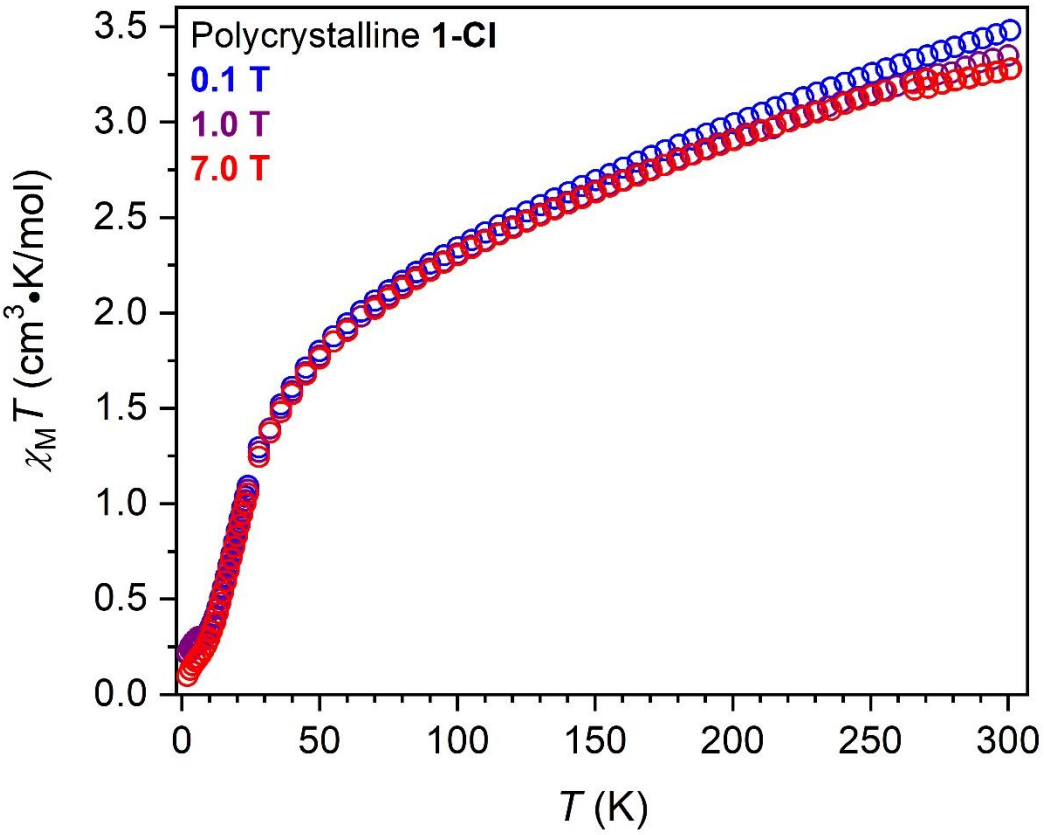

Figure S55. Plot of $\chi_M T$ versus T for a second sample of polycrystalline $(Cp^{iPr5})_3U_3Cl_6$ (**1-Cl**), which was synthesized in a separate batch. Measurements were performed using a Quantum Design MPMS 3 under dc fields of 0.1 T (blue circles), 1 T (purple circles), and 7 T (red circles) between 2 and 300 K.

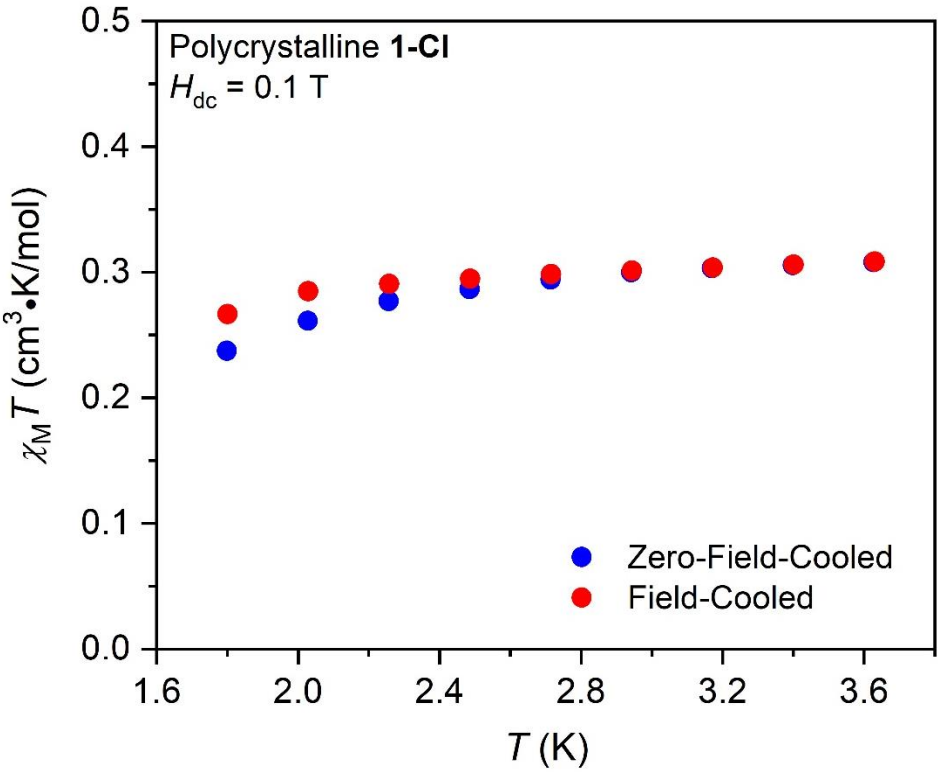

Figure S56. Plot of the field-cooled (red) and zero-field cooled (blue) $\chi_M T$ versus T data collected on a second polycrystalline sample of **1-Cl**. Measurements were performed using a Quantum Design MPMS 3 under a dc field of 0.1 T between 1.8 and 4 K (in increments of 0.2 K). The divergence in $\chi_M T$ below 3 K is the result of magnetic blocking.

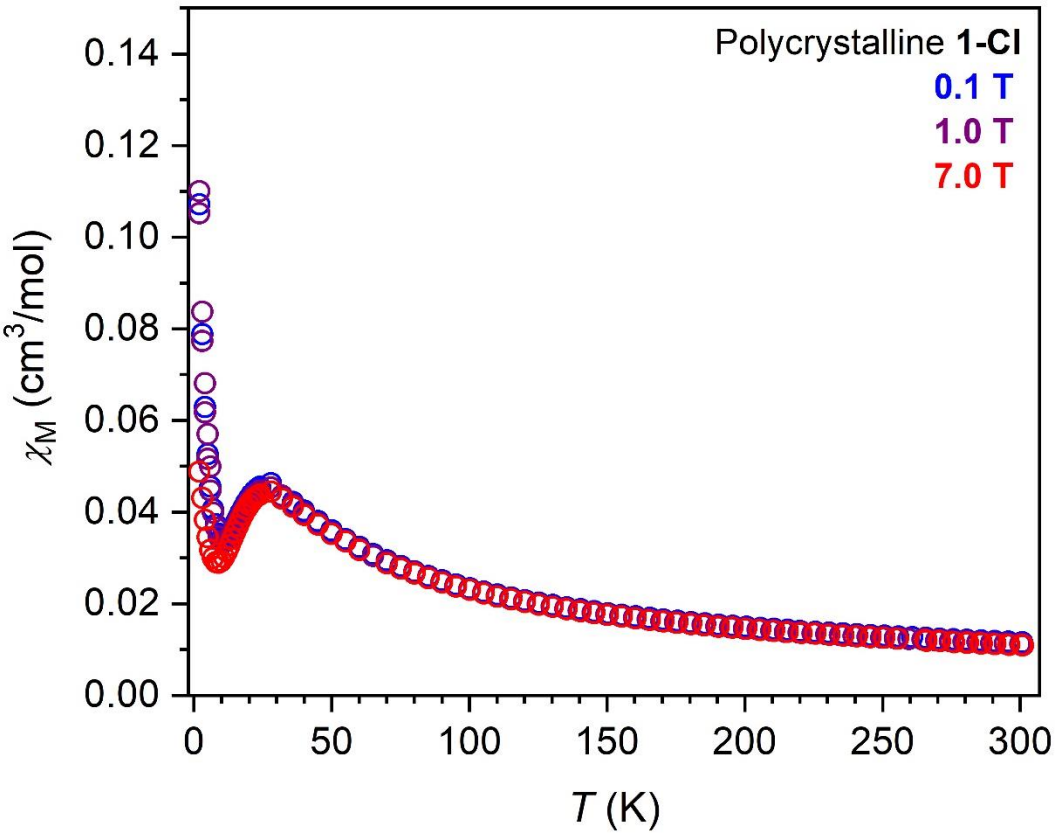

Figure S57. Plot of the molar magnetic susceptibility (χ_M) versus temperature for a second polycrystalline sample of **1-Cl** under dc fields of 0.1 T (blue circles), 1 T (purple circles), and 7 T (red circles).

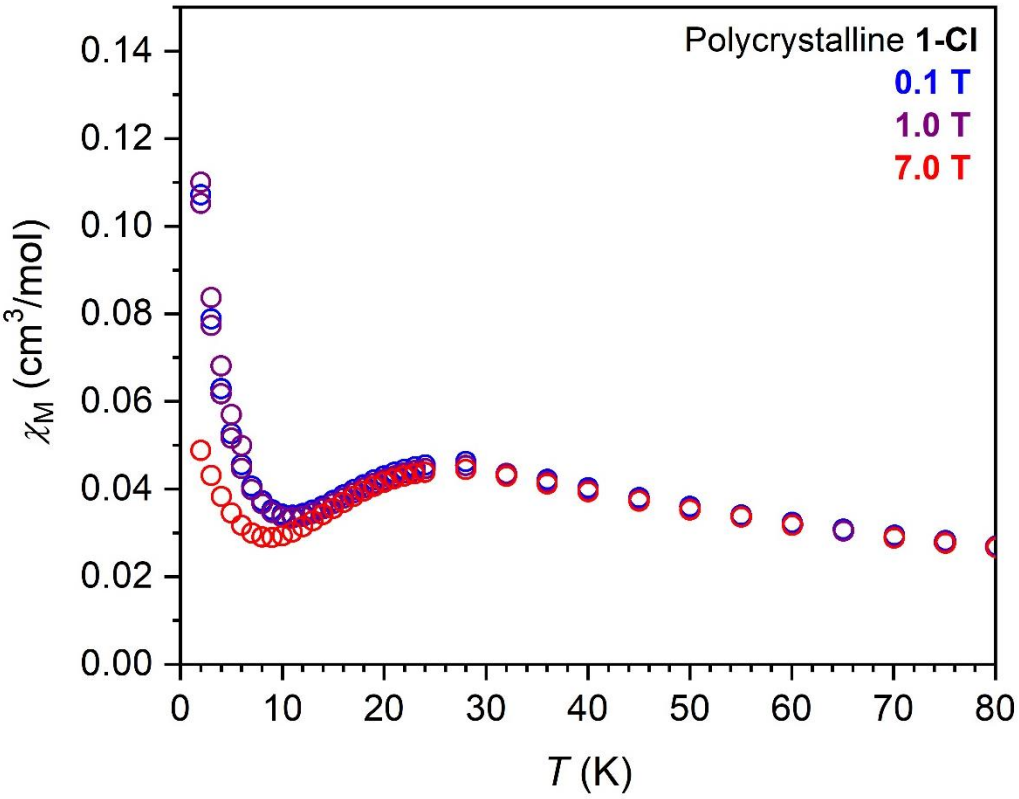

Figure S58. Plot χ_M versus T for a second polycrystalline sample of **1-Cl** under dc fields of 0.1 T (blue circles), 1 T (purple circles), and 7 T (red circles) between 2 and 80 K. There are maxima in χ_M at ~28 K at all applied fields, ascribed to antiferromagnetic coupling between uranium ions.

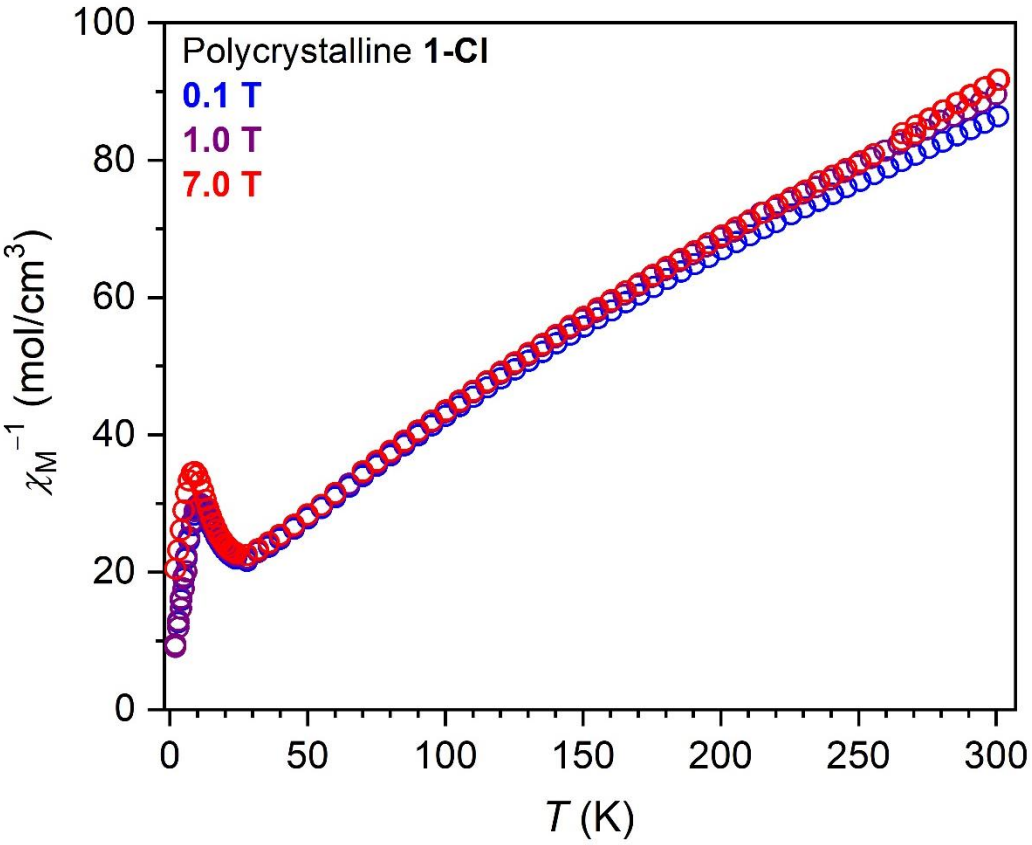

Figure S59. Plot of χ_M^{-1} versus T for a second polycrystalline sample of **1-Cl** under dc fields of 0.1 T (blue circles), 1 T (purple circles), and 7 T (red circles).

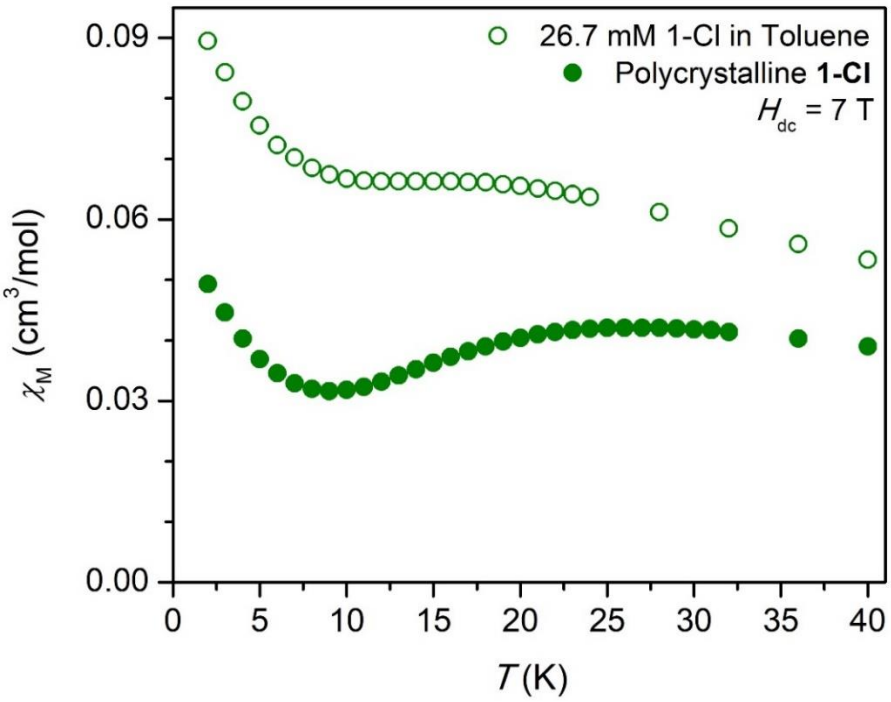

Figure S60. Plot of χ_M versus T between 0 and 40 K for polycrystalline **1-Cl** (filled circles) and a 26.7 mM frozen toluene frozen solution of **1-Cl** (open circles) under a dc field of 7 T. The magnitude of the exchange interaction, estimated based on the location of the maximum in χ_M, appears to be weaker for the solution-phase sample, presumably due to a structural change upon dissolution in toluene.

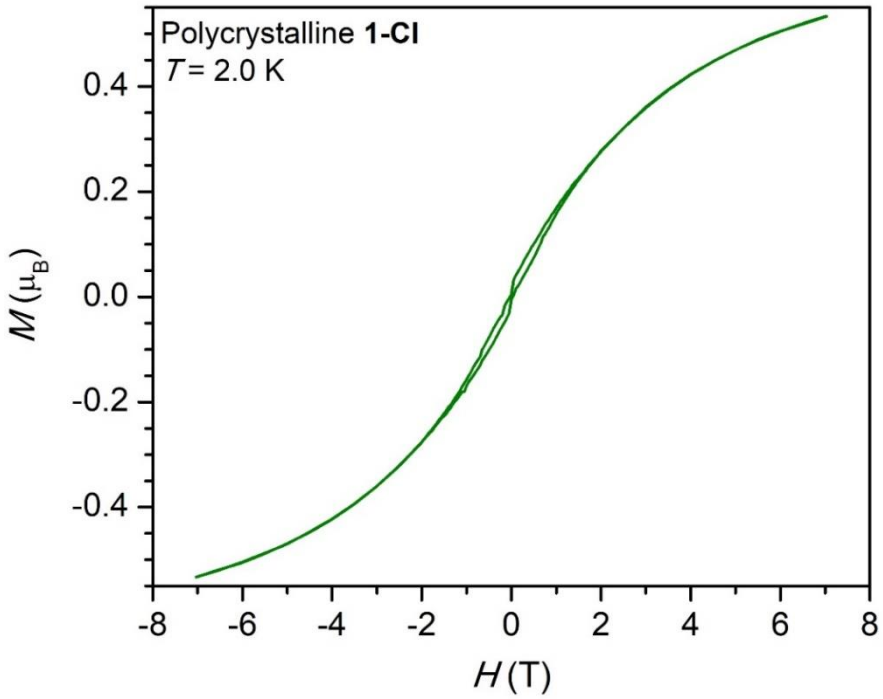

Figure S61. Variable-field magnetization data for polycrystalline **1-Cl** collected under fields ranging from ±7 T, showing magnetic hysteresis at 2.0 K. Sweep rates of 140(4) Oe/s and 33(1) Oe/s were used for $|H_{dc}| > 20$ kOe and $|H_{dc}| < 20$ kOe, respectively.

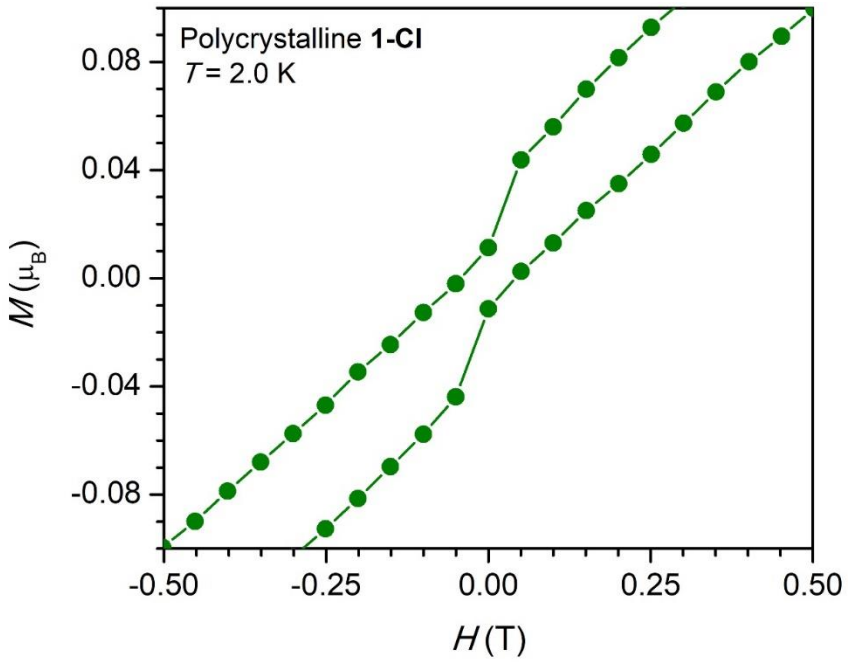

Figure S62. Expanded view of the variable-field magnetization data shown in Figure S61, highlighting the region between ±0.5 T. The drop in *M* upon approaching 0 T is ascribed to quantum tunneling.

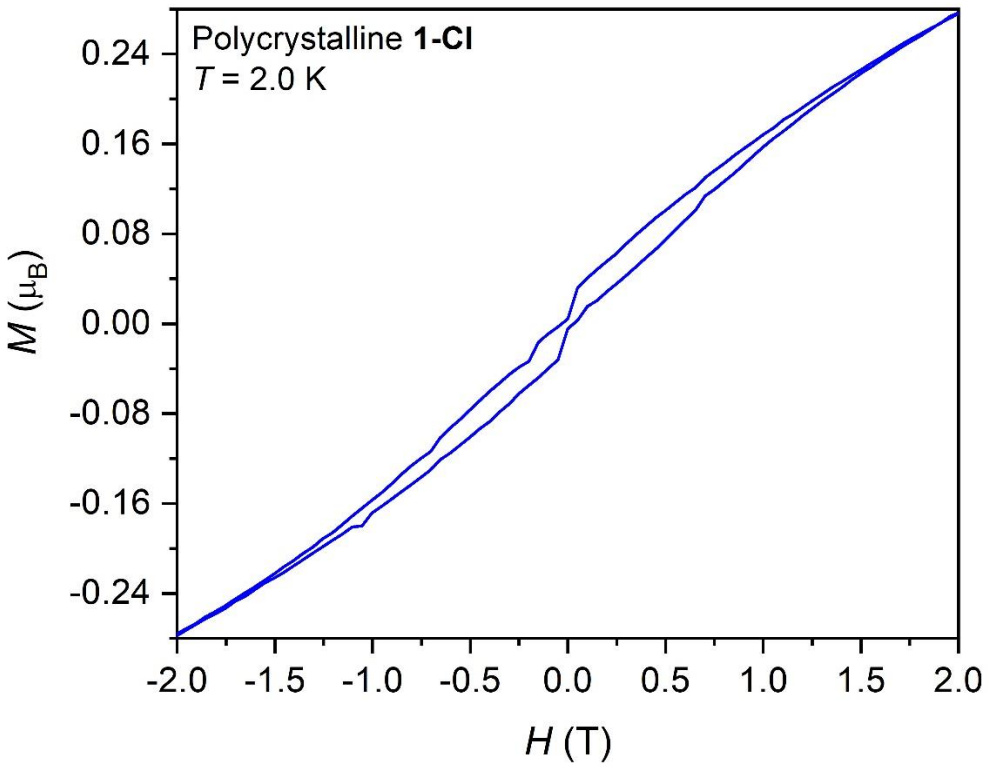

Figure S63. Variable-field magnetization of a second polycrystalline sample of **1-Cl** at 2.0 K. The drop in *M* upon approaching 0 T is ascribed to quantum tunneling. Sweep rates of 140(4) Oe/s and 33(1) Oe/s were used for $|H_{dc}| > 20$ kOe and $|H_{dc}| < 20$ kOe, respectively.

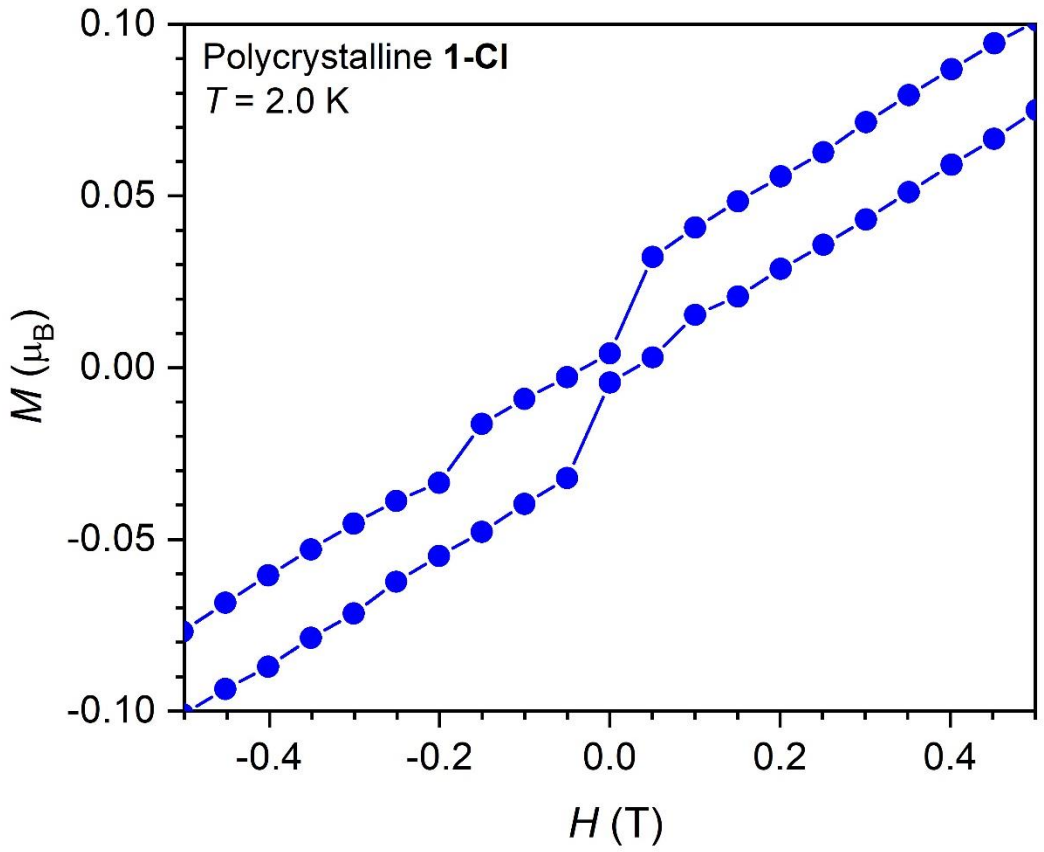

Figure S64. Expanded view of the variable-field magnetization of a second polycrystalline sample of **1-Cl**, highlighting magnetic hysteresis in the region between ±0.5 T at 2.0 K. The drop in *M* upon approaching 0 T is ascribed to quantum tunneling. Sweep rates of 140(4) Oe/s and 33(1) Oe/s were used for $|H_{dc}| > 20$ kOe and $|H_{dc}| < 20$ kOe, respectively.

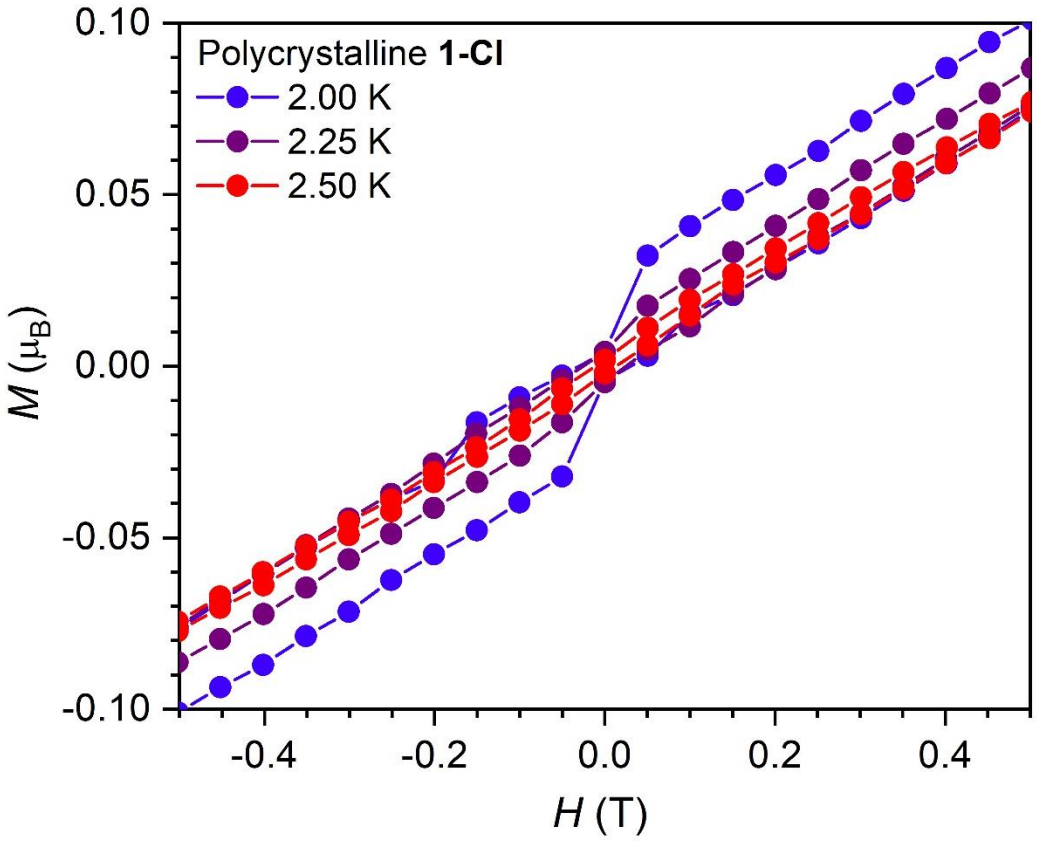

Figure S65. Variable temperature magnetization data collected on a second polycrystalline sample of **1-Cl**, highlighting magnetic hysteresis in the region between ±0.5 T from 2.0 to 2.5 K. Sweep rates of 140(4) Oe/s and 33(1) Oe/s were used for $|H_{dc}| > 20$ kOe and $|H_{dc}| < 20$ kOe, respectively.

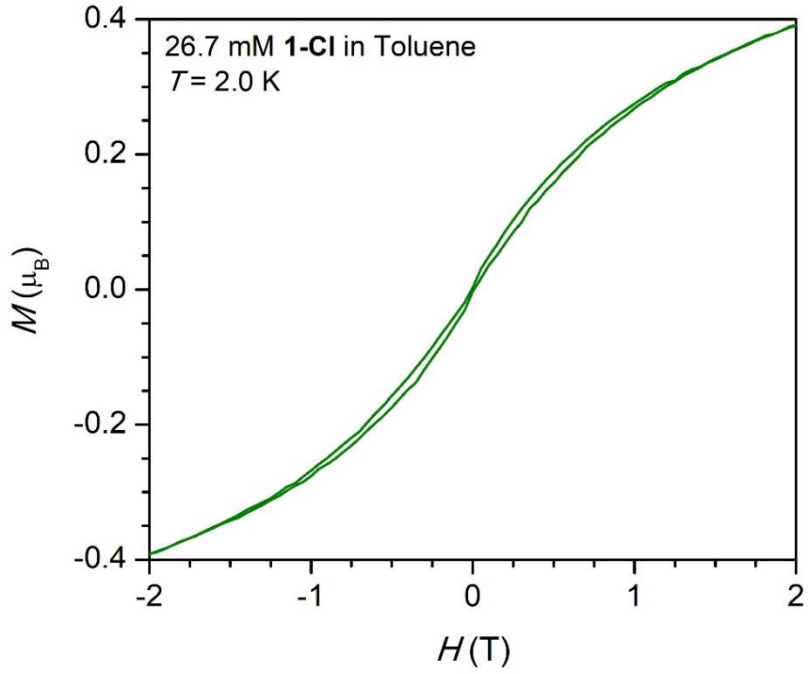

Figure S66. Variable-field magnetization data collected on a frozen toluene solution of **1-Cl**, showing magnetic hysteresis at 2.0 K under applied fields, *H*, ranging from ±7 T. Sweep rates of 140(4) Oe/s and 33(1) Oe/s were used for $|H_{dc}| > 20$ kOe and $|H_{dc}| < 20$ kOe, respectively.

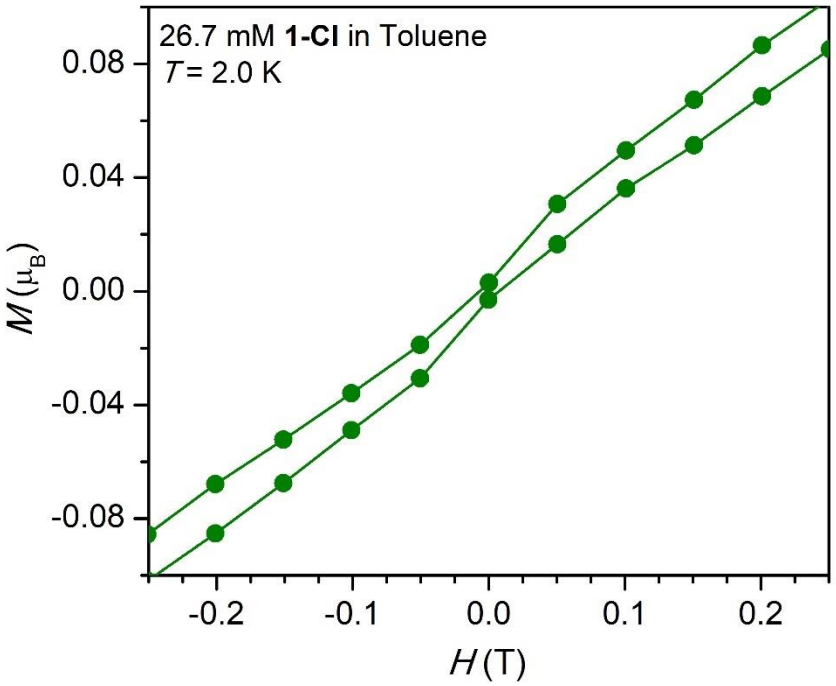

Figure S67. Expanded view of the variable-field magnetization data shown in Figure S66.

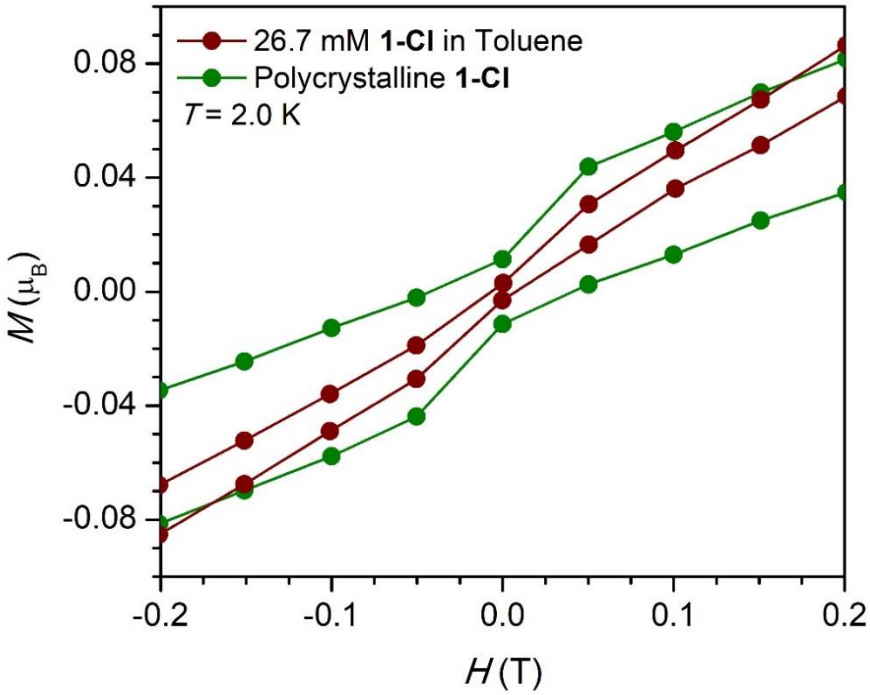

Figure S68. Comparison of the magnetic hysteresis of polycrystalline and frozen toluene solutions **1-Cl** at 2.0 K.

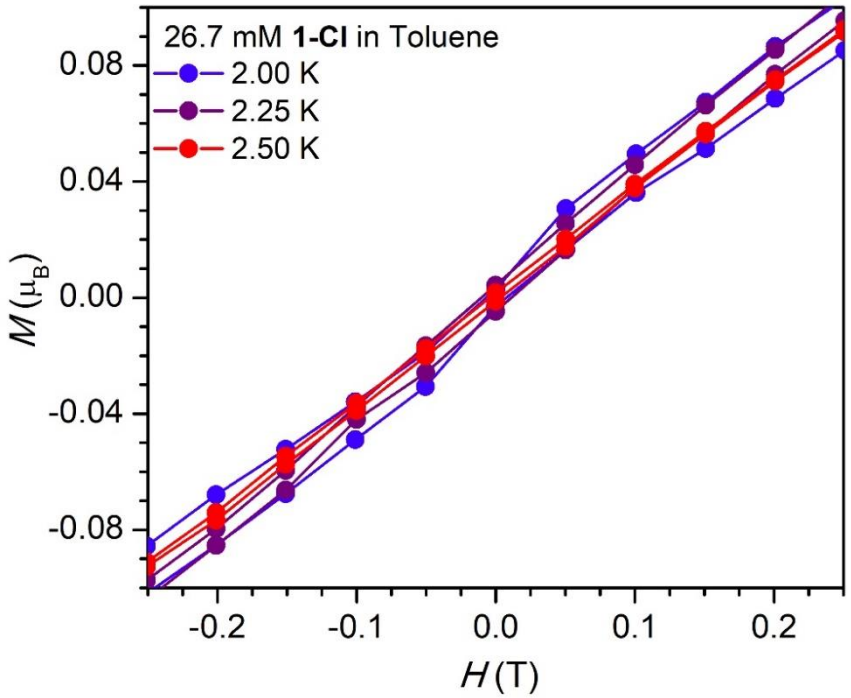

Figure S69. Variable field magnetization data collected on a frozen solution sample of **1-Cl**, revealing hysteresis within the temperature range of 2 to 2.5 K.

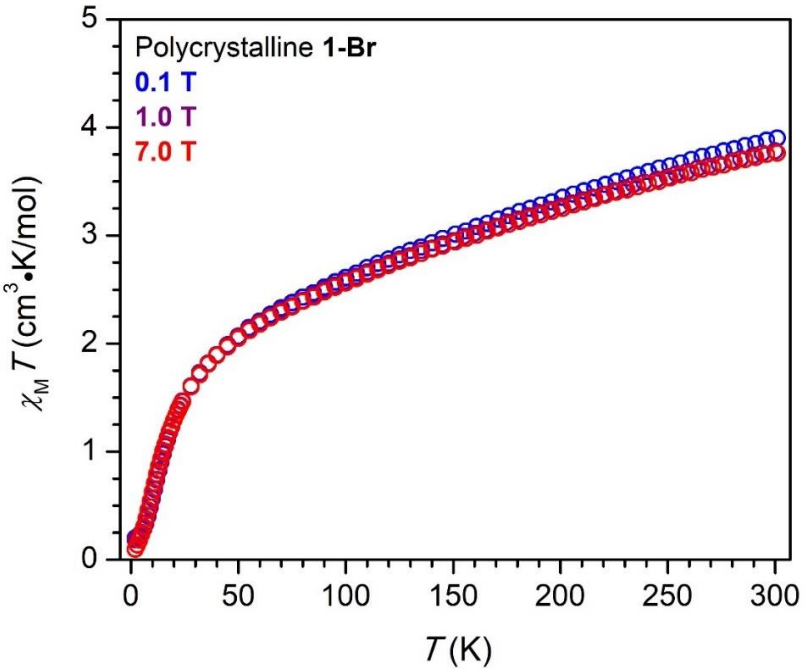

Figure S70. Plot of $\chi_M T$ versus T for polycrystalline **1-Br** under dc fields of 0.1 T (blue circles), 1 T (purple circles), and 7 T (red circles). The decrease in $\chi_M T$, particularly at low temperatures, is ascribed to antiferromagnetic exchange coupling as well as the thermal depopulation of excited crystal field states (i.e., M_J states) as a result of magnetic anisotropy and strong Zeeman splitting.

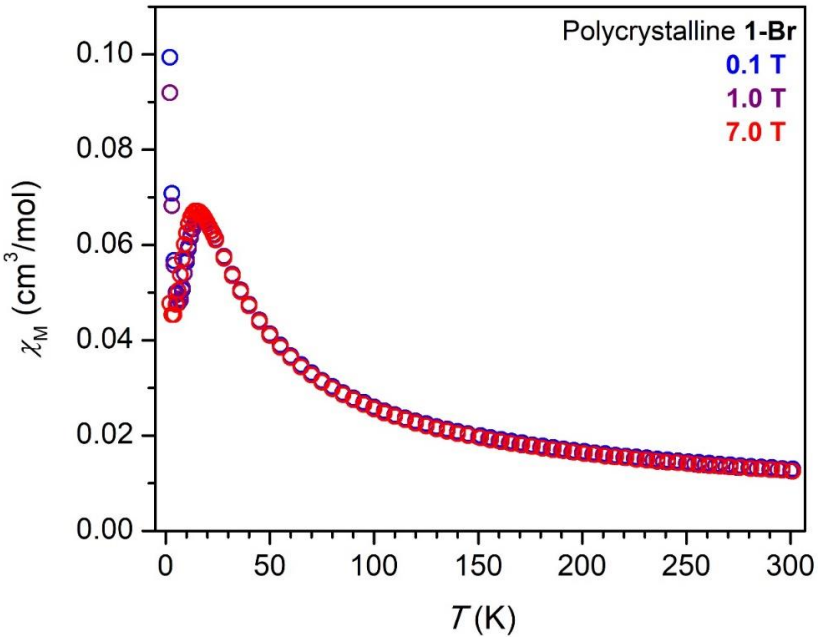

Figure S71. Plot of the molar magnetic susceptibility (χ_M) versus temperature for polycrystalline **1-Br** under dc fields of 0.1 T (blue circles), 1 T (purple circles), and 7 T (red circles).

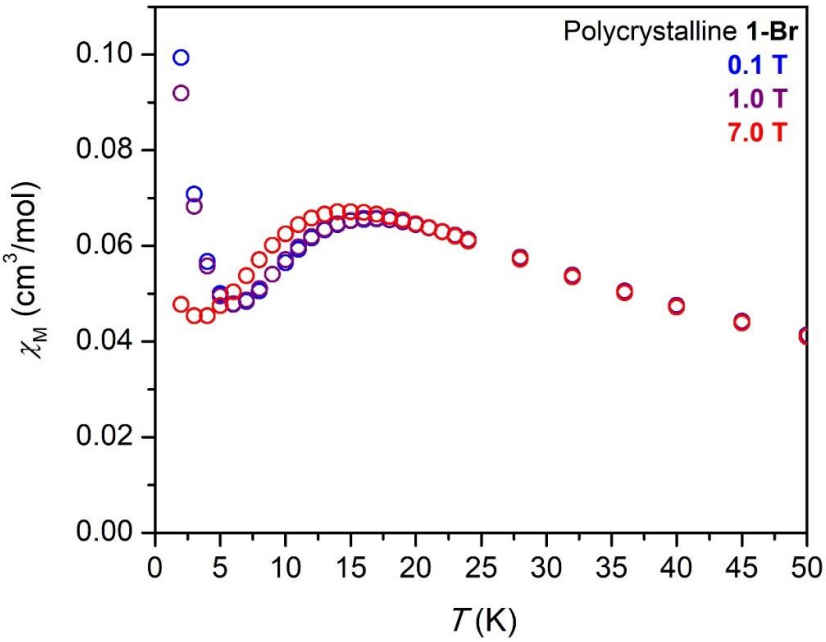

Figure S72. Plot of χ_M versus T for polycrystalline **1-Br** under dc fields of 0.1 T (blue circles), 1 T (purple circles), and 7 T (red circles) between 2 and 50 K. The maxima in χ_M at 17 K (0.1 T and 1.0 T) or 15 K (7.0 T) are ascribed to antiferromagnetic coupling between uranium ions. The decrease in the temperature of this maximum at higher-applied field strengths might be ascribed to a greater Zeeman splitting of the ferromagnetic excited state relative to the antiferromagnetic ground state, which could lead to a smaller energy gap at higher applied fields.[32]

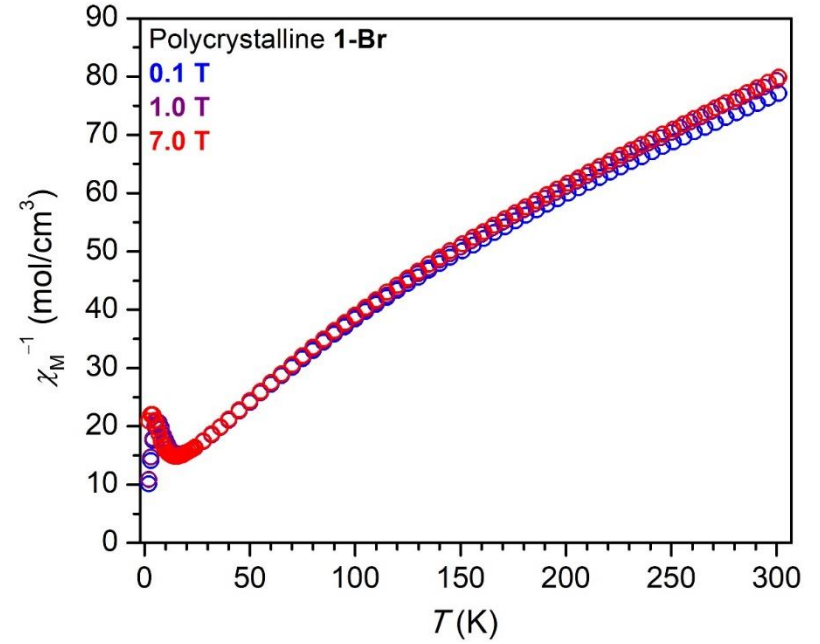

Figure S73. Plot of χ_M^{-1} versus T for polycrystalline **1-Br** under dc fields of 0.1 T (blue circles), 1 T (purple circles), and 7 T (red circles).

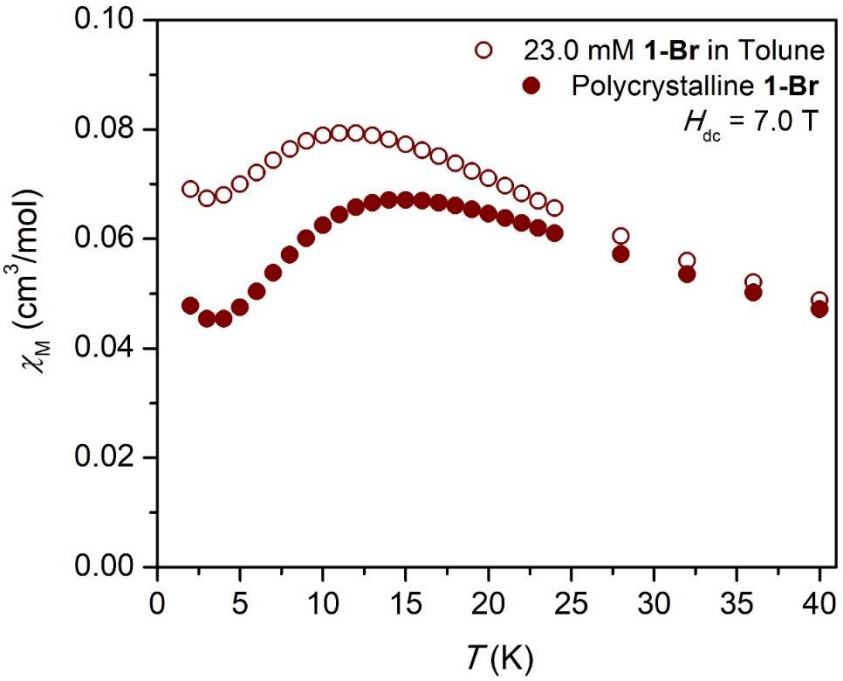

Figure S74. Plot of χ_M versus T for polycrystalline **1-Br** (filled symbols) and a 23.0 mM toluene frozen solution of **1-Br** (empty symbols) under a dc field 7 T. The maximum in χ_M decreases from 15 K (polycrystalline) to 11 K (toluene solution), presumably due to a structural change in solution leading to weaker magnetic exchange coupling.

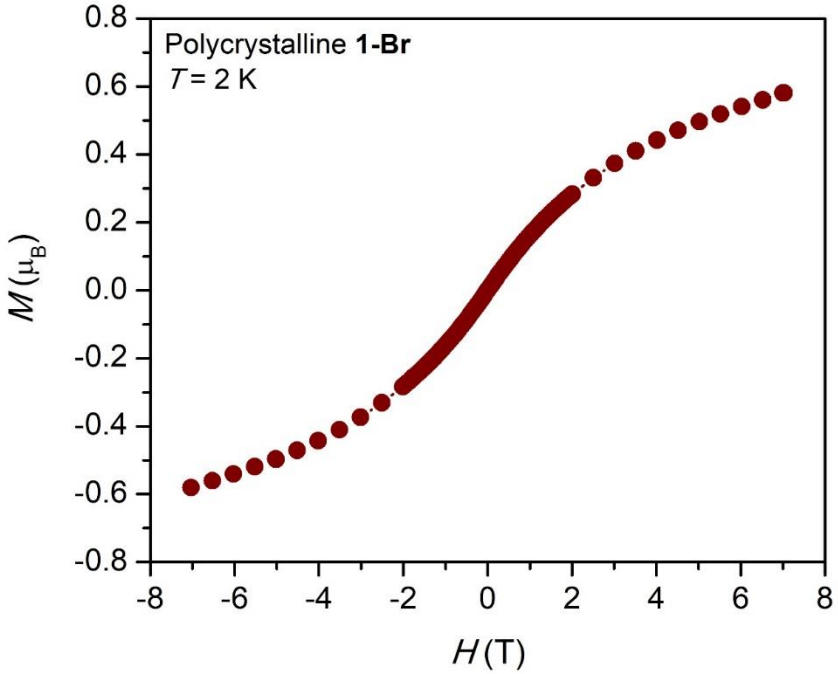

Figure S75. Variable-field magnetization data collected on polycrystalline **1-Br** at 2.0 K under applied fields from ±7 T. Sweep rates of 140(4) Oe/s and 33(1) Oe/s were used for $|H_{dc}| > 20$ kOe and $|H_{dc}| < 20$ kOe, respectively.

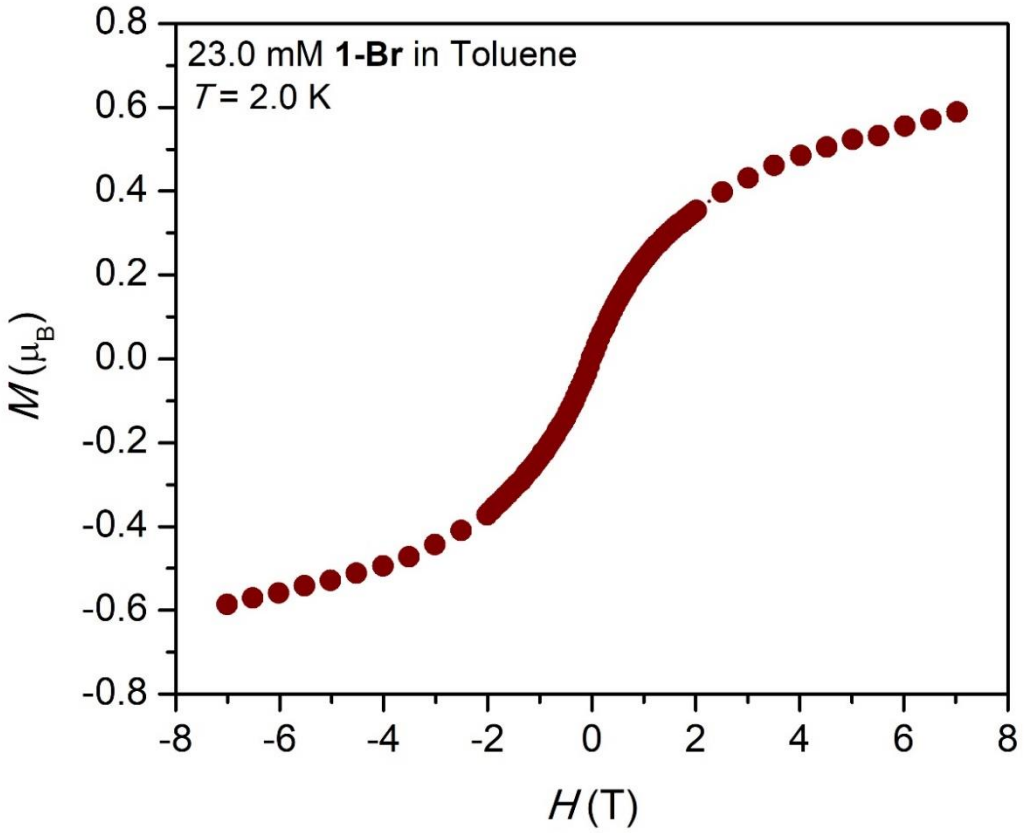

Figure S76. Variable-field magnetization data collected on a frozen 23.0 mM solution of **1-Br** in toluene, at 2.0 K, under applied fields ranging from ± 7 T. Sweep rates of 140(4) Oe/s and 33(1) Oe/s were used for $|H_{dc}| > 20$ kOe and $|H_{dc}| < 20$ kOe, respectively.

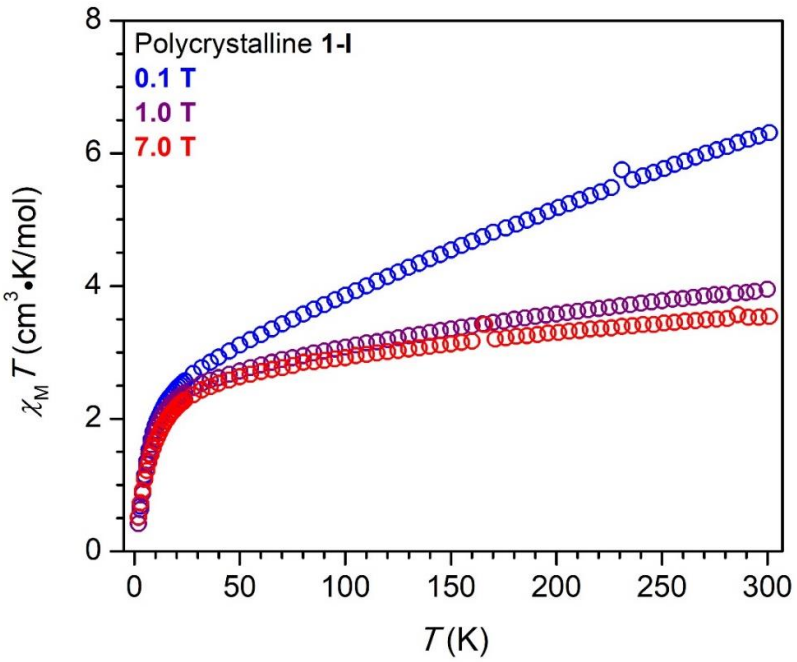

Figure S77. Plot of $\chi_M T$ versus T (without a ferromagnetic correction) for polycrystalline **1-I** under dc fields of 0.1 T (blue circles), 1 T (purple circles), and 7 T (red circles). The decrease in $\chi_M T$, particularly at low temperatures, is ascribed to a combination of antiferromagnetic exchange coupling as well as the thermal depopulation of excited crystal field states (i.e., M_J states) as a result of magnetic anisotropy and strong Zeeman splitting.

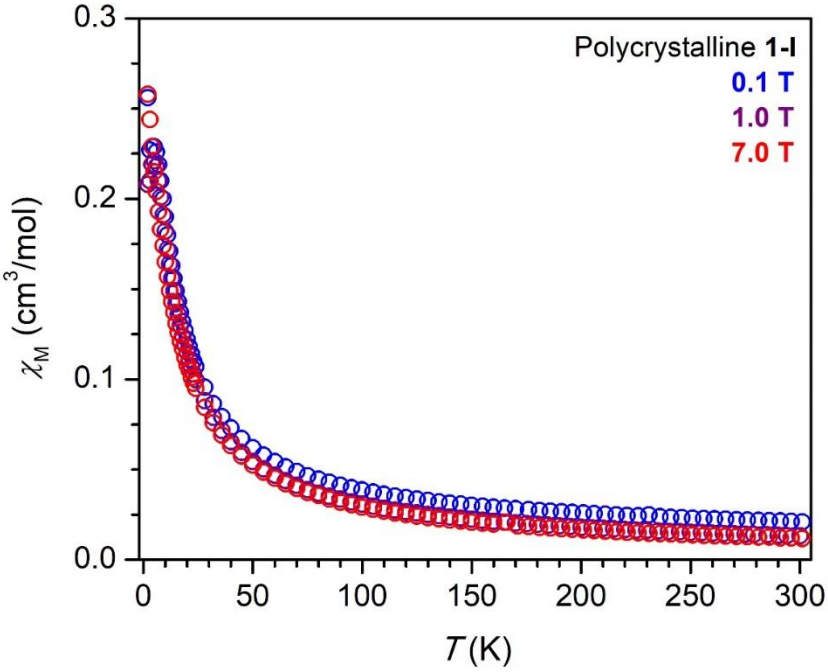

Figure S78. Plot of χ_M versus T (without a ferromagnetic correction) for polycrystalline **1-I** under dc fields of 0.1 T (blue circles), 1 T (purple circles), and 7 T (red circles).

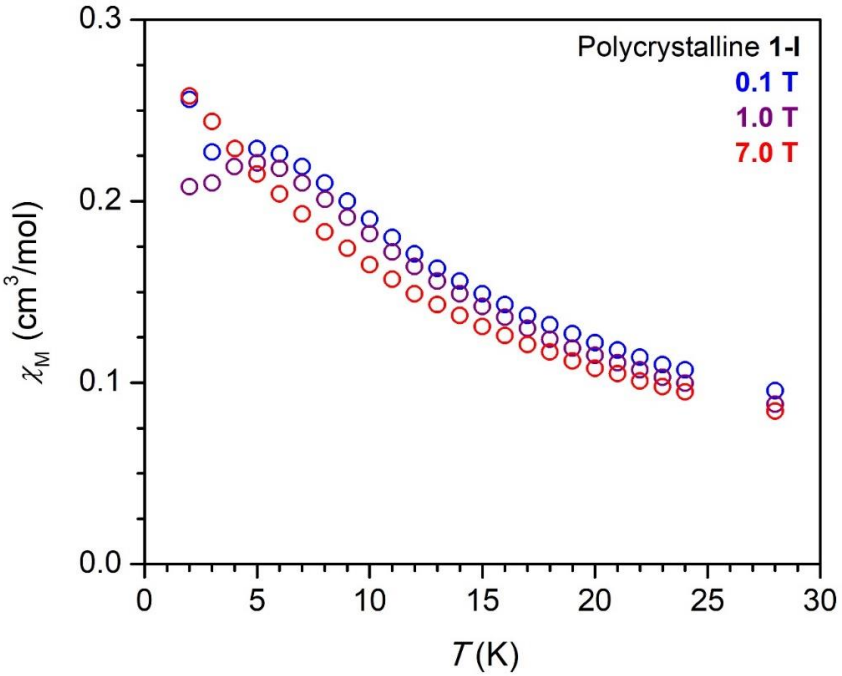

Figure S79. Plot of χ_M versus T (without a ferromagnetic correction) for polycrystalline **1-I** under dc fields of 0.1 T (blue circles), 1 T (purple circles), and 7 T (red circles) between 2 and 30 K.

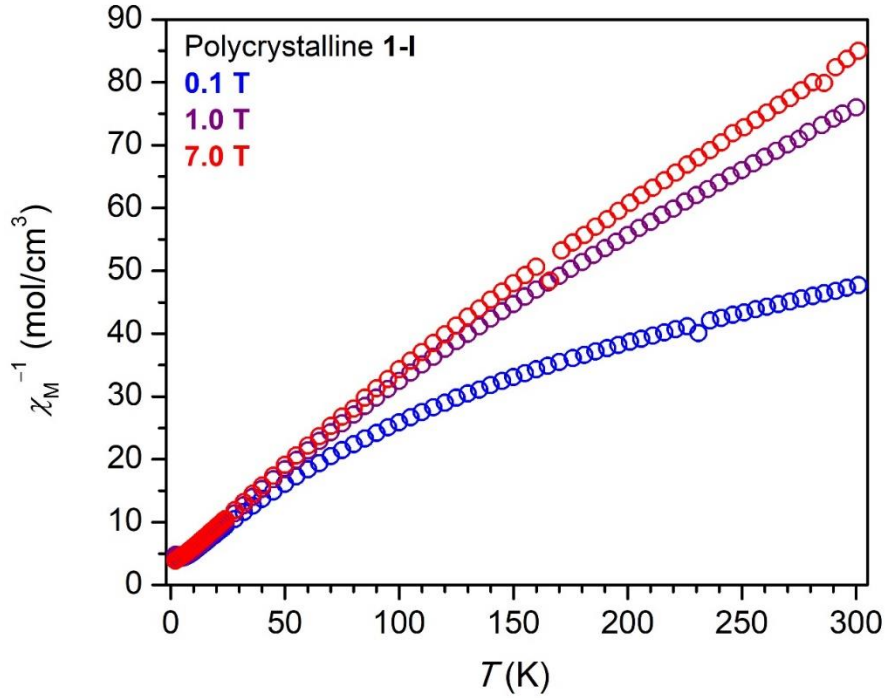

Figure S80. Plot of χ_M^{-1} versus T (without a ferromagnetic correction) for polycrystalline **1-I** under dc fields of 0.1 T (blue circles), 1 T (purple circles), and 7 T (red circles).

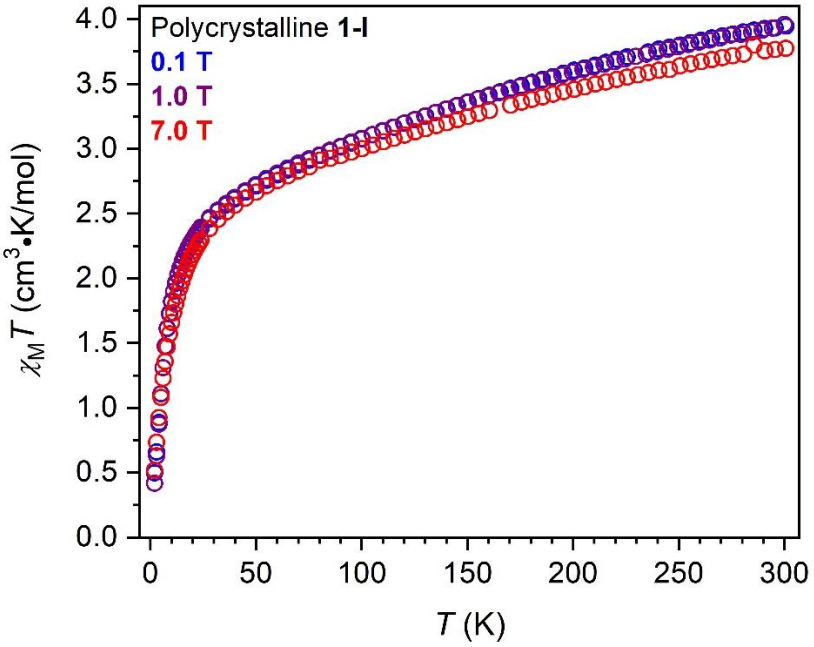

Figure S81. Plot of $\chi_M T$ versus T for polycrystalline **1-I** under dc fields of 0.1 T (blue circles), 1 T (purple circles), and 7 T (red circles). The susceptibilities have been corrected for the presence of a ferromagnetic impurity. The decrease in $\chi_M T$, particularly at low temperatures, is ascribed to a combination of antiferromagnetic exchange coupling as well as the thermal depopulation of excited crystal field states (i.e., M_J states) as a result of magnetic anisotropy and strong Zeeman splitting.

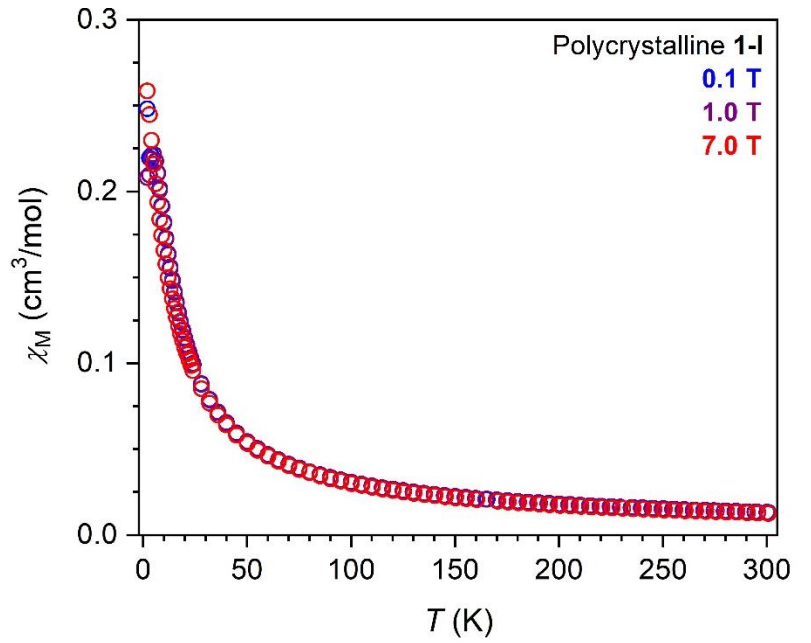

Figure S82. Plot of χ_M versus T for polycrystalline **1-I** under dc fields of 0.1 T (blue circles), 1 T (purple circles), and 7 T (red circles). The susceptibilities have been corrected for the presence of a ferromagnetic impurity.

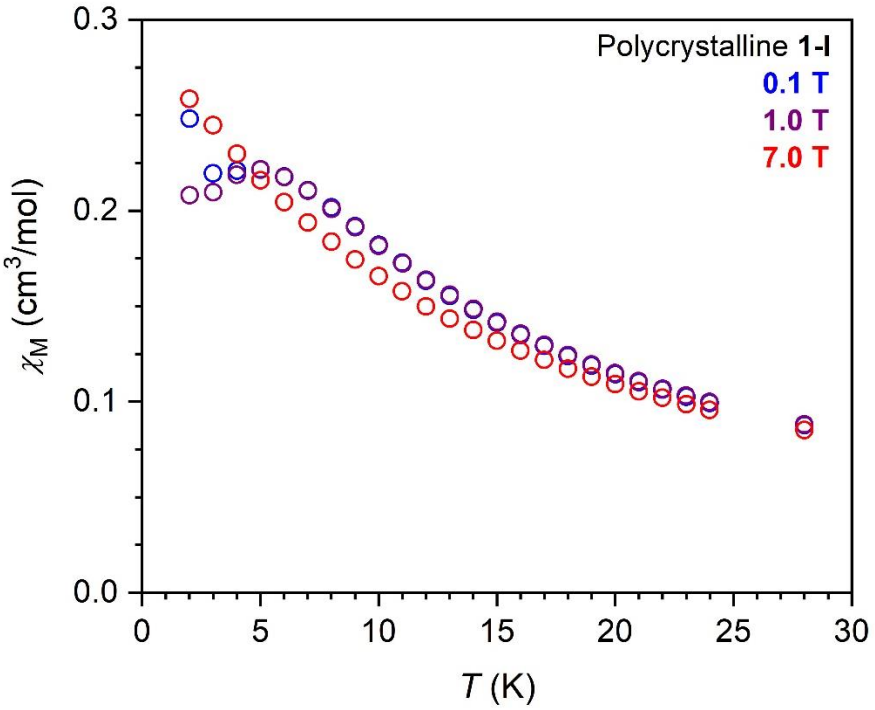

Figure S83. Plot of χ_M versus T for polycrystalline **1-I** under dc fields of 0.1 T (blue circles), 1 T (purple circles), and 7 T (red circles) between 2 and 30 K. The susceptibilities have been corrected for the presence of a ferromagnetic impurity. Under applied fields of 1 T and below, there is a maximum in χ_M at 5 K ascribed to antiferromagnetic coupling between uranium ions. Under a 7 T field, this maximum disappears, likely as strong Zeeman splitting leads to the ferromagnetically coupled excited state becoming the new ground state.

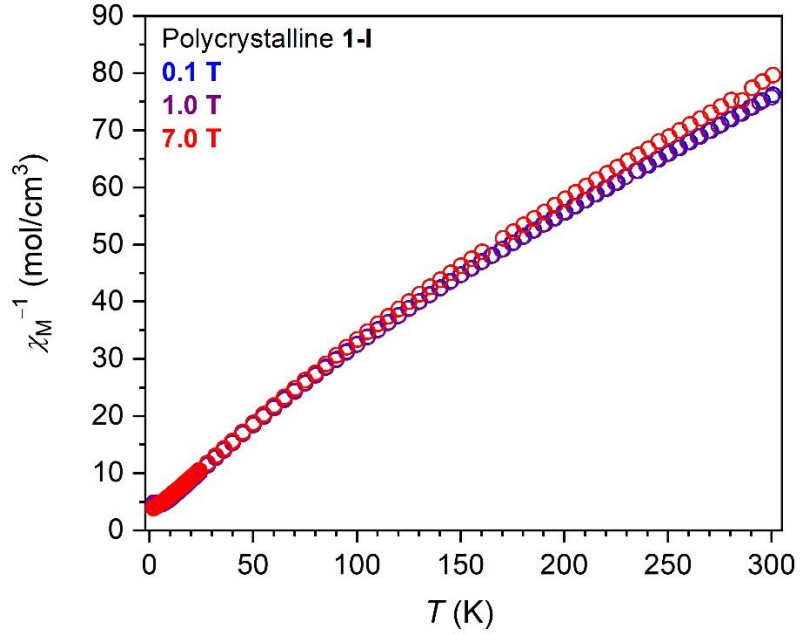

Figure S84. Plot of χ_M^{-1} versus T for polycrystalline **1-I** under dc fields of 0.1 T (blue circles), 1 T (purple circles), and 7 T (red circles). The susceptibilities have been corrected for the presence of a ferromagnetic impurity.

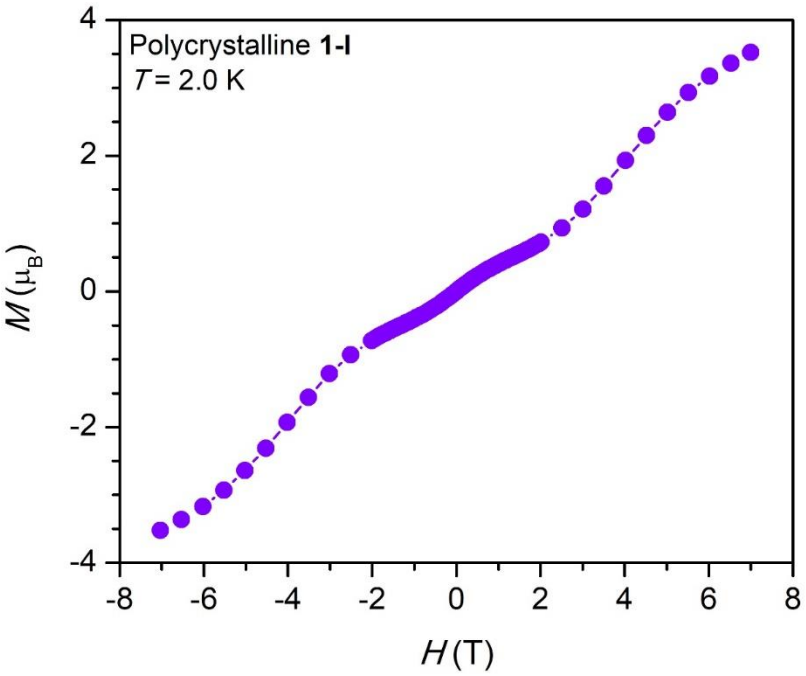

Figure S85. Variable-field magnetization collected on polycrystalline **1-I** at 2.0 K under applied fields ranging from ±7 T. Sweep rates of 140(4) Oe/s and 33(1) Oe/s were used for $|H_{dc}| > 20$ kOe and $|H_{dc}| < 20$ kOe, respectively.

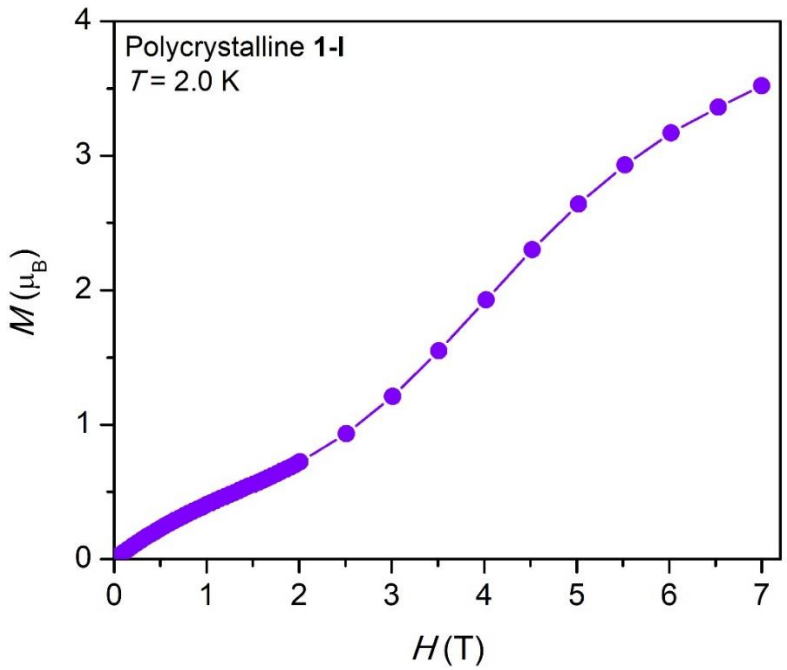

Figure S86. Variable-field magnetization data for **1-I** at 2.0 K under applied fields ranging from 0 to 7 T. When $H_{dc} \leq 1.5$ T, the magnetization approaches a value consistent with an antiferromagnetically-coupled ground state. As the field strength is increased beyond 2 T, *M* increases more dramatically, which we ascribe to a thermally-broadened ground-state crossover, as Zeeman splitting leads to a stabilization of a ferromagnetically-coupled ground state.[32]

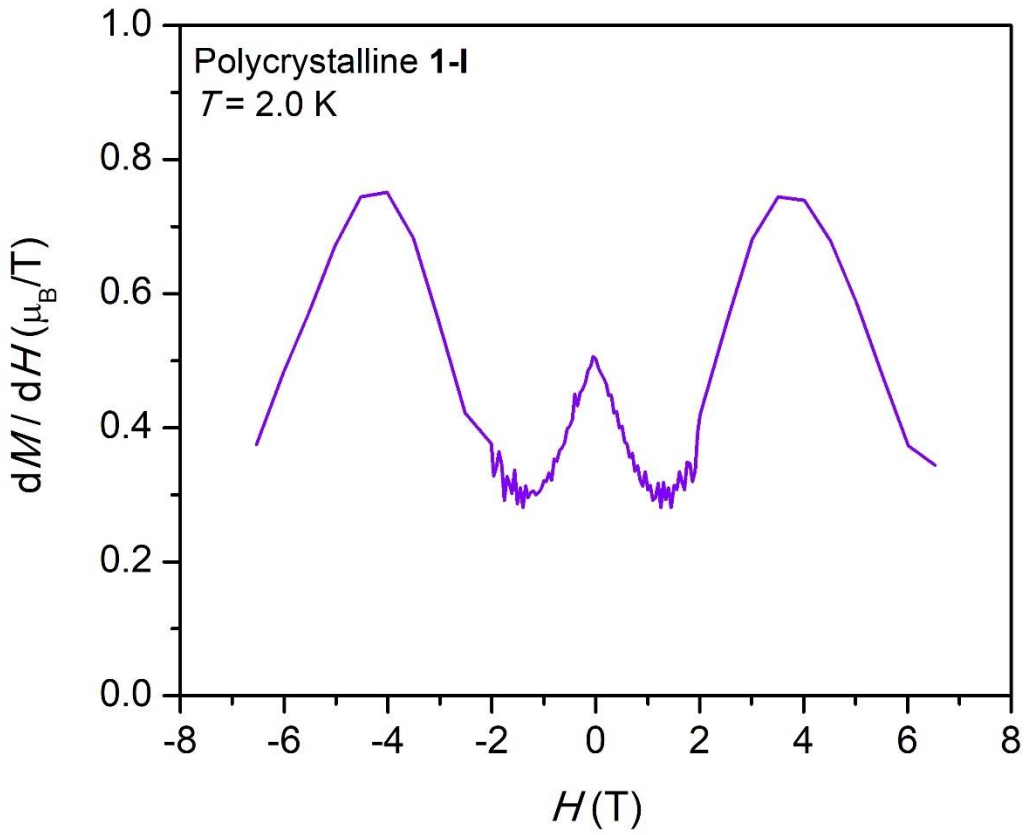

Figure S87. Differential magnetization, d*M*/d*H*, for **1-I** at 2.0 K under applied fields ranging from ±7 T. A maximum in d*M*/d*H* occurs at ± 3.5 T, and this point is known as the critical field, H_{CF}, at which the ground state of **1-I** changes from antiferromagnetically coupled to ferromagnetically-coupled.

6.3 EPR Spectroscopy

X-band electron paramagnetic resonance (EPR) spectroscopy data were collected for **1-X** using a Bruker Elexys E580 spectrometer equipped with a Bruker ER 4118X-MD5 X-band resonator operating in CW mode in an Oxford CF935 flow cryostat. Temperature was maintained using a ColdEdge Stinger closed-cycle helium recirculator. Samples of **1-X** (X = Cl, Br, I) were ground to a fine powder and loaded into 3 mm outer diameter quartz tubes that had been pre-sealed at one end. Each tube was closed off at the other end using a septum and then flame-sealed after cooling with liquid N_2. An additional sample of **1-Cl** was prepared as a solution of ca. 1 mg in 100 μL C_6D_6. All spectra were recorded with a microwave power of 0.47 mW, a modulation amplitude of 4 G, and a modulation frequency of 100 MHz. Spectra were recorded at 6 K for all samples, and in each case no signal attributable to the uranium complexes was observed between 50 and 1000 mT. In the spectra obtained for the solid **1-Br** sample and solution **1-Cl** sample, a small signal at g = 2 was present which we have attributed to contamination by a radical impurity.

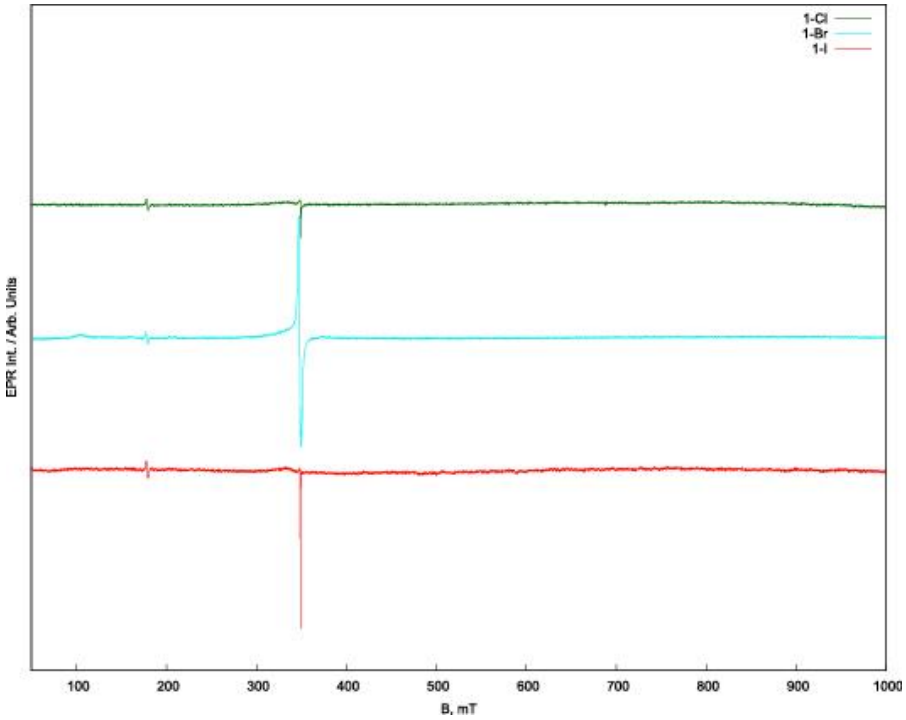

Figure S88. Representative X-band EPR spectra of powdered **1-Cl** (green), **1-Br** (cyan), and **I-I** (red) at 6 K. The small signals at 180 mT, present in all spectra, as well as the sharp negative signals at 350 mT (in **1-Cl** and **1-I**), are due to impurities in the sapphire insert of the resonator. The latter signal is obscured in **1-Br** by a signal originating from an organic radical impurity (g = 2).

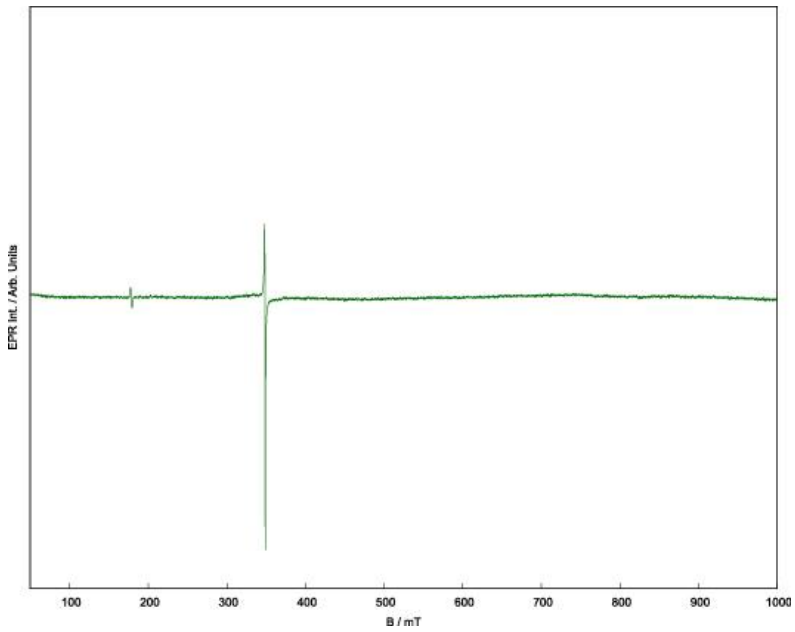

Figure S89. X-band EPR spectrum of **1-Cl** in C_6D_6 collected at 6 K. The small signal at 180 mT is due to impurities in the sapphire insert of the resonator. These impurities also contribute a sharp negative signal at 350 mT, though this is partially obscured by a signal originating from an organic radical impurity (g = 2).

6.4 Simplified Model of Magnetic Exchange in $(Cp^{iPr5})_3U_3X_6$ (X = Cl, Br, I) Using the Ising Model. The Ising model has been used to model magnetic exchange interactions in many anisotropic f-element complexes.[33,34] The main assumptions are: (i) the energy of the interaction is weak enough that only the ground M_J states of each ion are involved in the exchange interaction,[35] and (ii) that the M_J states are largely axial (g_x, g_y = 0), such that only the *z*-component of the exchange interaction can be modelled. A modified form of the Heisenberg Hamiltonian (which is used to model an isotropic magnetic exchange interaction) is then used to describe the exchange interaction involving the z-component of the M_J state for each interacting ion (Figure S73). A further simplification is to treat each M_J state as a pseudospin with a value of ±1/2.[35] In the case of **1-X**, requirement (i) is likely fulfilled—while many uranium(III) complexes are not axial, it is still likely the case that $g_z > g_x, g_y$, given the strong axial anisotropy provided by the crystal field splitting from Cp^{iPr5} on each uranium ion.[8] This is further corroborated by the EPR-silent nature of **1-X** (Figures S88 and S89), which indicates that the ground states are highly axial (i.e., non-zero g_x and g_y tensors are necessary to observe an EPR signal).[36] The *z* axis for the ground M_J state of each uranium ion in **1-X** is assumed to be parallel with the U–Cp(cent) bonding axis for the same ion.[8]

Based on the Ising model for **1-X**, antiferromagnetic coupling will result in three, doubly degenerate antiferromagnetically coupled states in which there is a non-colinear (i.e., non-parallel) alignment of two magnetic moments parallel with respect to each other, and antiparallel with the remaining magnetic moment. These antiferromagnetic states will differ in energy with respect to each other based on differences in the strength of the exchange interaction, *J*, between each pair of uranium ions. The three uranium ions in each compound are structurally very similar with respect to each other (Tables S7-S10), and so these energy differences are likely to be very small (Figure S90). As such, it is reasonable to consider these antiferromagnetic states as quasi-degenerate, similar to what has been observed in triangular, lanthanide Ising complexes.[37] These quasi-degenerate states will then be separated in energy from the doubly-degenerate, excited, ferromagnetic state by a value approximately equal to $2J_{z,avg}$, where $J_{z,avg}$ is the average exchange interaction along the z-direction (assuming $J_{AB} \approx J_{BC} \approx J_{AC} \approx J_{z,avg}$; see Figure S90).

While, in principle, $J_{z,avg}$ represents magnetic exchange interaction in the *z* direction, in **1-X**, this is complicated by the noncolinearity of the *z* axes for each uranium ion. In triangular lanthanide complexes, such as the toroidal magnetic molecule, $[Dy_3(\mu_3\text{-}OH)_2L_3Cl_2(H_2O)_4][Dy_3(\mu_3\text{-}OH)_2L_3Cl(H_2O)_5]Cl_5 \cdot 19\ H_2O$ (HL = *o*-vanillin),[33,38,39] and other structurally analogous complexes,[40,41] a correction can be made to the Ising Hamiltonian used to fit the solid-state dc susceptiblity data to account for non-colinear axes. In the case of such complexes, such as in the o-vanillin complexes, *ab initio* calculations indicate that the *z* axes for each Dy ion are related to each other by approximately 120°. Then, this colinearity can be accounted for within the Lines model[35] where $\tilde{J} = 25\cos\varphi J$, where φ is the angle between the anisotropy axes between the two metal ions involved in the exchange interaction, $\tilde{J}$ is the Lines exchange coupling parameter, and *J* is the exchange interaction extracted from fits of the powder susceptibility data using the Ising Hamiltonian. In the end, this results in an energy level scheme analogous to that shown in Figure S90. The applicability of the Ising model to such complexes is the result of both well-established *ab initio* computational methods that are available to model the electronic structure of Dy(III) ($4f^9$, $^6H_{15/2}$) and the highly axial nature of the ground M_J state of Dy(III) in an axial ligand field, resulting in anisotropy tensors (g_x, g_y, g_z) that show small deviations from that expected for $M_J = \pm 15/2$ (0, 0, 20). In such cases, *ab initio* calculations on mononuclear fragments of the exchange-coupled

complexes allows the anisotropy axes (i.e., *z* axes) for the ground M_J state of each Dy ion to be determined, as well as the relative orientations of these axes with respect to the other. Such information is crucial in order to accurately apply the Ising model to fit the dc magnetic susceptibility data in such highly-anisotropic complexes. The greater complexity of uranium's electronic structure makes analogous computational methods more difficult. To the best of our knowledge, such methods have not been used to model magnetic exchange in actinide complexes. Attempts at such methods are beyond the scope of this paper, but we note that we plan to pursue such methods for the subject of a follow-up study.

Since we have no knowledge of the anisotropy tensors of the ground M_J state of each uranium ion in **1-X**, we did not attempt to fit the dc magnetic susceptiblity data using the Ising model. We note that the Ising model has previously been used to fit dc susceptibility data in the diimide-bridged diuranium(V) complex, $[(MeC_5H_4)_3U]_2(\mu\text{-}1,4\text{-}N_2C_6H_4)]$,[42] resulting in a $J = -19$ cm^{-1} as well as in the trinuclear mixed-valence neptunyl(V/VI) complex, $(Np^{VI}O_2Cl_2)[Np^{V}O_2Cl(THF)_3]_2$, resulting in a $J = +7.5$ cm^{-1} between the Np(V) and Np(VI) ions.[43] The modelling of the exchange interaction in the former is simplified by the near-colinear nature of the magnetic moments of the uranium(V) ions. In the case of the latter, the relatively simpler electronic structures afforded by the $5f^1$ and $5f^2$ ions of Np(VI) and Np(V), respectively—relative to $5f^3$ uranium(III)—help simplify the number of crystal field parameters needed to describe the M_J states in the complex.

During our investigation of the dynamic magnetic properties of **1-Cl** and **1-Br**, we found that the temperature dependence of their magnetic relaxation times, τ, extracted from ac susceptibility measurements was best fit—all or in part—to an Orbach process, described by the equation $\tau^{-1} = \tau_0^{-1}\exp(-U_{eff}/k_BT)$ where U_{eff} is the thermal barrier to magnetic relaxation. Furthermore, our studies on dilute, frozen solution samples of these complexes indicated that the magnetic relaxation rates become faster in solution, which we can attribute, possibly, to structural changes leading to weaker magnetic exchange interactions in solution. This strongly suggested that U_{eff} is correlated with the strength of the exchange interaction in these complexes. This is similar to what has been observed in radical-bridged multinuclear lanthanide complexes that possess strong magnetic exchange interactions.[44,45] In such complexes, U_{eff} is related to the energy needed to flip one of the magnetic moments in the ground, exchange-coupled state into the opposite direction. By analogy, U_{eff} for **1-Cl** and **1-Br** would be related to the energy needed to flip the magnetic moment of the antiparallel-aligned magnetic moment within the antiferromagnetic ground state such that it becomes near-parallel with the other two magnetic moments. This flip in the direction of the magnetic moment will happen along the *z* axis for each respective uranium ion. Thus, this directional flip results in an arrangement consistent with the ferromagnetic excited state described by the Ising model. This state is higher in energy than the antiferromagnetic ground state by approximately $2J_{z,avg}$. Thus, even though our use of the Ising model does not provide any information on the net direction of the magnetic moments of the exchange-coupled states (except that it is somewhere in the triangular plane between the three uranium ions) or how the direction of these net magnetic moments are related to the anisotropy axes of the individual ions, we can use the measured values of U_{eff} to estimate $J_{z,avg}$. Then, assuming that exchange along the *x* and *y* axes of each uranium ion is negligible in comparison, we can further approximate $J_{z,avg} \approx J_{avg}$, the average exchange interaction between uranium ions in **1-X**. For **1-Br**, we obtained a value of $J_{avg} = -10.1$ cm^{-1}. Based on the temperature at which χ_M reaches a maximum for **1-Br**, 17 K (corresponding thermal energy of $k_BT = 11.8$ cm^{-1}), this exchange value is reasonable. The temperature at which χ_M reaches a maximum is related to the strength of the exchange

interaction.[34,46] For **1-Cl**, two relaxation processes were observed, suggesting that J_{avg} is within the range of −15.3 to −22.5 cm^{-1}, but is likely closer to the former because the temperature at which χ_M reaches a maximum is 28 K (19.5 cm^{-1}). The other relaxation process might involve excited M_J states, further emphasizing that the **1-X** complexes are not perfectly Ising.

The exchange interactions estimated here using $U_{eff} = 2J$ are likely overestimates of the actual exchange interaction.

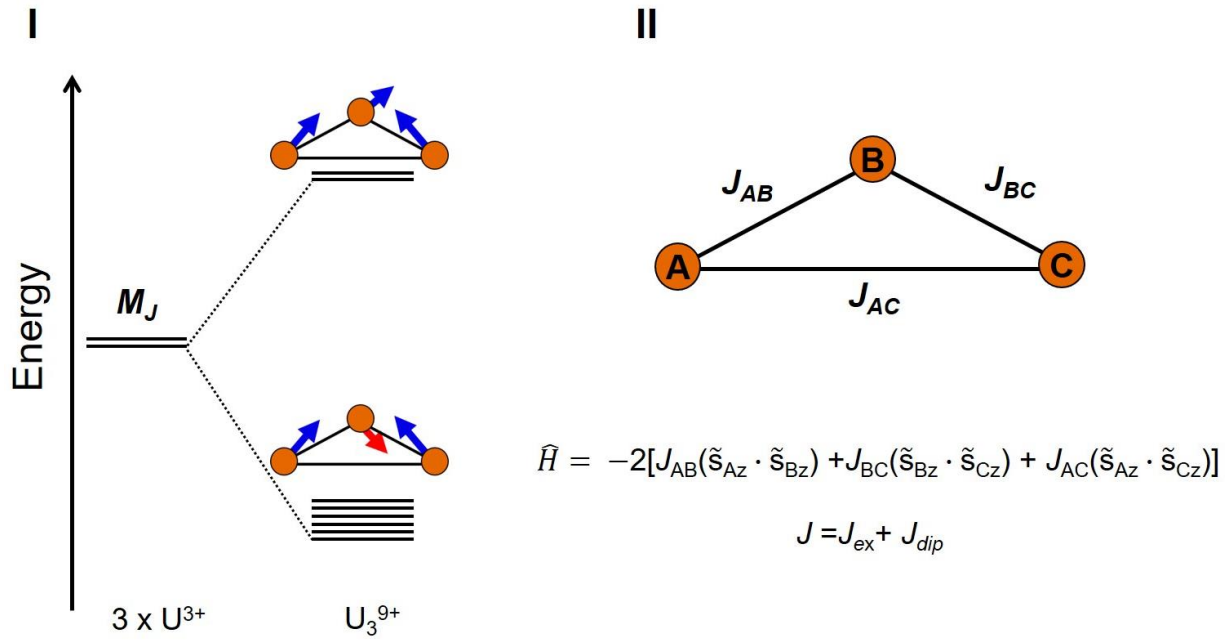

Figure S90. (I) Simplistic illustration of the exchange interactions in **1-X**, in which the ground Kramers doublet ($\pm M_J$ state) of each uranium ion interacts with the Kramers doublets of the other ions to produce three pairs of quasi-degenerate antiferromagnetic states and one doubly-degenerate ferromagnetic excited state. (II) The uranium ions in **1-X** are inequivalent with respect to each other, resulting in three pairs of exchange interactions. These exchange interactions were modeled using a pseudospin Hamiltonian.[34,35]

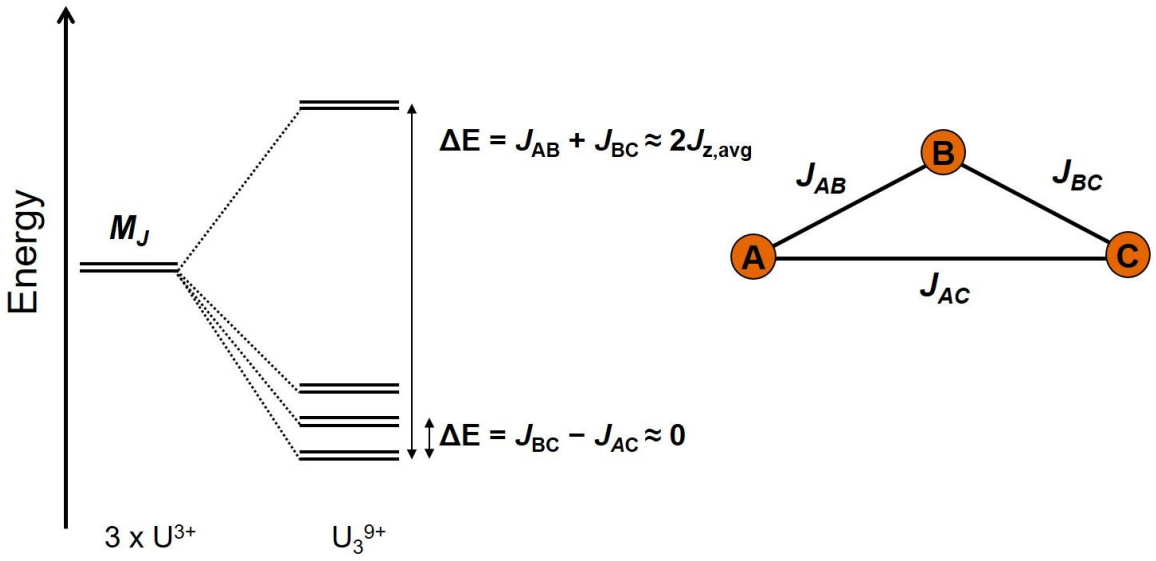

Figure S91. Exchange-coupled states in **1-X** based on the Hamiltonian in Figure S90. Here it is assumed that the differences between the exchange interactions involving atoms A, B, and C, are likely small, such that the three antiferromagnetic Kramers doublets are pseudo-degenerate.

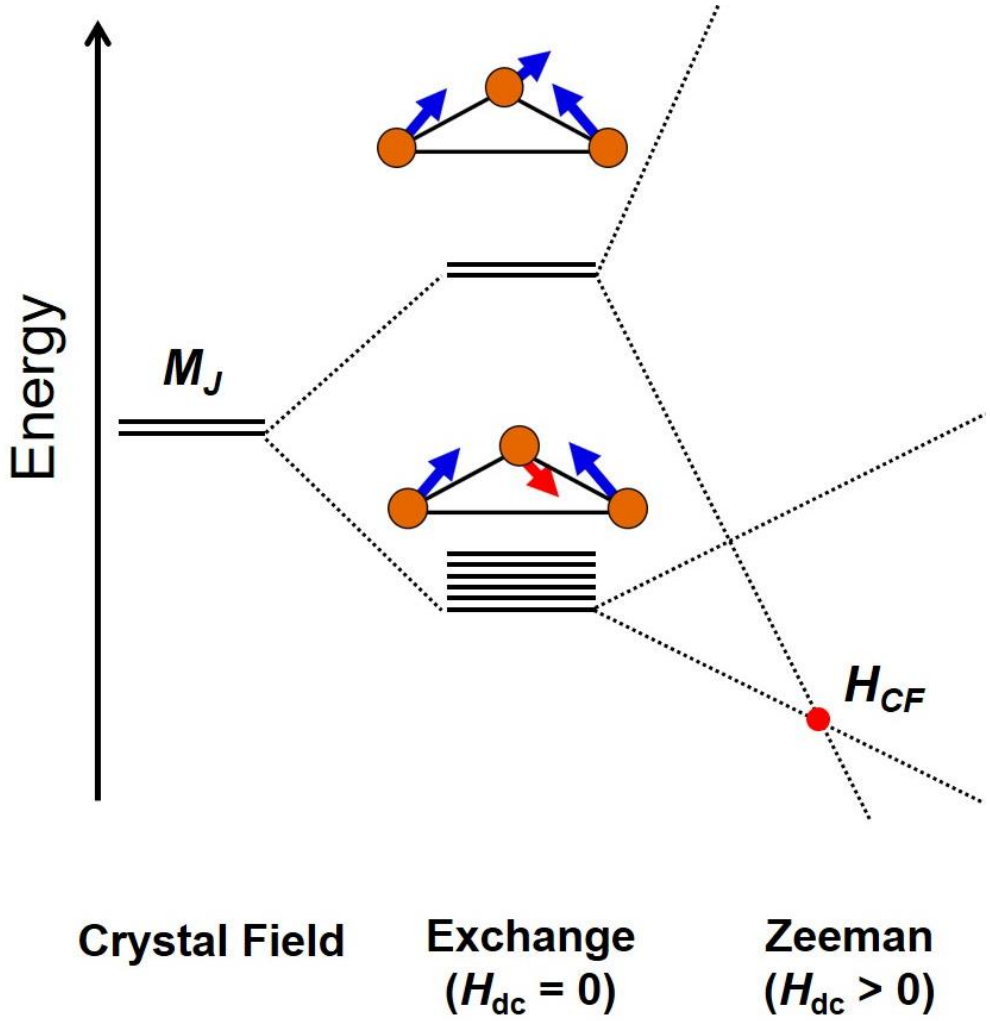

Figure S92. Exchange-coupled states in **1-X** based on the Hamiltonian shown in Figure S90. The ferromagnetic excited state will interact with an applied magnetic field more strongly than the antiferromagnetic ground states, such that upon reaching a critical field, H_{CF}, the ferromagnetic state becomes lower in energy that the antiferromagnetic states, such as what is observed in **1-I**.[32]

6.5 Estimation of the Dipolar Exchange Strength in 1-X. The dipolar interaction is a through-space interaction between magnetic moments, and can be modelled using the well-known Hamiltonian:[47]

$$\widehat{H}_{\text{dip}} = \frac{-\hat{\mu}_1 \cdot \hat{\mu}_2 - 3(\hat{\mu}_1 \cdot \vec{n}_{12})(\hat{\mu}_2 \cdot \vec{n}_{12})}{r_{12}^3}$$

Here, $\hat{\mu}_1$ and $\hat{\mu}_2$ are the magnetic moments of spins 1 and 2, r_{12} is the distance between the magnetic moments, and $\vec{n}_{12}$ is a unit vector along the r_{12} axis. For the f elements, if the dipolar interaction is weak relative to the magnetic anisotropy (i.e., crystal field splitting of the $\pm M_J$ Kramers doublets), then only interactions between the ground Kramers doublet of each metal ion need to be considered, and the magnetic moments can be simplified as pseudospins ($\hat{\tilde{s}}_i$ = ½):

$$\hat{\mu}_i = -\mu_B g_{zi}^{(i)} \hat{\tilde{s}}_{izi} \vec{e}_{zi} \; (i = 1, 2)$$

Where $g_{zi}^{(i)}$ is the anisotropy tensor for spin *i*, and $\vec{e}_{zi}$ is the principal magnetic axis for spin *i*. Then the dipolar interaction strength, J_{dip} can be written:

$$J_{\text{dip}} = \left(\frac{\mu_0}{4\pi}\right) \mu_B^2 g_{z1}^1 g_{z2}^2 \frac{(cos\theta_{12} - 3cos\theta_{1n} cos\theta_{2n})}{r_{12}^3}$$

Where θ_{12} is the angle between the principal anisotropy axes of the two spins, θ_{in} (i = 1,2) is the angle between the principal magnetic axis on center *i* and the vector $\vec{n}_{12}$ connecting the two spins, μ_0 is the vacuum permeability of free space (1.257×10^{-6} kg·m/s^2·A^2), μ_B is the Bohr magneton (9.274×10^{-24} m^2·A), and r_{12} is reported in meters, m, resulting in an interaction strength in units of Joules, J, that can be related to cm^{-1} (1 cm^{-1} = 9.274×10^{-23} J).

Without knowledge of the relative orientations (and anisotropy tensors) of the Kramers ground states in **1-X**, we cannot accurately calculate J_{dip}. Nevertheless, the maximum strength of the dipolar interaction arises when the spins are completely parallel with each other and with the axis joining them, such that $\theta_{12} = \theta_{in} = 0°$, allowing us to estimate the maximum possible interaction strength in these complexes (in reality, the Kramers doublets will be non-colinear with respect to each other, so the real J_{dip} will be smaller). If we assume that the ground state of each uranium ion in **1-X** is maximal, such that $M_J = \pm 9/2$, then (g_x, g_y, g_z) = (0, 0, 2·m_J·g_J) = (0, 0, 6.55), where g_J is the Landé *g*-factor. Then, the average dipolar interaction strength between two Kramers doublets in **1-X**, based on the average U···U separations in their crystal structures, will be 0.50 cm^{-1} (**1-Cl**), 0.44 cm^{-1} (**1-Br**), and 0.39 cm^{-1} (**1-I**). Based on the Ising model, the separation between the ground, antiferromagnetic states, and the excited, ferromagnetic states, will be roughly equivalent to 2*J*, where *J* is the magnetic exchange interaction ($J = J_{\text{dip}} + J_{\text{ex}}$). Even in the case that J_{dip} is

maximal, this will only correspond to energy gaps of 1.01 cm^{-1} (**1-Cl**), 0.89 cm^{-1} (**1-Br**), and 0.79 cm^{-1} (**1-I**), far smaller than the thermal energies (k_BT) at which the antiferromagnetic exchange begins to dominate the magnetic susceptibility in these complexes: 19.5 cm^{-1} (T = 28 K for **1-Cl**), 11.8 cm^{-1} (T = 17 K for **1-Br**), and 3.5 cm^{-1} (T = 5 K for **1-I**). As such, it is assumed here that the exchange interaction in these complexes is dominated by J_{ex}.

6.6 Ac magnetic susceptibility data collection and fitting. Alternating current (ac) magnetic susceptibility measurements were performed on samples of $(Cp^{iPr5})_2U_2(OPh^{tBu})_4$,, **1-Cl**, **1-Br**, and **1-I**, using a 4 Oe oscillating ac field under zero dc field and applied dc fields up to 3000 Oe over frequencies ranging from 0.1 to 1500 Hz. Ac susceptibility data were fit using a generalized Debye model[48] describing a distribution of relaxation times, with the frequency-dependence of the in-phase ($\chi'(\omega)$) and out-of-phase ($\chi''(\omega)$) magnetic susceptibilities being described by equations S1 and S2:

$$\chi'(\omega) = \chi_S + (\chi_T - \chi_S)\frac{1+(\omega\tau)^{1-\alpha}\sin\left(\frac{\pi\alpha}{2}\right)}{1+2(\omega\tau)^{1-\alpha}\sin\left(\frac{\pi\alpha}{2}\right)+(\omega\tau)^{2-2\alpha}} \qquad \text{(S1)}$$

$$\chi''(\omega) = (\chi_T - \chi_S)\frac{(\omega\tau)^{1-\alpha}\cos\left(\frac{\pi\alpha}{2}\right)}{1+2(\omega\tau)^{1-\alpha}\sin\left(\frac{\pi\alpha}{2}\right)+(\omega\tau)^{2-2\alpha}} \qquad \text{(S2)}$$

Herein, χ_S is the adiabatic susceptibility, χ_T is the isothermal susceptibility, ω is the frequency of the oscillating magnetic field, τ is the relaxation time, and α is a variable representing the distribution of relaxation times and can range from 0 to 1; values close to zero indicate uniform relaxation occurring primarily via one mechanism.

For **1-Cl** and **1-I**, ac susceptibility data required fits involving two relaxation processes, accomplished through the modification of equations S1 and S2:[49]

$$\chi'(\omega) = \chi_{S,Tot} + \Delta\chi_1\frac{1+(\omega\tau_1)^{1-\alpha_1}\sin\left(\frac{\pi\alpha_1}{2}\right)}{1+2(\omega\tau_1)^{1-\alpha_1}\sin\left(\frac{\pi\alpha_1}{2}\right)+(\omega\tau_1)^{2-2\alpha_1}} + \Delta\chi_2\frac{1+(\omega\tau_2)^{1-\alpha_2}\sin\left(\frac{\pi\alpha_2}{2}\right)}{1+2(\omega\tau_2)^{1-\alpha_2}\sin\left(\frac{\pi\alpha_2}{2}\right)+(\omega\tau_2)^{2-2\alpha_2}} \qquad \text{(S3)}$$

$$\chi''(\omega) = \Delta\chi_1\frac{1+(\omega\tau_1)^{1-\alpha_1}\cos\left(\frac{\pi\alpha_1}{2}\right)}{1+2(\omega\tau_1)^{1-\alpha_1}\sin\left(\frac{\pi\alpha_1}{2}\right)+(\omega\tau_1)^{2-2\alpha_1}} + \Delta\chi_2\frac{1+(\omega\tau_2)^{1-\alpha_2}\cos\left(\frac{\pi\alpha_2}{2}\right)}{1+2(\omega\tau_2)^{1-\alpha_2}\sin\left(\frac{\pi\alpha_2}{2}\right)+(\omega\tau_2)^{2-2\alpha_2}} \qquad \text{(S4)}$$

where $\chi'(\omega)$ and $\chi''(\omega)$ are the total in-phase and out-of-phase molar magnetic susceptibilities, respectively; $\chi_{S,Tot}$ is the total adiabatic susceptibility, $\Delta\chi_n$ (n = 1, 2) is the difference in the isothermal (χ_T) and adiabatic (χ_S) susceptibilities for relaxation process n, and all other parameters are defined the same as for S1 and S2.

The α values extracted from fits to χ' and χ'' data were used to calculate uncertainty ranges for τ according to equation S5:

$$\tau_{\pm}(1\sigma) = \tau_\mu e^{\frac{\pm 1.82\sqrt{\alpha}}{1-\alpha}} \qquad \text{(S5)}$$

Herein, $\tau_{\pm}(1\sigma)$ is the uncertainty range for one standard deviation from the mean and τ_μ is the mean relaxation time.[50]

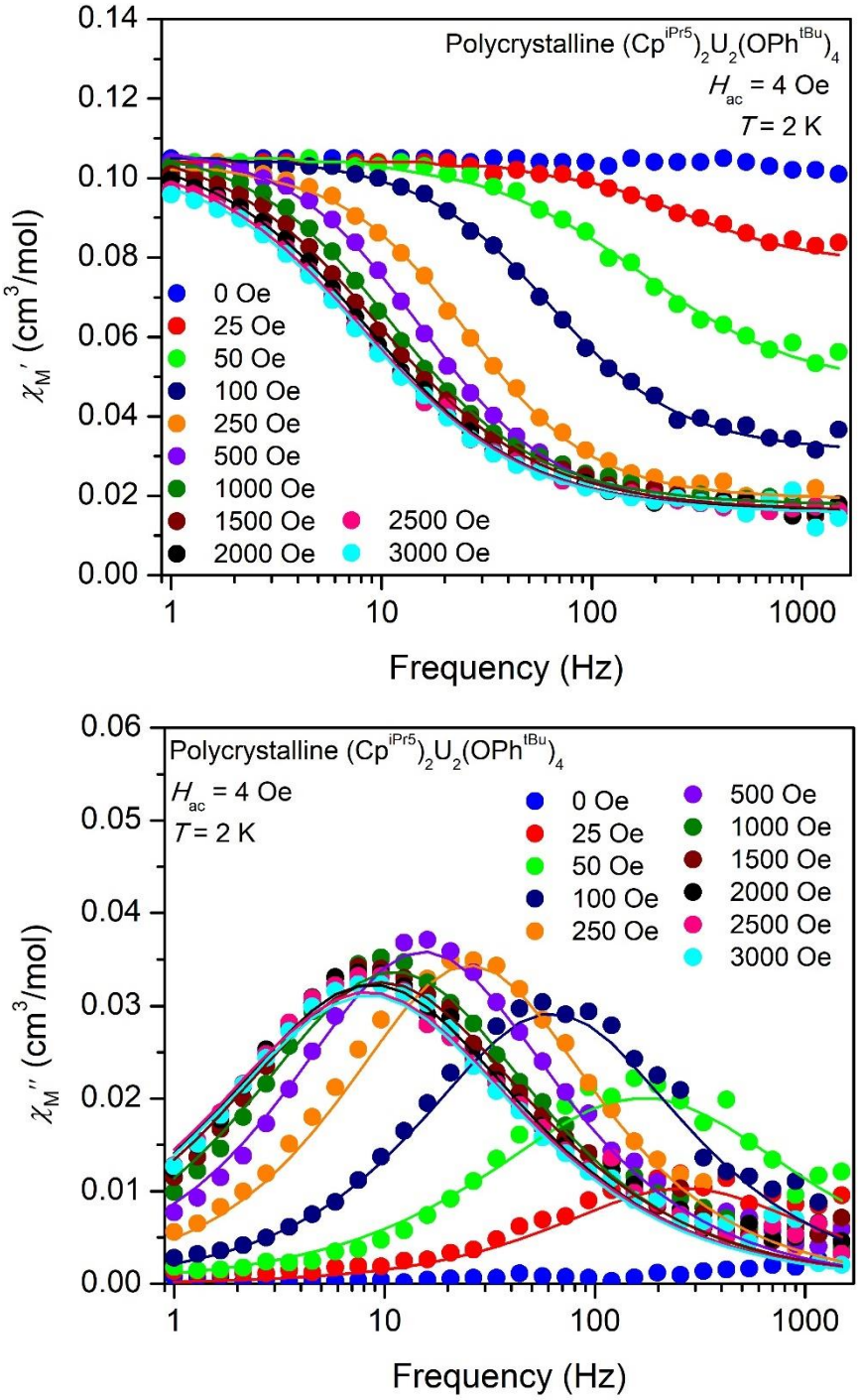

Figure S93. Plot of the in-phase (χ_M', top) and out-of-phase (χ_M'', bottom) molar magnetic susceptibility versus the frequency of the 4 Oe oscillating field for polycrystalline $(Cp^{iPr5})_2U_2(OPh^{tBu})_4$ at 2.0 K. Measurements were performed under frequencies ranging from 1 to 1500 Hz and applied dc fields ranging from 0 to 3000 Oe. Solid lines are fits of the data.

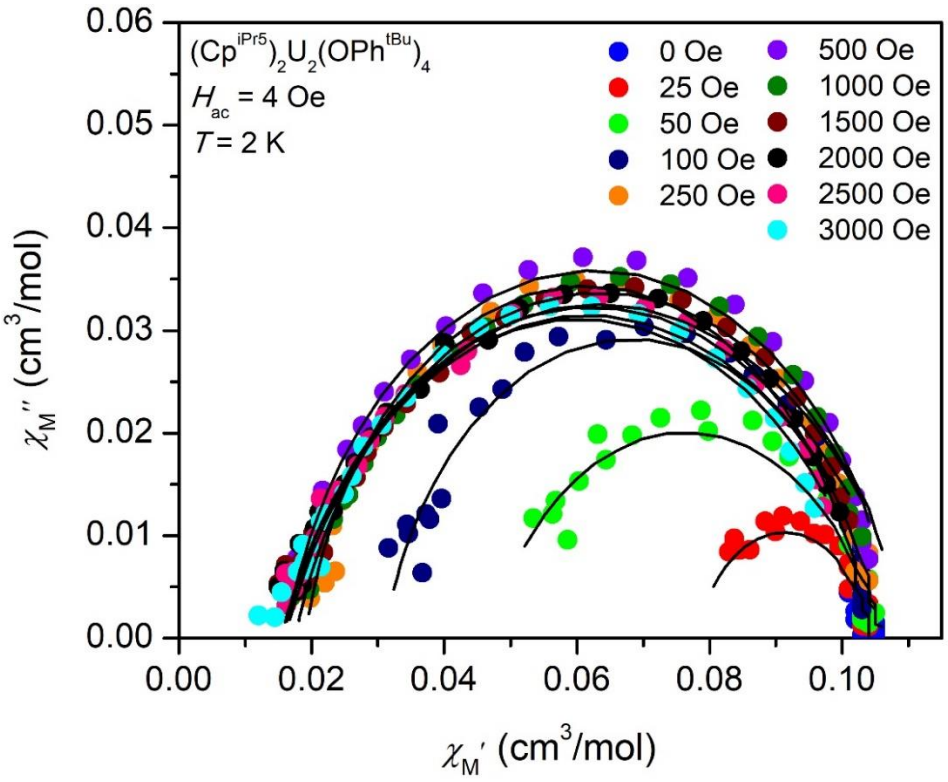

Figure S94. Cole-Cole plots for polycrystalline $(Cp^{iPr5})_2U_2(OPh^{tBu})_4$ collected at 2.0 K under static dc fields ranging from 0 to 3000 Oe. Measurements were performed with a 4 Oe oscillating field under frequencies ranging from 1 to 1500 Hz. Experimental data points are represented by colored circles, and the points representing the fit are connected by solid black lines. Note that χ' does not go to zero, suggesting that there is a fast relaxation process happening at frequencies too high to be probed by within the range of our ac susceptibility measurements (1–1500 Hz).

Table S11. Parameters used to fit ac magnetic relaxation data for $(Cp^{iPr5})_2U_2(OPh^{tBu})_4$ collected at 2.0 K under applied magnetic fields ranging from 25 to 3000 Oe, magnetic relaxation times extracted from these fits, and uncertainty ranges for the magnetic relaxation times.

H_{dc} (Oe)	χ_T (cm^3/mol)	χ_S (cm^3/mol)	α	τ (s)	$\boldsymbol{\tau_+(1\sigma)}^\dagger$ (s)	$\boldsymbol{\tau_-(1\sigma)}^\dagger$ (s)
25	0.104	0.0782	0.150	0.0006	0.001	0.0003
50	0.106	0.0466	0.243	0.0009	0.003	0.0003
100	0.106	0.0309	0.155	0.0025	0.0059	0.0011
250	0.104	0.0191	0.132	0.0063	0.013	0.0029
500	0.109	0.0160	0.166	0.0103	0.0252	0.00430
1000	0.110	0.0175	0.196	0.0143	0.0389	0.00520
1500	0.111	0.0160	0.233	0.0165	0.0519	0.00520
2000	0.109	0.0156	0.229	0.0183	0.0566	0.00590
2500	0.108	0.0153	0.241	0.0192	0.0621	0.00590
3000	0.106	0.0154	0.231	0.0189	0.0590	0.00610

$^\dagger\tau_\pm(1\sigma)$ is the uncertainty range for one standard deviation from the mean

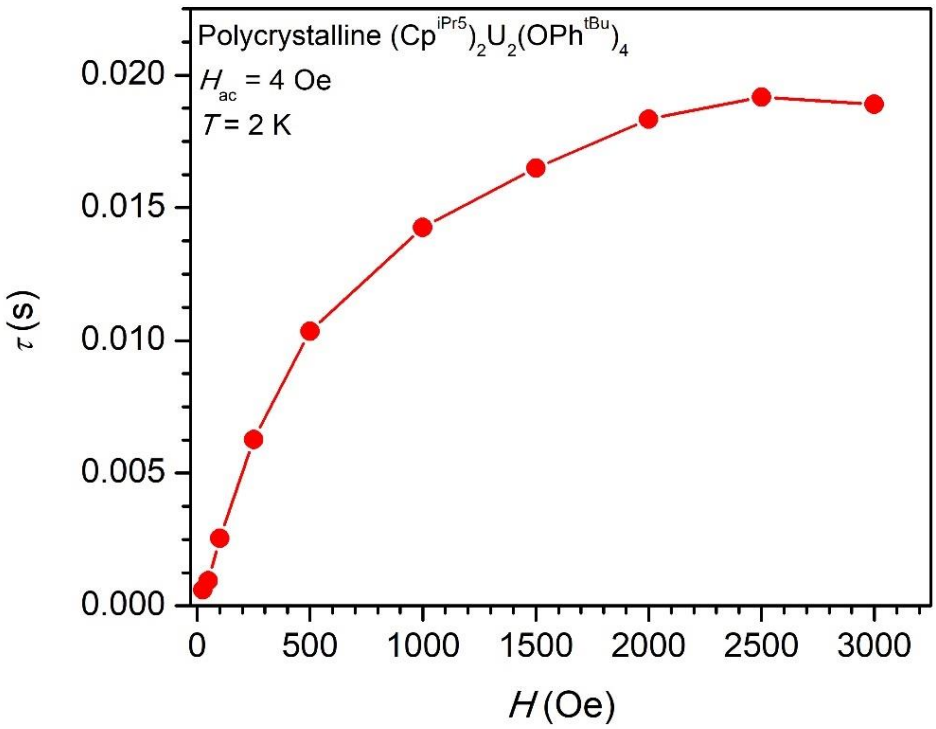

Figure S95. Field dependence of relaxation times extracted from ac magnetic susceptibility measurements on polycrystalline $(Cp^{iPr5})_2U_2(OPh^{tBu})_4$ collected at 2.0 K and applied dc fields ranging from 25 to 3000 Oe. The rapid rise in relaxation times at low fields is consistent with a suppression of quantum tunneling of the magnetization, which arises due to non-axial components in the ground crystal field state. The decrease in relaxation times after 2500 Oe is likely a result of a more efficient direct relaxation process becoming faster at high applied-field strengths.

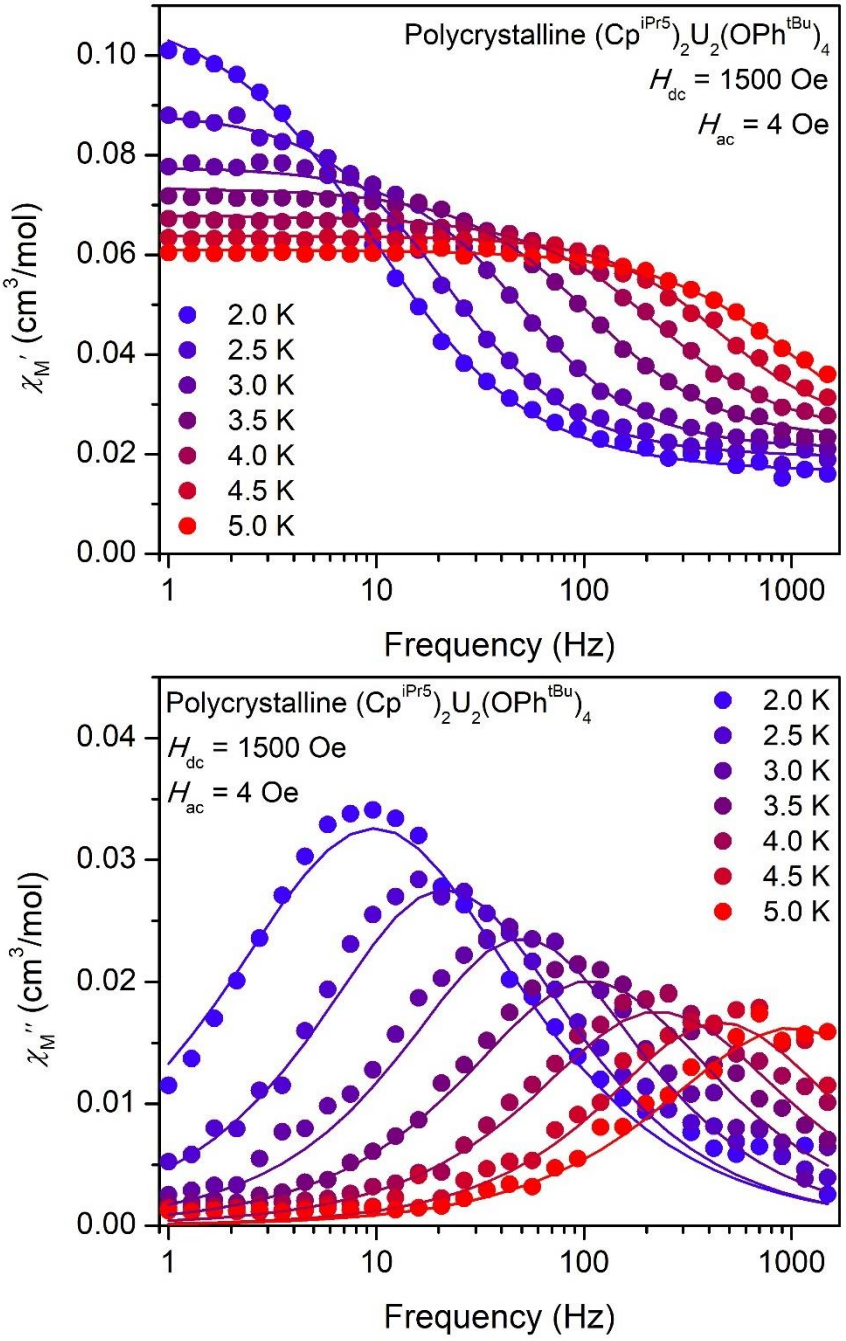

Figure S96. Plot of the in-phase (χ_M', top) and out-of-phase (χ_M'', bottom) molar magnetic susceptibility versus the frequency of the 4 Oe oscillating field for polycrystalline $(Cp^{iPr5})_2U_2(OPh^{tBu})_4$ under a 1500 Oe dc field. Measurement frequencies range from 1 to 1500 Hz, and temperatures range from 2.0 to 5.0 K. Solid lines are fits of the data.

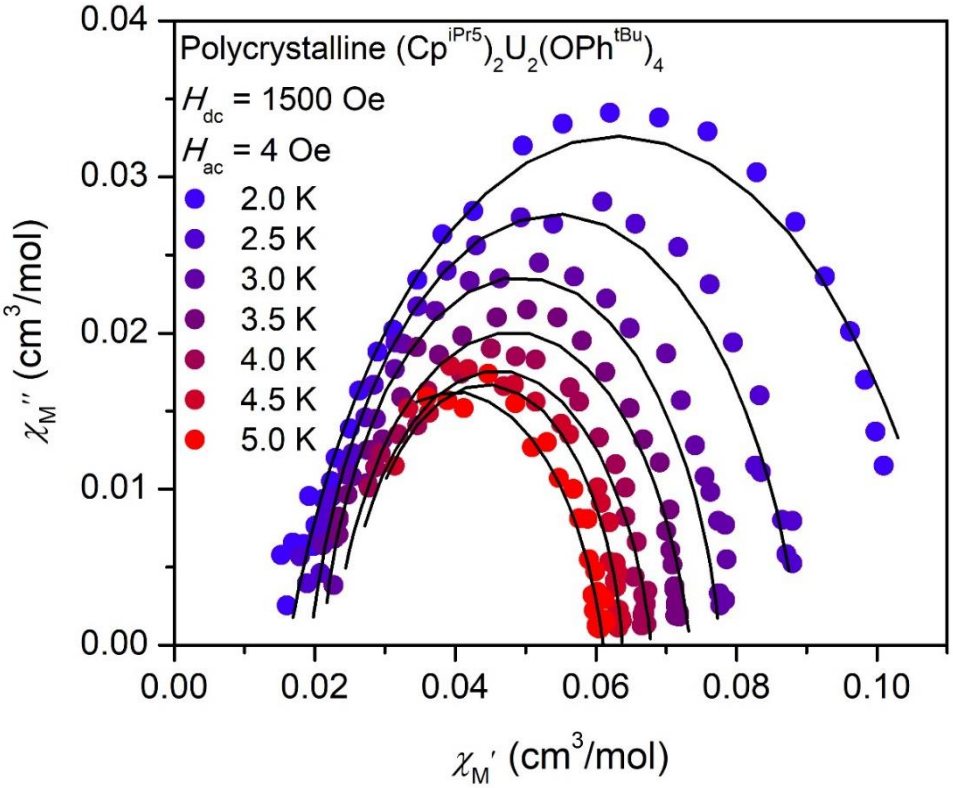

Figure S97. Cole-Cole plots for polycrystalline $(Cp^{iPr5})_2U_2(OPh^{tBu})_4$ collected under a 1500 Oe applied dc field in the temperature range of 2.0 K to 5.0 K. Experimental data points are represented by colored circles, and the points representing the fit are connected by solid black lines. Note that χ' does not go to zero, suggesting that there is a fast relaxation process happening at frequencies too high to be probed by within the range of our ac susceptibility measurements (1–1500 Hz).

Table S12. Parameters used to fit ac magnetic relaxation data for $(Cp^{iPr5})_2U_2(OPh^{tBu})_4$ collected under an applied magnetic field of 1500 Oe over the temperature range of 2.0 K to 5.0 K, magnetic relaxation times extracted from these fits, and uncertainty ranges for the magnetic relaxation times.

T (K)	χ_T (cm^3/mol)	χ_S (cm^3/mol)	α	τ (s)	$\boldsymbol{\tau_+(1\sigma)}^\dagger$ (s)	$\boldsymbol{\tau_-(1\sigma)}^\dagger$ (s)
2.0	0.110	0.0162	0.228	0.0164	0.0507	0.00530
2.5	0.089	0.0193	0.147	0.0074	0.017	0.0033
3.0	0.078	0.0210	0.116	0.0032	0.0064	0.0016
3.5	0.073	0.0227	0.147	0.0015	0.0034	0.00070
4.0	0.068	0.0238	0.142	0.0007	0.002	0.0003
4.5	0.064	0.0249	0.096	0.0004	0.0007	0.0002
5.0	0.061	0.0186	0.168	0.0002	0.0004	0.0001

$^\dagger\tau_\pm(1\sigma)$ is the uncertainty range for one standard deviation from the mean

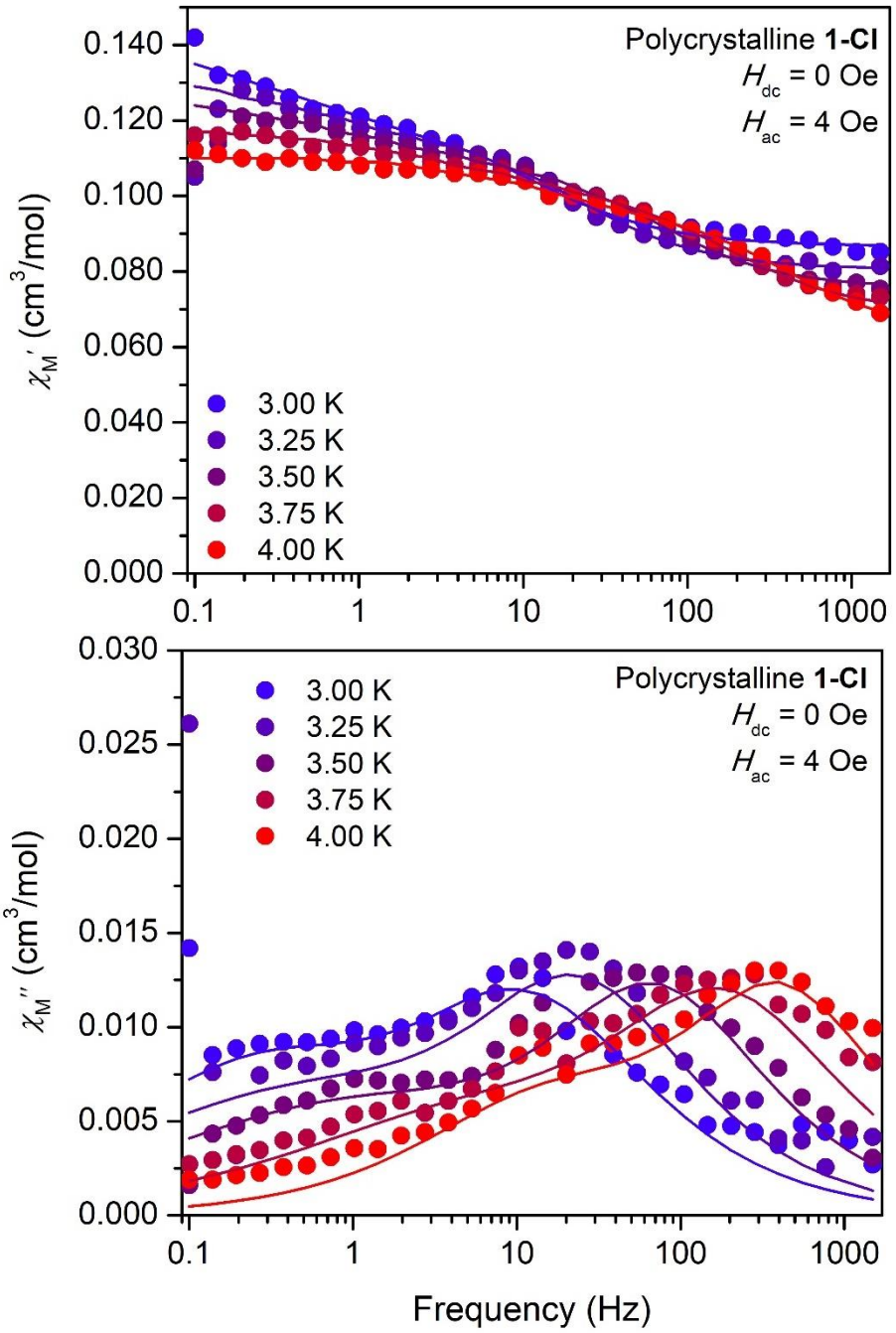

Figure S98. Plot of the in-phase (χ_M', top) and out-of-phase (χ_M'', bottom) molar magnetic susceptibility versus the frequency of the 4 Oe oscillating field for polycrystalline **1-Cl** under zero dc field. Measurement frequencies range from 0.1 to 1500 Hz, and temperatures range from 3 to 4 K. Solid lines are fits of the data.

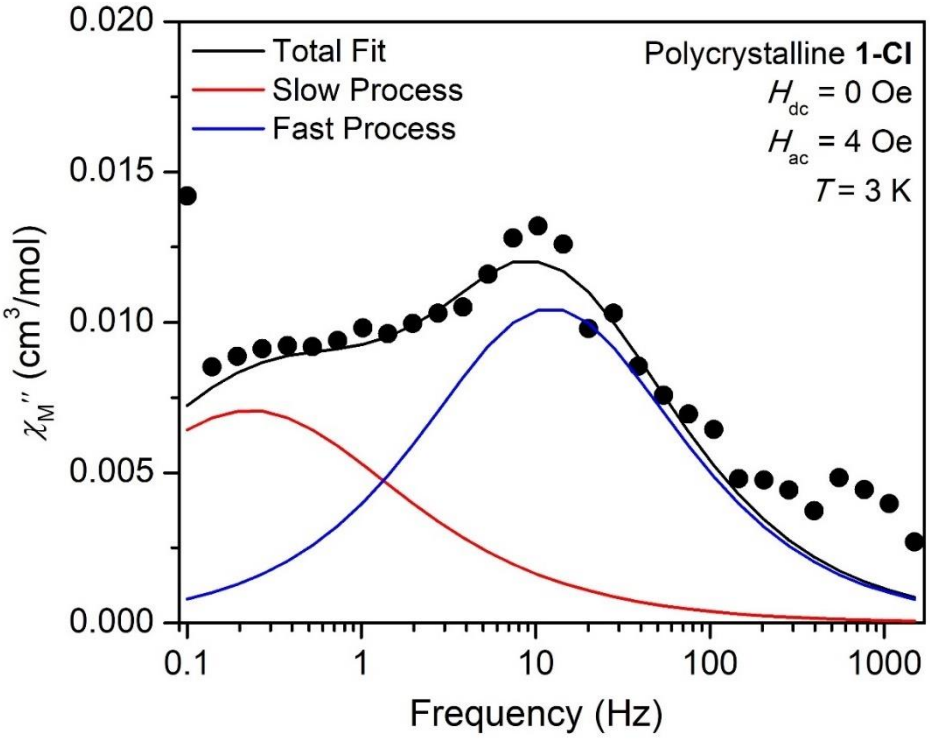

Figure S99. Plot of the out-of-phase (χ_M'') molar magnetic susceptibility of polycrystalline **1-Cl** collected at 3 K under zero dc field including fits involving two relaxation processes.

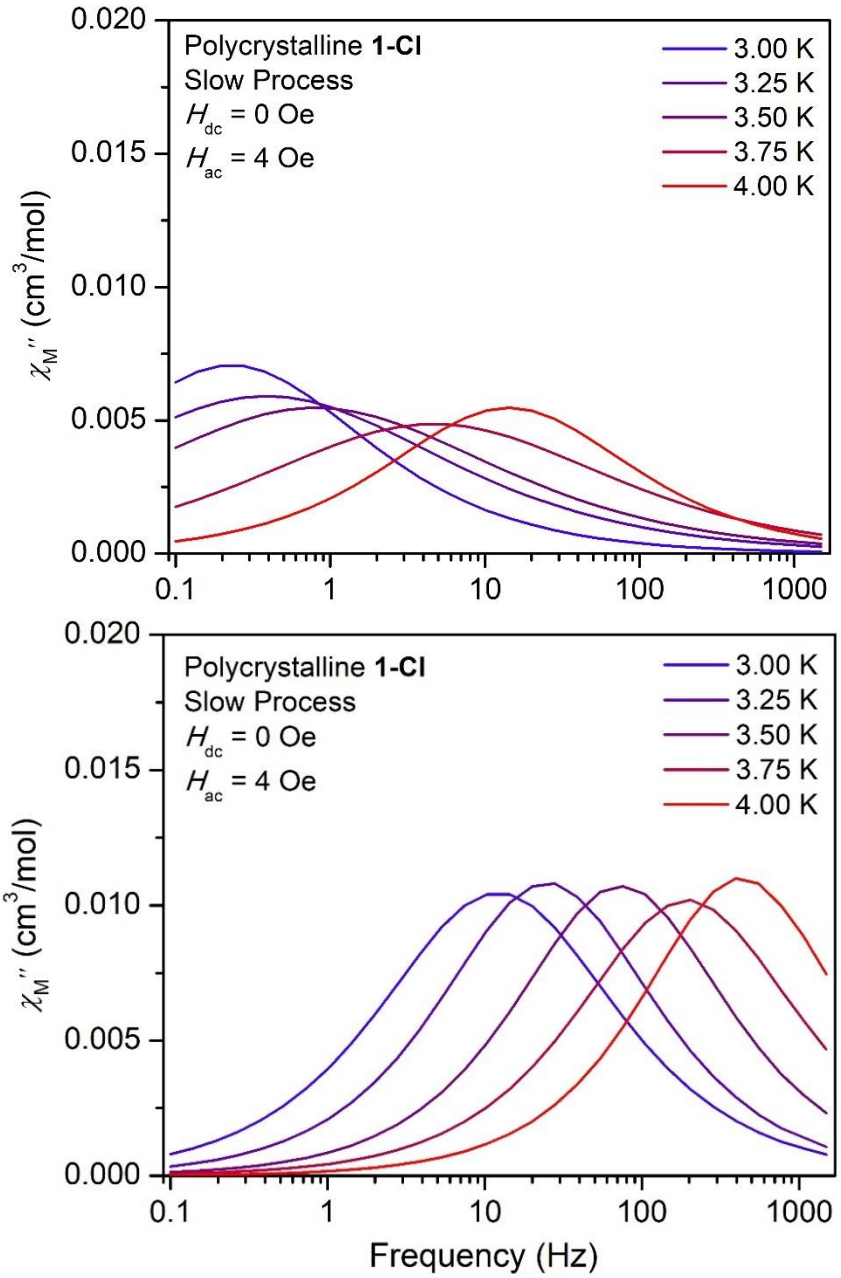

Figure S100. Fit lines illustrating the temperature dependence of the slow and fast relaxation processes in the out-of-phase (χ_M'') molar magnetic susceptibility of polycrystalline **1-Cl**.

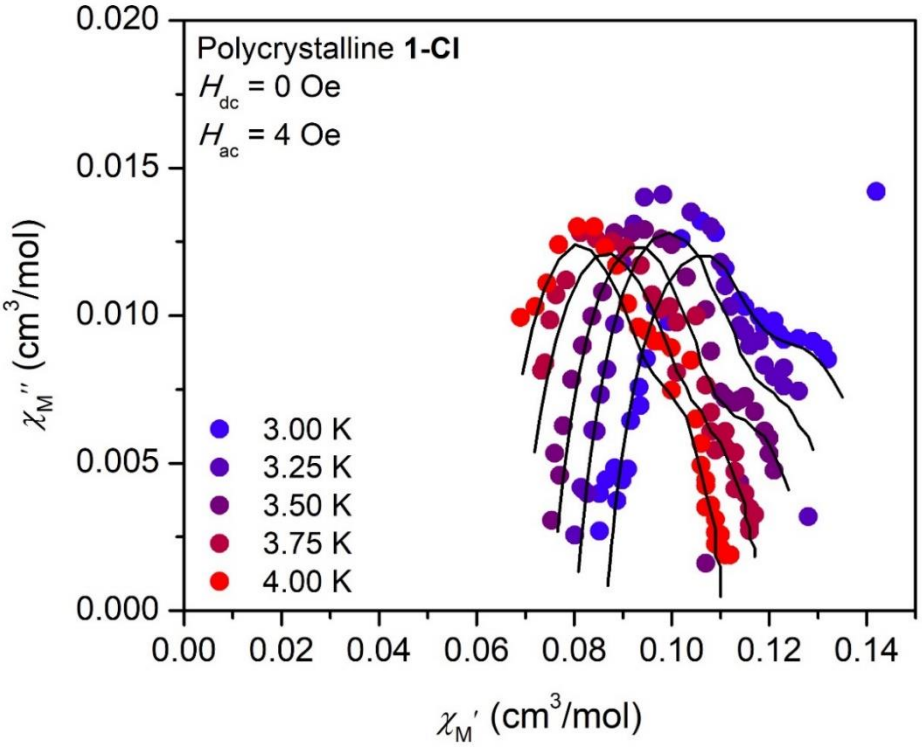

Figure S101. Cole-Cole plots for polycrystalline **1-Cl** collected under zero dc field in the temperature range of 3 to 4 K. Experimental data points are represented by colored circles, and the points representing the fit are connected by solid black lines. Note that χ' does not go to zero, suggesting that there is a fast relaxation process happening at frequencies too high to be probed by within the range of our ac susceptibility measurements (1–1500 Hz). We note that this behavior has been observed in other exchange-coupled actinide single-molecule magnets[51,52] and may be due to rapid relaxation arising from intermolecular interactions.

Table S13. Parameters used to fit the slow process in the ac susceptibility data for polycrystalline **1-Cl** collected under zero dc field and temperatures from 3 to 4 K, magnetic relaxation times extracted from these fits, and uncertainty ranges for the magnetic relaxation times.

T (K)	$\Delta\chi_1$ (cm^3/mol)	$\chi_{S,Total}$ (cm^3/mol)	α_1	τ_1 (s)	$\boldsymbol{\tau_{+,1}(1\sigma)}^{\dagger}$ (s)	$\boldsymbol{\tau_{-,1}(1\sigma)}^{\dagger}$ (s)
3.00	0.03	0.087	0.3	0.7	3.5	0.1
3.25	0.03	0.080	0.5	0.4	4.5	0.04
3.50	0.03	0.075	0.5	0.2	2.3	0.02
3.75	0.02	0.069	0.5	0.03	0.4	0.003
4.00	0.02	0.064	0.3	0.01	0.05	0.003

$^{\dagger}\tau_{\pm,1}(1\sigma)$ is the uncertainty range for one standard deviation from the mean for the slow process

Table S14. Parameters used to fit the fast process in the ac susceptibility data for polycrystalline **1-Cl** collected under zero dc field and temperatures from 3 to 4 K, magnetic relaxation times extracted from these fits, and uncertainty ranges for the magnetic relaxation times.

T (K)	$\Delta\chi_2$ (cm^3/mol)	$\chi_{S,Total}$ (cm^3/mol)	α_2	τ_2 (s)	$\boldsymbol{\tau_{+,2}(1\sigma)}^{\dagger}$ (s)	$\boldsymbol{\tau_{-,2}(1\sigma)}^{\dagger}$ (s)
3.00	0.03	0.087	0.25	0.013	0.045	0.0038
3.25	0.03	0.080	0.20	0.006	0.02	0.002
3.50	0.03	0.075	0.19	0.002	0.006	0.0008
3.75	0.03	0.069	0.22	0.0008	0.002	0.0003
4.00	0.03	0.064	0.16	0.0004	0.0009	0.0002

$^{\dagger}\tau_{\pm,2}(1\sigma)$ is the uncertainty range for one standard deviation from the mean for the fast process

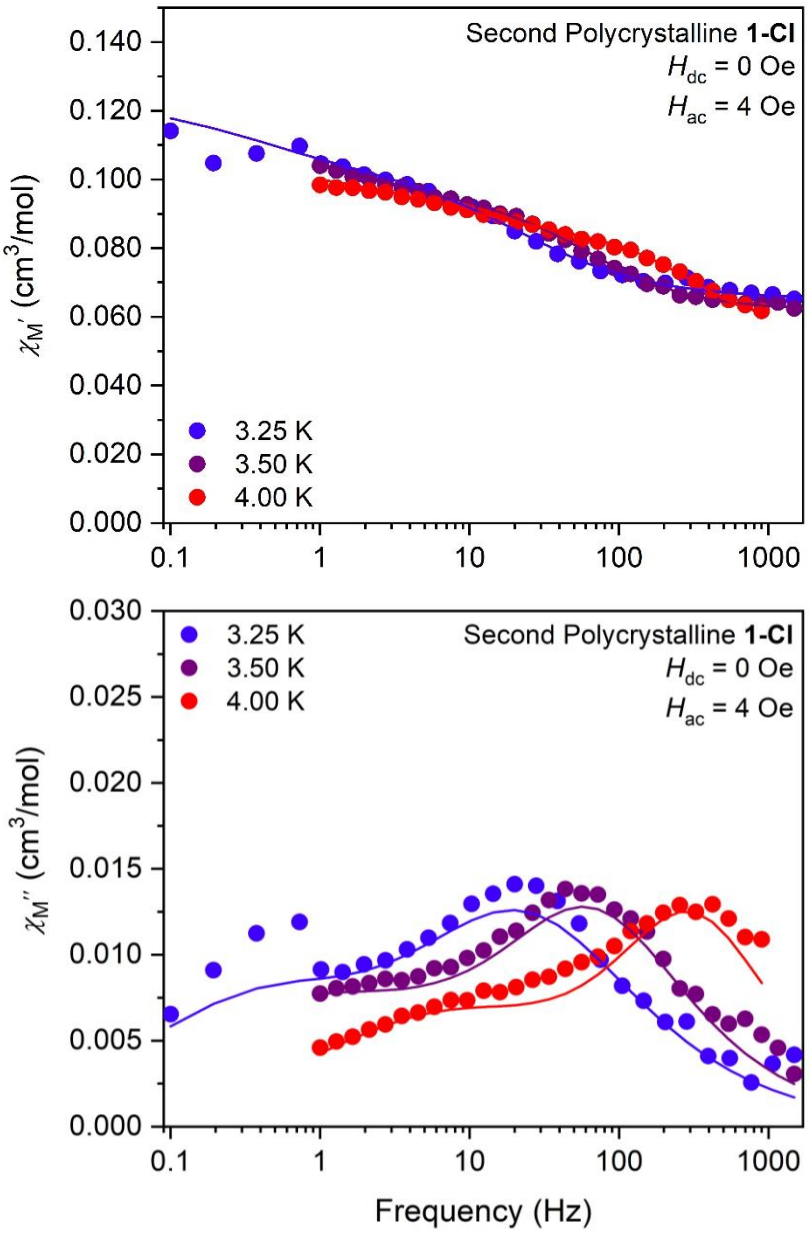

Figure S102. Plot of the in-phase (χ_M', top) and out-of-phase (χ_M'', bottom) molar magnetic susceptibility versus the frequency of the 4 Oe oscillating field for a second polycrystalline sample of **1-Cl** under zero dc field. Measurement frequencies range from 0.1 to 1500 Hz, and temperatures range from 3.25 to 4 K. Solid lines are fits of the data.

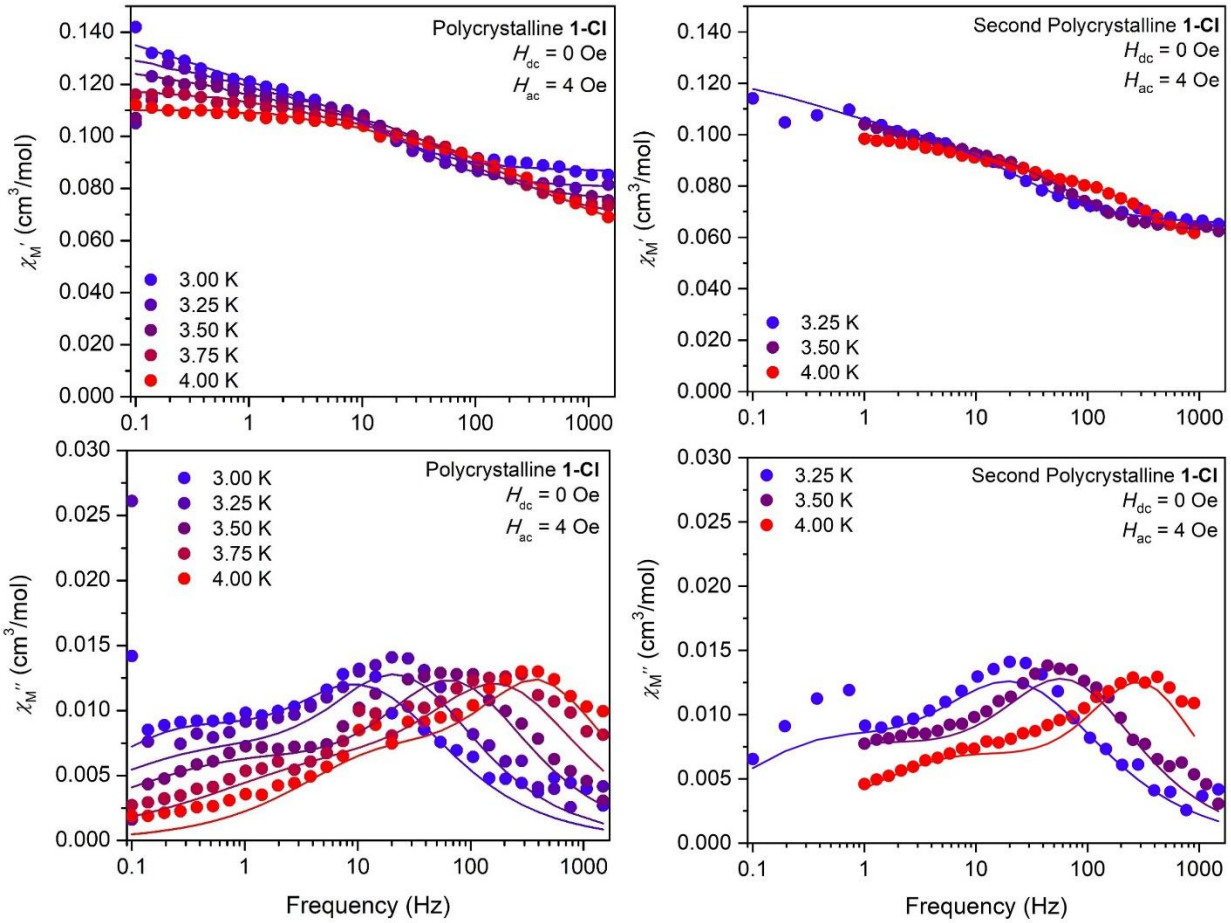

Figure S103. Side-by-side comparison of the in-phase (χ_M', top) and out-of-phase (χ_M'', bottom) molar magnetic susceptibility versus the frequency of the 4 Oe oscillating field for two different samples of polycrystalline **1-Cl** under zero dc field, showing consistency in the data for the two samples. Measurement frequencies range from 0.1 to 1500 Hz. Solid lines are fits of the data.

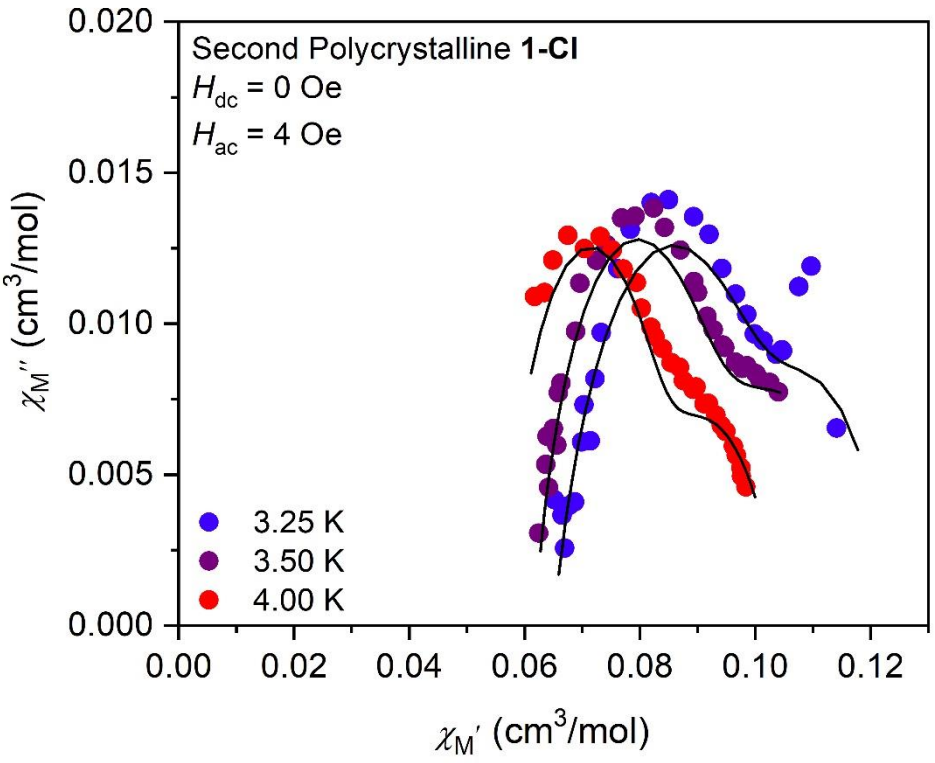

Figure S104. Cole-Cole plots for a second polycrystalline sample of **1-Cl** collected under zero dc field in the temperature range of 3.25 to 4 K. Experimental data points are represented by colored circles, and the points representing the fit are connected by solid black lines. Note that χ' does not go to zero, suggesting that there is a fast relaxation process happening at frequencies too high to be probed by within the range of our ac susceptibility measurements (1–1500 Hz). We note that this behavior has been observed in other exchange-coupled actinide single-molecule magnets[51,52] and may be due to rapid relaxation arising from intermolecular interactions.

Table S15. Parameters used to fit the slow process in the ac susceptibility data for a second polycrystalline sample of **1-Cl** collected under zero dc field in the temperature range of 3.25 to 4 K, magnetic relaxation times extracted from these fits, and uncertainty ranges for the magnetic relaxation times.

T (K)	$\Delta\chi_1$ (cm^3/mol)	$\chi_{S,Total}$ (cm^3/mol)	α_1	τ_1 (s)	$\boldsymbol{\tau_{+,1}(1\sigma)}^{\dagger}$ (s)	$\boldsymbol{\tau_{-,1}(1\sigma)}^{\dagger}$ (s)
3.25	0.02	0.065	0.3	0.5	2.2	0.09
3.50	0.03	0.062	0.5	0.2	2.0	0.02
4.00	0.02	0.057	0.4	0.03	0.15	0.004

$^{\dagger}\tau_{\pm,1}(1\sigma)$ is the uncertainty range for one standard deviation from the mean for the slow process

Table S16. Parameters used to fit the fast process in the ac susceptibility data for a second polycrystalline sample of **1-Cl** collected under zero dc field in the temperature range of 3.25 to 4 K, magnetic relaxation times extracted from these fits, and uncertainty ranges for the magnetic relaxation times.

T (K)	$\Delta\chi_2$ (cm^3/mol)	$\chi_{S,Total}$ (cm^3/mol)	α_2	τ_2 (s)	$\boldsymbol{\tau_{+,2}(1\sigma)}^{\dagger}$ (s)	$\boldsymbol{\tau_{-,2}(1\sigma)}^{\dagger}$ (s)
3.25	0.04	0.065	0.29	0.007	0.03	0.002
3.50	0.03	0.062	0.18	0.002	0.006	0.0009
4.00	0.02	0.057	0.08	0.0005	0.0009	0.0003

$^{\dagger}\tau_{\pm,2}(1\sigma)$ is the uncertainty range for one standard deviation from the mean for the fast process

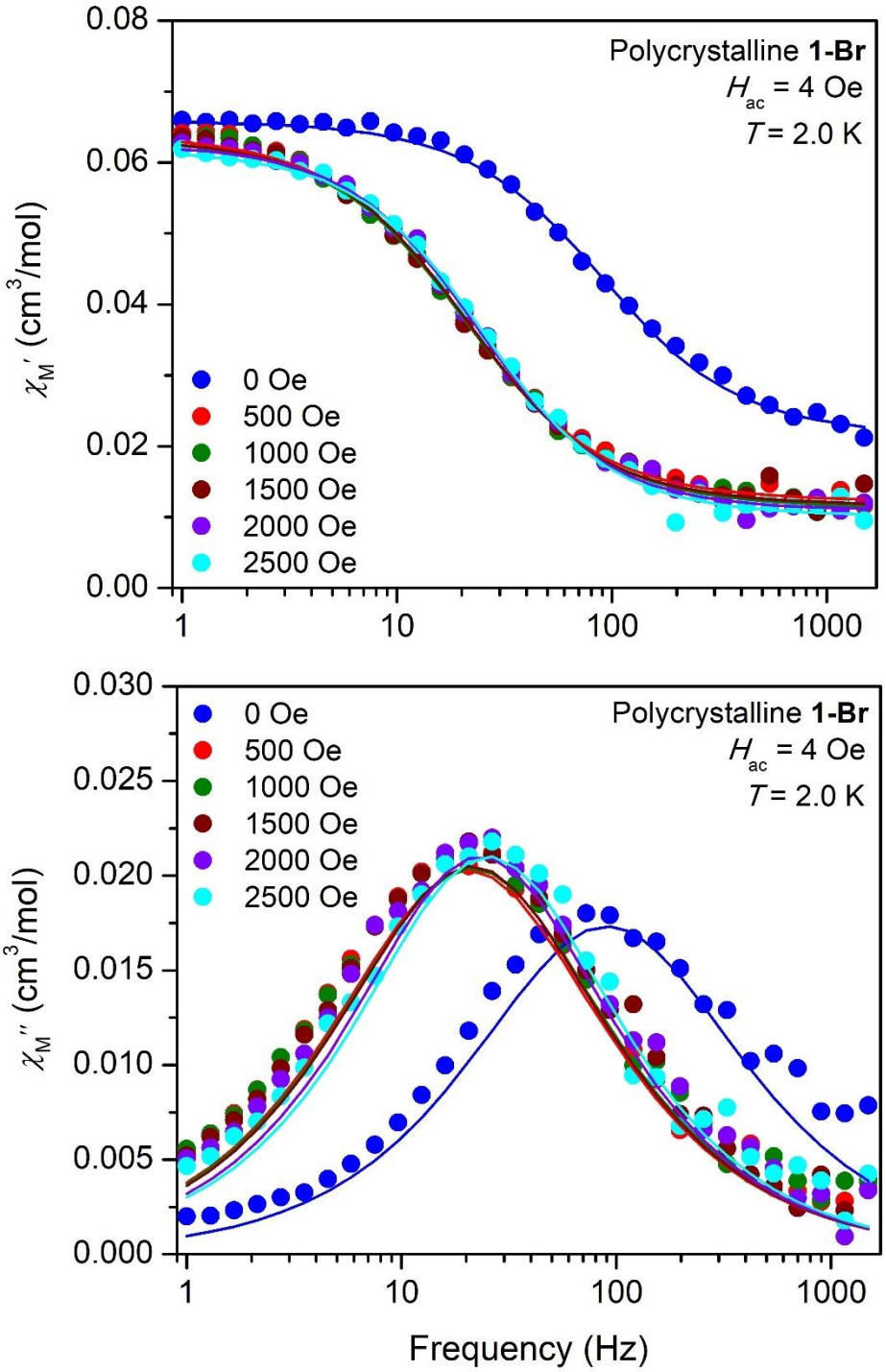

Figure S105. Plot of the in-phase (χ_M', top) and out-of-phase (χ_M'', bottom) molar magnetic susceptibility versus the frequency of the 4 Oe oscillating field for polycrystalline **1-Br** at 2.0 K. Measurements were performed under frequencies ranging from 1 to 1500 Hz and applied dc fields ranging from 0 to 2500 Oe. Solid lines are fits of the data.

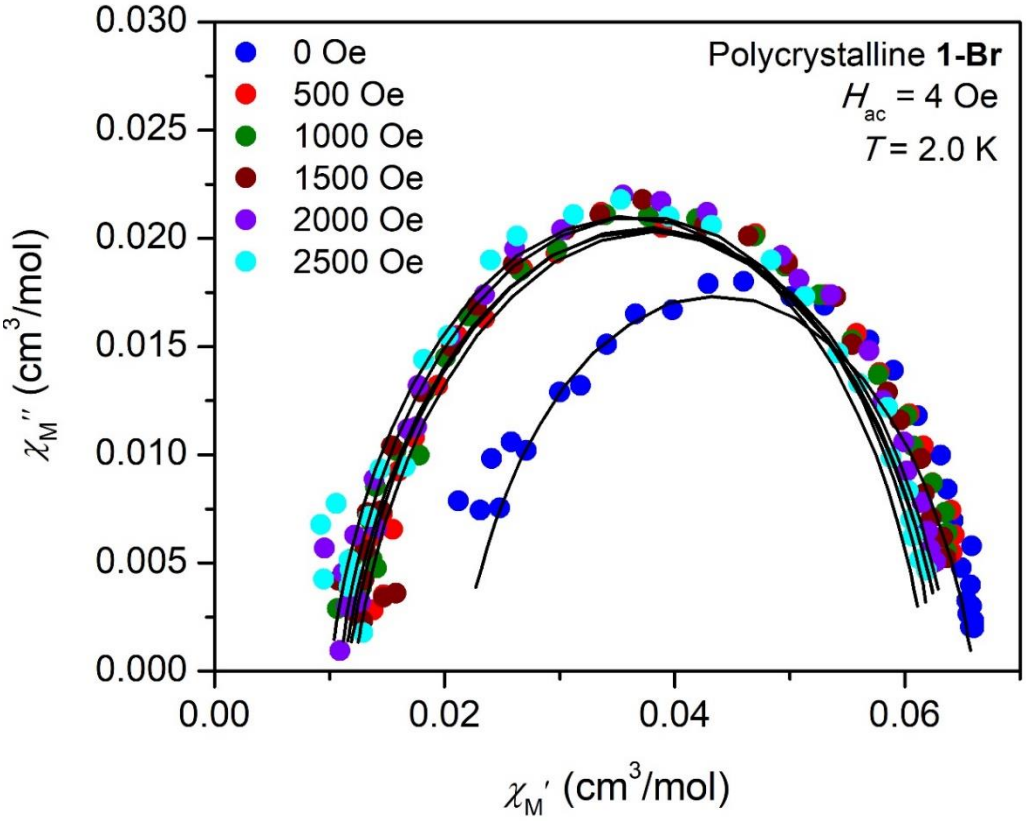

Figure S106. Cole-Cole plots for polycrystalline **1-Br** collected at 2.0 K in static dc fields ranging from 0 to 2500 Oe. Measurements were performed with a 4 Oe oscillating field under frequencies ranging from 1-1500 Hz. Experimental data points are represented by colored circles, and the points representing the fit are connected by solid black lines. Note that χ' does not go to zero, suggesting that there is a fast relaxation process happening at frequencies too high to be probed by within the range of our ac susceptibility measurements (1–1500 Hz). We note that this behavior has been observed in other exchange-coupled actinide single-molecule magnets[51,52] and may be due to rapid relaxation arising from intermolecular interactions.

Table S17. Parameters used to fit ac magnetic relaxation data for **1-Br** collected at 2.0 K under applied magnetic fields ranging from 0 to 2500 Oe, magnetic relaxation times extracted from these fits, and uncertainty ranges for the magnetic relaxation times.

H_{dc} (Oe)	χ_T (cm^3/mol)	χ_S (cm^3/mol)	α	τ (s)	$\boldsymbol{\tau_+(1\sigma)}^\dagger$ (s)	$\boldsymbol{\tau_-(1\sigma)}^\dagger$ (s)
0	0.066	0.021	0.16	0.0018	0.0042	0.00070
500	0.064	0.012	0.16	0.0078	0.018	0.0033
1000	0.064	0.011	0.16	0.0075	0.018	0.0032
1500	0.064	0.012	0.15	0.0075	0.017	0.0033
2000	0.063	0.011	0.13	0.0068	0.015	0.0031
2500	0.062	0.010	0.13	0.0063	0.014	0.0029

$^\dagger\tau_\pm(1\sigma)$ is the uncertainty range for one standard deviation from the mean

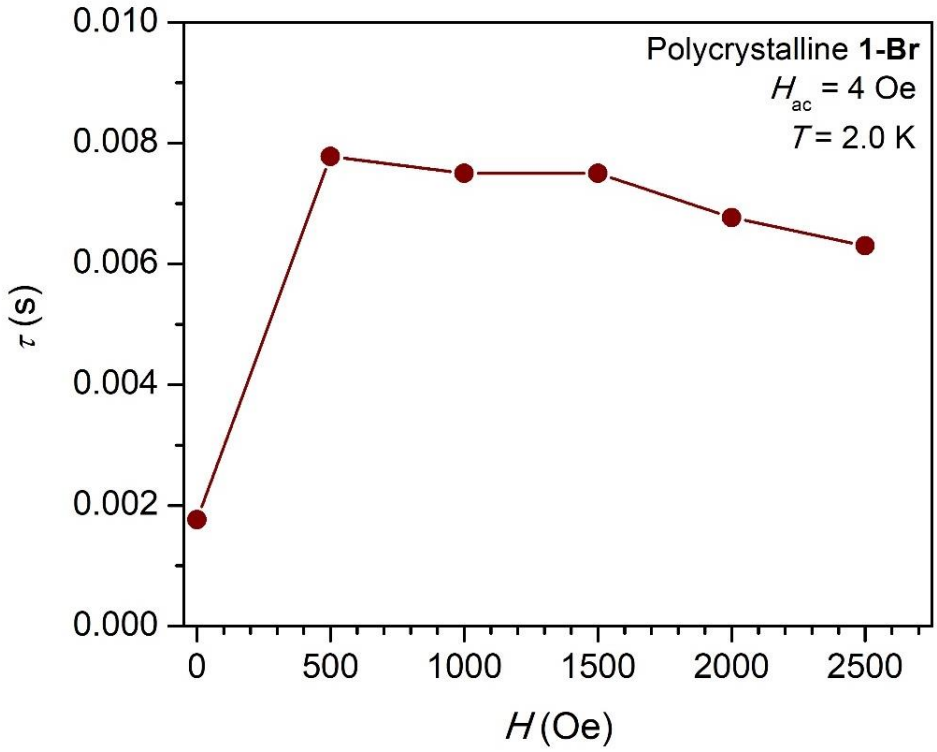

Figure S107. Field dependence of relaxation times extracted from ac magnetic susceptibility measurements on polycrystalline **1-Br** collected at 2.0 K and under applied dc fields ranging from 0 to 2500 Oe. The rapid rise in relaxation times at low fields is consistent with a suppression of quantum tunneling of the magnetization. The slight decrease in relaxation times after 500 Oe is likely due to a combination of Zeeman splitting decreasing the energy gap the ground and excited exchange-coupled states, as well as a possible direct process becoming active.

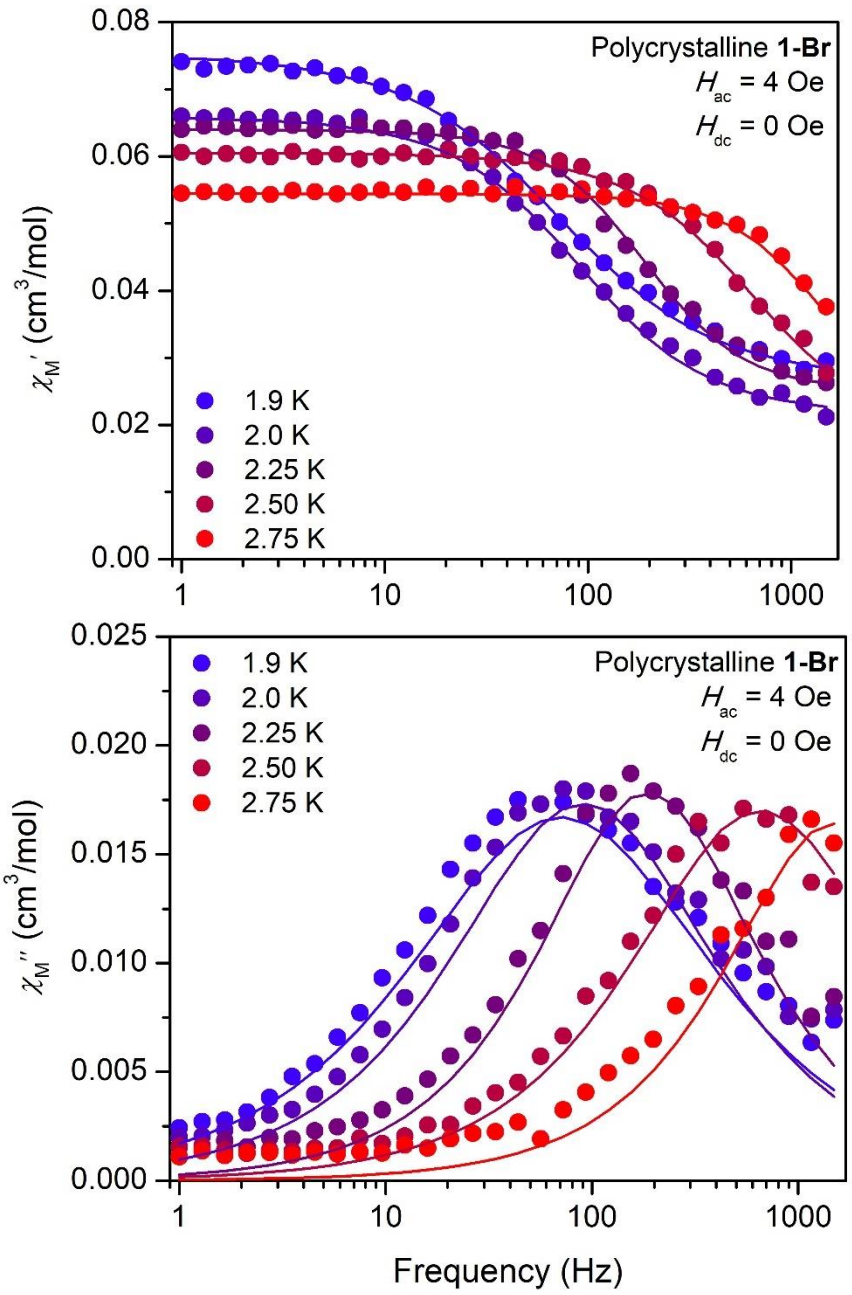

Figure S108. Plot of the in-phase (χ_M', top) and out-of-phase (χ_M'', bottom) molar magnetic susceptibility versus the frequency of the 4 Oe oscillating field for polycrystalline **1-Br** under zero dc field. Measurement frequencies range from 1 to 1500 Hz, and temperatures range from 1.9 to 2.75 K. Solid lines are fits of the data.

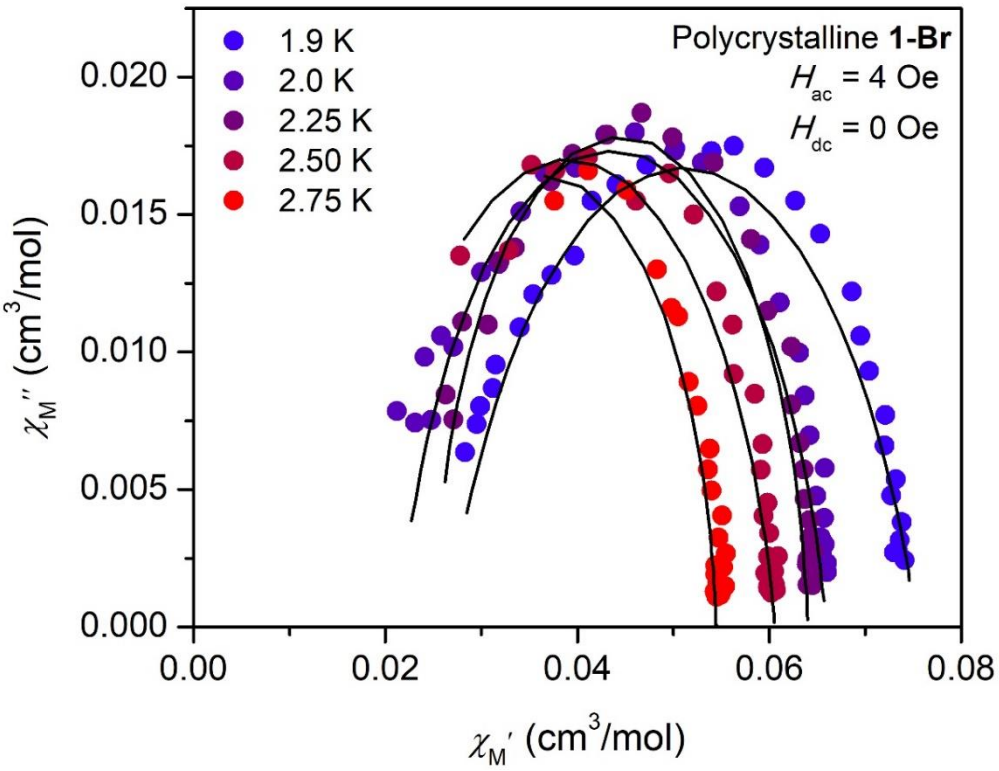

Figure S109. Cole-Cole plots for polycrystalline **1-Br** collected under zero dc field in the temperature range of 1.9 to 2.75 K. Experimental data points are represented by colored circles, and the points representing the fit are connected by solid black lines. Note that χ' does not go to zero, suggesting that there is a fast relaxation process happening at frequencies too high to be probed by within the range of our ac susceptibility measurements (1–1500 Hz). We note that this behavior has been observed in other exchange-coupled actinide single-molecule magnets[51,52] and may be due to rapid relaxation arising from intermolecular interactions.

Table S18. Parameters used to fit ac magnetic relaxation data for **1-Br** collected at zero field over the temperature range of 1.9 to 2.75 K, magnetic relaxation times extracted from these fits, and uncertainty ranges for the magnetic relaxation times.

T (K)	χ_T (cm^3/mol)	χ_S (cm^3/mol)	α	τ (s)	$\boldsymbol{\tau_+(1\sigma)}^\dagger$ (s)	$\boldsymbol{\tau_-(1\sigma)}^\dagger$ (s)
1.90	0.076	0.025	0.28	0.0022	0.0081	0.00060
2.00	0.066	0.021	0.16	0.0018	0.0042	0.00070
2.25	0.064	0.025	0.06	0.0008	0.001	0.0005
2.50	0.061	0.018	0.15	0.0002	0.0006	0.0001
2.75	0.055	0.019	0.06	0.0001	0.0002	0.0001

$^\dagger\tau_\pm(1\sigma)$ is the uncertainty range for one standard deviation from the mean

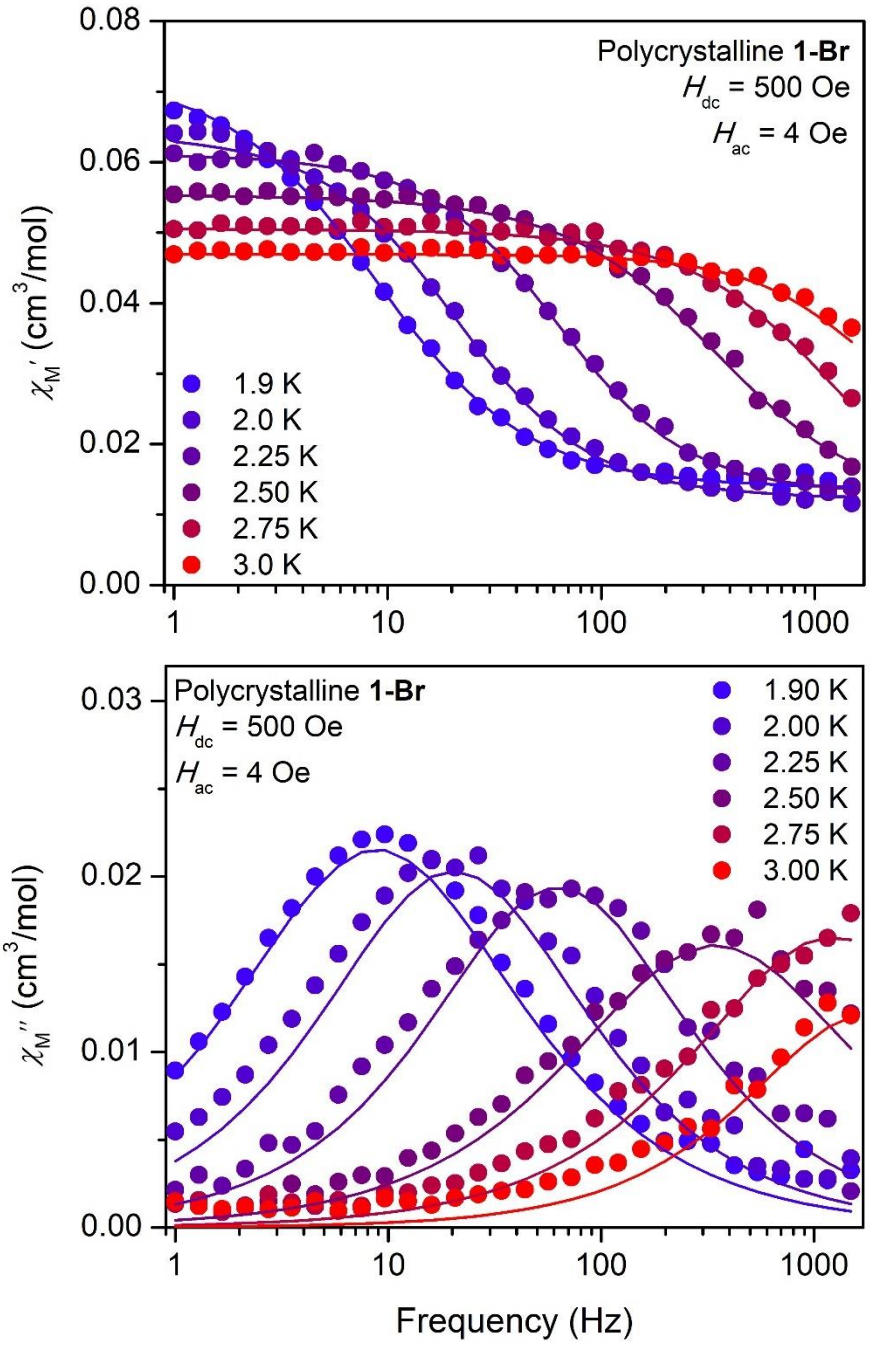

Figure S110. Plot of the in-phase (χ_M', top) and out-of-phase (χ_M'', bottom) molar magnetic susceptibility versus the frequency of the 4 Oe oscillating field for polycrystalline **1-Br** under a 500 Oe dc field. Measurement frequencies range from 1 to 1500 Hz, and temperatures range from 1.9 to 3 K. Solid lines are fits of the data.

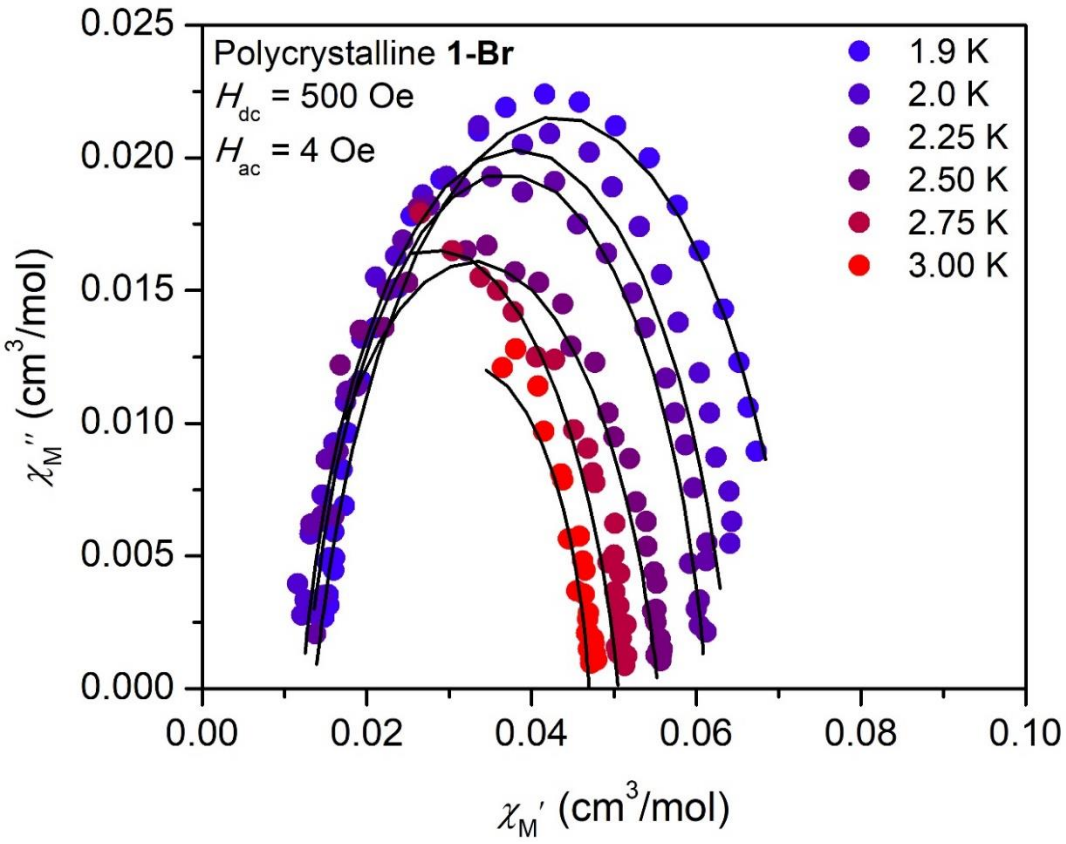

Figure S111. Cole-Cole plots for polycrystalline **1-Br** collected under a 500 Oe dc field in the temperature range of 1.9 K to 3 K. Experimental data points are represented by colored circles, and the points representing the fit are connected by solid black lines. Note that χ' does not go to zero, suggesting that there is a fast relaxation process happening at frequencies too high to be probed by within the range of our ac susceptibility measurements (1–1500 Hz). We note that this behavior has been observed in other exchange-coupled actinide single-molecule magnets[51,52] and may be due to rapid relaxation arising from intermolecular interactions.

Table S19. Parameters used to fit ac magnetic relaxation data for **1-Br** collected under an applied magnetic field of 500 Oe over the temperature range of 1.9 to 2.75 K, magnetic relaxation times extracted from these fits, and uncertainty ranges for the magnetic relaxation times.

T (K)	χ_T (cm^3/mol)	χ_S (cm^3/mol)	α	τ (s)	$\boldsymbol{\tau_+(1\sigma)}^\dagger$ (s)	$\boldsymbol{\tau_-(1\sigma)}^\dagger$ (s)
1.90	0.073	0.014	0.20	0.0180	0.0499	0.00650
2.00	0.064	0.012	0.16	0.0078	0.018	0.0033
2.25	0.061	0.013	0.14	0.0025	0.0056	0.0012
2.50	0.055	0.011	0.21	0.0005	0.0013	0.0002
2.75	0.051	0.006	0.19	0.0001	0.0003	0.00005

$^\dagger\tau_\pm(1\sigma)$ is the uncertainty range for one standard deviation from the mean

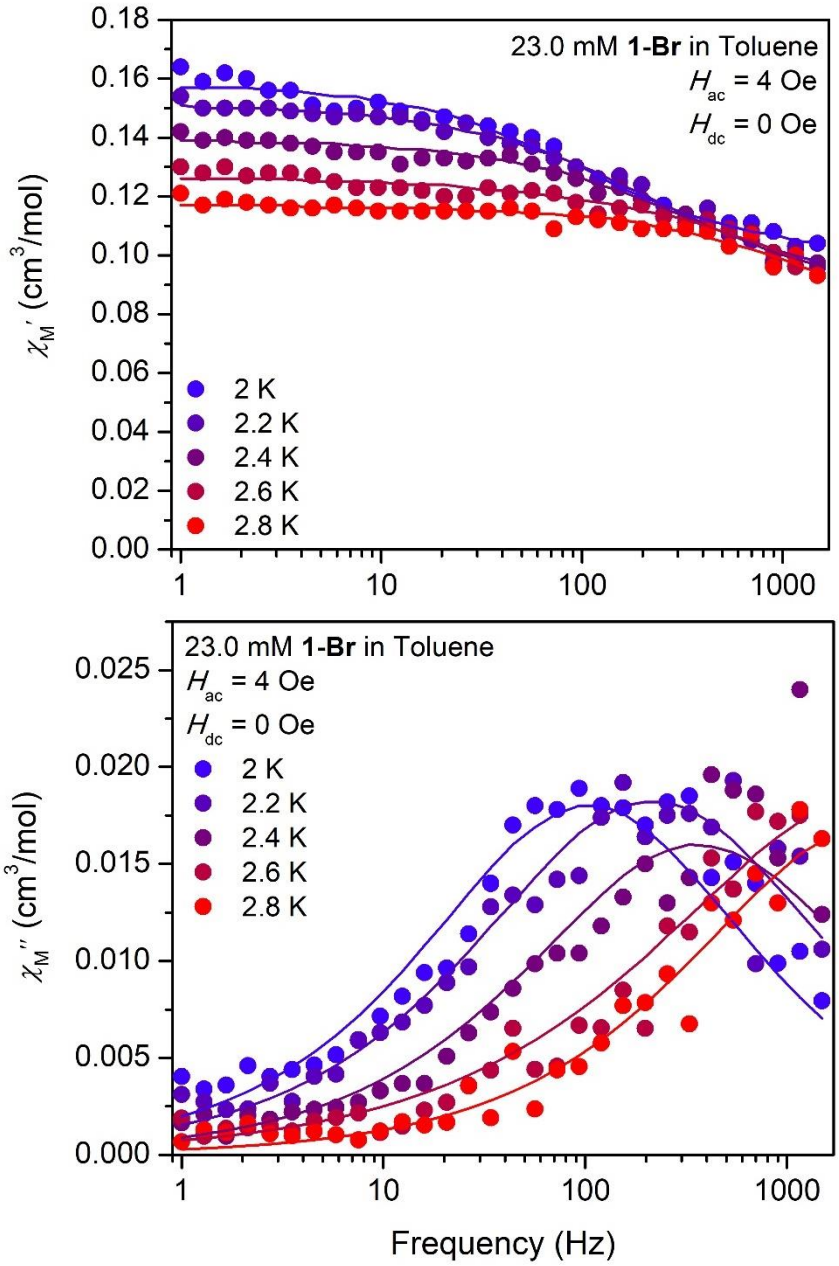

Figure S112. Plot of the in-phase (χ_M', top) and out-of-phase (χ_M'', bottom) molar magnetic susceptibility versus the frequency of the 4 Oe oscillating field for a 23.0 mM frozen toluene solution of **1-Br** under zero dc field. Measurement frequencies range from 1 to 1500 Hz, and temperatures range from 2 to 2.8 K. Solid lines are fits of the data.

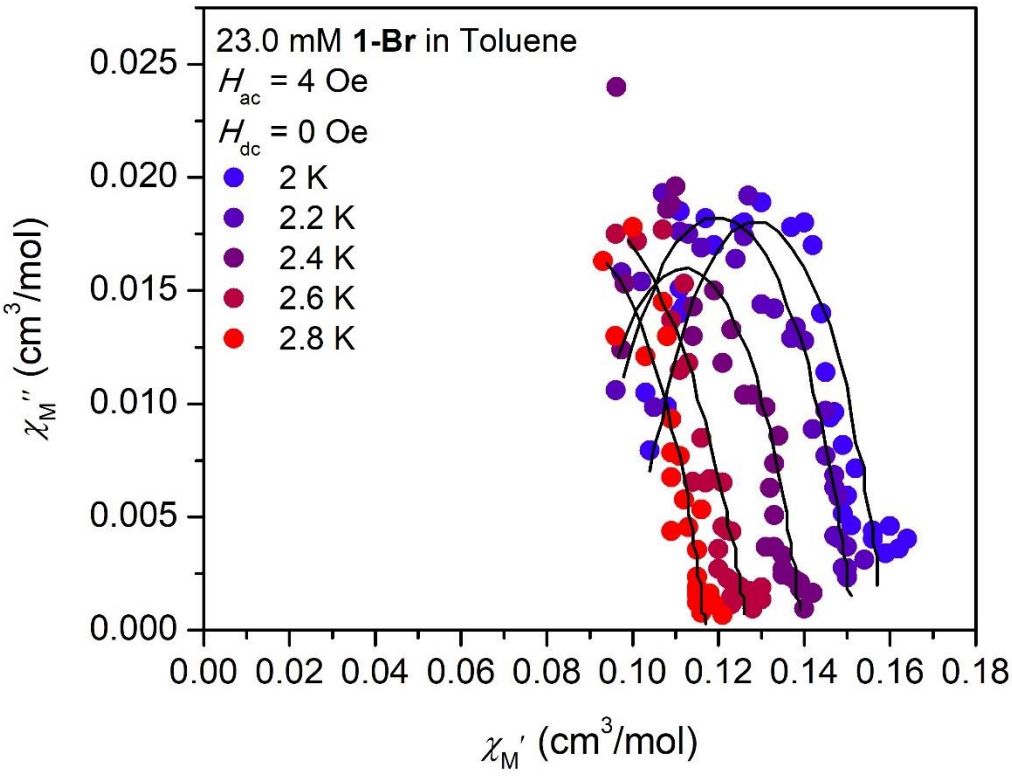

Figure S113. Cole-Cole plots for a 23.0 mM frozen toluene solution of **1-Br** collected under zero dc field in the temperature range of 2 K to 2.8 K. Experimental data points are represented by colored circles, and the points representing the fit are connected by solid black lines. Note that χ' does not go to zero, suggesting that there is a fast relaxation process happening at frequencies too high to be probed by within the range of our ac susceptibility measurements (1–1500 Hz). We note that this behavior has been observed in other exchange-coupled actinide single-molecule magnets.[51,52]

Table S20. Parameters used to fit ac magnetic relaxation data for a 23.0 mM frozen toluene solution of **1-Br** collected under zero applied dc field over the temperature range of 2 to 2.8 K, magnetic relaxation times extracted from these fits, and uncertainty ranges for the magnetic relaxation times. Only temperatures at which there is a clear maximum in χ_M'' (i.e., 2 to 2.4 K) were used in subsequent analyses.

T (K)	χ_T (cm^3/mol)	χ_S (cm^3/mol)	α	τ (s)	$\boldsymbol{\tau_+(1\sigma)}^\dagger$ (s)	$\boldsymbol{\tau_-(1\sigma)}^\dagger$ (s)
2.00	0.16	0.099	0.30	0.0015	0.0064	0.00040
2.20	0.15	0.088	0.34	0.0007	0.004	0.0002
2.40	0.14	0.084	0.33	0.0004	0.002	0.0001

$^\dagger\tau_\pm(1\sigma)$ is the uncertainty range for one standard deviation from the mean

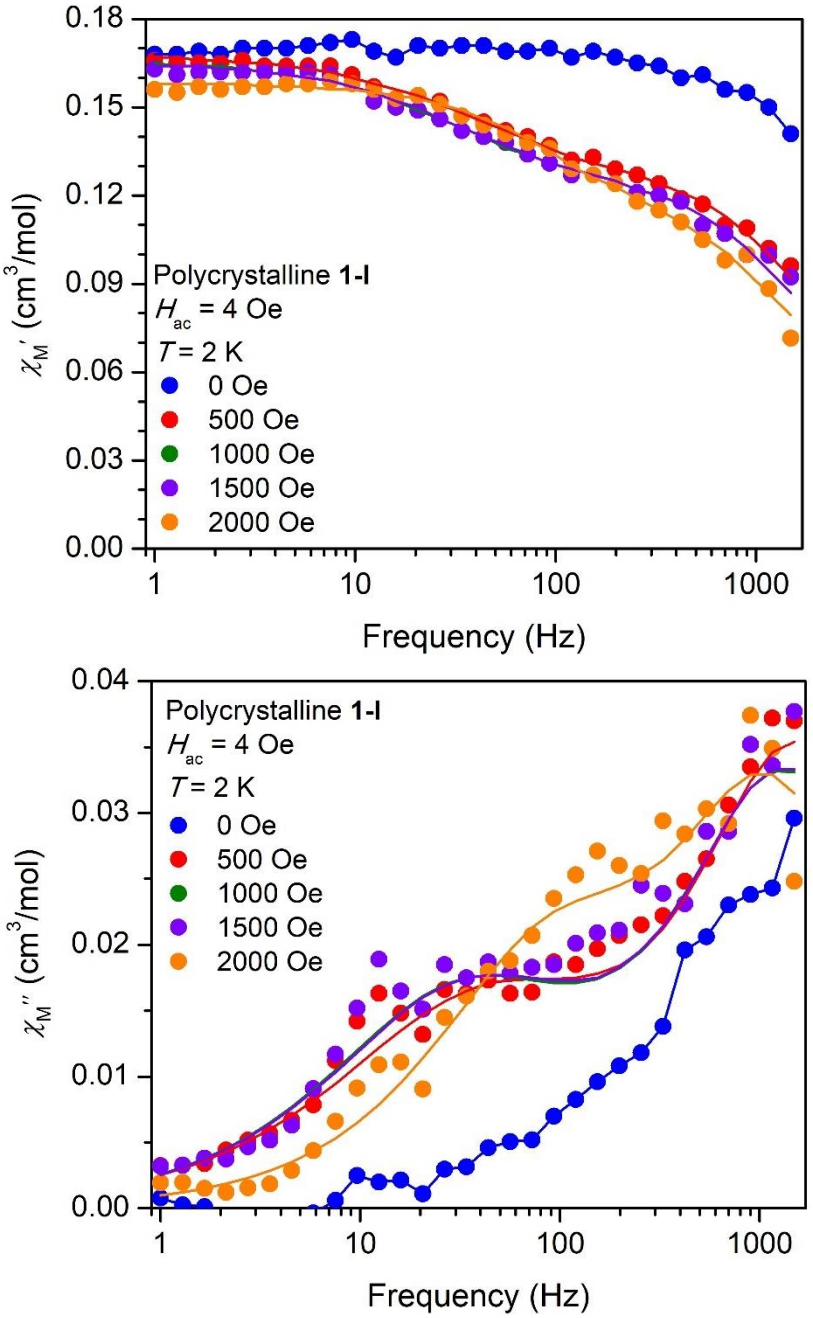

Figure S114. Plot of the in-phase (χ_M', top) and out-of-phase (χ_M'', bottom) molar magnetic susceptibility versus the frequency of the 4 Oe oscillating field for polycrystalline **1-I** at 2.0 K. Measurements were performed under frequencies ranging from 1 to 1500 Hz and applied dc fields ranging from 0 to 2000 Oe. Solid lines, with the exception of H_{dc} = 0 Oe, are fits of the data.

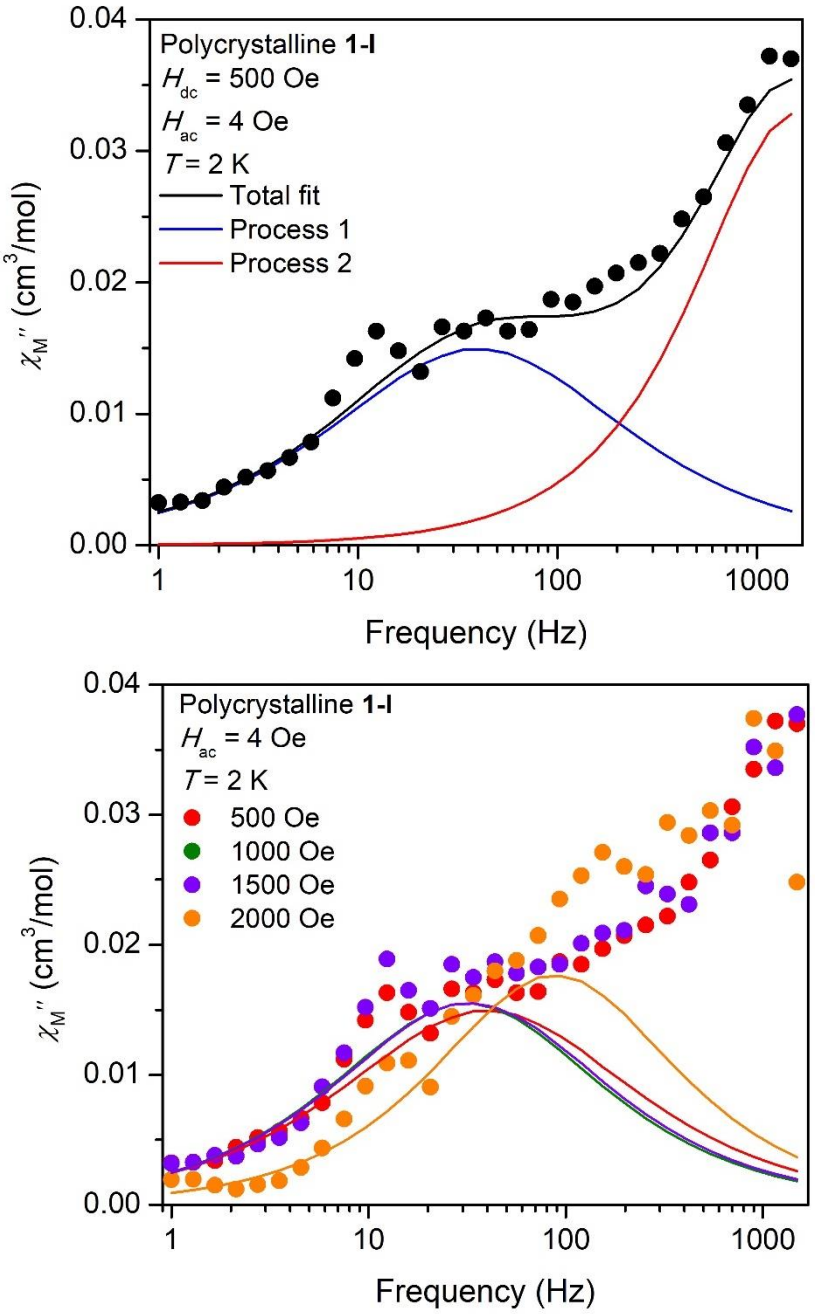

Figure S115. (Upper) Plot of the molar out-of-phase (χ_M'') magnetic susceptibility of polycrystalline **1-I** collected at 2.0 K under a 500 Oe dc field along with fits corresponding to two relaxation processes. (Lower) Field dependence of the molar out-of-phase (χ_M'') magnetic susceptibility plotted together with fits of the slower process, process 1, which illustrate how it relates to the total measured out-of-phase susceptibility.

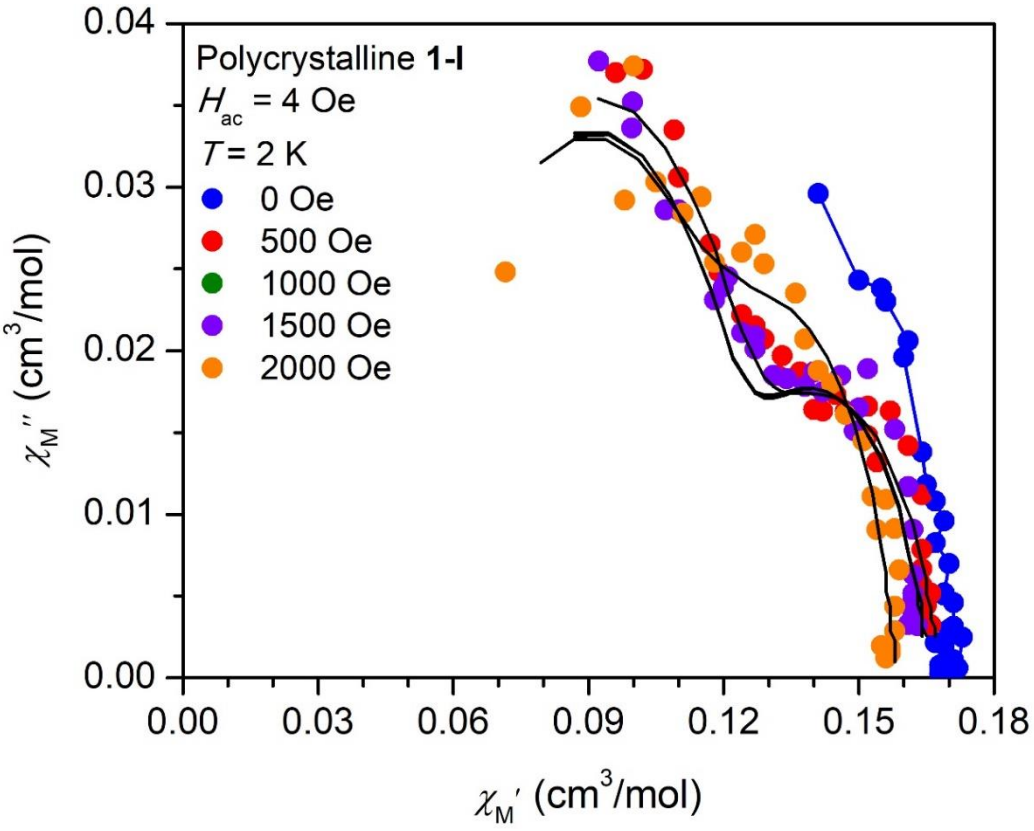

Figure S116. Cole-Cole plots for **1-I** collected at 2.0 K in static dc fields ranging from 0 to 2000 Oe. Measurements were performed with a 4 Oe oscillating field under frequencies ranging from 1-1500 Hz. Experimental data points are represented by colored circles, and the points representing the fit are connected by solid black lines. Note that χ' does not go to zero, suggesting that there is a fast relaxation process happening at frequencies too high to be probed by within the range of our ac susceptibility measurements (1–1500 Hz). We note that this behavior has been observed in other exchange-coupled actinide single-molecule magnets.[51,52]

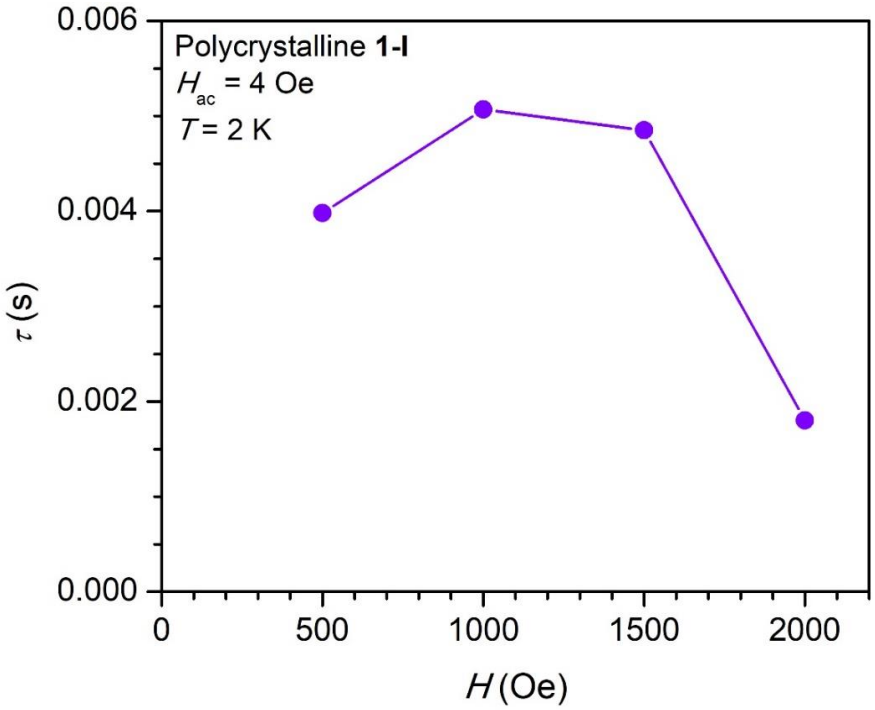

Figure S117. Field dependence of relaxation times extracted from ac magnetic susceptibility measurements on polycrystalline **1-I** collected at 2.0 K and applied dc fields ranging from 500 Oe to 2000 Oe. For the purpose of comparison with **1-Cl** and **1-Br**, subsequent, variable-temperature ac magnetic susceptibility measurements on **1-I** were performed under a 500 Oe dc field.

Table S21. Parameters used to fit process 1 in the ac susceptibility data for polycrystalline **1-I** collected at 2.0 K under applied magnetic fields ranging from 500 to 2000 Oe, magnetic relaxation times extracted from these fits, and uncertainty ranges for the magnetic relaxation times.

H (Oe)	$\Delta\chi_1$ (cm^3/mol)	$\chi_{S,Total}$ (cm^3/mol)	α_1	τ_1 (s)	$\boldsymbol{\tau_{+,1}(1\sigma)}^{\dagger}$ (s)	$\boldsymbol{\tau_{-,1}(1\sigma)}^{\dagger}$ (s)
500	0.045	0.054	0.25	0.0040	0.013	0.0012
1000	0.043	0.054	0.20	0.0051	0.014	0.0018
1500	0.043	0.054	0.21	0.0049	0.014	0.0017
2000	0.044	0.055	0.14	0.0018	0.0040	0.00080

$^{\dagger}\tau_{\pm,1}(1\sigma)$ is the uncertainty range for one standard deviation from the mean for process 1

Table S22. Parameters used to fit process 2 in the ac susceptibility data for polycrystalline **1-I** collected at 2.0 K under applied magnetic fields ranging from 500 to 2000 Oe, magnetic relaxation times extracted from these fits, and uncertainty ranges for the magnetic relaxation times.

H (Oe)	$\Delta\chi_2$ (cm^3/mol)	$\chi_{S,Total}$ (cm^3/mol)	α_2	τ_2 (s)	$\boldsymbol{\tau_{+,2}(1\sigma)}^{\dagger}$ (s)	$\boldsymbol{\tau_{-,2}(1\sigma)}^{\dagger}$ (s)
500	0.069	0.054	0.03	0.0001	0.0001	0.0001
1000	0.068	0.054	0.06	0.0001	0.0002	0.0001
1500	0.068	0.054	0.05	0.0001	0.0002	0.0001
2000	0.059	0.055	0.02	0.0001	0.0002	0.0001

$^{\dagger}\tau_{\pm,2}(1\sigma)$ is the uncertainty range for one standard deviation from the mean for process 2

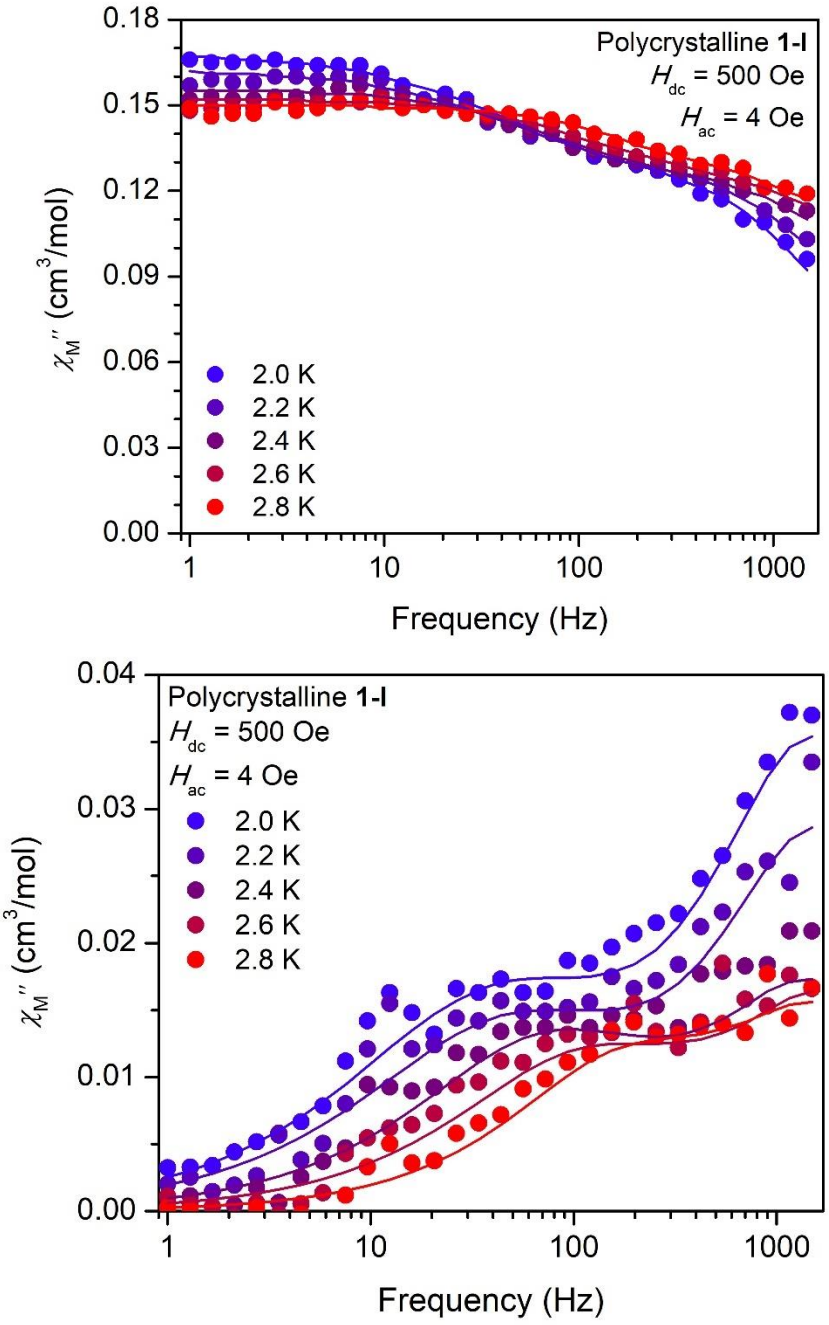

Figure S118. Plot of the in-phase (χ_M', top) and out-of-phase (χ_M'', bottom) molar magnetic susceptibility versus the frequency of the 4 Oe oscillating field for polycrystalline **1-I**. Measurements were performed under a 500 Oe applied dc field, at frequencies ranging from 1 to 1500 Hz, and temperatures ranging from 2.0 to 2.8 K. Solid lines are fits of the data.

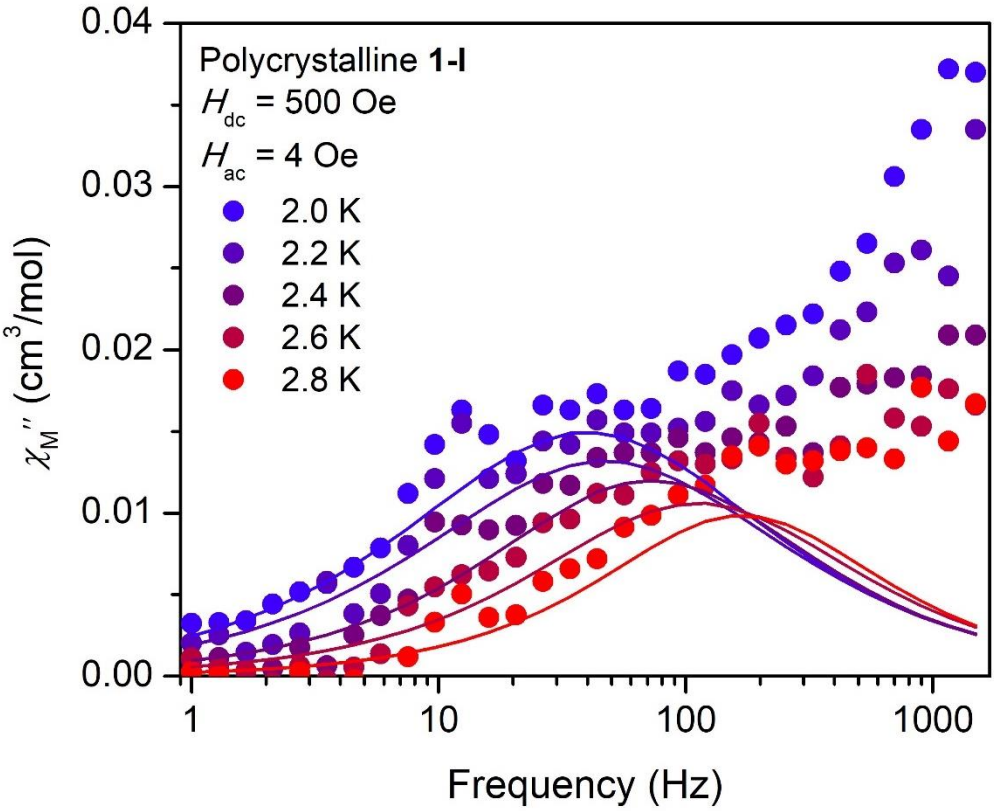

Figure S119. Plot of the out-of-phase (χ_M'', bottom) molar magnetic susceptibility versus the frequency of the 4 Oe oscillating field for polycrystalline **1-I**. Measurements were performed under a 500 Oe applied dc field, at frequencies ranging from 1 to 1500 Hz, and temperatures ranging from 2.0 to 2.8 K. Solid lines represent fits to process 1.

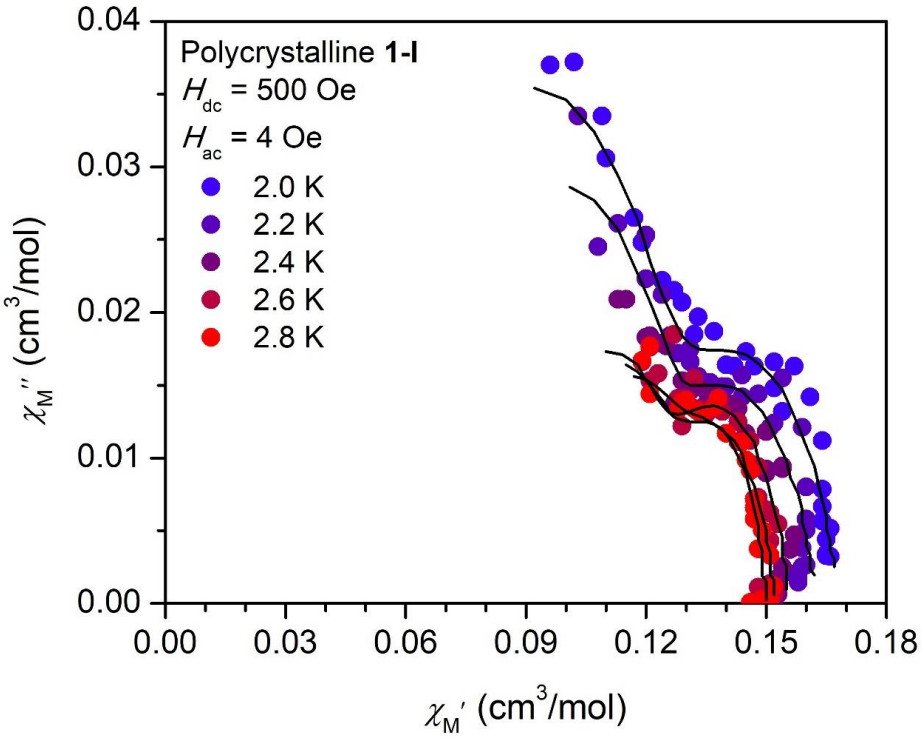

Figure S120. Cole-Cole plots for polycrystalline **1-I** collected under a 500 Oe applied dc field in the temperature range of 2.0 to 2.8 K. Experimental data points are represented by colored circles, and the points representing the fit are connected by solid black lines. Note that χ' does not go to zero, suggesting that there is a fast relaxation process happening at frequencies too high to be probed by within the range of our ac susceptibility measurements (1–1500 Hz). We note that this behavior has been observed in other exchange-coupled actinide single-molecule magnets[51,52] and may be due to rapid relaxation arising from intermolecular interactions.

Tables S23. Parameters used to fit process 1 in the ac susceptibility data for polycrystalline **1-I** collected under a 500 Oe dc field in the temperature range of 2 to 2.8 K, magnetic relaxation times extracted from these fits, and uncertainty ranges for the magnetic relaxation times.

T (K)	$\Delta\chi_1$ (cm^3/mol)	$\chi_{S,Total}$ (cm^3/mol)	α_1	τ_1 (s)	$\boldsymbol{\tau_{+,1}(1\sigma)}^{\dagger}$ (s)	$\boldsymbol{\tau_{-,1}(1\sigma)}^{\dagger}$ (s)
2.00	0.045	0.054	0.25	0.0040	0.013	0.0012
2.20	0.039	0.071	0.25	0.0034	0.011	0.0010
2.40	0.033	0.094	0.19	0.0022	0.0058	0.00080
2.60	0.028	0.096	0.18	0.0014	0.0037	0.00060
2.80	0.023	0.100	0.11	0.0009	0.002	0.0005

$^{\dagger}\tau_{\pm,1}(1\sigma)$ is the uncertainty range for one standard deviation from the mean for process 1

Tables S24. Parameters used to fit process 2 in the ac susceptibility data for polycrystalline **1-I** collected under a 500 Oe applied magnetic field in the temperature range of 2 to 2.8 K, magnetic relaxation times extracted from these fits, and uncertainty ranges for the magnetic relaxation times.

T (K)	$\Delta\chi_2$ (cm^3/mol)	$\chi_{S,Total}$ (cm^3/mol)	α_2	τ_2 (s)	$\boldsymbol{\tau_{+,2}(1\sigma)}^{\dagger}$ (s)	$\boldsymbol{\tau_{-,2}(1\sigma)}^{\dagger}$ (s)
2.00	0.069	0.054	0.033	0.0001	0.0001	0.0001
2.20	0.053	0.071	0.002	0.0001	0.0001	0.0001
2.40	0.030	0.094	0.001	0.0001	0.0001	0.0001
2.60	0.028	0.096	0.0001	0.0001	0.0001	0.0001
2.80	0.026	0.101	0.0005	0.0001	0.0001	0.0001

$^{\dagger}\tau_{\pm,2}(1\sigma)$ is the uncertainty range for one standard deviation from the mean for process 2

6.7 Dc Magnetic Relaxation Data. Dc magnetic relaxation data were collected for polycrystalline **1-Cl** after magnetizing the sample at 2 T at 10 K for 5 min and then, after cooling to measurement temperature, zeroing the field (or setting the field to 500 Oe; no overshoot, hi-res disabled for both cases). The magnetization was then measured at periodic time intervals. Dc magnetic relaxation data were fit to a stretched exponential function given by equation S6:[48]

$$M(t) = M_1 + (M_0 - M_1)e^{\left(-(t/\tau)^n\right)} \qquad \text{(S6)}$$

Where $M(t)$ is the magnetization at time t, M_0 is the initial magnetization measured after the field has been removed, M_1 is the final value of the magnetization at $t = \infty$, τ is the magnetic relaxation time, and n is a free variable. For data collected after the field was set to zero, M_1 should equal zero, however, non-zero values were obtained for all temperatures, which likely is due to a small remnant field being present during the measurement. In these cases, fits of $M(t)$ were made by first setting M_1 equal to the last value of the magnetization measured for these experiments. However, better fits were obtained by treating M_1 as a free variable, and a similar fit strategy has been used to model dc relaxation in lanthanide-based complexes.[44]

The n values extracted from fits to the dc relaxation data were used to determine uncertainty ranges in τ according to the following equation:[50,53]

$$\tau_{\pm}(1\sigma) = \tau_{\mu} e^{\frac{\pm 1.64 tan\left[\frac{\pi}{2}(1-n)\right]}{(1-n)^{0.141}}} \qquad \text{(S7)}$$

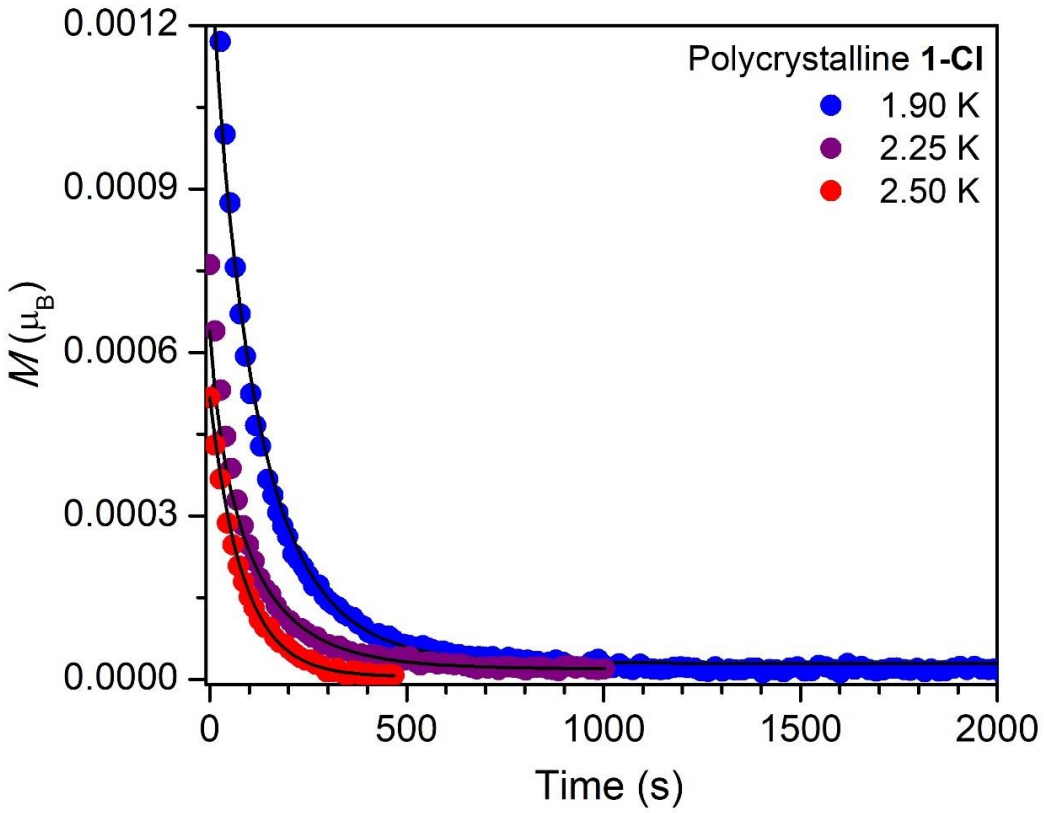

Figure S121. Dc magnetic relaxation data for polycrystalline **1-Cl** collected at 1.90 K, 2.25 K, and 2.50 K at zero field following magnetization at 2 T. Black lines represent fits to the data using stretched exponential functions, which were used to extract τ.

Table S25. Parameters used to fit dc magnetic relaxation data for a polycrystalline sample of **1-Cl** collected under zero applied magnetic field, the magnetic relaxation times extracted from these fits, and the uncertainty ranges for the magnetic relaxation times.

T (K)	M_0 (μ_B)	M_1 (μ_B)	n	τ (s)	$\boldsymbol{\tau_+(1\sigma)}^\dagger$ (s)	$\boldsymbol{\tau_-(1\sigma)}^\dagger$ (s)
1.90	1.4×10^{-3}	3.0×10^{-5}	0.89	111	165	74.7
2.25	6.4×10^{-4}	1.9×10^{-5}	0.81	94	180	49
2.50	5.2×10^{-4}	4.6×10^{-6}	1	83	85	81

$^\dagger\tau_{\pm,}(1\sigma)$ is the uncertainty range for one standard deviation from the mean

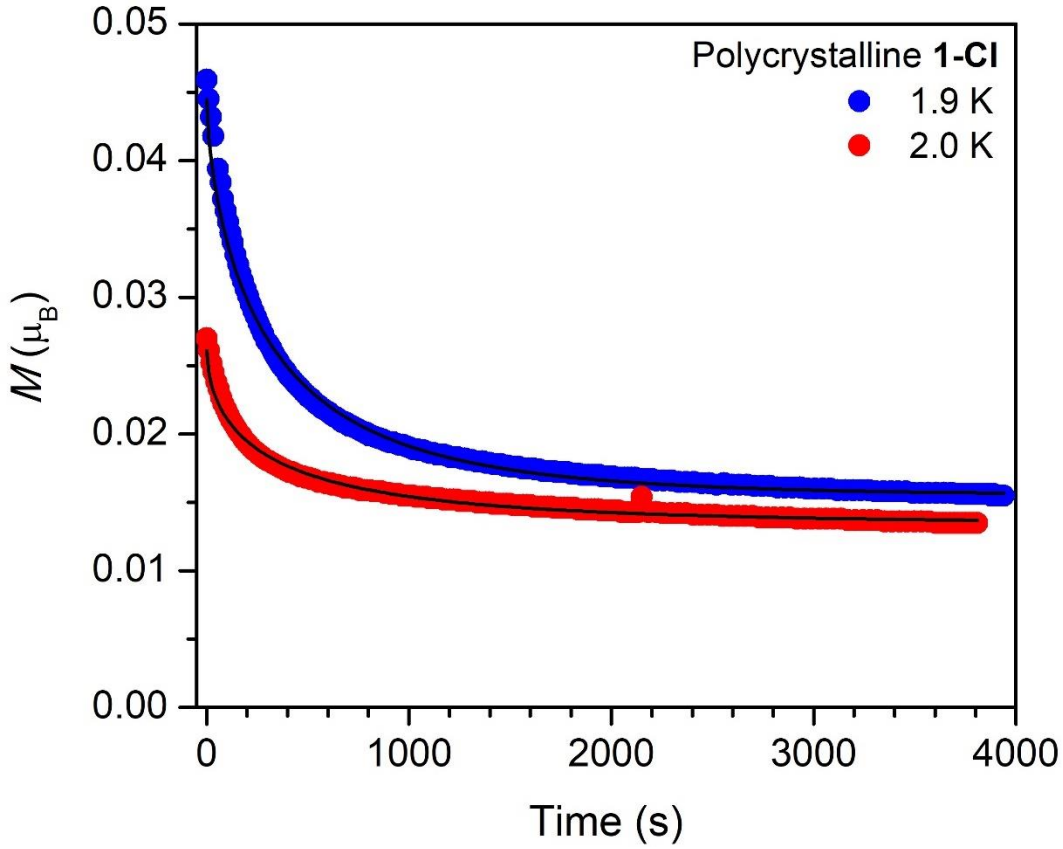

Figure S122. Dc magnetic relaxation data for polycrystalline **1-Cl** collected at 1.90 and 2.00 K at 500 Oe following magnetization at 2 T. Black lines represent fits to the data using stretched exponential functions, which were used to extract τ.

Table S26. Parameters used to fit dc magnetic relaxation data for a polycrystalline sample of **1-Cl** collected under a 500 Oe applied magnetic field, the magnetic relaxation times extracted from these fits, and the uncertainty ranges for the magnetic relaxation times.

T (K)	M_0 (μ_B)	M_1 (μ_B)	n	τ (s)	$\boldsymbol{\tau_+(1\sigma)}^{\dagger}$ (s)	$\boldsymbol{\tau_-(1\sigma)}^{\dagger}$ (s)
1.90	4.5×10^{-2}	1.6×10^{-2}	0.67	335	992	113
2.00	2.6×10^{-2}	1.4×10^{-2}	0.57	339	1480	77.8

$^{\dagger}\tau_{\pm,}(1\sigma)$ is the uncertainty range for one standard deviation from the mean

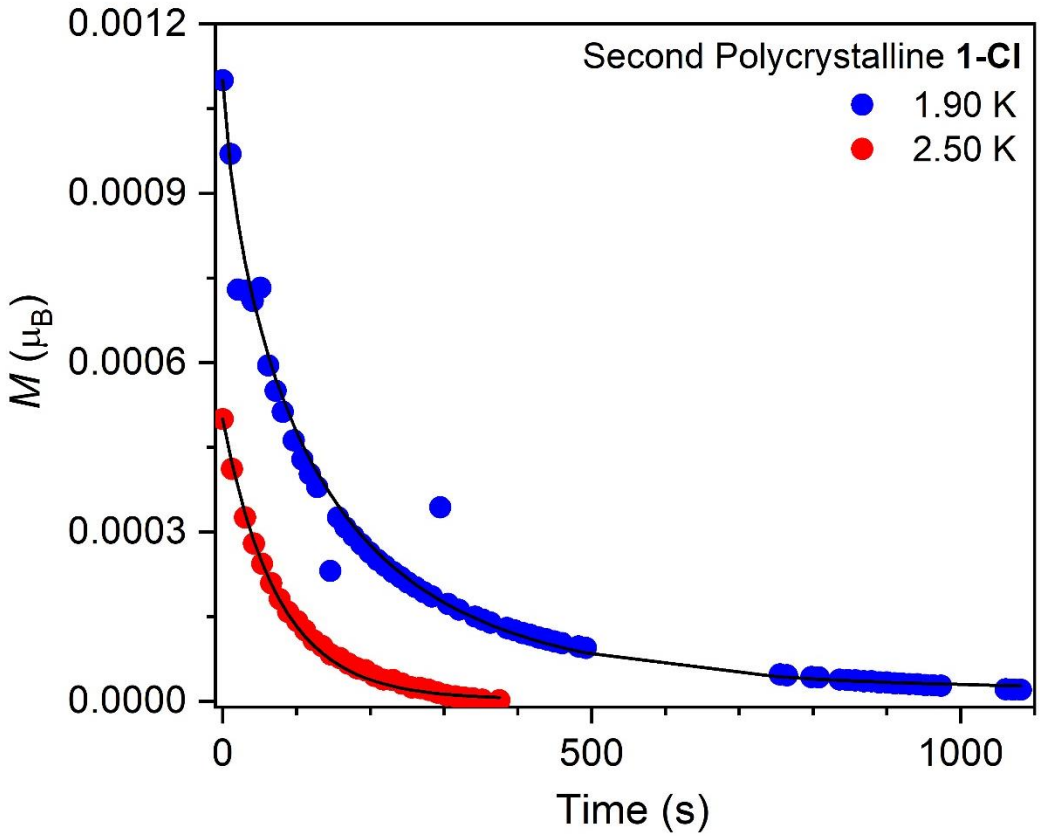

Figure S123. Dc magnetic relaxation data for a second polycrystalline sample of **1-Cl** collected at 1.90 and 2.50 K at zero field following magnetization at 2 T. Black lines represent fits to the data using stretched exponential functions, which were used to extract τ.

Table S27. Parameters used to fit dc magnetic relaxation data for a second polycrystalline sample of **1-Cl** collected under zero applied magnetic field, the magnetic relaxation times extracted from these fits, and the uncertainty ranges for the magnetic relaxation times.

T (K)	M_0 (μ_B)	M_1 (μ_B)	n	τ (s)	$\boldsymbol{\tau_+(1\sigma)}^{\dagger}$ (s)	$\boldsymbol{\tau_-(1\sigma)}^{\dagger}$ (s)
1.90	1.1×10^{-3}	2.0×10^{-5}	0.74	123	287	52.4
2.50	5.0×10^{-4}	3.6×10^{-6}	1	74	78	71

$^{\dagger}\tau_{\pm,}(1\sigma)$ is the uncertainty range for one standard deviation from the mean

6.8 Analysis of Magnetic Relaxation Dynamics. Plots of the natural logarithm of the relaxation times, ln(τ), versus the inverse temperature, 1/*T*, (i.e., Arrhenius plots) for values extracted from ac susceptibility data for $(Cp^{iPr5})_2U_2(OPh^{tBu})_4$ and **1-X** (X = Cl, Br, I) (as well as dc relaxtion data, in the case of **1-Cl**) were fit to a sum of one more terms describing the mechanism(s) of magnetic relaxation according to the equation:

$$\tau^{-1} = \tau_0^{-1} e^{-U_{\text{eff}}/k_B T} + CT^n + \tau_{\text{tunnel}}^{-1}$$

where τ is the magnetic relaxation time, τ_0 is the attempt time (for an Orbach relaxation process), U_{eff} is the thermal barrier to magnetization reversal (for Orbach process), k_B is the Boltzmann constant (0.695 $cm^{-1}K^{-1}$), *T* is the temperature (in K), *C* and *n* are free-fit parameters that describe Raman relaxation, and τ_{tunnel} is the relaxation time for quantum tunneling of the magnetization.

The magnetic relaxation behavior observed for the measured samples can be divided into two categories: (1) complexes with weak/negligible magnetic exchange coupling, namely $(Cp^{iPr5})_2U_2(OPh^{tBu})_4$ and **1-I**, for which plots of ln(τ) versus 1/T are non-linear, and can be fit adequately using a sum of through-barrier magnetic relaxation processes, namely Raman relaxation and quantum tunneling:

$$\tau^{-1} = CT^n + \tau_{\text{tunnel}}^{-1}$$

In contrast, category (2) involves the complexes exhibiting strong magnetic exchange coupling, **1-Cl** and **1-Br**, for which all or part of the plots of ln(τ) versus 1/*T* was found to be linear, and could be fit to an Orbach relaxation process, or sum of Orbach and quantum tunneling processes:

$$\tau^{-1} = \tau_0^{-1} e^{-U_{\text{eff}}/k_B T} + \tau_{\text{tunnel}}^{-1}$$

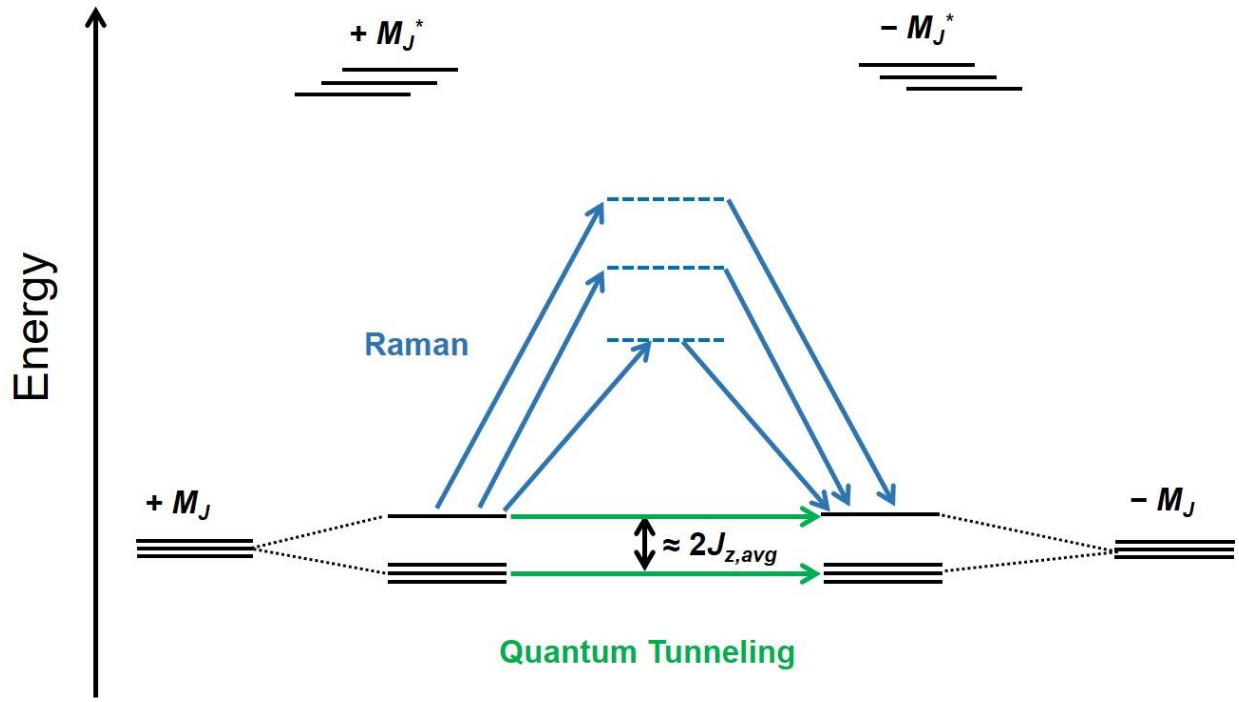

Figure S124. Magnetic relaxation in complexes with relatively weak magnetic exchange interactions (using the Ising model). If the exchange-coupling is weak enough, such as in $(Cp^{iPr5})_3U_3I_6$ (**1-I**), then the excited exchange-coupled states are also thermally populated and magnetic relaxation is associated with the magnetic moments of the individual uranium ions. For **1-I**, in which all three uranium ions are inequivalent by symmetry, three relaxation processes are possible, in principle. In both cases, through-barrier relaxation processes, namely quantum tunneling and Raman relaxation, dominate the magnetization dynamics.

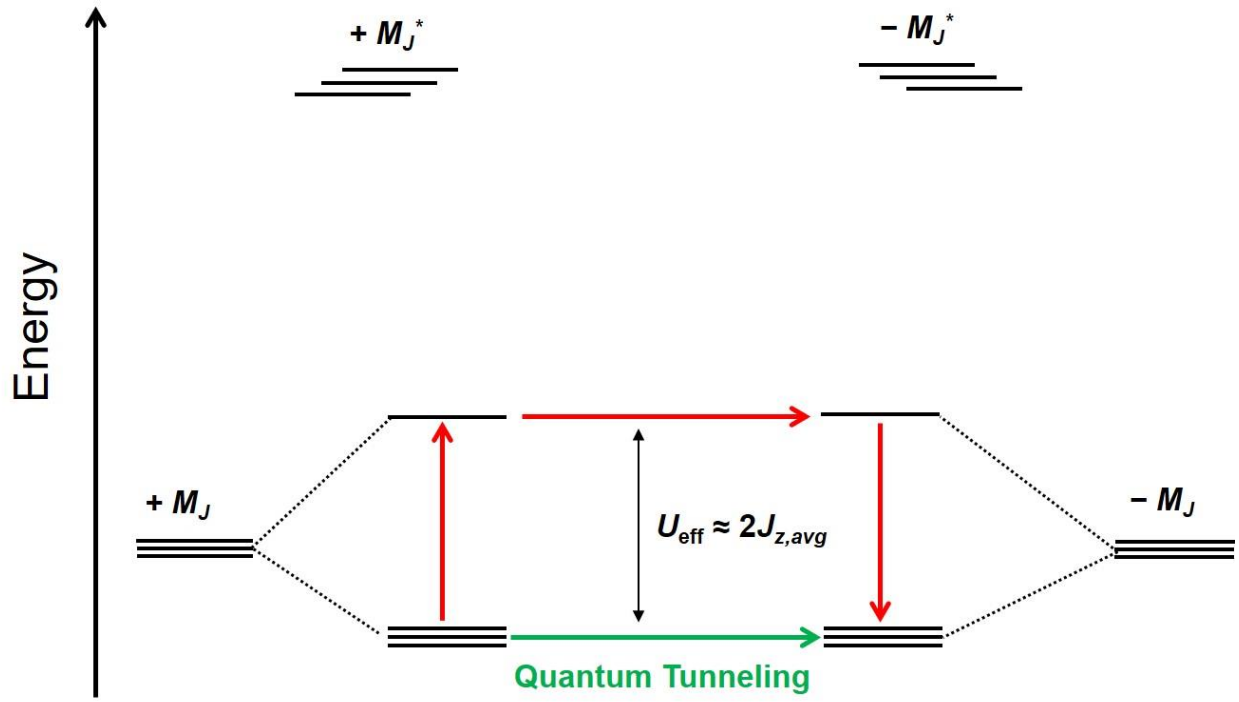

Figure S125. Magnetic relaxation in complexes exhibiting relatively strong magnetic exchange (using the Ising model). If the exchange-coupling is strong enough for the excited exchange-coupled states to remain thermally unpopulated, such as is proposed for $(Cp^{iPr5})_3U_3Cl_6$ (**1-Cl**) and $(Cp^{iPr5})_3U_3Br_6$ (**1-Br**), then magnetic relaxation would occur between the exchange-coupled states, and the magnetization dynamics would be dominated by Orbach relaxation processes. The evidence of quantum tunneling in **1-Cl** and **1-Br** at very low temperatures in the zero-field ac data indicates that the ground M_J states of each uranium ion are not fully axial (if g_x, $g_y > 0$, tunnel splitting occurs), and therefore the Ising model is not fully valid.[48] In perfectly Ising systems, this quantum tunneling process will not occur. Nevertheless, assuming that $g_z > g_x$, g_y in these complexes, we have used the measured barrier to relaxation, U_{eff}, for **1-Cl** and **1-Br** to approximate the average exchange coupling strength in both complexes, using the relation $U_{eff} \approx 2J_{z,avg} \approx 2J_{avg}$ (J_{avg} is the average exchange interaction), which is valid if the energetic separation between the ground antiferromagnetic states are negligible. In the case of **1-Cl**, two relaxation processes are observed, suggesting that magnetic relaxation may also be occurring via an excited state of an individual uranium ion ($\pm M_J^*$).

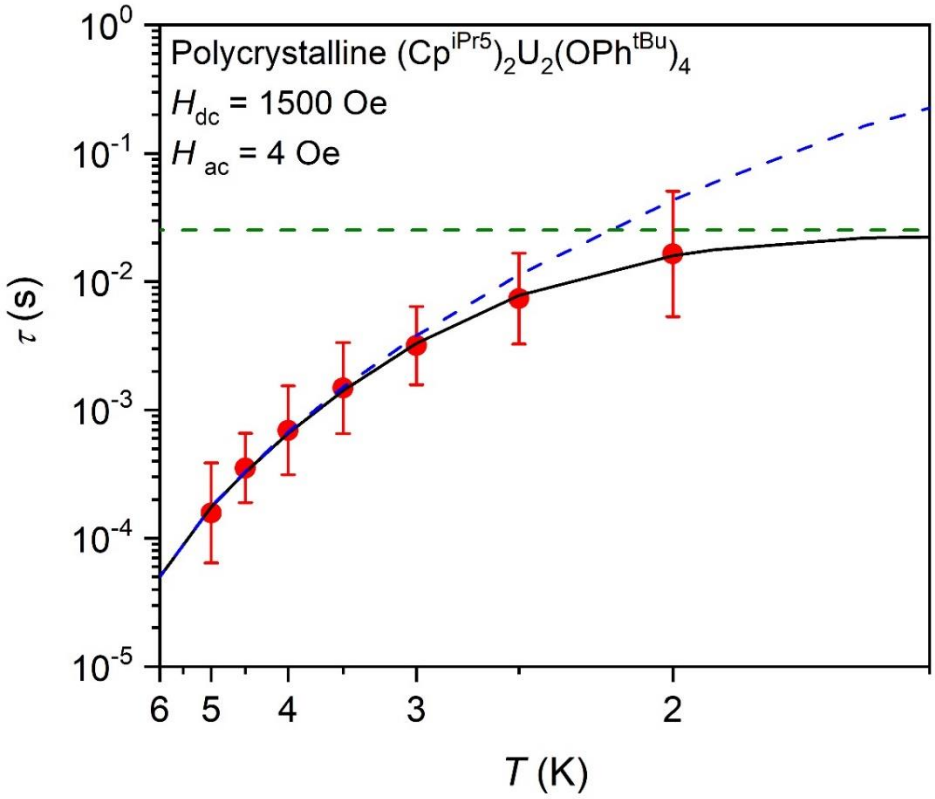

Figure S126. Plot of the relaxation time, τ (natural log scale) versus T (inverse scale) for $(Cp^{iPr5})_2U_2(OPh^{tBu})_4$ collected under a 1500 Oe applied dc field, in the temperature range of 2.0 to 5.0 K. The black line represents the total fit to the data, while the green and blue dashed lines represent the tunneling and Raman components to the total fit, respectively, yielding τ_{tunnel} = 0.0253(9) s, C = 0.36(3) s^{-1} K^{-n}, and n = 6.00(5). The $\tau_{\pm}(1\sigma)$ uncertainty ranges for each τ value are displayed as error bars.

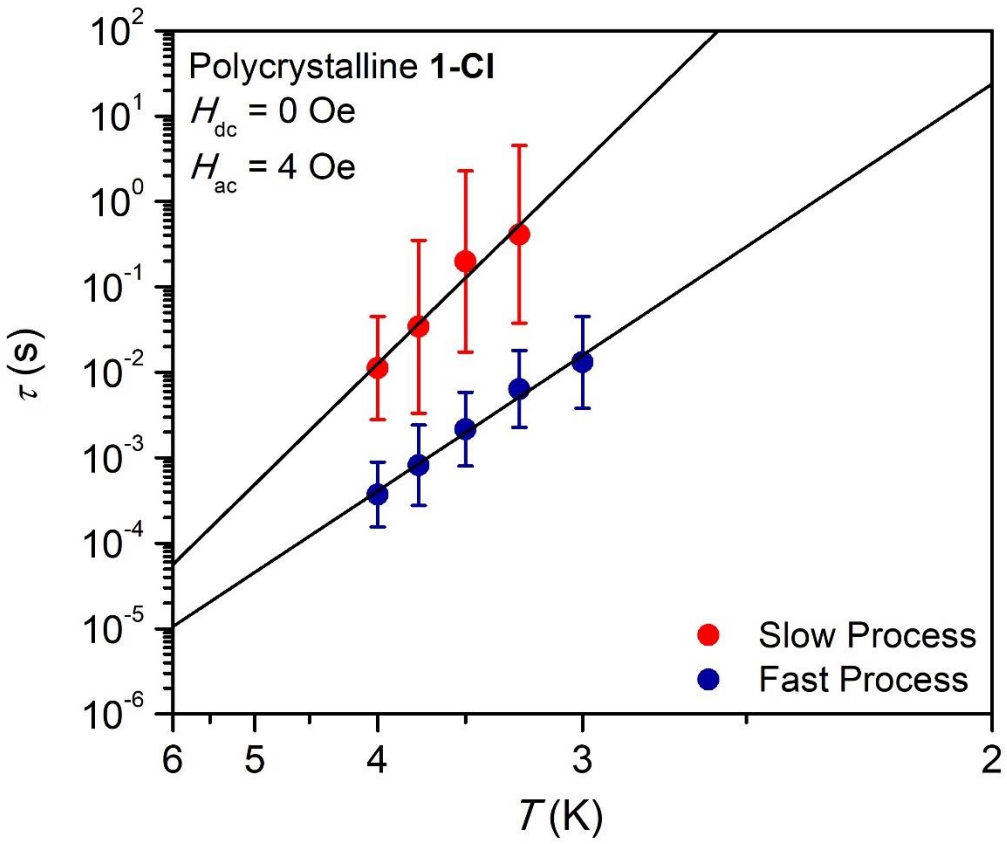

Figure S127. Plot of the relaxation time, τ (natural log scale) versus T (inverse scale) for **1-Cl**. Relaxation times were extracted from fits to the ac susceptibility data collected under zero applied field. Relaxation times for the slow and fact process are shown as red and blue circles, respectively. Black lines represent fits of the data to an Orbach relaxation process, yielding U_{eff} = 45.1(1) cm^{-1} and 30.49(9) cm^{-1}, and $\tau_0 = 10^{-8.94(3)}$ s and $10^{-8.15(2)}$ s for the slow and fast processes, respectively. The $\tau_{\pm}(1\sigma)$ uncertainty ranges for each τ value are displayed as error bars.

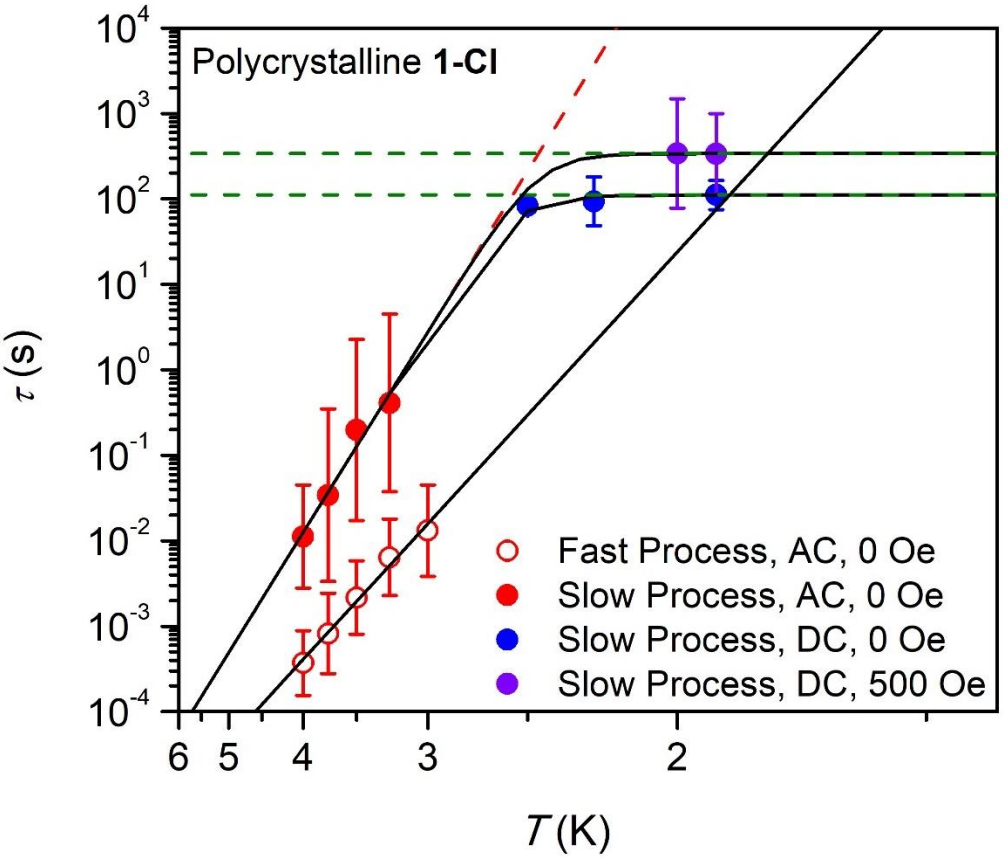

Figure S128. Plot of the relaxation time, τ (natural log scale) versus T (inverse scale) for polycrystalline **1-Cl**. Relaxation times extracted from ac susceptibility measurements are represented by red circles (filled circles for slow process and open circles for fast process); relaxation times extracted from dc susceptibility measurements are represented by blue circles (0 Oe) and violet circles (500 Oe). Dashed green and red lines represent fits to quantum tunneling and Orbach relaxation processes, respectively. Solid black lines represent the total fit to the data. The $\tau_{\pm}(1\sigma)$ uncertainty ranges for each τ value are displayed as error bars.

Table S28. Parameters used to fit Arrhenius plots for polycrystalline **1-Cl**. Values of τ_0 and U_{eff} obtained from fitting the zero-field data for the slow process were used as fixed parameters in fitting the 500 Oe data to extract τ_{tunnel}.

Process	H_{dc} (Oe)	τ_{tunnel} (s)	τ_0 (s)	U_{eff} (cm^{-1})
Slow	0	111(9)	$10^{-8.94(3)}$	45.1(1)
	500	339(23)	$10^{-8.94(3)}$	45.1(1)
Fast	0	–	$10^{-8.15(2)}$	30.49(9)

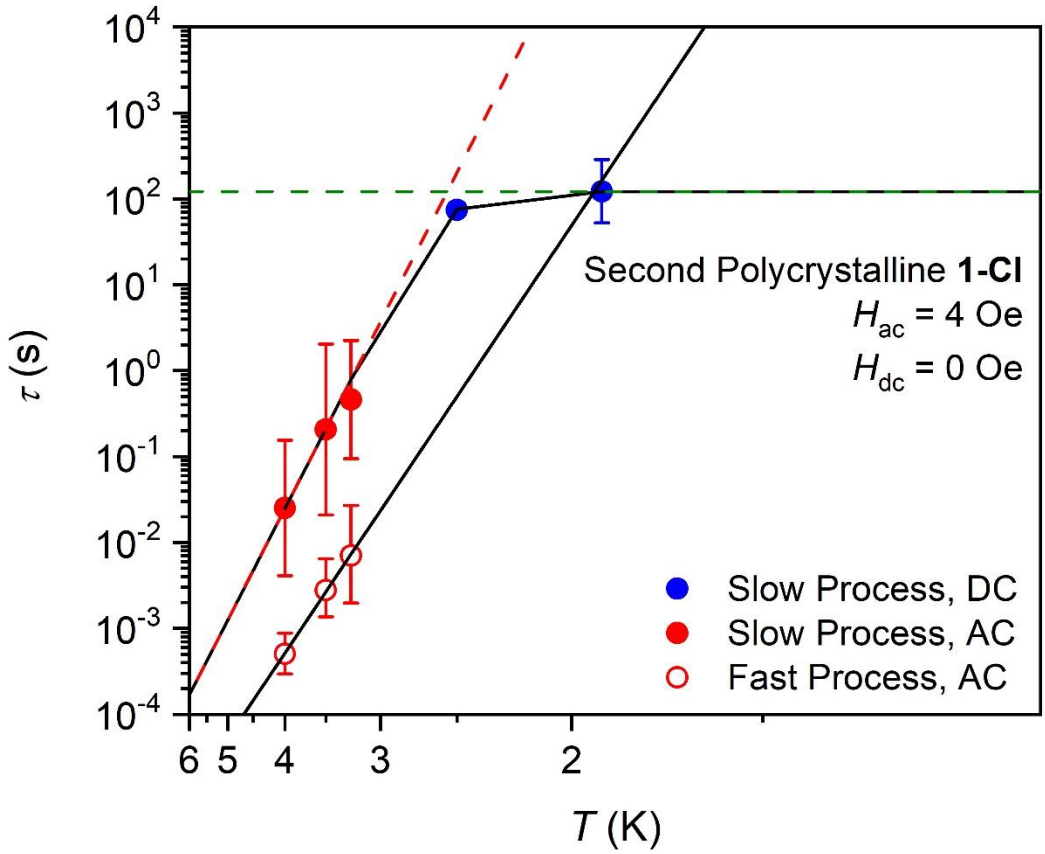

Figure S129. Plot of the relaxation time, τ (natural log scale) versus T (inverse scale) for polycrystalline **1-Cl**. Relaxation times extracted from ac susceptibility measurements are represented by red circles (filled circles for slow process and open circles for fast process); relaxation times extracted from dc susceptibility measurements are represented by blue circles (0 Oe) and violet circles (500 Oe). Dashed green and red lines represent fits to quantum tunneling and Orbach relaxation processes, respectively. Solid black lines represent the total fit to the data. The $\tau_{\pm}(1\sigma)$ uncertainty ranges for each τ value are displayed as error bars.

Table S29. Parameters used to fit Arrhenius plots for a second polycrystalline sample of **1-Cl**.

Process	H_{dc} (Oe)	τ_{tunnel} (s)	τ_0 (s)	U_{eff} (cm^{-1})
Slow	0	121.1(7)	$10^{-8.12(1)}$	41.71(1)
Fast	0	–	$10^{-8.26(2)}$	31.86(1)

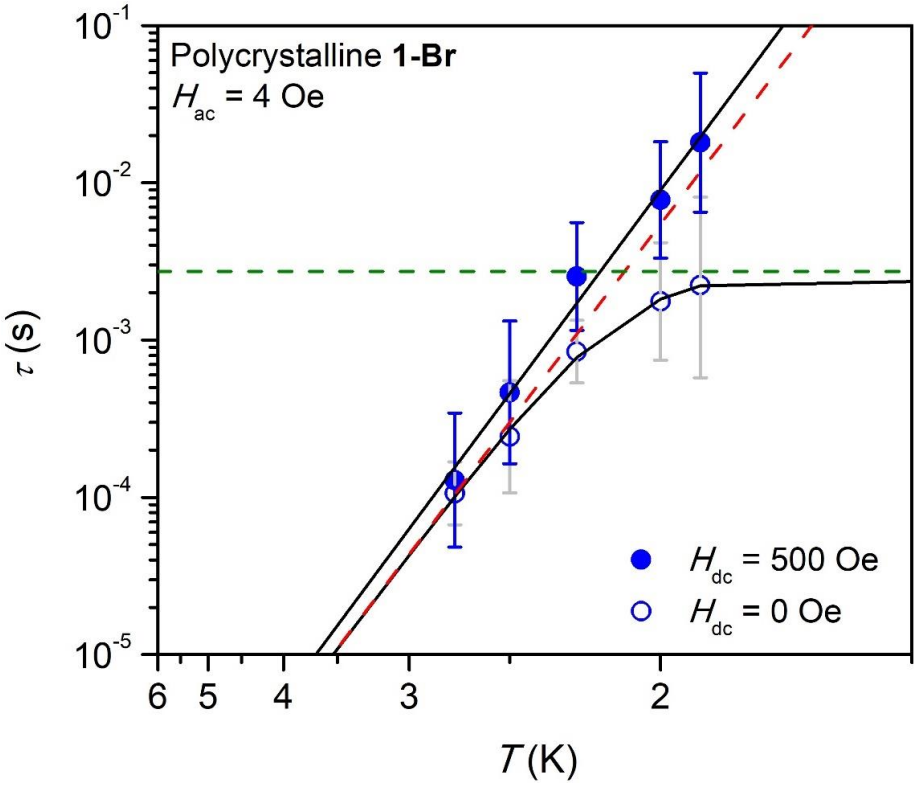

Figure S130. Plot of the relaxation time, τ (natural log scale) versus T (inverse scale) for polycrystalline **1-Br** collected under both 0 Oe (open circles) and 500 Oe (filled blue circles) applied dc field, in the temperature range of 1.9 to 3.0 K. All relaxation times were extracted from fits to ac susceptibility data. The black lines represent the total fits to the data, while the green and red dashed lines represent the tunneling and Orbach components to the total fit, respectively, yielding U_{eff} = 20.1(1) and 20.7(1) cm^{-1} and $\tau_0 = 10^{-8.56(2)}$ and $10^{-8.50(4)}$ s for the 0 and 500 Oe data, respectively (additionally, τ_{tunnel} = 0.0027(1) s for the 0 Oe data). The $\tau_{\pm}(1\sigma)$ uncertainty ranges for each τ value are displayed as error bars in light gray (for zero field data) or blue (for 500 Oe data).

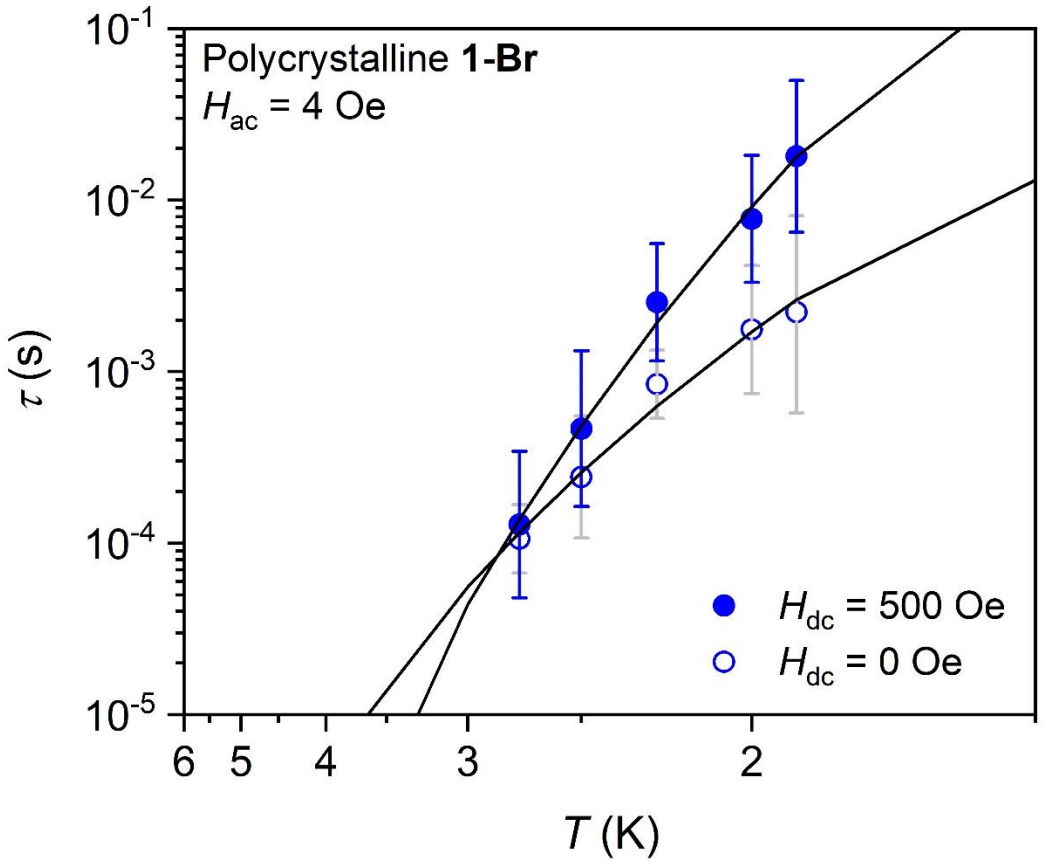

Figure S131. Plot of the relaxation time, τ (natural log scale) versus T (inverse scale) for polycrystalline **1-Br** collected under zero applied field (open circles) and a 500 Oe applied field (filled blue circles) in the temperature range of 1.9 to 3.0 K. All relaxation times were extracted from fits to ac susceptibility data. Black lines represent fits to a Raman relaxation process, according to the equation $\tau^{-1} = CT^n$. In principle, n should have a value of 9 for a Kramers system,[54] but other values have been found in practice, due to the inadequacy of the Debye model to adequately describe the phonon density distributions in molecular solids,[54,55] and n is therefore typically treated as a free-fit parameter. For the 0 Oe data, we obtained C = 1.7(1) s^{-1} K^{-n} and n = 8.45(4). However, fitting the 500 Oe relaxation data to a Raman process resulted in significantly different values of C = 0.0119(8) s^{-1} K^{-n} and n = 13.17(5). In Kramers systems, it has been shown that Raman relaxation is largely independent of the strength of the applied field.[56] Furthermore, to the best of our knowledge, there is no known precedent for an n value greater than 10 to describe a Raman process. These results strongly suggest then that a Raman relaxation mechanism is not leading to the observed temperature-dependent relaxation in polycrystalline **1-Br**.

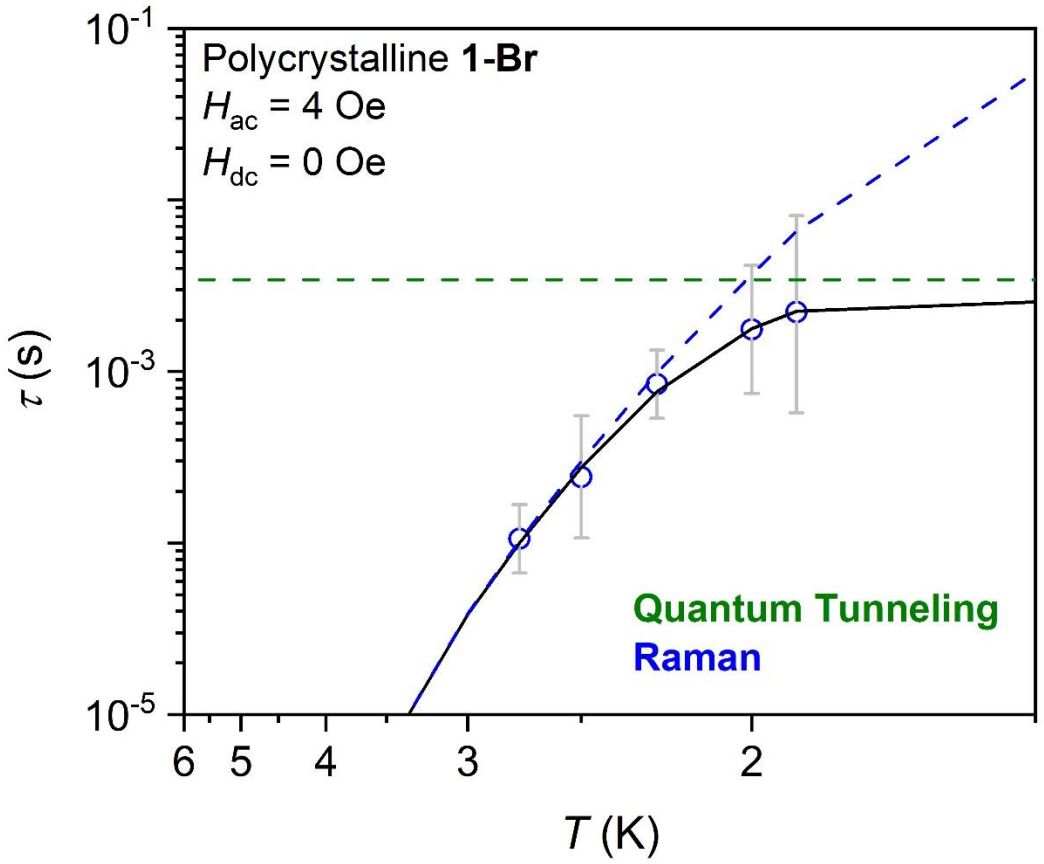

Figure S132. Plot of the relaxation time, τ (natural log scale) versus T (inverse scale) for polycrystalline **1-Br** collected under zero applied field in the temperature range of 1.9 to 3.0 K. Relaxation times were extracted from fits to ac susceptibility data. The black line represents the total fit of the data. Here, we attempted to improve upon the Raman fit (under zero field) in Figure S4.109 through the inclusion of a tunneling process at low temperatures. The blue and green dashed lines correspond to Raman and quantum tunneling processes. In principle, n should have a value of 9 for a Kramers system,[54] but other values have been found in practice, due to the inadequacy of the Debye model to adequately describe the phonon density distributions in molecular solids,[54,55] and n is therefore typically treated as a free-fit parameter. However, in order to fit this data, we had to relax the constraints such that n values greater than 10 could be possible, yielding C = 0.112 (6) s^{-1} K^{-n}, n = 11.23(3), and τ_{tunnel} = 0.0034(2) s. Generally, deviations from the Debye model will lead to smaller n values.[55] To the best of our knowledge, there is no known precedent for values greater than 10. Therefore, a Raman-dominated process does not seem reasonable to explain magnetic relaxation in **1-Br** under zero field.

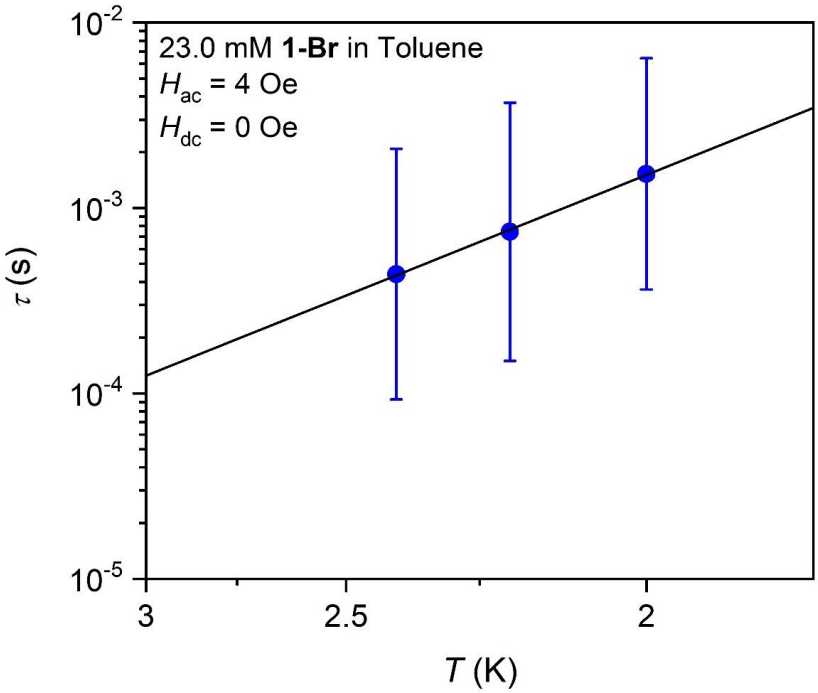

Figure S133. Plot of the relaxation time, τ (natural log scale) versus T (inverse scale) for a 23.0 mM frozen toluene solution of **1-Br** collected under zero dc field, in the temperature range of 2 to 2.4 K. Relaxation times were extracted from fits to ac susceptibility data. The black line represents the fit of the data to an Orbach relaxation process, yielding U_{eff} = 10.406(8) cm^{-1} and $\tau_0 = 10^{-6.070(2)}$ s, and the $\tau_{\pm}(1\sigma)$ uncertainty ranges for each τ value are displayed as error bars. The very small temperature range over which relaxation times could be observed during ac susceptibility measurements, along with the large uncertainties in the measured relaxation times, makes the validity of fitting the relaxation to an Orbach process uncertain. We alternatively found that we could fit the relaxation times to a Raman process, yielding C = 5.83(6) s^{-1} K^{-n} and n = 6.841(6), which are also reasonable for uranium-based single-molecule magnets.[57]

Table S30. Parameters used to fit Arrhenius plots for polycrystalline and 23.0 mM frozen toluene solutions of **1-Br**.

Sample	H_{dc} (Oe)	τ_{tunnel} (s)	τ_0 (s)	U_{eff} (cm^{-1})
Polycrystalline	0	0.0027(1)	$10^{-8.56(2)}$	20.1(1)
	500	–	$10^{-8.50(4)}$	20.7(1)
23.0 mM Solution	0	–	$10^{-6.070(2)}$	10.406(8)

Table S31. Estimated values of the average exchange interaction, J_{avg}, for **1-Cl** and **1-Br**, based on their corresponding U_{eff} values, and comparison with the temperature at which χ_M reaches a maximum (H_{dc} = 0.1 T for polycrystalline samples; H_{dc} = 7.0 T for 23.0 mM **1-Br**).

Sample	H_{dc} (Oe)	U_{eff} (cm^{-1})	J (cm^{-1})	$T_{\chi,max}$ (K)
Polycrystalline 1-Cl	0	45.1(1)	−22.5(1)	28
		30.49(9)	−15.25(5)	
Polycrystalline 1-Br	0	20.1(1)	−10.1(1)	17
	500	20.7(1)	−10.3(1)	
23.0 mM 1-Br	0	10.406(8)	−5.203(4)	11

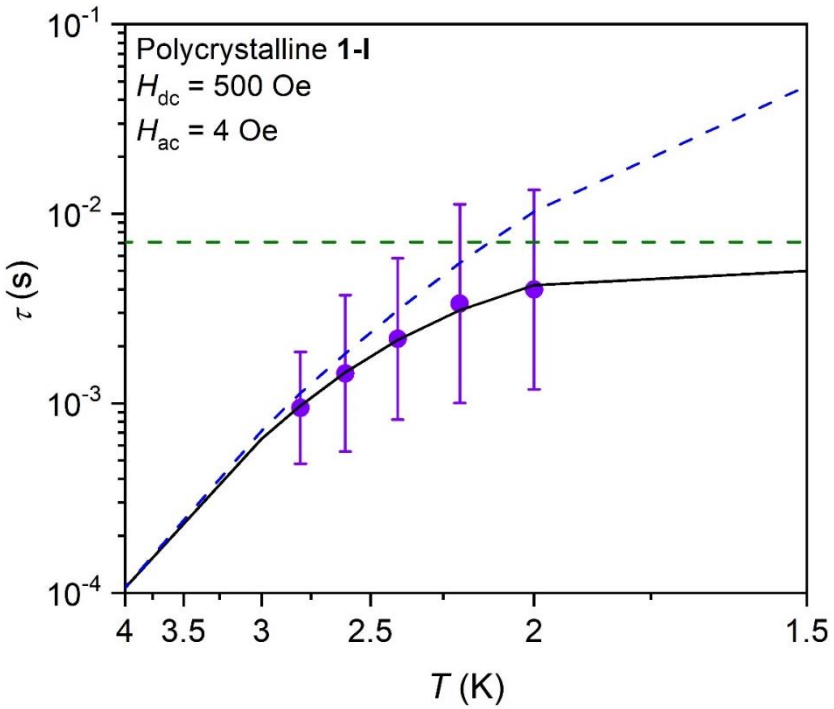

Figure S134. Plot of the relaxation time, τ (natural log scale) versus T (inverse scale) for **1-I**. Relaxation times were extracted from ac susceptibility data collected under a 500 Oe dc field, in the temperature range of 2 to 2.8 K. The black line represents the total fit to the data, while the green and blue dashed lines represent the tunneling and Raman components to the total fit, respectively, yielding τ_{tunnel} = 0.0071(2) s, C = 1.01(3) s^{-1} K^{-n}, and n = 6.59(2). The $\tau_{\pm}(1\sigma)$ uncertainty ranges for each τ value are displayed as error bars. We note that attempts to fit the magnetic relaxation times to a sum of Orbach and tunneling processes yielded a reasonable fit, with U_{eff} = 14.95(5) cm^{-1}, $\tau_0 = 10^{-6.270(7)}$ s, and τ_{tunnel} = 0.00486(7) s, suggesting that a thermal barrier to relaxation might be present.[58] However, this barrier would imply a J_{avg} = 7.5 cm^{-1} that is larger than what might be expected based on the temperature at which χ_M reaches a maximum, 5 K (k_BT = 3.5 cm^{-1}). This discrepancy might be due to deviations from Ising behavior; however, the value of τ_0 for **1-I** is also larger than those obtained from fits of the relaxation times for **1-Cl** and **1-Br**, which would imply a weaker spin-phonon interaction in **1-I**.[59,60] This seems unlikely, given the weaker exchange interaction present in **1-I**. Furthermore, the presence of another, faster relaxation process in the ac measurements on **1-I** implies that the uranium ions are relaxing independently of each other, suggesting that magnetic relaxation is not occurring between the exchange-coupled states, similar to the case in many multinuclear lanthanide complexes with weak exchange interactions.[61] We acknowledge that a similar argument, based on the magnitude of τ_0, may hold for the data collected for the solution sample of **1-Br**. As mentioned in Figure S133, the relaxation behavior for the frozen toluene solution of **1-Br** could also reasonably be fit using the equation for Raman relaxation. The ambiguity in the mechanism of magnetic relaxation for the toluene solution of **1-Br** and the polycrystalline sample of **1-I** strongly suggests that as the magnetic exchange interactions in **1-X** become weaker, magnetic relaxation occurs via a Raman process associated with individual uranium(III) ions.

7. Supplementary Information References

(1) Fulmer, G. R.; Miller, A. J. M.; Sherden, N. H.; Gottlieb, H. E.; Nudelman, A.; Stoltz, B. M.; Bercaw, J. E.; Goldberg, K. I. NMR Chemical Shifts of Trace Impurities: Common Laboratory Solvents, Organics, and Gases in Deuterated Solvents Relevant to the Organometallic Chemist. *Organometallics* **2010**, *29* (9), 2176–2179.

(2) Dezember, T.; Sitzmann, H. Die Fulven-Route Zum Pentaisopropylcyclopentadienid / The Fulvene Route to Pentaisopropylcyclopentadienide. *Z. Für Naturforschung B* **1997**, *52* (8), 911–918.

(3) McClain, K. R.; Gould, C. A.; Chakarawet, K.; Teat, S. J.; Groshens, T. J.; Long, J. R.; Harvey, B. G. High-Temperature Magnetic Blocking and Magneto-Structural Correlations in a Series of Dysprosium(III) Metallocenium Single-Molecule Magnets. *Chem. Sci.* **2018**, *9* (45), 8492–8503.

(4) Monreal, M. J.; Thomson, R. K.; Cantat, T.; Travia, N. E.; Scott, B. L.; Kiplinger, J. L. $UI_4(1,4\text{-Dioxane})_2$, $[UCl_4(1,4\text{-Dioxane})]_2$, and $UI_3(1,4\text{-Dioxane})_{1.5}$: Stable and Versatile Starting Materials for Low- and High-Valent Uranium Chemistry. *Organometallics* **2011**, *30* (7), 2031–2038.

(5) Cloke, F. G. N.; Hitchcock, P. B. Reversible Binding and Reduction of Dinitrogen by a Uranium(III) Pentalene Complex. *J. Am. Chem. Soc.* **2002**, *124* (32), 9352–9353.

(6) Spedding, F. H.; Newton, A. S. Uranium Hydride; Preparation, Composition and Physical Properties. *Nucleonics* **1949**, *4* (1), 4.

(7) Gould, C. A.; McClain, K. R.; Reta, D.; Kragskow, J. G. C.; Marchiori, D. A.; Lachman, E.; Choi, E.-S.; Analytis, J. G.; Britt, R. D.; Chilton, N. F.; Harvey, B. G.; Long, J. R. Ultrahard Magnetism from Mixed-Valence Dilanthanide Complexes with Metal-Metal Bonding. *Science* **2022**, *375* (6577), 198–202.

(8) Guo, F.-S.; Chen, Y.-C.; Tong, M.-L.; Mansikkamäki, A.; Layfield, R. A. Uranocenium: Synthesis, Structure, and Chemical Bonding. *Angew. Chem. Int. Ed.* **2019**, *58* (30), 10163–10167.

(9) Arnold, P. L.; Stevens, C. J.; Farnaby, J. H.; Gardiner, M. G.; Nichol, G. S.; Love, J. B. New Chemistry from an Old Reagent: Mono- and Dinuclear Macrocyclic Uranium(III) Complexes from $[U(BH_4)_3(THF)_2]$. *J. Am. Chem. Soc.* **2014**, *136* (29), 10218–10221.

(10) Boronski, J. T.; Doyle, L. R.; Seed, J. A.; Wooles, A. J.; Liddle, S. T. F-Element Half-Sandwich Complexes: A Tetrasilylcyclobutadienyl–Uranium(IV)–Tris(Tetrahydroborate) Anion Pianostool Complex. *Angew. Chem. Int. Ed.* **2020**, *59* (1), 295–299.

(11) Boreen, M. A.; Lussier, D. J.; Skeel, B. A.; Lohrey, T. D.; Watt, F. A.; Shuh, D. K.; Long, J. R.; Hohloch, S.; Arnold, J. Structural, Electrochemical, and Magnetic Studies of Bulky Uranium(III) and Uranium(IV) Metallocenes. *Inorg. Chem.* **2019**, *58* (24), 16629–16641.

(12) Karbowiak, M.; Drożdżyński, J. Absorption Spectrum Analysis of Uranium(III) Formate. *J. Alloys Compd.* **2000**, *300–301*, 329–333.

(13) Mills, D. P.; Moro, F.; McMaster, J.; van Slageren, J.; Lewis, W.; Blake, A. J.; Liddle, S. T. A Delocalized Arene-Bridged Diuranium Single-Molecule Magnet. *Nat. Chem.* **2011**, *3* (6), 454–460.

(14) Liddle, S. T. The Renaissance of Non-Aqueous Uranium Chemistry. *Angew. Chem. Int. Ed.* **2015**, *54* (30), 8604–8641.

(15) *The Chemistry of the Actinide and Transactinide Elements*; Morss, L. R., Edelstein, N. M., Fuger, J., Eds.; Springer Netherlands: Dordrecht, **2006**.

(16) Norel, L.; Darago, L. E.; Le Guennic, B.; Chakarawet, K.; Gonzalez, M. I.; Olshansky, J. H.; Rigaut, S.; Long, J. R. A Terminal Fluoride Ligand Generates Axial Magnetic Anisotropy in Dysprosium Complexes. *Angew. Chem. Int. Ed.* **2018**, *57* (7), 1933–1938.
(17) Escalera-Moreno, L.; Baldoví, J. J.; Gaita-Ariño, A.; Coronado, E. Design of High-Temperature f-Block Molecular Nanomagnets through the Control of Vibration-Induced Spin Relaxation. *Chem. Sci.* **2020**, *11* (6), 1593–1598.
(18) Benelli, C.; Gatteschi, D. *Introduction to Molecular Magnetism: From Transition Metals to Lanthanides*; Wiley-VCH: Weinheim, **2015**.
(19) Rinehart, J. D.; Long, J. R. Exploiting Single-Ion Anisotropy in the Design of f-Element Single-Molecule Magnets. *Chem. Sci.* **2011**, *2* (11), 2078–2085.
(20) Selbin, J.; Ortego, J. D. Chemistry of Uranium (V). *Chem. Rev.* **1969**, *69* (5), 657–671.
(21) Lewis, A. J.; Mullane, K. C.; Nakamaru-Ogiso, E.; Carroll, P. J.; Schelter, E. J. The Inverse Trans Influence in a Family of Pentavalent Uranium Complexes. *Inorg. Chem.* **2014**, *53* (13), 6944–6953.
(22) Neidig, M. L.; Clark, D. L.; Martin, R. L. Covalency in F-Element Complexes. *Coord. Chem. Rev.* **2013**, *257* (2), 394–406.
(23) Sheldrick, G. M. Crystal Structure Refinement with SHELXL. *Acta Crystallogr. Sect. C Struct. Chem.* **2015**, *71* (1), 3–8.
(24) Dolomanov, O. V.; Bourhis, L. J.; Gildea, R. J.; Howard, J. a. K.; Puschmann, H. OLEX2: A Complete Structure Solution, Refinement and Analysis Program. *J. Appl. Crystallogr.* **2009**, *42* (2), 339–341.
(25) Boronski, J. T.; Doyle, L. R.; Wooles, A. J.; Seed, J. A.; Liddle, S. T. Synthesis and Characterization of an Oxo-Centered Homotrimetallic Uranium(IV)–Cyclobutadienyl Dianion Complex. *Organometallics* **2020**, *39*, 10, 1824–1831.
(26) Larch, C. P.; Cloke, F. G. N.; Hitchcock, P. B. Activation and Reduction of Diethyl Ether by Low Valent Uranium: Formation of the Trimetallic, Mixed Valence Uranium Oxo Species $[U(Cp^{RR'})(\mu\text{-}I)_2]_3(\mu^3\text{-}O)$ ($Cp^{RR'} = C_5Me_5$, C_5Me_4H, $C_5H_4SiMe_3$). *Chem. Commun.* **2007**, No. 1, 82–84.
(27) Bain, G. A.; Berry, J. F. Diamagnetic Corrections and Pascal's Constants. *J. Chem. Educ.* **2008**, *85* (4), 532.
(28) Myers, A. J.; Rungthanaphatsophon, P.; Behrle, A. C.; Vilanova, S. P.; Kelley, S. P.; Lukens, W. W.; Walensky, J. R. Structure and Properties of $[(4,6\text{-}^tBu_2C_6H_2O)_2Se]_2An(THF)_2$, An = U, Np, and Their Reaction with p-Benzoquinone. *Chem. Commun.* **2018**, *54* (74), 10435–10438.
(29) Myers, A. J.; Tarlton, M. L.; Kelley, S. P.; Lukens, W. W.; Walensky, J. R. Synthesis and Utility of Neptunium(III) Hydrocarbyl Complex. *Angew. Chem. Int. Ed.* **2019**, *58* (42), 14891–14895.
(30) Boreen, M. A.; Gould, C. A.; Booth, C. H.; Hohloch, S.; Arnold, J. Structure and Magnetism of a Tetrahedral Uranium(III) β-Diketiminate Complex. *Dalton Trans.* **2020**, *49* (23), 7938–7944.
(31) Behrle, A. C.; Myers, A. J.; Rungthanaphatsophon, P.; Lukens, W. W.; Barnes, C. L.; Walensky, J. R. Uranium(III) and Thorium(IV) Alkyl Complexes as Potential Starting Materials. *Chem. Commun.* **2016**, *52* (100), 14373–14375.
(32) Shapira, Y.; Bindilatti, V. Magnetization-Step Studies of Antiferromagnetic Clusters and Single Ions: Exchange, Anisotropy, and Statistics. *J. Appl. Phys.* **2002**, *92* (8), 4155–4185.

(33) Ungur, L.; Heuvel, W. V. den; Chibotaru, L. F. Ab Initio Investigation of the Non-Collinear Magnetic Structure and the Lowest Magnetic Excitations in Dysprosium Triangles. *New J. Chem.* **2009**, *33* (6), 1224–1230.
(34) Carlin, R. L. *Magnetochemistry*; Springer Berlin Heidelberg, **1986**.
(35) Lines, M. E. Orbital Angular Momentum in the Theory of Paramagnetic Clusters. *J. Chem. Phys.* **2003**, *55* (6), 2977–2984.
(36) Abragam, A.; Bleaney, B. *Electron Paramagnetic Resonance of Transition Ions*; Oxford Classic Texts in the Physical Sciences; OUP Oxford, **2012**.
(37) Meng, Y.-S.; Qiao, Y.-S.; Yang, M.-W.; Xiong, J.; Liu, T.; Zhang, Y.-Q.; Jiang, S.-D.; Wang, B.-W.; Gao, S. Weak Exchange Coupling Effects Leading to Fast Magnetic Relaxations in a Trinuclear Dysprosium Single-Molecule Magnet. *Inorg. Chem. Front.* **2020**, *7* (2), 447–454.
(38) Tang, J.; Hewitt, I.; Madhu, N. T.; Chastanet, G.; Wernsdorfer, W.; Anson, C. E.; Benelli, C.; Sessoli, R.; Powell, A. K. Dysprosium Triangles Showing Single-Molecule Magnet Behavior of Thermally Excited Spin States. *Angew. Chem. Int. Ed.* **2006**, *45* (11), 1729–1733.
(39) Chibotaru, L. F.; Ungur, L.; Soncini, A. The Origin of Nonmagnetic Kramers Doublets in the Ground State of Dysprosium Triangles: Evidence for a Toroidal Magnetic Moment. *Angew. Chem. Int. Ed.* **2008**, *47* (22), 4126–4129.
(40) Wang, W.; Shang, T.; Wang, J.; Yao, B.-L.; Li, L.-C.; Ma, Y.; Wang, Q.-L.; Zhang, Y.-Z.; Zhang, Y.-Q.; Zhao, B. Slow Magnetic Relaxation in a Dy_3 Triangle and a Bistriangular Dy_6 Cluster. *Dalton Trans.* **2022**, *51* (24), 9404–9411.
(41) Wu, J.; Zhang, F.; Wang, G.-L.; Demeshko, S.; Dechert, S.; Zhang, Y.-Q.; Meyer, F. Ligand Modulation of the Structures and Magnetic Relaxation in Triangular Dy_3 Complexes Based on a Tricompartmental Scaffold. *Chem. – Eur. J.* **2023**, *29* (24), e202203494.
(42) Rosen, R. K.; Andersen, R. A.; Edelstein, N. M. $[(MeC_5H_4)_3U]_2[\mu\text{-}1,4\text{-}N_2C_6H_4]$: A Bimetallic Molecule with Antiferromagnetic Coupling between the Uranium Centers. *J. Am. Chem. Soc.* **1990**, *112* (11), 4588–4590.
(43) Magnani, N.; Colineau, E.; Eloirdi, R.; Griveau, J.-C.; Caciuffo, R.; Cornet, S. M.; May, I.; Sharrad, C. A.; Collison, D.; Winpenny, R. E. P. Superexchange Coupling and Slow Magnetic Relaxation in a Transuranium Polymetallic Complex. *Phys. Rev. Lett.* **2010**, *104* (19), 197202.
(44) Gould, C. A.; Mu, E.; Vieru, V.; Darago, L. E.; Chakarawet, K.; Gonzalez, M. I.; Demir, S.; Long, J. R. Substituent Effects on Exchange Coupling and Magnetic Relaxation in 2,2′-Bipyrimidine Radical-Bridged Dilanthanide Complexes. *J. Am. Chem. Soc.* **2020**, *142* (50), 21197–21209.
(45) Prša, K.; Nehrkorn, J.; Corbey, J. F.; Evans, W. J.; Demir, S.; Long, J. R.; Guidi, T.; Waldmann, O. Perspectives on Neutron Scattering in Lanthanide-Based Single-Molecule Magnets and a Case Study of the $Tb_2(\mu\text{-}N_2)$ System. *Magnetochemistry* **2016**, *2* (4), 45–63.
(46) Kahn, O. *Molecular Magnetism*; VCH, **1993**.
(47) Gao, S. *Molecular Nanomagnets and Related Phenomena*, Springer: Berlin **2015**.
(48) Gatteschi, D.; Sessoli, R.; Villain, J. *Molecular Nanomagnets*; Mesoscopic Physics and Nanotechnology; Oxford University Press: Oxford; New York, **2006**.
(49) Guo, Y.-N.; Xu, G.-F.; Guo, Y.; Tang, J. Relaxation Dynamics of Dysprosium(III) Single Molecule Magnets. *Dalton Trans.* **2011**, *40* (39), 9953–9963.

(50) Reta, D.; Chilton, N. F. Uncertainty Estimates for Magnetic Relaxation Times and Magnetic Relaxation Parameters. *Phys. Chem. Chem. Phys.* **2019**, *21* (42), 23567–23575.
(51) Mougel, V.; Chatelain, L.; Pécaut, J.; Caciuffo, R.; Colineau, E.; Griveau, J.-C.; Mazzanti, M. Uranium and Manganese Assembled in a Wheel-Shaped Nanoscale Single-Molecule Magnet with High Spin-Reversal Barrier. *Nat. Chem.* **2012**, *4* (12), 1011–1017.
(52) Chatelain, L.; Walsh, J. P. S.; Pécaut, J.; Tuna, F.; Mazzanti, M. Self-Assembly of a 3d–5f Trinuclear Single-Molecule Magnet from a Pentavalent Uranyl Complex. *Angew. Chem. Int. Ed.* **2014**, *53* (49), 13434–13438.
(53) Blackmore, W. J. A.; Gransbury, G. K.; Evans, P.; Kragskow, J. G. C.; Mills, D. P.; Chilton, N. F. Characterisation of Magnetic Relaxation on Extremely Long Timescales. *Phys. Chem. Chem. Phys.* **2023**, 25, 16735–16744.
(54) Liddle, S. T.; Slageren, J. van. Improving F-Element Single Molecule Magnets. *Chem. Soc. Rev.* **2015**, *44* (19), 6655–6669.
(55) Gu, L.; Wu, R. Origin of the Anomalously Low Raman Exponents in Single Molecule Magnets. *Phys. Rev. B* **2021**, *103* (1), 014401.
(56) Ho, L. T. A.; Chibotaru, L. F. Spin-Lattice Relaxation of Magnetic Centers in Molecular Crystals at Low Temperature. *Phys. Rev. B* **2018**, *97* (2), 024427.
(57) Meihaus, K. R.; Long, J. R. Actinide-Based Single-Molecule Magnets. *Dalton Trans.* **2015**, *44* (6), 2517–2528.
(58) Liu, M.; Peng, X.-H.; Guo, F.-S.; Tong, M.-L. Actinide-Based Single-Molecule Magnets: Alone or in a Group? *Inorg. Chem. Front.* **2023**, 10, 3742–3755.
(59) Lunghi, A.; Totti, F.; Sanvito, S.; Sessoli, R. Intra-Molecular Origin of the Spin-Phonon Coupling in Slow-Relaxing Molecular Magnets. *Chem. Sci.* **2017**, *8* (9), 6051–6059.
(60) Orbach, R.; Bleaney, B. Spin-Lattice Relaxation in Rare-Earth Salts. *Proc. R. Soc. Lond. Ser. Math. Phys. Sci.* **1997**, *264* (1319), 458–484.
(61) Chilton, N. F.; Deacon, G. B.; Gazukin, O.; Junk, P. C.; Kersting, B.; Langley, S. K.; Moubaraki, B.; Murray, K. S.; Schleife, F.; Shome, M.; Turner, D. R.; Walker, J. A. Structure, Magnetic Behavior, and Anisotropy of Homoleptic Trinuclear Lanthanoid 8-Quinolinolate Complexes. *Inorg. Chem.* **2014**, *53* (5), 2528–2534.